



Simulations of Three-Wave Interactions in Microwave Heated Fusion Plasmas

Senstius, Mads Givskov

Publication date:
2020

Document Version
Publisher's PDF, also known as Version of record

[Link back to DTU Orbit](#)

Citation (APA):
Senstius, M. G. (2020). *Simulations of Three-Wave Interactions in Microwave Heated Fusion Plasmas*. Department of Physics, Technical University of Denmark.

General rights

Copyright and moral rights for the publications made accessible in the public portal are retained by the authors and/or other copyright owners and it is a condition of accessing publications that users recognise and abide by the legal requirements associated with these rights.

- Users may download and print one copy of any publication from the public portal for the purpose of private study or research.
- You may not further distribute the material or use it for any profit-making activity or commercial gain
- You may freely distribute the URL identifying the publication in the public portal

If you believe that this document breaches copyright please contact us providing details, and we will remove access to the work immediately and investigate your claim.

PhD Thesis

Simulations of Three-Wave Interactions in Microwave Heated Fusion Plasmas

Mads Givskov Senstius

Supervisors: Stefan Kragh Nielsen and Roddy G. L. Vann

Section for Plasma Physics and Fusion Energy
Department of Physics
Technical University of Denmark

31 March 2020

Abstract

Through thermonuclear fusion of light elements, we wish to develop a clean, safe and reliable source of energy. A popular concept for such a fusion reactor is based on confining a hot plasma fuel by subjecting it to a strong magnetic field. Microwave beams are commonly employed to both heat and diagnose the plasma. During the past 20 years, the microwave beam power has increased to a point where reactors may now be equipped with several microwave source capable of producing a MW each. According to traditional estimates, a microwave beam carrying such power should still behave as predicted by linear theory. An exception was known to be in a resonant region of the plasma called the UH layer. At the UH layer, wave amplification can lead to nonlinear three-wave interactions known as parametric decay instabilities (PDIs). PDIs can excite daughter waves in the plasma at the expense of a strong pump wave such as a high power microwave beam. The pump wave may decay into the daughter waves if selection rules are satisfied and the process becomes unstable above a pump amplitude threshold. In spite of being below estimates for pump amplitude thresholds, observations of signatures of PDIs during heating experiments have started to be reported with the increase in microwave beam power. Although the heating beams do not reach the UH layer in those experiments, the UH layer is still believed to play an important role.

In this thesis, we study PDIs near the UH layer numerically using a particle-in-cell (PIC) code. PIC codes are fully kinetic and make only few assumptions about how the fusion plasma behaves. This way, we can uncover which effects are important in reproducing experimental observations without making potentially biased assumptions about them first. The price is that the simulations are demanding and require the use of high performance computing (HPC) clusters.

First, a relatively simple setup of PDI near the fundamental UH layer is investigated. This is relevant, in particular, to a diagnostic known as collective Thomson scattering (CTS) and heating using electron Bernstein waves (EBWs). We show that wave amplification near the UH layer occurs, which helps overcome the PDI pump threshold. Above a threshold we demonstrate that an electron pump wave can excite an ion wave and another electron wave, satisfying PDI selection rules. Additionally, linear mode conversion is shown to take place at the UH layer. It is shown that the wave resulting from the linear conversion also decays through PDIs.

Next, we investigate PDIs into trapped waves in non-monotonic background density perturbations. The trapping mechanism is linear wave conversion at the UH layer. With a non-monotonic density profile, multiple UH layers can form and some waves can be trapped in a perpetual cycle of linear mode conversion. We show that two types of PDIs known as two plasmon decay (TPD) and stimulated Raman scattering (SRS) can excite the trapped waves.

The TPD instability is shown to have a higher growth rate than the SRS instability. For the first time, we demonstrate numerically that PDI into trapped waves can occur for parameters relevant to microwave beams in magnetically confined fusion plasmas. Furthermore, we show that PDI is possible over a range of density shapes and magnitudes. We study the eigenmode nature of the waves trapped in non-monotonic density profiles and demonstrate that PDIs excite trapped waves only at a discrete spectrum of frequencies. Waves at these frequencies satisfy quantization conditions as they traverse their trapping regions. We show that exciting these eigenmodes can absorb a substantial part of the pump wave. The eigenmodes may in turn become unstable to further PDIs involving other eigenmodes and ion waves. With our PIC simulations, we demonstrate that a series of PDIs can produce emissions akin to experimentally observed spectra. This provides unprecedented numerical evidence that microwave beams in magnetically confined fusion reactors may be at risk of PDIs. The emissions produced in the PDIs may damage microwave sensitive diagnostics if they are not properly shielded.

Resumé

Gennem termonuklear fusion af lette elementer søger vi at udvikle en ren, sikker og pålidelig energikilde. Et af de mest populære fusionsreaktorkoncepter tager udgangspunkt i at indeslutte et varmt plasmabændstof ved at påtvinge det et stærkt magnetisk felt. Mikrobølger bliver ofte brugt til både at opvarme og diagnosticere plasmaet. Gennem de sidste 20 år er den effekt, som man kan generere mikrobølgestråler ved, steget til et punkt, hvor mange reaktorer nu er udstyret med adskillige mikrobølgekilder, der hver kan producere MW stråler. Ifølge traditionelle estimater vil en sådan mikrobølgestråle stadigvæk opføre sig i overensstemmelse med lineær teori. Det har dog været vidst, at et resonant område af plasmaet kaldet det øvre hybridlag (UH-laget) udgjorde en undtagelse. Ved UH-laget kan bølgeforstærkning føre til ikkelineære trebølgevekselvirkninger, som også er kendt som parametriske henfaldsinstabiliteter (PDI'er). PDI'er kan generere datterbølger i plasmaet på bekostning af en stærk pumpbølge såsom en mikrobølgestråle. Pumpbølgen kan henfalde til datterbølgerne, hvis et sæt udvælgelsesregler er opfyldt, og vekselvirkningerne bliver ustabile, når pumpbølgen overstiger en amplitudetærskel. Observationer af signature af PDI'er under pumpbølgens amplitudetærskel er dog blevet rapporteret i takt med, at mikrobølgekilderne er blevet kraftigere. Dette sker på trods af, at opvarmningsstrålerne ikke når UH-laget. Dog menes det, at UH-laget stadigvæk spiller en vigtig rolle.

I denne afhandling undersøger vi PDI'er nær UH-laget numerisk ved brug af en partikel-i-celle-kode (PIC-kode). PIC-koder er fuldt kinetiske og gør kun brug af få antagelser om, hvordan et fusionsplasma opfører sig. På denne måde kan vi afdække hvilke effekter, der er nødvendige for at genskabe de eksperimentelle observationer uden først at lave antagelser, som kan vise sig at være ugyldige. Prisen er, at simuleringerne er krævende og skal køres på supercomputere (HPC'er).

Først undersøger vi PDI ved UH-laget. Dette er relevant især for en type diagnostik kaldet kollektiv Thomson-spredning (CTS) samt ved opvarmning gennem elektron Bernstein-bølger (EBW'er). Vi ser, at der forekommer bølgeforstærkning nær UH-laget, hvilket kan hjælpe med at overkomme PDI pumpamplitudetærsklen. Over en tærskelværdi ser vi, at en elektronpumbølge kan generere en ionbølge samt en anden elektronbølge, som tilsammen opfylder PDI-udvælgelsesreglerne. Ydermere viser vi, at lineær konvertering finder sted ved UH laget. Vi viser desuden, at bølgen, som kommer ud af den lineære konvertering, også kan henfalde gennem PDI'er.

Vi undersøger efterfølgende PDI'er med bølger, der er fangede i ikkemonotone tæthedsforstyrrelser. Mekanismen, som fanger bølgerne, er lineær konvertering ved UH-laget. Med en ikkemonoton tæthedsprofil kan der opstå flere UH-lag, og visse bølger kan blive fanget mellem

dem i endeløse cyklusser af lineær konvertering. Vi viser, at der er to slags PDI kendt som to-plasmon-henfald (TPD) og stimuleret Raman-spredning (SRS), der kan generere fangede bølger. TPD-instabiliteten viser sig at have en højere vækstrate end SRS-instabiliteten. For første gang demonstrerer vi med kinetiske simuleringer, at PDI kan generere fangede bølger gennem mikrobølgestråler i magnetisk indesluttede fusionsplasmaer. Ydermere viser vi, at sådanne PDI'er er muligw over en række af tæthedsprofiler og -størrelser. Vi undersøger de fangede bølgers egenskaber som egentilstande af de ikke monotone tæthedsprofiler og viser, at PDI kun genererer bølger i et diskret spektrum af frekvenser. Bølger ved disse frekvenser tilfredsstiller kvantiseringsbetingelser ved en rundtur gennem det område de er fanget i. Vi viser, at disse bølger kan absorbere en betydelig mængde energi, når de genereres. Egentilstandene kan også blive ustabile og henfalde yderligere gennem PDI til andre egentilstande samt ionbølger. Med vores PIC-simuleringer demonstrerer vi numerisk, at en række af PDI'er kan producere mikrobølgestråling lig den, der er blevet observeret eksperimentelt. Mikrobølgestrålingen kan skade udstyr, som er følsomt overfor mikrobølger, hvis de ikke er beskyttet tilstrækkeligt.

Preface

The present thesis is submitted as fulfillment of the prerequisites for obtaining the PhD degree at the Technical University of Denmark (DTU). The work has been carried out at the Department of Physics with the section for Plasma Physics and Fusion Energy from April 2017 to March 2020 and with an external research stay at York Plasma Institute (YPI) from September 2017 to March 2018. The work was supported by research grant 15483 from Villum Fonden.

I would like to show my gratitude to my supervisors for their expertise and guidance throughout the project: Dr. Stefan Kragh Nielsen (DTU) for his endless excitement and dedication to our research; and Prof. Roddy Vann (YPI) for his comments and questions which helped push the work forward. A special thanks goes out to my zealous fellow students of PDI for the useful discussions: Søren Kjer Hansen and Andrea Tancetti. To my office mates in the senior PhD office and fellow PhD students in the soon-to-be senior PhD office at DTU, for all the interesting discussions related and unrelated to work as well as for the shared journeys to various conferences and summer schools: thank you Alexander Simon Thrysoe, Jeppe Miki Busk Olsen, Galina Avdeeva, Aslak Sinbjerg Poulsen, Birgitte Madsen, Raheesty Devi Nem, Henrik Järleblad and Raul Gerru Miguelañez. I thank the group at DTU in general for persevering during challenging and noisy times, and for getting me interested in fusion research during my bachelor's and master's studies.

From my stay at YPI, I would like to thank the 2017 Fusion CDT cohort for the camaraderie as well as Jenni Priestley and Ruth Lowman for their always friendly and welcoming attitudes, even when I first appeared somewhat ahead of time as a dirty festivalgoer who wanted to leave a tent behind in a professor's office. On a more personal level, I am truly grateful for the amazing trips and adventures I had with York University Caving and Potholing Club (YUCPC) which gave me something other than work to care about during my stay. I also thank Fabio Federici of the Fusion CDT for his friendship, for showing me that his pen had an eraser and for joining me in various activities ranging from YUCPC trips to artsy film screenings and even a silly border crossing between Belgium and the Netherlands at night by foot.

Lastly, I thank family and friends for their support, and a big thank you goes out to anyone who kept Denmark running and allowed me to finish my thesis mostly unimpeded by a pandemic that broke out in the final months of my project.

Mads Givskov Senstius
Section for Plasma Physics and Fusion Energy
Department of Physics
Technical University of Denmark
31 March 2020

Contents

List of figures	x
List of tables	xi
List of Acronyms	xii
1 Introduction	1
1.1 Fusion energy	1
1.2 Basic plasma physics in magnetically confined fusion	2
1.3 Applications of microwaves in magnetically confined fusion	4
1.3.1 Heating of a magnetically confined fusion plasma	4
1.3.2 Microwave based diagnostics	6
1.4 Parametric decay instabilities of microwaves in plasmas	7
2 Waves in plasmas	9
2.1 Cold waves	9
2.2 Warm and hot corrections	16
2.2.1 The kinetic picture	16
2.2.2 Electron cyclotron resonances	16
2.2.3 Bernstein waves	17
2.3 Beam paths in fusion plasmas	21
2.3.1 The WKB approximation and geometric optics	22
2.3.2 Gaussian beam propagation	22
2.3.3 Electron cyclotron heating	23
2.3.4 Bernstein wave heating	24
2.4 Three-wave interactions	26
2.4.1 The Piliya-Rosenbluth criterion in inhomogeneous monotonic plasmas	27
2.4.2 Reduced power threshold PDIs at the UH layer	29
2.4.3 PDIs due to trapping between UH layers	31
3 Particle-in-cell codes	36
3.1 Basic concept of particle-in-cell codes	36
3.2 Derivation of EPOCH's equations	37
3.2.1 Discretization of continuous functions	37

3.2.2	The FDTD scheme and the Yee grid	38
3.2.3	The particle pusher	42
3.3	Other types of codes	45
3.3.1	Vlasov solvers	46
3.3.2	Beam tracers	47
3.4	Proof of basic functionality in EPOCH	47
3.4.1	Density and magnetic field gradients in EPOCH	48
3.4.2	O- and X-mode cutoffs	48
3.4.3	O- and X-mode wavenumbers	50
3.4.4	X-mode polarization	53
3.4.5	Gaussian wave propagation in 2D	54
4	PDI at the UH layer	56
4.1	Summary of the article	56
4.1.1	Physical setting	56
4.1.2	Simulation design choices	57
4.1.3	Analysis of data and results	57
5	PDI in non-monotonic density profiles	73
5.1	Summary of the article	73
5.1.1	The simplified model	73
5.1.2	Simulation design choices	73
5.1.3	Analysis of data and results	74
6	PDI of eigenmodes of a non-monotonic density profile	90
6.1	Manifestation of eigenmodes	90
6.1.1	Stationary structures	90
6.1.2	Smallest density structure	91
6.1.3	Absorption	96
6.2	Subsequent decay	98
6.2.1	Eigenmodes in the Fourier spectrum	99
6.2.2	Escaping waves	101
7	Conclusions and outlook	108

List of Figures

2.1	CMA-like plots of O- and X-mode properties such as wavenumber, group velocity and polarization.	15
2.2	The EBW dispersion relation for the first four branches.	18
2.3	A comparison of cold and warm X-mode, as well as the first EBW branch.	20
2.4	The IBW dispersion relation near the LH layer at low density.	21
2.5	Illustrations of the O-X-B and X-B conversion schemes.	25
2.6	An illustration of PDI in an inhomogeneous medium whereby daughter waves are amplified from their thermal level.	27
2.7	Wavenumber mismatch for a PDI of X-mode into an EBW and an LH wave as a function of density and LH daughter frequency.	28
2.8	Figures showing wave amplification of a slow X-mode and an EBW propagating from high density to the UH layer using a WKB approximation.	30
2.9	An example of a plasma profile where trapping of UH waves may occur.	31
2.10	A non-monotonic density profile that allows for a pump wave to decay into two trapped daughter waves.	32
2.11	Normalized electrostatic potentials of selected eigenmodes plotted for the parameters outlined in figure 2.10.	34
3.1	An illustration of how the forward-, backward- and central difference schemes estimate the derivative of a function, which is sampled across a grid.	38
3.2	The Yee cell with \mathbf{E}_{jkl} and \mathbf{B}_{jkl} components shifted as they are in EPOCH's update scheme.	40
3.3	A CMA-like diagram with O- and X-mode resonances and cutoffs, and simulations beam paths.	49
3.4	Simulations showing wavefront propagation of O- and X-mode from vacuum to cutoffs.	51
3.5	Simulations showing the wavenumber of propagating O- and X-mode from vacuum to cutoffs using CWTs.	52
3.6	Fast X-mode polarization in simulations with different temperatures.	53
3.7	Averaged main absolute electric field component of a Gaussian beam in 2D.	55
4.1	Wave amplification near the UH layer in simulations presented in the article included in chapter 4.	58

5.1	Illustrations of measures to promote desired PDI into desired trapped waves. . .	75
6.1	Simulations showing stationary density perturbations due to large amplitude eigenmodes.	92
6.2	Eigenfrequencies for different density bump parameters.	94
6.3	Simulations showing the time evolution of the longitudinal electric field when varying the size of the density bump.	95
6.4	Growth rates for primary daughter waves in simulations versus the characteristic density lengthscale.	96
6.5	The absorption of a pump wave traversing a density bump due to PDIs.	98
6.6	FFT spectra of the longitudinal electric field showing several peaks associated with eigenmodes of a cavity.	100
6.7	The frequency spectrum of escaping X-mode waves near half integers of the pump frequency on the boundaries.	102
6.8	Illustration of a cascade of PIs that produces the up- and downshifted main sidebands in figure 6.7a.	103
6.9	Spectra in wavenumber and frequency space near the pump frequency and near the LH frequency for the simulation in section 6.2.2.	107

List of Tables

- 3.1 Simulation parameters for the simulations shown in figures 3.4a, 3.4b, 3.5a and 3.5b. 50
- 3.2 Simulation parameters for the simulations shown in figures 3.4c and 3.5c. 50
- 3.3 Simulation parameters for the simulation shown in figure 3.6. 53
- 3.4 Simulation parameters for the 2D simulation shown in figure 3.7. 54

- 6.1 Simulation parameters for the simulation in section 6.1.1. 90
- 6.2 Simulation parameters for the simulation in section 6.2. 99
- 6.3 A table showing the energy and momentum conservation calculations for the cascade of PDIs in section 6.2.2. 104

List of Acronyms

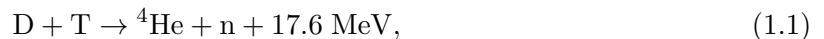
Acronym	Full name
CTS	Collective Thomson scattering
CWT	Continuous wavelet transform
D-D	Deuterium-deuterium
D-T	Deuterium-tritium
EBW	Electron Bernstein wave
EC	Electron cyclotron
ECE	Electron cyclotron emission
ECR	Electron cyclotron resonance
ECRH	Electron cyclotron resonance heating
FDTD	Finite difference time domain
FFT	Fast Fourier transform
FWHM	Full width at half maximum
HPC	High performance computing
IBW	Ion Bernstein wave
LH	Lower hybrid
NBI	Neutral beam injection
O-mode	Ordinary mode
PDI	Parametric decay instability
PI	Parametric Instability
PIC	Particle-in-cell
SRS	Stimulated Raman scattering
TPD	Two plasmon decay
UH	Upper hybrid
X-mode	Extraordinary mode

Chapter 1

Introduction

1.1 Fusion energy

Fusion as a source of energy is a proposed type of power whereby energy from nuclear fusion is converted into heat and electricity. Because the binding energy of nuclei vary, some elements may reach a lower energy state by either combining into heavier elements or splitting in into lighter elements. Iron-56 has the highest known binding energy per nucleon and deuterium, i.e. hydrogen-2, the lowest nonzero binding energy per nucleon. Generally but not always, elements lighter than Iron-56 reach a lower energy state by fusing into heavier elements. The main fusion process of interest is deuterium-tritium (D-T) fusion



where D is for deuterium and T is for tritium, i.e. hydrogen-3. Deuterium is a stable isotope of hydrogen and is available in abundance on Earth with one in 6420 hydrogen atoms being deuterium. Whereas deuterium can be separated out from water, tritium is not readily available in natural reserves as it is radioactive with a half life of 12.26 years. Instead, the most commonly suggested method of obtaining tritium is to produce it by bombarding lithium with neutrons in order to facilitate either of the two nuclear reactions



The neutron produced in the D-T fusion process can in principle be used to produce tritium from lithium in any of the above processes but it must first be cooled down to have an appropriate kinetic energy as the cross section is otherwise too small. By breeding tritium from lithium, the landbound reserves can last up to about 500 years of the world's energy requirements[1]. After that, it is still possible to extract lithium from seawater which could in theory provide 300 times the landbound reserves. Whether it is feasible to extract that much lithium is a discussion we will not go into here.

Other fusion processes are also available such as deuterium-deuterium (D-D) fusion which is

equally likely to produce any of the following reactions



Although these processes release noticeably less energy per reaction, they are still more energy dense than other fuels already in use. The energy from burning 10^6 tonnes of oil corresponds roughly to fission of 0.8 tonnes of uranium or fusion of 0.14 tonnes of deuterium[2]. With D-D fusion, the estimated reserves are on the order of 100 billion years worth with the 2006 energy consumption[3].

In the current political climate, there is a desire to rid society from the dependence on fossil fuels for a number of reasons including the emissions of CO_2 and pollutants as well as geopolitical ties associated with fossil fuels. Nuclear fission, while largely free of CO_2 emissions, suffers from concerns in the general populace due to the radioactive waste produced and the risk of meltdowns, with the most infamous incident being the Chernobyl nuclear accident in 1986 and a more recent being the one at the Fukushima Daiichi power plant in 2011. Sustainable energy sources such as wind energy do not have the same catastrophic consequences associated with them. Unfortunately, they generally cannot deliver a desired power output on demand but instead perform somewhat unpredictably as the wind blows and similar for other concepts. The ambition with fusion energy is to produce energy reliably without greenhouse gas emissions and the risk of meltdowns. Although tritium is radioactive and the neutrons created in D-T fusion will activate some of the reactor material, the time it takes to be considered safe is much shorter than in a fission reactor[3]. In D-D fusion, this might not be an issue, however not only does D-D fusion give less energy, it is also harder to get going.

Nucleons are held together by the strong force which dominates at short range. In order for two nuclei to fuse, they must come sufficiently close that the attraction from the strong force can overcome the Coulomb repulsion, which dominates at longer range. Heating the nuclei may give them enough kinetic energy to overcome or, more likely, tunnel through the Coulomb barrier but higher kinetic energy also decreases the cross-section for collisions. The trade off means that there is an optimal temperature for a fusion process to take place. For the D-T reaction, the cross section peaks at about 120 keV whereas the D-D cross section peaks around 1000 keV and is only around a 100th of the D-T peak cross section so the D-D fusion event is less likely to occur. For constant fusion operation, the increase in temperature proves problematic as for example radiative losses increase with temperature and fusion of certain elements may therefore simply not be feasible.

1.2 Basic plasma physics in magnetically confined fusion

As the ionization potential of hydrogen isotopes is on the order of just 10 eV, D-T fuel can be expected to be in an ionized plasma state in a fusion reactor. Several fusion reactor concepts exist but in this work, we only consider magnetically confined fusion in the style of tokamaks and stellarators.

Because a fully ionized fusion plasma is essentially a collection of charged particles, i.e. negative electrons and positive ions, it can be manipulated with the Lorentz force. The motion

of a non-relativistic charged particle of species ζ in an electric and magnetic field can be described by the equation

$$m_\zeta \frac{d\mathbf{v}_\zeta(t)}{dt} = q_\zeta [\mathbf{E}_0 + \mathbf{v}_\zeta \times \mathbf{B}_0], \quad (1.6)$$

where m_ζ is its mass, $\mathbf{v}_\zeta(t)$ its velocity, q_ζ its charge, and \mathbf{E}_0 and \mathbf{B}_0 the electric and magnetic field respectively which, for the sake of simplicity, are assumed constant and homogeneous. Without loss of generality, the magnetic field is assumed to point in the z -direction. For the component parallel to the magnetic field, the solution to the equation reads

$$u_{\zeta,z}(t) = \frac{q_\zeta E_{0,z}}{m_\zeta} t + u_{\zeta,z,0}, \quad (1.7)$$

where $u_{\zeta,z,0}$ is a velocity at $t = 0$. Because of the cross product between velocity and magnetic field, only the electric field changes the velocity. The much smaller mass of electrons when compared to ions means that the electrons react much faster to an electric field and this also holds for other forces. Assuming first that the electric field is parallel to the magnetic field, a solution to the perpendicular components is

$$\mathbf{v}_{\zeta,\perp,\text{hom}} = u_{\zeta,\perp,0} [\sin(\omega_{c\zeta} t) \hat{\mathbf{x}} + \cos(\omega_{c\zeta} t) \hat{\mathbf{y}}], \quad (1.8)$$

where $u_{\zeta,\perp,0}$ is a perpendicular velocity, $\omega_{c\zeta} = q_\zeta B_0 / m_\zeta$ is called the cyclotron angular frequency, and $\hat{\mathbf{x}}, \hat{\mathbf{y}}$ are the unit vectors in the x - and y -directions. The cross product means that the particle is always accelerated in a direction perpendicular to the magnetic field, causing it to gyrate around the magnetic field lines with an angular frequency of $\omega_{c\zeta}$. We remind ourselves that an angular frequency is related to a frequency by the simple scaling $\omega_\iota = 2\pi f_\iota$ where ι is any label and we will be using both scalings throughout this work. Positive ions gyrate with left hand motion around the field lines and negative electrons perform right hand motion. From the kinetic energy of the particle, its thermal velocity can be defined as

$$v_{t\zeta} = \sqrt{\frac{2T_\zeta}{m_\zeta}}, \quad (1.9)$$

where T_ζ is the temperature, or kinetic energy, of the particle in units of energy by having absorbed the Boltzmann constant. Assuming that the perpendicular velocity is equal to the thermal energy of the particle, a measure of the radius of gyration known as the Larmor radius can be defined as

$$\rho_{L\zeta} = \frac{v_{t\zeta}}{\omega_{c\zeta}} = \sqrt{\frac{2m_\zeta T_\zeta}{q_\zeta^2 B^2}}. \quad (1.10)$$

There are different ways of defining the thermal velocity and Larmor radius; some prefer to define the perpendicular velocity as only the relevant fraction of the thermal velocity and others prefer to leave out numerical factors. In any case, the order of magnitude is the same. Because electrons are much lighter than ions, their Larmor radius is much smaller for the same temperature. When the electric field also has a perpendicular component, the gyration remains but the center of

gyration then starts drifting. Looking for dynamics on a time scale much slower than f_{ce}^{-1} , the guiding center motion for the $\mathbf{E} \times \mathbf{B}$ -drift is found to be

$$\mathbf{v}_{G,\perp,E \times B} = \frac{\mathbf{E} \times \mathbf{B}}{B^2}. \quad (1.11)$$

If a charge imbalance occurs in the plasma, the $\mathbf{E} \times \mathbf{B}$ -drift can cause the particles to drift indiscriminately of their species.

Assuming that the plasma is quasi neutral, the charged particles gyrate around the magnetic field lines and mainly move parallel to them. The particles can therefore be confined if the field lines form closed loops. The problem with this is that such a setup leads to an inhomogeneous magnetic field which also leads to a particle drift, as does the curvature of the field lines. The directions of these drifts depend on charge and they therefore lead to charge separation, which in turn leads to an $\mathbf{E} \times \mathbf{B}$ -drift that moves the bulk of the plasma in the same direction, typically resulting in a great loss of confinement. The two most popular designs that attempt to remedy this are the tokamak and the stellarator.

In a tokamak, the plasma is kept inside an approximately toroidally shaped vacuum chamber with an externally applied magnetic field pointing in the toroidal direction, which means that particles traveling along the field lines are confined. Currents in the plasma give rise to a poloidal magnetic field component so that the resulting field lines twist inside the toroidal chamber and drifts are averaged out as the particles travel around the poloidal cross section. The stellarator works by a principle similar to the tokamak but rely on averaging out the drifts by designing the external field coils to produce twisting field lines inside the confined plasma rather than relying on a plasma current. Such designs allow fusion reactors to confine hot plasmas for long enough that fusion events can take place. However, the record fusion reactor power output was in the 1997 JET tokamak experiment where the fusion output of 16 MW was still lower than the input of 24 MW, and the self-sustaining fusion reactor has still to be demonstrated on Earth. One of the objectives of the ITER tokamak, which is currently being build in a combined effort by a large number of countries, is to generate a fusion output of 10 times the input.

1.3 Applications of microwaves in magnetically confined fusion

For large contemporary tokamak and stellarator devices, the magnetic field is on the order of 1 T which results in an electron cyclotron (EC) frequency in the microwave range. As will be discussed in greater detail in chapter 2, the EC frequency is important because waves in the plasma are resonant at harmonics of it, and this is the basis of a number of both heating and current drive schemes, as well as diagnostics.

1.3.1 Heating of a magnetically confined fusion plasma

As already mentioned, microwaves can be used for plasma heating at harmonics of the EC frequency. The plasma supports a number of electromagnetic and electrostatic waves which have different propagation characteristics and allow for great flexibility over a wide range of plasma parameters. Although the ion cyclotron frequencies have similar properties, waves in the EC range typically have better accessibility to the plasma core because high density cutoffs also are

found in the microwave range. In plasmas where the density is particularly high compared to the magnetic field that confines it, such as in some spherical tokamaks[4], the core can be inaccessible to injected electromagnetic waves in the EC range as well but wave coupling schemes exist that still allow for heating. Heating at the EC resonance, also known as EC resonance heating (ECRH), can be done without driving a lot of plasma current which is desirable for stellarators, however, they can also be used specifically to drive current locally which can be used to modify the magnetic field[5] or to target unwanted plasma modes and avoid instabilities[6]. Studies have shown that experimental ECRH power deposition agrees reasonably well with theory[7] both in terms of magnitude and location. With confidence in the predictability of ECRH, larger contemporary devices such as the ASDEX Upgrade tokamak[8] and the Wendelstein 7-X stellarator[9] have installed several MWs worth of microwave sources and ITER is planned to be equipped with several tens of MWs in microwave power. In chapter 2, we discuss a number of microwave based heating schemes and in what situations they are utilized. Although ECRH generally is considered predictable in its behavior, there have also been reportings of unexpected behavior in recent years. In particular, seemingly unusually high heat fluxes have been observed during ECRH in some machines[10], suggesting that the power deposition was not in agreement with standard theory. Furthermore, it has been reported that ECRH would sometimes produce a population of suprathermal ions even when the energy exchange between electrons and ions was expected to be low[11]. This is most unexpected since ECRH heats the ions only indirectly through heating the electrons first which may then heat the ions. Lastly, there have been observations of nonlinear three-wave interactions which we will introduce in greater detail in section 1.4.

We now mention two other heating schemes not utilizing injected electromagnetic radiation. The first is one based on ohmic heating. Because the plasma is mainly composed of charged particles, a current can be driven through it by using it as a secondary winding of a transformer circuit. This is mostly useful in tokamaks during startup as the dissipated power is proportional to the resistance of the plasma, R_p , which decreases with electron temperature as $R_p \propto T_e^{-3/2}$ [12]. Radiative losses increase with temperature, e.g. the bremsstrahlung power loss density increases with temperature as $S_B \propto T_e^{1/2}$ [2], so ohmic heating may not be sufficient to reach desired fusion reactor temperatures on its own. In stellarators, a strong plasma current would perturb the magnetic field lines with a negative impact on its plasma confinement and ohmic heating is therefore generally not used in stellarators.

Lastly, another popular heating method is known as neutral beam injection (NBI). NBI works by injecting high energy neutral particles into the plasma and letting the particle thermalize through collisions, thereby raising the temperature of the rest of the plasma. The injected particles can enter the plasma as the magnetic confinement does not affect them and NBI can therefore reach any region of the plasma. Once the neutral particles are inside the plasma, they may be ionized through collisions and will then become a part of the confined plasma. By using neutral deuterium for NBI, it also serves as a method of fueling which produces a population of energetic ions. The injected particles should be warmer than the plasma they are to heat, and they are therefore typically heated to temperatures in the range 40 keV - 1 MeV[13]. The challenge with NBI is that it takes a lot of highly energetic particles to deliver the necessary heating. For 1 MW of NBI, on the order of 10^{19} particles of 100 keV must be injected

per second[12]. One can increase the power of the injected beam by injected particles with a higher energy but this does not necessarily increase the heating efficiency as the collision rates for some particle species decrease with higher temperatures[14] which may lead to a significant shintthrough of the NBI beam. For high density plasmas, one can instead have the situation where the majority of the beam of neutrals does not penetrate deep into the plasma but is ionized at the edge.

1.3.2 Microwave based diagnostics

Microwave based diagnostics can be grouped into passive and active diagnostics, and like microwave based heating, they benefit from generally good accessibility and predictability of microwave beam behavior. Passive diagnostics are diagnostic techniques that rely on measuring waves, particles and fields emanating from the plasma, of which microwaves based ones of course only make up a subset of the available diagnostics. The gyrating electrons in the plasma not only absorb radiation at the EC frequency, they also emit radiation known as EC emission (ECE) at same frequency. The level of ECE is related to the temperature of the electrons, and its frequency is determined by the local magnetic field experienced by the electrons. This means that the level of ECE at a particular frequency can be related to the electrons found at the corresponding magnetic field strength. In plasmas with high density to magnetic field, it may be necessary for the ECE to undergo several conversion processes to be picked up by an external receiver[15].

Active diagnostics work by acting on the plasma and measuring its response. A microwave beam that propagates through a plasma will undergo a change in phase and polarization depending on the integrated plasma parameters along the path that it takes. Interferometry compares the phase shift of beam traveling through the plasma with one that bypasses it while polarimetry compares the phase difference of different polarization states. Both can be used to determine the line integrated density and magnetic field. Externally launched waves typically also have cutoffs in the microwave range. Provided that the density profile is monotonic and the magnetic field is known, the density profile can be determined through reflectometry by measuring the delay of reflected waves at different frequencies in a radar-like manner. Finally, we mention collective Thomson scattering (CTS)[16, 17] used to measure ion properties. Regular Thomson scattering works by measuring the scattering of an injected wave on electron motion. A wave scattered on an electron is Doppler shifted which produces a widened peak in the scattered frequency spectrum from which the electron velocity distribution and density can be inferred. CTS instead scatters on the collective motion of electrons around the ions which in the end reflects the properties of the ion distribution function. Whereas Thomson scattering relies on visible and near-infrared lasers, CTS requires a much longer wavelength and typically utilize high power microwave beams similar to those of ECRH beams.

Although not all of these diagnostics perturb the plasma using high power microwave beams, the sensors they rely on are highly sensitive to microwave radiation. While ECRH beams can inject MW power levels at particular frequencies, microwave diagnostics may have a tolerance of just μW or less[18]. Microwave sensitive components have to be shielded against waves at the injected ECRH frequency and are vulnerable to any process that can convert a fraction of the injected ECRH power into waves at other frequencies.

1.4 Parametric decay instabilities of microwaves in plasmas

A plasma is a nonlinear medium that can facilitate nonlinear three-wave interactions known as parametric instabilities (PIs). PIs are higher order wave effects and are not limited to plasmas. Rather, they are found also in fluids[19], nonlinear optical crystals[20] and mechanical systems[21]. The most commonly observed form of PI is known as a parametric decay instabilities (PDI) where a strong pump wave starts to decay partially into daughter waves when it exceeds an amplitude threshold. It is also possible for a strong pump to scatter on other waves or for two strong waves to combine into a third. In a plasma experiment, PDIs will produce stimulated emission spectra with peaks shifted relative to the pump frequency by natural frequencies of the plasma.

Due to the charge rich nature of the ionosphere, signatures of PDIs have been observed when high power radio waves are injected into the ionosphere. It has been proposed that PDIs can be utilized as a means of modifying the plasma parameters and that the resulting spectra can serve as a means of diagnosing the plasma composition[22, 23, 24]. PDIs have also been observed in inertial confinement fusion. Inertial confinement fusion is an entirely different approach to controlled fusion which is based on compressing a D-T fuel to extreme densities while also heating it to fusion relevant temperatures and thereby achieving optimal fusion conditions. The high degree of compression is typically achieved by irradiating it or a hohlraum surrounding it with very intense laser pulses from several lasers at the same time. It is because of the extreme radiation experienced by the fuel that a number PDIs are commonly observed in this kind fusion experiments. PDIs are here highly undesirable because they can lead to unwanted asymmetries and preheating of the fuel[25, 26, 27].

According to the early models on PDIs in plasmas[28, 29, 30], even high power microwave beams of 1 MW utilized nowadays in magnetically confined fusion plasmas are generally expected to interact only linearly with the plasma as the beam propagates through it. Noticeable exceptions were known to be at resonances where nonlinear effects become important[31, 32]. Scattering of the gyrotron beam at frequencies shifted by a characteristic ion frequency has been observed in CTS experiments[17]. The observations strongly indicate that a PDI produced the scattering even though the ion wave corresponding to the frequency shift was not observed in the experiments. Furthermore, the gyrotron beam itself would not have acted as pump wave directly, rather, the PDI pump wave would have been a fraction of the CTS beam that converted into another type of wave and propagated to a resonance. The observations have since been treated analytically as being a result of PDIs to determine a threshold power level for scattering[33, 34] as it can be damaging to CTS and other microwave sensitive equipment. The power threshold has been tested on a large number of discharges at the ASDEX Upgrade tokamak with good agreement[35]. This is the subject of chapter 4, where we study this problem numerically using a fully kinetic particle-in-cell (PIC) code, which is introduced in chapter 3. We verify that a PDI does occur and that the necessary waves including the undetected ion wave are excited. Furthermore, we find good agreement with the analytically derived PDI gyrotron power threshold.

It has also been reported in experiments that signatures of PDIs were detected during ECRH at the second harmonic[36, 37] when waves were not expected to reach any fundamental resonance. At the time, this observation was unexpected and it was therefore not routinely looked

for. Based on the observations, analytical theory has since been developed to explain the PDI signatures at a reduced gyrotron power threshold as a result of PDIs in non-monotonic plasma density perturbations[38, 39, 40, 41, 42]. These models rely on excitation of trapped waves through PDIs which further decay in cascades of subsequent PIs and eventually produce the observed scattering. Estimates of the effective loss of ECRH power depends strongly on local plasma parameters but are given as 10% in [41]. It should therefore be considered a potentially significant impediment on ECRH efficiency and on the overall machine performance. However, the analytical theory requires a number of approximations to be made[18] and it remains disputed what impact the non-monotonic structures have on high power microwave beams and what kind of structures can facilitate PDIs. Density perturbations can occur for a number of reasons in a magnetically confined fusion plasmas and can vary in size. The PDI signatures have been reported to damage sensors[18] that were not shielded to withstand radiation due to PDIs. A better understanding of these nonlinear effects is therefore needed. This problem is the topic of chapters 5 and 6 where we again use a PIC code to study the PIs. In chapter 5 we map out which PDIs can excite the trapped waves and how changes to the shape of the density perturbation affects the excited waves. In chapter 6, we focus on showing that the excited trapped waves are eigenmodes of the density perturbation and discuss the consequences of this. We also present a cascade of PIs which produces stimulated emission patterns with qualities similar to the experimentally observed scattering spectra.

Chapter 2

Waves in plasmas

A wide variety of waves can propagate in a magnetized plasma. The typical combination of light electrons and heavy ions leads to waves at frequencies several orders of magnitude apart; both high frequency waves corresponding to the fast electron response and low frequency waves caused by the slow ions. A magnetic field in a plasma causes the plasma to become an anisotropic medium with polarization and direction of propagation having a profound effect on a wave's behavior. Some electromagnetic waves can propagate through a plasma in a light like manner with negligible interference from the charges that make up the typically quasi-neutral plasma. Waves that are excited externally and injected into the plasma from vacuum are examples of such waves and may be described by the cold wave model which is presented in section 2.1. In chapters 5 and 6, the pump wave is well described by this model. Other waves propagate by displacing the mobile charges harmonically whereby they give rise to charge deficiencies which propagate the oscillatory electric fields. These waves get a longitudinal nature and Bernstein waves are examples of such waves which are described by kinetic theory and discussed in section 2.2. Some waves may interact linearly with each other and the plasma in certain regions, however, getting a microwave beam to a desired region and in the correct mode can require some planning as will be mentioned in section 2.3. Lastly, nonlinear three-wave interactions or PDIs are the subject of section 2.4 which builds on all the other sections in this chapter and is the main subject of the thesis.

2.1 Cold waves

In this section, we derive the cold X-mode dispersion relation which is used for the pump wave in chapters 5 and 6. Cold plasma waves are treated in a number of textbooks as they can be derived from relatively simple expressions and they display features even relevant to fusion plasmas. We will loosely follow [43, 44, 45] in the derivation. It is assumed that cold plasma waves have no dependence on temperature, finite Larmor effects are neglected and the plasma is assumed to be entirely non-relativistic and homogeneous to zeroth order.

The evolution of the electric and magnetic field, $\mathbf{E}(\mathbf{r}, t)$ and $\mathbf{B}(\mathbf{r}, t)$, is described by Maxwell's

equations

$$\nabla \cdot \mathbf{E}(\mathbf{r}, t) = \frac{\sum_{\varsigma} q_{\varsigma} n_{\varsigma}(\mathbf{r}, t)}{\epsilon_0}, \quad (2.1)$$

$$\nabla \cdot \mathbf{B}(\mathbf{r}, t) = 0, \quad (2.2)$$

$$\nabla \times \mathbf{E}(\mathbf{r}, t) = -\partial_t \mathbf{B}(\mathbf{r}, t), \quad (2.3)$$

$$\nabla \times \mathbf{B}(\mathbf{r}, t) = \mu_0 [\mathbf{J}(\mathbf{r}, t) + \epsilon_0 \partial_t \mathbf{E}(\mathbf{r}, t)], \quad (2.4)$$

where the index ς refers to the particle species that make up the plasma, q_{ς} and $n_{\varsigma}(\mathbf{r}, t)$ are the charge and density of the species, ϵ_0 is the vacuum permittivity and $\mathbf{J}(\mathbf{r}, t)$ is the current density in the plasma. By taking the curl of equation (2.3) and inserting $\nabla \times \mathbf{B}(\mathbf{r}, t)$ from equation (2.4), \mathbf{B} can be eliminated

$$\nabla \times (\nabla \times \mathbf{E}(\mathbf{r}, t)) = -\mu_0 [\partial_t \mathbf{J}(\mathbf{r}, t) + \epsilon_0 \partial_t^2 \mathbf{E}(\mathbf{r}, t)]. \quad (2.5)$$

Using a commonly known vector triple product rule[46], the left hand side can be rewritten, giving the equation

$$\nabla(\nabla \cdot \mathbf{E}(\mathbf{r}, t)) - \nabla^2 \mathbf{E}(\mathbf{r}, t) = -\mu_0 [\partial_t \mathbf{J}(\mathbf{r}, t) + \epsilon_0 \partial_t^2 \mathbf{E}(\mathbf{r}, t)]. \quad (2.6)$$

Note that the divergence of $\mathbf{E}(\mathbf{r}, t)$ in the first term can be substituted for the right hand side of equation (2.1) so in the case of a vacuum where there are no charges to move around, the above expression reduces to the well known wave equation $\partial_t^2 \mathbf{E}(\mathbf{r}, t) = c^2 \nabla^2 \mathbf{E}(\mathbf{r}, t)$ which appropriately describes the propagation of electromagnetic waves in vacuum. To rid the equation above of the many derivatives, it is transformed using Fourier transform from \mathbf{r} to \mathbf{k} and a Laplace transform from t to ω defined as

$$\varphi(\mathbf{k}, \omega) \equiv \int_{\text{All } \mathbf{r}} \int_0^{\infty} \varphi(\mathbf{r}, t) e^{i(\omega t - \mathbf{k} \cdot \mathbf{r})} dt d\mathbf{r}. \quad (2.7)$$

Note that the Laplace transform is usually defined as $\int_0^{\infty} \varphi e^{st} dt$ where $s \in \mathbb{C}$ but substituting s for $-i\omega$ works the same provided $\omega \in \mathbb{C}$. Assuming that all relevant quantities will vanish when evaluated at pairs of integration boundaries, the usual rules apply to derivatives[46], i.e. $\nabla \rightarrow i\mathbf{k}$ and $\partial_t \rightarrow -i\omega$, and equation (2.6) can be written as

$$-\mathbf{k}\mathbf{k} \cdot \mathbf{E}(\mathbf{k}, \omega) + k^2 \mathbf{E}(\mathbf{k}, \omega) = i\mu_0 \omega \mathbf{J}(\mathbf{k}, \omega) + \frac{\omega^2}{c^2} \mathbf{E}(\mathbf{k}, \omega), \quad (2.8)$$

where $\mathbf{k}\mathbf{k} \equiv \mathbf{k} \otimes \mathbf{k}$, \otimes is the tensor product and c is the vacuum speed of light. At this point, $\mathbf{E}(\mathbf{k}, \omega)$ can be factored out of all but one term. To progress with the derivation, we would like to express $\mathbf{J}(\mathbf{k}, \omega)$ in terms of $\mathbf{E}(\mathbf{k}, \omega)$ but this requires us to make some assumptions about how the electric field induces a current in the plasma. For the cold waves, we neglect any collective effects from a thermal distribution of particles and simply assume that the current is generated by a non-relativistic fluid of particles of different species

$$\mathbf{J}(\mathbf{r}, t) = \sum_{\varsigma} q_{\varsigma} n_{\varsigma}(\mathbf{r}, t) \mathbf{u}_{\varsigma}(\mathbf{r}, t), \quad (2.9)$$

where m_ζ is the mass of species ζ , $\mathbf{u}_\zeta(\mathbf{r}, t)$ is their fluid velocity. Neglecting collisions and gravity, the momentum equation for species ζ of the cold plasma fluid is given by

$$n_\zeta(\mathbf{r}, t)m_\zeta [\partial_t + \mathbf{u}_\zeta(\mathbf{r}, t) \cdot \nabla] \mathbf{u}_\zeta(\mathbf{r}, t) = n_\zeta(\mathbf{r}, t)q_\zeta [\mathbf{E}(\mathbf{r}, t) + \mathbf{u}_\zeta(\mathbf{r}, t) \times \mathbf{B}(\mathbf{r}, t)]. \quad (2.10)$$

We limit ourselves and linearize the above equation by perturbing it around a quasi-neutral homogeneous plasma at rest in a constant magnetic field, i.e. $\mathbf{E}^{(0)}(\mathbf{r}, t) = \mathbf{0}$, $\mathbf{B}^{(0)}(\mathbf{r}, t) = \mathbf{B}_0$, $\mathbf{u}_\zeta^{(0)}(\mathbf{r}, t) = \mathbf{0}$ and $n_\zeta^{(0)}(\mathbf{r}, t) = n_{\zeta,0}$. To first order, the momentum equation reduces to

$$\partial_t [q_\zeta n_{\zeta,0} \mathbf{u}_{\zeta,1}(\mathbf{r}, t)] = \frac{q_\zeta^2 n_{\zeta,0}}{m_\zeta} [\mathbf{E}_1(\mathbf{r}, t) + \mathbf{u}_{\zeta,1}(\mathbf{r}, t) \times \mathbf{B}_0]. \quad (2.11)$$

The left hand side is now seen to be the time derivative of the contribution of species ζ to the first order current, $\mathbf{J}_{\zeta,1}(\mathbf{r}, t) = q_\zeta n_{\zeta,0} \mathbf{u}_{\zeta,1}(\mathbf{r}, t)$. The first order velocity on the right hand side can also be substituted for $\mathbf{J}_{\zeta,1}(\mathbf{r}, t)$. With a Fourier-Laplace transform, the expression now becomes

$$i\omega \mathbf{J}_{\zeta,1}(\mathbf{k}, \omega) - \frac{q_\zeta}{m_\zeta} \mathbf{B}_0 \times \mathbf{J}_{\zeta,1}(\mathbf{k}, \omega) = -\frac{q_\zeta^2 n_{\zeta,0}}{m_\zeta} \mathbf{E}_1(\mathbf{k}, \omega). \quad (2.12)$$

Aligning the coordinate system so that the z -axis is along the background magnetic field, i.e. $\mathbf{B}_0 = B_0 \hat{\mathbf{z}}$, the above is written as a matrix-vector equation

$$\begin{pmatrix} i\omega & \frac{q_\zeta B_0}{m_\zeta} & 0 \\ -\frac{q_\zeta B_0}{m_\zeta} & i\omega & 0 \\ 0 & 0 & i\omega \end{pmatrix} \cdot \mathbf{J}_{\zeta,1}(\mathbf{k}, \omega) = -\varepsilon_0 \frac{q_\zeta^2 n_{\zeta,0}}{\varepsilon_0 m_\zeta} \mathbf{E}_1(\mathbf{k}, \omega). \quad (2.13)$$

The off-diagonal elements of the matrix on the left hand side have units of an angular frequency and is commonly known as the cyclotron angular frequency for species ζ . Similarly, the fraction on the right hand side has units of a squared angular frequency and is known as the plasma angular frequency for species ζ . Introducing $\omega_{c\zeta} \equiv q_\zeta B_0 / m_\zeta$ and $\omega_{p\zeta}^2 \equiv q_\zeta^2 n_{\zeta,0} / (\varepsilon_0 m_\zeta)$, and inverting the matrix using Cramer's rule, an expression for the transformed current contribution can be determined

$$\mathbf{J}_{\zeta,1}(\mathbf{k}, \omega) = -\frac{\varepsilon_0 \omega_{p\zeta}^2}{i\omega(\omega^2 - \omega_{c\zeta}^2)} \begin{pmatrix} \omega^2 & i\omega\omega_{c\zeta} & 0 \\ -i\omega\omega_{c\zeta} & \omega^2 & 0 \\ 0 & 0 & \omega^2 - \omega_{c\zeta}^2 \end{pmatrix} \mathbf{E}_1(\mathbf{k}, \omega). \quad (2.14)$$

In using Cramer's rule, we assume $\omega \neq \pm\omega_{c\zeta}$ but we will return to this frequency later. Summing up the transformed current for each species of the plasma yields the total transformed linear plasma current induced by a transformed electric field, and the tensor that connects the two is typically called the conductivity tensor denoted $\boldsymbol{\sigma}(\mathbf{r}, t)$. Note that summing up the above equation for all ζ will give the Fourier-Laplace transformed conductivity instead, which is what we need for this derivation. Writing equation (2.8) to first order and inserting the found current

gives

$$\mathbf{0} = \left[\mathbf{k}\mathbf{k} - k^2\mathbf{1} + \frac{\omega^2}{c^2}\mathbf{1} + i\mu_0\omega\boldsymbol{\sigma}(\mathbf{k}, \omega) \right] \cdot \mathbf{E}_1(\mathbf{k}, \omega), \quad (2.15)$$

$$\boldsymbol{\sigma}(\mathbf{k}, \omega) = -\frac{\varepsilon_0\omega}{i} \sum_{\varsigma} \begin{pmatrix} \frac{\omega_{p\varsigma}^2}{\omega^2 - \omega_{c\varsigma}^2} & i\frac{\omega_{c\varsigma}\omega_{p\varsigma}^2}{\omega(\omega^2 - \omega_{c\varsigma}^2)} & 0 \\ -i\frac{\omega_{c\varsigma}\omega_{p\varsigma}^2}{\omega(\omega^2 - \omega_{c\varsigma}^2)} & \frac{\omega_{p\varsigma}^2}{\omega^2 - \omega_{c\varsigma}^2} & 0 \\ 0 & 0 & \frac{\omega_{p\varsigma}^2}{\omega^2} \end{pmatrix}, \quad (2.16)$$

where $\mathbf{1}$ is the identity matrix. In the literature, the tensor $\boldsymbol{\varepsilon}(\mathbf{k}, \omega) = \mathbf{1} + i\boldsymbol{\sigma}(\mathbf{k}, \omega)/(\varepsilon_0\omega) = \mathbf{1} + \sum_{\varsigma} \boldsymbol{\chi}_{\varsigma}(\mathbf{k}, \omega)$ is sometimes introduced as the dielectric tensor and $\boldsymbol{\chi}(\mathbf{k}, \omega)$ as the susceptibility tensor of species ς . Equation (2.15) is a homogeneous set of equations which have a solution if the total matrix inside the square brackets is not invertible, which means the determinant must be zero[46]. The angle between the wave vector \mathbf{k} and the background magnetic field \mathbf{B}_0 affects the waves that may propagate. In this work, waves for which $\mathbf{k} \perp \mathbf{B}_0$ are of interest, so $\mathbf{k} = k\hat{\mathbf{x}}$ is assumed, yielding the condition

$$0 = \begin{vmatrix} S & -iD & 0 \\ iD & S - \frac{c^2k^2}{\omega^2} & 0 \\ 0 & 0 & P - \frac{c^2k^2}{\omega^2} \end{vmatrix}, \quad (2.17)$$

where Stix notation[44] has been used, introducing $S \equiv \frac{R+L}{2}$ as Sum, $D \equiv \frac{R-L}{2}$ as Difference, $R \equiv 1 - \sum_{\varsigma} \frac{\omega_{p\varsigma}^2}{\omega(\omega + \omega_{c\varsigma})}$ as Right, $L \equiv 1 - \sum_{\varsigma} \frac{\omega_{p\varsigma}^2}{\omega(\omega - \omega_{c\varsigma})}$ as Left and $P \equiv 1 - \sum_{\varsigma} \frac{\omega_{p\varsigma}^2}{\omega^2}$ as Parallel. The names Sum and Difference stem from the way they are constructed from R and L . Right and Left come from the resonances at $\omega = \omega_{p\varsigma}$ which due to the sign and definition of $\omega_{p\varsigma}$ occur at the right hand gyrating electron frequency for R but at left hand gyration ion frequencies for L . Lastly, Parallel is because this is the only component of the dielectric tensor coupling to the parallel direction. From the determinant above, it is seen that a solution is found when $c^2k^2/\omega^2 = P$ or when $c^2k^2/\omega^2 = (S^2 - D^2)/S$. The former leads to the dispersion relation waves known as ordinary mode (O-mode) waves and the latter to extraordinary mode (X-mode) waves. While there are electrostatic waves at ion frequencies in this work, the electromagnetic waves described by the cold model will have a frequency much greater than the ion cyclotron and plasma frequency range. This means that all the ion terms in the sums can be neglected and the dispersion relations are then obtained as

$$\text{O - mode : } k_{\text{O}}^2 = \frac{\omega^2 - \omega_{pe}^2}{c^2}, \quad (2.18)$$

$$\text{X - mode : } k_{\text{X}}^2 = \frac{1}{c^2} \left(\omega^2 - \omega_{pe}^2 \frac{\omega^2 - \omega_{pe}^2}{\omega^2 - \omega_{\text{UH}}^2} \right), \quad (2.19)$$

where $\omega_{\text{UH}} \equiv \sqrt{\omega_{ce}^2 + \omega_{pe}^2}$ is the upper hybrid (UH) angular frequency. It is noted that only X-mode depends on the background magnetic field but that it reduces to the O-mode dispersion relation for $\omega \gg \omega_{pe}, \omega_{ce}$. For $k^2 > 0$, k is real and the wave can propagate. For $k^2 < 0$, k is purely imaginary and the wave is unable to propagate. Although it was assumed that plasma parameters are homogeneous to zeroth order, they may change with a characteristic length scale much longer than the relevant wavelengths and $k = 0$ then represents a cutoff point where a wave can only propagate on one side and therefore is reflected. The O-mode wave only has a cutoff frequency at $\omega = \omega_{pe}$, whereas the X-mode wave experiences a cutoff at $R = 0$ or $L = 0$, leading to two solutions for each, of which only one of each pair is positive, yielding

$$\omega_{\text{R}} = \frac{|\omega_{ce}| + \sqrt{\omega_{ce}^2 + 4\omega_{pe}^2}}{2}, \quad (2.20)$$

$$\omega_{\text{L}} = \frac{-|\omega_{ce}| + \sqrt{\omega_{ce}^2 + 4\omega_{pe}^2}}{2}, \quad (2.21)$$

which are known as the R- and L-cutoffs respectively. For O-mode, k_{O}^2 is finite everywhere, whereas for X-mode, k_{X}^2 diverges at $\omega = \omega_{\text{UH}}$ which is known as the UH resonance. The O- and X-mode dispersion relations are plotted in figures 2.1a and 2.1b for $\omega \sim \omega_{ce}, \omega_{pe}$. Figure 2.1a shows that k_{O} generally is similar to the vacuum wavenumber, i.e. ω/c , above the electron plasma frequency but that it drops off near it and vanishes below it, as expected. For X-mode, figure 2.1b shows that also k_{X} is generally close to its vacuum wavenumber except near cutoffs and the UH resonance. While ω_{L} acts as a high density cutoff for X-mode similar to ω_{pe} for O-mode, ω_{R} and ω_{UH} are seen to bound an evanescent region which cuts off waves coming from low density and magnetic field. The group velocities of O- and X-mode waves are calculated as $v_{\text{g},l} = \partial\omega/\partial k_l = 2k_l/(\partial k_l^2/\partial\omega)$, giving the group velocities

$$v_{\text{g},\text{O}} = \frac{c^2 k_{\text{O}}}{\omega}, \quad (2.22)$$

$$v_{\text{g},\text{X}} = \frac{\omega k_{\text{X}}}{k_{\text{X}}^2 + \frac{1}{c^2} \left[\frac{\omega^2 \omega_{pe}^2 - 2\omega_{pe}^4}{\omega^2 - \omega_{\text{UH}}^2} + \frac{\omega^2 \omega_{pe}^2 - \omega_{pe}^4}{(\omega^2 - \omega_{\text{UH}}^2)^2} \omega_{\text{UH}}^2 \right]}, \quad (2.23)$$

where $v_{\text{g},\text{O}}$ and $v_{\text{g},\text{X}}$ are the O- and X-mode group velocities. The X-mode group velocity is shown in figure 2.1c. X-mode waves are seen to propagate at a speed similar to the vacuum speed of light except in the vicinity of the UH resonance and the cutoffs where the group velocity drops off. X-mode on the low field- and density side of the R cutoff is often referred to as fast X-mode whereas X-mode on the high field- and density side, near the UH resonance, is referred to as slow X-mode due to the group velocity generally being lower. Inserting k_{O} and k_{X} into equation (2.15), polarization vectors can be determined as

$$\text{O - mode : } \mathbf{E}_{\text{O}} = E_{\text{O}} \hat{\mathbf{z}}, \quad (2.24)$$

$$\text{X - mode : } \mathbf{E}_{\text{X}} = E_{\text{X}} \left(\frac{iD}{S} \hat{\mathbf{x}} + \hat{\mathbf{y}} \right). \quad (2.25)$$

O-mode waves are always linearly polarized with the electric field in the direction of the background magnetic field. An X-mode wave, on the other hand, is seen to be elliptically polarized with a dependence on plasma parameters, see figure 2.1d. In vacuum, $D \rightarrow 0$ and $S \rightarrow 1$ so X-mode is linearly polarized in direction the direction perpendicular to both the background magnetic field and to the direction of propagation, i.e. $\mathbf{B}_0 \perp \mathbf{E}_X \perp \mathbf{k}$. As the density increases, however, X-mode waves attain a longitudinal component and become mostly longitudinal near the UH resonance. This is an important detail in coupling to electrostatic modes. However due to the decreasing group velocity at the UH resonance, an X-mode wave propagating towards it will experience wave amplification in order to conserve power flux[47, 48] which renders the linear approximation invalid. Furthermore, $k \rightarrow \infty$ near a resonance means that wavelength becomes comparable to the Larmor radii of the particles which is not taken into account in the cold model. As a rule of thumb, the cold wave approximation is therefore only valid away from resonances.

For frequencies much smaller than the electron range, i.e. for $\omega \ll \omega_{ce}, \omega_{pe}$, the ion terms of the sums in S and D cannot be neglected. The X-mode dispersion relation is still given by $c^2 k^2 / \omega^2 = (S^2 - D^2) / S$ so a resonance is found when $S = 0$ which for a single ionic species occurs at a frequency known as the lower hybrid (LH) frequency

$$\omega_{\text{LH}} = \sqrt{\frac{\omega_{ci}\omega_{ce}}{\omega_{\text{UH}}^2} (\omega_{ci}\omega_{ce} + \omega_{pe}^2)}. \quad (2.26)$$

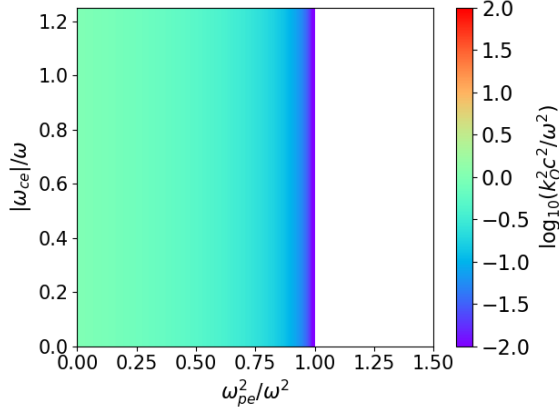
The resonance is known as the LH resonance but it does not play as important a role as the UH resonance in this work. However, waves near the LH frequency do play an important role and the LH frequency therefore deserves a mention. Other than the UH and LH resonances, it is also clear that there is a resonance when $S^2 - D^2 \rightarrow \pm\infty$ which happens whenever $\omega = \pm\omega_{cs}$ but this we assumed would not happen when we used Cramer's rule[46]. These resonances are known as cyclotron resonances and will be discussed in the next section.

Whilst only wave propagation perpendicular to the background magnetic field was discussed above, the results have been generalized to propagation at an arbitrary angle to the background magnetic field. Neglecting the ions, a neatly formulated dispersion relation for such waves is known as the Appleton-Hartree formula[49]

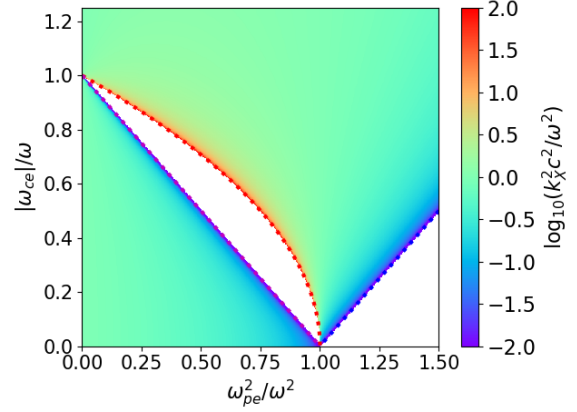
$$\frac{k^2 c^2}{\omega^2} = 1 - \frac{2X(1-X)}{2(1-X) - Y^2 \sin^2 \theta \pm \Gamma}, \quad (2.27)$$

$$\Gamma = \sqrt{Y^4 \sin^4 \theta + 4Y^2(1-X)^2 \cos^2 \theta}, \quad (2.28)$$

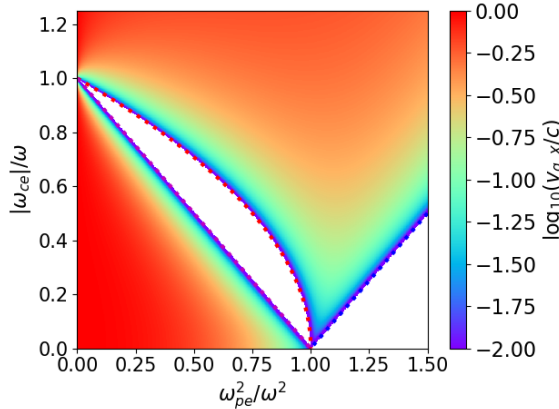
where θ is the angle of propagation to the magnetic field, and the normalized quantities $X = \omega_{pe}^2 / \omega^2$ and $Y = \omega_{ce} / \omega$ have been introduced. For perpendicular propagation, the + solution reduces to the O-mode dispersion relation in equation (2.18) and the - solution reduces to the X-mode dispersion relation in equation (2.19). For almost perpendicular propagation, the O- and X-mode solutions retain most of their features. Provided that $\theta \neq \pi/2$, both solutions reduce to the same expression at $X = 1$, i.e. at the plasma frequency. This is a key step in the O-X-B conversion scheme which will be discussed in section 2.3.



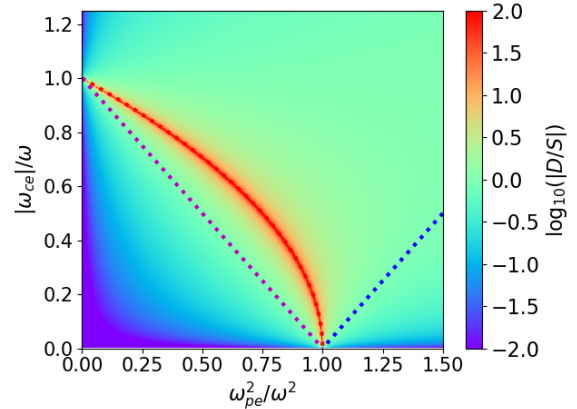
(a) The squared O-mode wavenumber from equation (2.18) normalized to ω^2/c^2 in a CMA-like plot. The white region is the evanescent region below the electron plasma frequency.



(b) The squared X-mode wavenumber from equation (2.19) normalized to ω^2/c^2 in a CMA-like plot. The white regions are evanescent regions.



(c) The X-mode group velocity normalized to c and calculated as $v_{g,x} = \partial\omega/\partial k_x$ using equation (2.19) in a CMA-like plot. The white region is the evanescent region below the electron plasma frequency.



(d) The ratio between the longitudinal and transverse component of the X-mode polarization in a CMA-like plot. Low $|D/S|$ means mainly transverse and high $|D/S|$ means mainly longitudinal, see equation (2.25).

Figure 2.1: CMA-like plots where the x -axis is proportional to the electron density, n_e , and the y -axis is proportional to the background magnetic field, B_0 . The plots are underlayed with wavenumbers, polarization and group velocity. X-mode plots have the frequencies $\omega = \omega_{UH}$, $\omega = \omega_R$ and $\omega = \omega_L$ plotted as the dashed red, magenta and blue lines respectively. Note that divergent points exceed the color scales which are limited as indicated for the sake of overview.

2.2 Warm and hot corrections

Although the cold model generally describes propagation of O- and X-mode away from resonances well, the divergent results near the UH and cyclotron resonances are not physical. Furthermore, the linearization in the derivation lead to a linear plasma response to the waves even though a plasma is a nonlinear medium. Near resonances, in particular, the linear model breaks down. Fortunately, this can be remedied by including thermal and kinetic effect in the model although that typically comes at the cost of a significantly more complicated system of equations. As those derivations can become rather lengthy and are found in a number of textbooks[43, 47, 44, 50], we will only go over the starting point and the results.

2.2.1 The kinetic picture

Whilst Maxwell's equations still describe the evolution of the electric and magnetic fields, the cold fluid momentum equation in (2.10) is no longer used. In the kinetic picture, a plasma consists of a large collection of electrons and ions at different positions and with different velocities described by a distribution function. A plasma that is left to thermalize through collisions will have a Maxwellian distribution with a mean energy that is considered the temperature of the plasma. As the temperature of the plasma increases, not only does the average energy of the particles go up but the high energy tail also becomes more pronounced. Since the Larmor radius of a charged particle is proportional to the square root of its perpendicular energy, it can be neglected for cold particles. To take the distribution of particles into account, the Boltzmann equation can be used instead of the cold fluid momentum equation

$$\partial_t f_\zeta(\mathbf{r}, \mathbf{v}, t) + \mathbf{v} \cdot \nabla_{\mathbf{r}} f_\zeta(\mathbf{r}, \mathbf{v}, t) + \frac{q_\zeta}{m_\zeta} [\mathbf{E}(\mathbf{r}, t) + \mathbf{v} \times \mathbf{B}(\mathbf{r}, t)] \cdot \nabla_{\mathbf{v}} f_\zeta(\mathbf{r}, \mathbf{v}, t) = [\partial_t f_\zeta(\mathbf{r}, \mathbf{v}, t)]_{\text{coll}}, \quad (2.29)$$

where $f_\zeta(\mathbf{r}, \mathbf{v}, t)$ is the distribution function of particle species ζ in position-, \mathbf{r} , and velocity space, \mathbf{v} , $\nabla_{\mathbf{r}} = \nabla = (\partial_x, \partial_y, \partial_z)$ is the spatial derivative, $\nabla_{\mathbf{v}} = (\partial_{v_x}, \partial_{v_y}, \partial_{v_z})$ is a derivative in velocity space, and $[\partial_t f_\zeta(\mathbf{r}, \mathbf{v}, t)]_{\text{coll}}$ is the change in the distribution function due to collisions. One may look for a solution along an unperturbed zeroth order trajectory using the method of characteristics[47, 44]. Letting $f_\zeta(\mathbf{r}, \mathbf{v}, t) = f_{\zeta,0}(\mathbf{r}, \mathbf{v}) + f_{\zeta,1}(\mathbf{r}, \mathbf{v}, t)$, $\mathbf{B}(\mathbf{r}, t) = \mathbf{B}_0(\mathbf{r}) + \mathbf{B}_1(\mathbf{r}, t)$, and $\mathbf{E}(\mathbf{r}, t) = \mathbf{E}_1(\mathbf{r}, t)$, with $f_{\zeta,0}(\mathbf{r}, \mathbf{v})$ typically being a Maxwellian distribution and $\mathbf{B}_0(\mathbf{r})$ an externally applied magnetic field, one can obtain an expression for the perturbed current density through

$$\mathbf{J}_1(\mathbf{r}, t) = \int q_\zeta \mathbf{v} f_1(\mathbf{r}, \mathbf{v}, t) d\mathbf{v}. \quad (2.30)$$

With the current density, a significantly more complicated hot dielectric tensor, ϵ_h , can be obtained. Finding the waves that can propagate in the plasma is then once again a matter of solving the matrix-vector equation $\mathbf{0} = \left[\mathbf{k}\mathbf{k} - k^2 \mathbf{1} + \frac{\omega^2}{c^2} \epsilon_h \right] \cdot \mathbf{E}_1$.

2.2.2 Electron cyclotron resonances

As a result of including kinetic and collisional effects, the cyclotron resonance frequencies, which were divergent points before, are now resonances where energy from an electromagnetic O-

or X-mode wave can be absorbed by the plasma, allowing for plasma heating using injected electromagnetic radiation. The plasma now also absorbs energy at harmonics of the cyclotron resonance, i.e. at $\omega = n|q_\zeta|B_0/m_\zeta$ where $n \in \mathbb{N}$, however, the optical thickness of these resonances and harmonics are not equal. Bornitici *et al* have published tables of absorption and emission at the cyclotron frequencies based on analytical theory, see [51]. Assuming that the plasma is weakly underdense, i.e. $\omega_{pe} \approx \omega_{ce}$ but $\omega_{pe} < \omega_{ce}$, the absorption is strongest at the fundamental, i.e. $n = 1$, O-mode and second harmonic, i.e. $n = 2$, X-mode and is on the order

$$\alpha_1^{(O)} \approx \alpha_2^{(X)} \approx \left(\frac{\omega_{pe}}{\omega_{ce}}\right)^2 \frac{\omega_{ce}}{c}. \quad (2.31)$$

The absorption at the fundamental X-mode is temperature dependent and is approximately given by

$$\alpha_1^{(X)} \approx \left(\frac{\omega_{ce}}{\omega_{pe}}\right)^2 \left(\frac{v_{te}}{c}\right)^2 \frac{\omega_{ce}}{c}. \quad (2.32)$$

The second harmonic O-mode and third harmonic X-mode are of similar order but slightly smaller than $\alpha_1^{(X)}$ and scale differently with density and magnetic field. Higher harmonics go as $(v_{te}/c)^4$ which is generally very small and the above mentioned harmonics are therefore of most interest to heating applications. Gyration particles also emit radiation at the frequency of gyration and this is the basis for ECE spectroscopy where the radiation spectrum at a particular frequency is related to the plasma parameters in regions of relevant magnetic field strength.

2.2.3 Bernstein waves

In a hot plasma, the finite Larmor radii of the particles also means that the plasma can display coherent density oscillations as particles gyrate in and out of phase. Of special importance to this work is the emergence of electrostatic waves known as Bernstein waves[52, 53] which propagate perpendicularly to the background magnetic field and satisfy the dispersion relation[47]

$$k^2 = \sum_{\zeta} 4 \frac{\omega_{p\zeta}^2}{v_{t\zeta}^2} e^{-\lambda_{\zeta}} \sum_{n=1}^{\infty} \frac{I_n(\lambda_{\zeta})}{\frac{\omega^2}{n^2 \omega_{c\zeta}^2} - 1}, \quad (2.33)$$

where $\lambda_{\zeta} = k^2 \rho_{L\zeta}^2 / 2$ and I_n is the modified Bessel function of the first kind. As can be seen above, there is a resonance at every harmonic of the cyclotron frequencies, and the lowest order resonances are stronger since I_n becomes small for large n . In a single ion species plasma, the waves are typically divided into electron Bernstein waves (EBWs), being the waves near harmonics of ω_{ce} , and ion Bernstein waves (IBWs), near the harmonics of ω_{ci} . Solving the dispersion relation analytically requires some assumptions to be made. Even solving the equation numerically is challenging since, in part, the solutions are not bijective functions of neither ω nor k , but also because the exponential drops off to zero quickly while the resonances diverge, often resulting in numerical overflow. For EBWs, this can be overcome by first assuming that the ion terms can be neglected as the very high harmonics of the ion cyclotron frequency, which are in

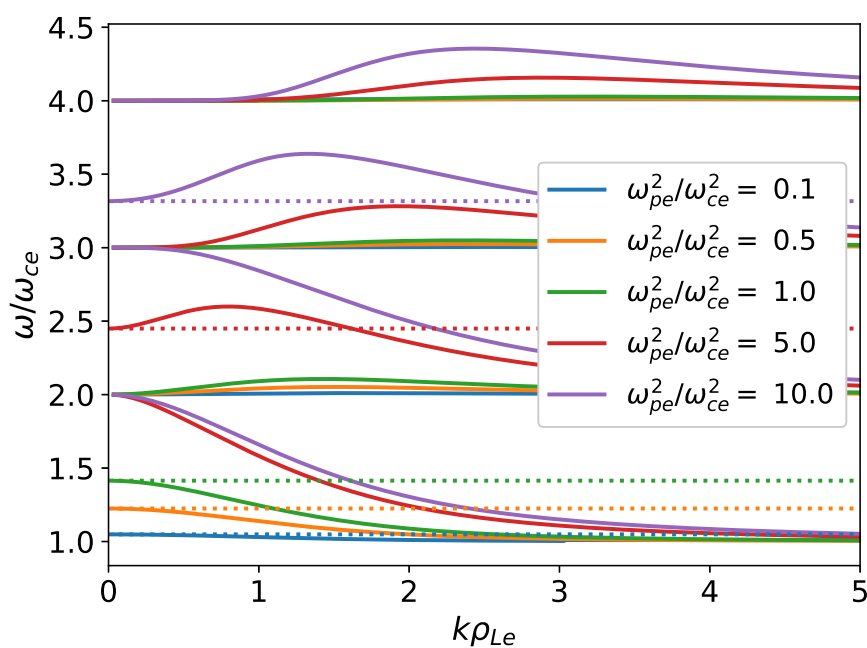


Figure 2.2: Solutions to equation (2.34) for different ratios of $\omega_{pe}^2/\omega_{ce}^2 \propto n_e/B_0^2$ as indicated by their color. Dotted horizontal lines show the UH frequency with the color again indicating plasma parameters. EBWs exist in bands between each harmonic of the EC frequency. At low $k\rho_{Le}$, their frequencies are closer to the UH frequency, within the limits of their frequency bands.

the EC range, are too weak to matter. The process for IBWs is analogous[43]. Next, taking the logarithm of the dispersion relation allows the product between the small exponential and the diverging sum to be separated into terms that are added,

$$0 = \ln \left(\frac{4\omega_{pe}^2}{k_{EBW}^2 v_{te}^2} \right) - \lambda_e + \ln \left(\sum_{n=1}^{\infty} \frac{I_n(\lambda_e)}{\frac{\omega^2}{n^2 \omega_{ce}^2} - 1} \right). \quad (2.34)$$

It is often easier to write a script that solves this equation by minimizing the absolute value of the right hand side. Figure 2.2 shows numerical solutions to the above equation below $5\omega_{ce}$ for different plasma parameters. First, we note that there is just one branch between every harmonic of ω_{ce} from the fundamental and up, and that the n th branch has a resonance at $n\omega_{ce}$. In an underdense plasma, i.e. $\omega_{pe}^2 < \omega_{ce}^2$, EBWs propagate only very close to $n\omega_{ce}$. The limited dynamics can be rationalized by noting that a stronger magnetic field reduces the Larmor radius which is the mechanism that propagates the density perturbations. At higher density to magnetic field ratio, the branches display more intricate shapes. The branch closest to the UH frequency is seen to go to ω_{UH} for small k while the branches below go to $(n+1)\omega_{ce}$ and the branches above to $n\omega_{ce}$ for small k . There is no high density cutoff for these waves. The part of the spectra found not in the immediate vicinity of a cyclotron resonance typically has $k\rho_{Le} \sim 1$ meaning that the wavelengths of EBWs are on the order of the electron Larmor radius.

Similar observations can be made for IBWs with the substitution of electron to ion scales, i.e. $\omega_{ce} \rightarrow \omega_{ci}$, $\omega_{UH} \rightarrow \omega_{LH}$ and $\rho_{Le} \rightarrow \rho_{Li}$. However since $\omega_{pi}^2/\omega_{ci}^2 = (m_i/m_e)\omega_{pe}^2/\omega_{ce}^2$, the IBWs behave as if they experience a weaker magnetic field than the EBWs and the LH frequency is typically found at much higher ion cyclotron harmonics. The branch of IBWs nearest to the LH frequency will be referred to as warm LH waves, see figure 2.4. It is also possible to make other simplifications when solving for IBWs as the Larmor radii of the ions are significantly larger than those of the electrons, see for instance [47].

The EBW branch closest to the UH frequency is special as it connects with the X-mode dispersion line. When kinetic effects are taken into account, the X-mode no longer has a true resonance at the UH frequency. Instead it becomes longitudinal and experiences a finite wave amplification before connecting with an EBW at what will be referred to as the UH layer. For the special case of slow X-mode connecting with the first EBW branch, the wavenumbers of the two waves near the UH layer are both solutions to the dispersion relation[39, 41]

$$\mathcal{D} = \ell_{Te}^2 (k_x^2 + k_y^2)^2 + S(k_x^2 + k_y^2) - \frac{\omega^2}{c^2} (S^2 - D^2) = 0, \quad (2.35)$$

$$\ell_{Te}^2 = \frac{3}{2} \frac{v_{Te}^2}{4\omega_{ce}^2 - \omega^2} \frac{\omega_{pe}^2}{\omega^2 - \omega_{ce}^2}. \quad (2.36)$$

Solving for k_x gives the relatively simple relation

$$k_x^{\pm} = \frac{1}{\ell_{Te}} \sqrt{-\frac{S}{2} \mp \frac{S}{2} \sqrt{1 + \frac{4\omega^2}{c^2} \frac{S^2 - D^2}{S^2} \ell_{Te}^2 - k_y^2 \ell_{Te}^2}}, \quad (2.37)$$

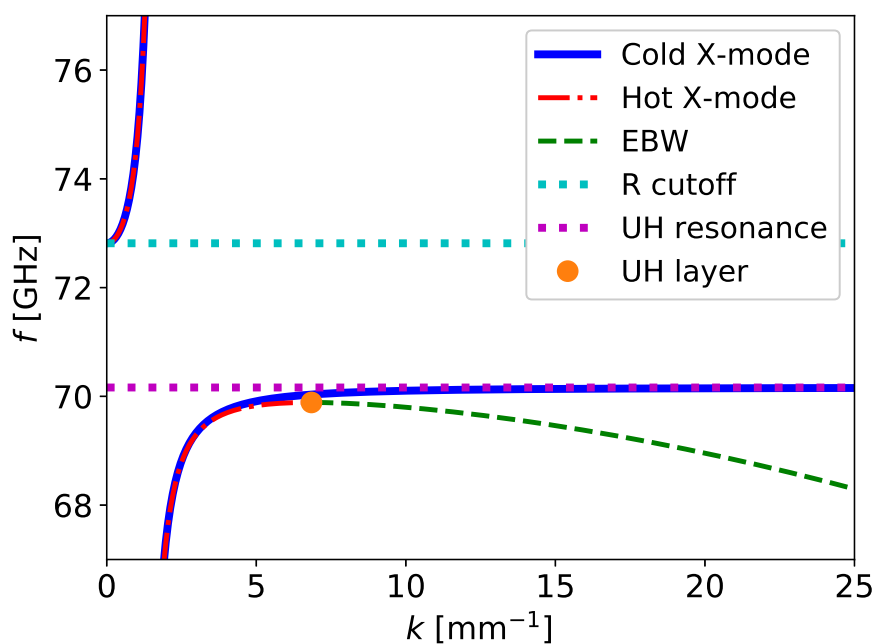


Figure 2.3: A comparison of cold X-mode, equation (2.19), and warm X-mode, k^- in equation (2.37), with the first EBW branch, k^+ in equation (2.37), as indicated by the legend. The hot X-mode and EBW lines meet at the UH layer, which is marked with an orange circle. Plasma parameters are $n_e = 5.1 \times 10^{18} \text{ m}^{-3}$, $B = 2.4 \text{ T}$ and $T_e = 1 \text{ keV}$. These parameters are relevant to chapter 5 except for the electron temperature which has been increased to emphasize the difference between cold and warm X-mode.

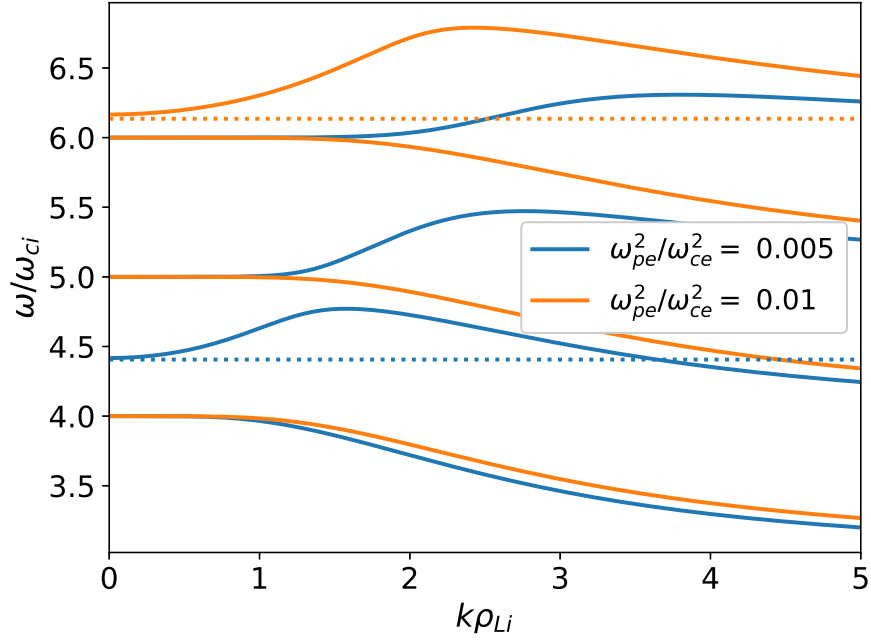


Figure 2.4: Solutions to equation (2.34) but with the substitutions $\omega_{pe} \rightarrow \omega_{pi}, \omega_{ce} \rightarrow \omega_{ci}, v_{te} \rightarrow v_{ti}$ and λ_i . Solutions are shown for two different ratios of $\omega_{pe}^2/\omega_{ce}^2 \propto n_e/B_0^2$ as indicated by their color. Dotted horizontal lines show the LH frequency from which the LH wave extends with the color again indicating plasma parameters. Comparing it to figure 2.2, ω_{LH}/ω_{ci} is much higher than ω_{UH}/ω_{ce} because of the mass ratio between electrons and ions.

where + refers to the EBWs and – to X-mode. These dispersion relations along with the cold X-mode dispersion relation in equation (2.19) are shown in figure 2.3 near the R cutoff and the UH layer. As can be seen in the figure, the cold and hot X-mode dispersion relation are very similar except right at the UH layer where slow X-mode in the kinetic model does not diverge. Instead, a slow X-mode may convert linearly into an EBW and vice versa at the UH layer which is slightly below the UH frequency. Unlike an electromagnetic X-mode wave, EBWs cannot be excited in vacuum and injected into a plasma as there are no or too few particles to carry them so the UH layer is key in exciting these electrostatic waves. This will be discussed in greater detail in the next section.

2.3 Beam paths in fusion plasmas

Having described basic properties of certain waves in the preceding section, this section is dedicated to applications and excitation of the same waves in fusion plasmas.

2.3.1 The WKB approximation and geometric optics

Our dispersion relations so far in this chapter have been based on the assumption that the plasmas had an entirely homogeneous background level and this is obviously not the case for a physical plasma. Our dispersion relations may still be of great interest provided that the background plasma parameters change sufficiently slowly as seen by a wave propagating through it. The approach we are motivating is known as the WKB approximation, see for instance [43] which we follow, and is very useful in applying our dispersion relations to an inhomogeneous plasma. We assume that the approximate solution to a wave propagating through an inhomogeneous plasma is to write it as a wave whose wavenumber, $k_{\text{WKB}} = k_{\text{WKB}}(x)$, always satisfies the homogeneous dispersion relation for local plasma parameters and the amplitude of it adjusts to conserve energy. For a wave propagating in the x -direction, the electric field of a monochromatic wave may then be written as

$$\mathbf{E}_1(x) \approx \frac{1}{\sqrt{k_{\text{WKB}}}} \exp\left(i \left[\int^x k_{\text{WKB}} dx' - \omega_{\text{WKB}} t \right]\right) \hat{\mathbf{e}}_1, \quad (2.38)$$

where ω_{WKB} is the frequency of the wave, which does not change, and $\hat{\mathbf{e}}_1$ is its polarization. This approximation is valid under the assumption that the plasma inhomogeneity lengthscale is much longer than the wavelength which can be formulated as

$$\frac{1}{k_{\text{WKB}}^2} \frac{dk_{\text{WKB}}}{dx} \ll 1. \quad (2.39)$$

This approach can be used to calculate the path of a ray through a plasma, and it is then known as geometric optics. By writing our dispersion relation in the form $\mathcal{D}(\mathbf{r}, \mathbf{k}) = 0$, we demand that it is also satisfied at some nearby position, i.e. $\mathcal{D}(\mathbf{r} + \delta\mathbf{r}, \mathbf{k} + \delta\mathbf{k}) = 0$. Taylor expanding this along a path s , coupled equations similar to Hamilton's equations are obtained

$$\frac{d\mathbf{k}}{ds} = -\frac{\partial \mathcal{D}}{\partial \mathbf{r}}, \quad (2.40)$$

$$\frac{d\mathbf{r}}{ds} = -\frac{\partial \mathcal{D}}{\partial \mathbf{k}}. \quad (2.41)$$

The equations can be utilized for ray tracing of waves through an inhomogeneous plasma provided that the criterion for WKB is satisfied along the path of the ray. However, this approach does not take diffraction into account which, as we will discuss in the next section, affects the shape of a beam as it propagates through a plasma.

2.3.2 Gaussian beam propagation

As O- and X-mode can be coupled to electromagnetic waves in vacuum, they can be excited externally and injected into a magnetically confined fusion plasma for heating and diagnostic purposes. For typical medium and large tokamak or stellarator plasma parameters, electron frequencies such as ω_{pe} and ω_{ce} lie in the microwave spectrum. Gyrotrons[54] are typically used to produce high power Gaussian beams of up to 1 MW power. Gyrotrons work by sending electrons into a cavity under an applied magnetic field. The gyrotron cavity is constructed

such that the electrons can couple to resonant modes at desired frequencies and produce ECE radiation which can be led out of the cavity. The resulting beam can then be polarized and guided into the plasma.

Propagation of a beam in a plasma is not trivial as the refractive index of the plasma depends on the background density and magnetic field which are generally dependent on position and time. Further complicating things even in a homogeneous and linear plasma, the Helmholtz equation, which describes the propagation of a wave[12] in such a medium, does not allow a beam with a Gaussian amplitude profile to keep its shape as it propagates. Instead, the beam will have a minimal beam width at a focal point and will defocus when moving away from it. The electric field of a beam propagating in the x -direction with a focal point at $x = 0$ is given by[12]

$$E(x, y, z) = E_0 \frac{w_0}{w(x)} \exp \left(-\frac{y^2 + z^2}{w^2(x)} - ik \left[x + \frac{y^2 + z^2}{2R(x)} \right] \right), \quad (2.42)$$

$$w(x) = w_0 \sqrt{1 + \left(\frac{x}{x_R} \right)^2}, \quad (2.43)$$

$$R(x) = x \left[1 + \left(\frac{x_R}{x} \right)^2 \right], \quad (2.44)$$

where w_0 is called the beam waist, which represents the width of the beam at the focal point, and $x_R \equiv kw_0^2/2$ is called the Rayleigh length, which is the characteristic length scale over which diffraction causes the beam to spread out. The width of the beam at a given position is $w(x)$ so in order to conserve power, the field amplitude must be scaled with the ratio of the beam waist to beam width. This means that care must be taken to ensure that the width of the gyrotron beam is appropriate in relation to the size of the plasma and that the focal point is placed at a desirable position in the plasma. As can be seen above, not only does the beam width increase away from the focal point, the planes of constant phase curve as dictated by $R(x)$.

2.3.3 Electron cyclotron heating

Heating the plasma using O- and X-mode waves is a matter of getting the right mode to a desirable resonance, preferably in the plasma core. In an underdense plasma, O-mode may propagate relatively unimpeded from vacuum to the fundamental EC resonance (ECR) as seen in figure 2.1a where it experiences strong absorption. Fundamental X-mode heating is at a disadvantage when compared to fundamental O-mode heating on a number of points. As seen in figure 2.1b, an X-mode beam entering from vacuum on the low field side of the ECR will be blocked by the R cutoff. While it in principle is possible to inject X-mode from the high field side of a tokamak or stellarator, engineering this presents several issues. Lastly, X-mode experiences a weaker absorption at the fundamental ECR than O-mode does in a weakly underdense plasma.

In a high magnetic field device, the fundamental ECR may be found outside the plasma core on the high field side. As $\alpha_1^{(O)} \propto \omega_{pe}^2$, it might instead be more favorable to use X-mode aimed at the second harmonic ECR, which may be placed at higher density and is not blocked by the R cutoff below a given density. Depending on the plasma profile, it may also be favorable to aim

for the second harmonic ECR with O-mode or the third harmonic ECR with X-mode if these are found close to the plasma core.

2.3.4 Bernstein wave heating

In an overdense plasma, the fundamental ECR is inaccessible to O-mode radiation and typically also to X-mode even though the L cutoff allows it to propagate to higher density. The electrostatic EBWs, on the other hand, do not have a high density cutoff and have a resonance at all harmonics of the ECR. The EBWs may therefore be used as a means of heating overdense plasmas such as those typically found in spherical tokamaks, e.g. MAST-Upgrade[4]. The challenge with using EBWs for heating is that they cannot be excited from vacuum. As mentioned earlier, the dispersion relations for slow X-mode and EBWs coincide at the UH layer, thus allowing for linear conversion between the two types of waves there. However, the R-cutoff separates slow X-mode from fast X-mode, which can be excited from the low field side of the ECR, and the challenge therefore also becomes one of how to excite slow X-mode. There are two linear conversion schemes into EBWs which have been demonstrated experimentally, O-X-B and X-B.

The O-X-B[55, 32] scheme relies on linear conversion of O-mode to X-mode which can be realized at the plasma frequency. Inspecting the dispersion relations for perpendicularly propagating O-mode, i.e. equation (2.18), and X-mode, equation (2.19), it can be seen that they coincide for $B_0 = 0$, however, this special case is of little use. Looking instead at the Appleton-Hartree formula for propagation at an arbitrary angle to the magnetic field in equation (2.27), both solutions are equal at the plasma frequency. In the general case of oblique propagation, either O-mode meets an evanescent region coming from lower density or slow X-mode meets an evanescent region coming from higher density, but for a given magnetic field, there is an optimal angle where they meet without having to tunnel through an evanescent region on either side[55]. After conversion, the slow X-mode can continue to the L cutoff where it is reflected. It then returns towards lower density where it eventually gets to the UH layer and linear conversion into an EBW is possible. EBWs are backward propagating waves so after the last conversion, the EBW changes its direction again, propagating towards higher density and, possibly, the ECR. The conversion scheme is illustrated in figure 2.5a.

The X-B[56] scheme cuts out the initial O-mode of the O-X-B scheme and instead relies on tunneling of injected fast X-mode through the evanescent region between the R cutoff and the UH layer, and into slow X-mode on the other side. For the tunneling to be reasonably successful, the density profile must be very steep so as to minimize the distance that must be tunneled between the R cutoff and the UH layer. The part that makes it past the evanescent region into slow X-mode then propagates to higher density where it is reflected at the L cutoff. Returning to lower density again, the slow X-mode is converted linearly into an EBW at the UH layer. Due to the formation of a triplet[57, 58] consisting of a cutoff, a resonance and another cutoff, the placement of these layers can have the effect of constructive interference on the slow X-mode wave, which increases the overall performance of the X-B conversion scheme. The X-B scheme is illustrated in figure 2.5b. Of course, part of the energy can be lost from this resonator via tunneling out through the evanescent region again which may also happen in the O-X-B scheme. Of more interest to this work, however, are the nonlinear effects which may arise when wave amplification and significant change in wavenumber near the UH layer allows for the slow

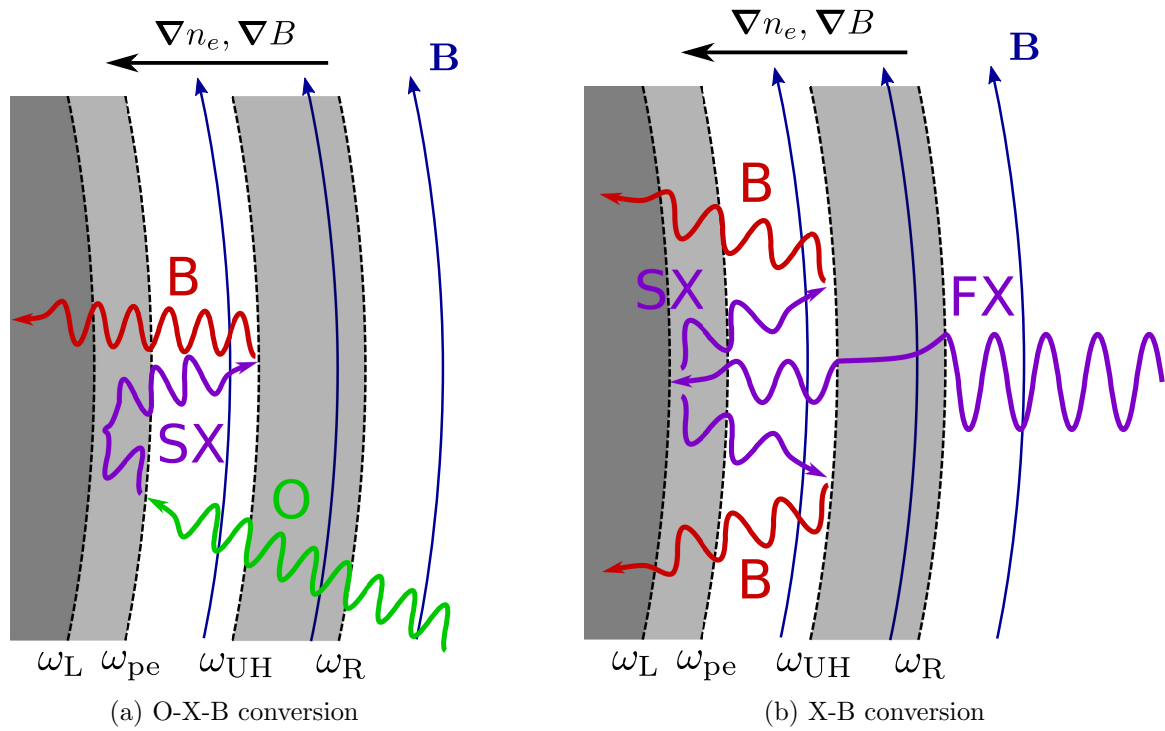


Figure 2.5: Illustrations of the O-X-B and X-B conversion schemes as indicated under the figures. Both use the short hand notation O for O-mode, B for EBW, SX for slow X-mode and FX for fast X-mode. Grey regions are evanescent regions for some waves. Note that the spreading of the SX and B waves in figure 2.5b is mainly for illustrative purposes as it would make the resonator less efficient.

X-mode to act as a pump for three wave interactions involving thermally excited waves. This will be discussed in the following section.

2.4 Three-wave interactions

Nonlinear effects can lead to wave phenomena which can be thought of as decay and scattering processes of waves. Three-wave interactions are nonlinear wave phenomena involving three waves which may be of different frequency but the interactions must conserve energy and momentum, i.e. total frequency and wavenumber. Three-wave interactions can occur in any medium with a quadratic nonlinearity. The fluid momentum equation, equation (2.10), and the Boltzmann equation, equation (2.29), are examples of equations with quadratic nonlinearities. The product of two sines generates two other sines, i.e. $a_1 \cos \varphi_1 a_2 \cos \varphi_2 = \frac{a_1 a_2}{2} [\cos(\varphi_1 + \varphi_2) + \cos(\varphi_1 - \varphi_2)]$, so expanding fields into sums of oscillations and inserting into one of the above mentioned differential equations will give rise to nonlinear mixing of waves. Two waves of f_1, \mathbf{k}_1 and f_2, \mathbf{k}_2 will then interact with waves of f_0, \mathbf{k}_0 only if they satisfy

$$\omega_0 = \omega_1 + \omega_2, \quad \mathbf{k}_0 = \mathbf{k}_1 + \mathbf{k}_2, \quad (2.45)$$

or any permutation of the indices. The above relations are equivalent to conservation of energy and momentum and the strength of the mixing terms increases with the amplitudes of the implicated waves. Similarly, four-wave interactions may occur if the medium has a cubic nonlinearity.

For low amplitude waves, the higher order terms produced by nonlinearities are insignificant contributions and may be cancelled by the dampening the resulting wave experiences. Three-wave interactions can be grouped as either scattering or combination of two waves into a third, or as a pump wave decaying into two daughter waves depending on the exchange of energy between the modes. Above a pump wave amplitude threshold the interactions become unstable. An unstable decay process is called a PDI. Depending on the types of implicated waves, the PDIs may go by different names, see for instance [59, 60]. In this work, we will also use the terms two plasmon decay (TPD) and stimulated Raman scattering (SRS). The TPD instability is a PDI where an electromagnetic wave excites two UH waves, i.e. any combination of slow X-mode and EBWs. The daughter waves exist between the EC frequency and the UH frequency and will therefore typically be of similar frequencies. For SRS in this work, an electromagnetic wave scatters off of a UH wave to produce a downshifted wave. This can also be thought of as decay of an electromagnetic wave into a UH wave and another electromagnetic wave. Those terms will be used so that this work can be related to other relevant work, however, we will often simply use the term PDI as an umbrella term for any PI.

Above the PDI pump threshold, the daughter wave amplitudes will have a nonlinear dependence on the pump amplitude. Exceeding the threshold by a large amount, the pump wave may experience a significant drain of power into the daughter waves. For heating applications using gyrotron beams, possible consequences are that a threshold exists above which the heating efficiency becomes unreliable as power may be diverted into unintended modes. For diagnostics, the complications include to interfere with measurements and to possibly damage sensors if an unexpectedly large amount of radiation is generated by nonlinear processes. Possible applications include transferring energy from electrons to ions through the excitation of ion waves

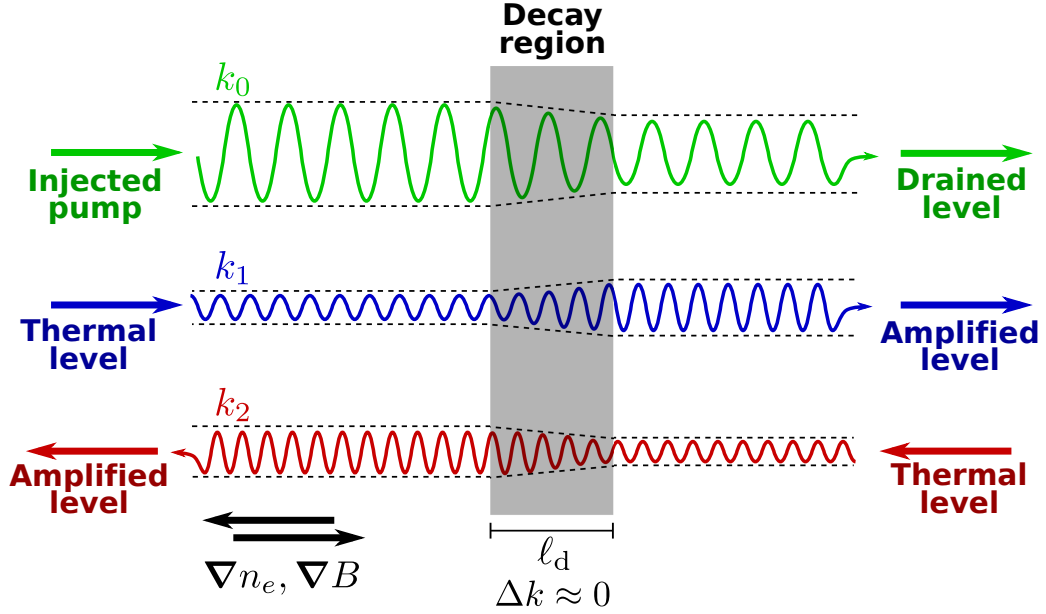


Figure 2.6: An illustration of a PDI of a strong pump, k_0 , into two daughter waves, k_1 and k_2 , in an inhomogeneous medium. As the pump passes through a decay region, two daughter waves are amplified from their thermal background level due to the PDI. At the same time, the pump is drained while passing through the decay region. Directions of propagation need not be exactly as indicated in the figure. The amplitudes of the waves will usually not be comparable.

and diagnostics based on PDI daughter waves as the dominant daughter waves depend on local plasma parameters.

2.4.1 The Piliya-Rosenbluth criterion in inhomogeneous monotonic plasmas

In an inhomogeneous plasma, the wave vector of a wave propagating through the plasma will change as the plasma parameters change. This means that particular three-wave interactions may only conserve frequency and wave vector locally, and that the growth of daughter waves inside the decay region must overcome not only wave dampening but also convection of the waves out of the decay region. Provided that there is a frequency match for three waves, the extend of the decay region is the length over which the wavenumbers approximately match $\ell_d = |\mathrm{d}\Delta k/\mathrm{d}x|^{-1/2}$, where $\Delta k = k_0 - k_1 - k_2$ and x is the direction of propagation. PDIs in an inhomogeneous medium typically are not absolute instabilities where the daughter waves grow exponentially in time. Instead, there is a finite amplification of the daughter waves as they pass through the decay region and part of the pump wave decays, see figure 2.6. Assuming for simplicity that the plasma is monotonic such that the conservation equations for PDI in (2.45) are satisfied only in one region, the gain of daughter wave j can be defined as $G = \ln\left(\frac{I_{j,\mathrm{out}}}{I_{j,\mathrm{in}}}\right)$, where $I_{j,\mathrm{in}}, I_{j,\mathrm{out}}$ are the intensities of the daughter wave as it enters and exits the decay region.

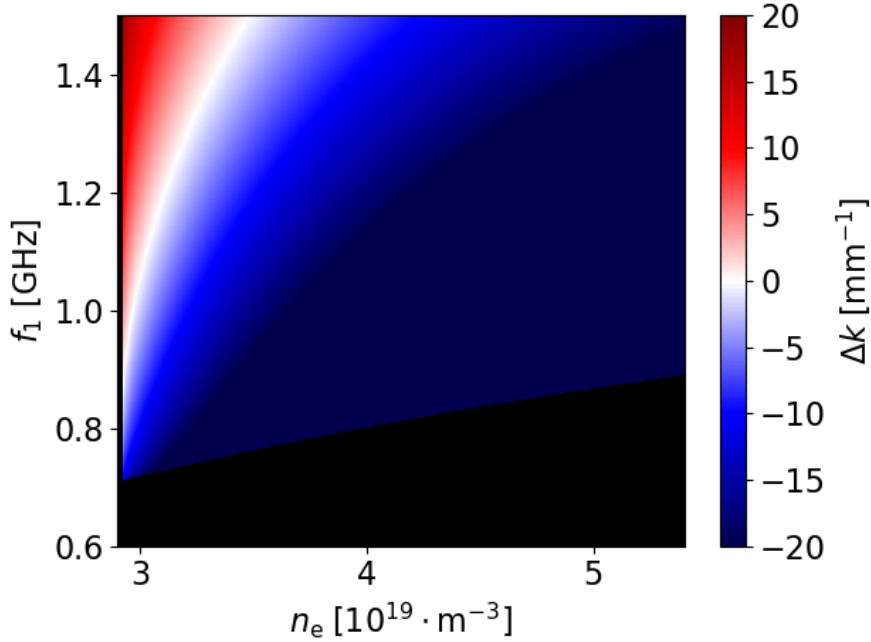


Figure 2.7: Wavenumber mismatch for a PDI of X-mode into an EBW and an LH wave as a function of density and LH daughter frequency. There is a match only along the white line and black region signify that one or more of the waves cannot propagate in that region. The parameters are $n_e = n_i$, $B = B_z = 3.35$ T, $T_e = T_i = 300$ eV and $f_0 = 105$ GHz. These parameters correspond to the parameters of the inhomogeneous simulations in the article [61] which is included in chapter 4.

This leads to the Piliya-Rosenbluth criterion[28, 29, 30] for PDIs

$$G = \frac{2\pi\gamma^2\ell_d^2}{|v_{g,1}v_{g,2}|} > G_{\text{th}}, \quad (2.46)$$

where γ is the growth rate of the PDI in a homogeneous medium, $v_{g,1}$ and $v_{g,2}$ are the group velocities of the daughter waves, and G_{th} is a positive gain threshold value which is usually set to $G_{\text{th}} = 2\pi$ out of convention[59, 33]. Provided that the dispersion relations and plasma parameters are known, ℓ_d is straightforward albeit possibly tedious to calculate and the group velocities can be calculated as $v_{g,j} = \partial\omega_j/\partial k_j$. An analytical expression for the homogeneous growth rate, γ , is typically very specific to the problem being studied and is derived using relevant assumptions to get a closed expression. However in general, γ increases as some positive power of the pump electric field amplitude[59]. From the Piliya-Rosenbluth criterion, there are therefore two obvious ways the threshold for a particular PDI can be reduced: if the pump electric field is large (γ is large), or if the daughter waves are kept in the decay region for longer, i.e. if density and magnetic field gradients in the decay region are small (ℓ_d is large) or if the group velocities of the daughter waves are small in the decay region.

2.4.2 Reduced power threshold PDIs at the UH layer

The subject of chapter 4 is PDIs of X-mode near the UH layer. This has been studied analytically in a number of articles that found that decay of the slow X-mode into an EBW and an LH wave is most likely[62, 34, 35]. In order for decay to take place, the conservation equations in (2.45) must be satisfied. Assuming that f_0, \mathbf{k}_0 is a slow X-mode gyrotron pump wave, f_1, \mathbf{k}_1 is the LH wave and f_2, \mathbf{k}_2 is the EBW wave, the frequency of the EBW will be downshifted by the LH wave such that $f_2 = f_0 - f_1$. Assuming furthermore that all waves propagate along the x -axis, a wavenumber mismatch can be introduced as $\Delta k \equiv k_0 - k_1 - k_2$. The wavenumbers for the pump wave, k_0 , and the downshifted EBW daughter wave, k_2 , can be determined from equation (2.37) provided that the plasma is underdense, and the wavenumber of the LH wave can be found from equation (2.33). The wavenumber mismatch near the UH layer is plotted in figure 2.7 and it is clear that a match is possible for a continuum of daughter frequencies.

Having established that the pump can become unstable to PDIs into a range of daughter frequencies, the Piliya-Rosenbluth criterion in equation (2.46) must be considered to see if any process is unstable at a given pump intensity. The pump electric field amplitude appears in the growth rate of the homogeneous PDI, which can be written in the form[18, 62]

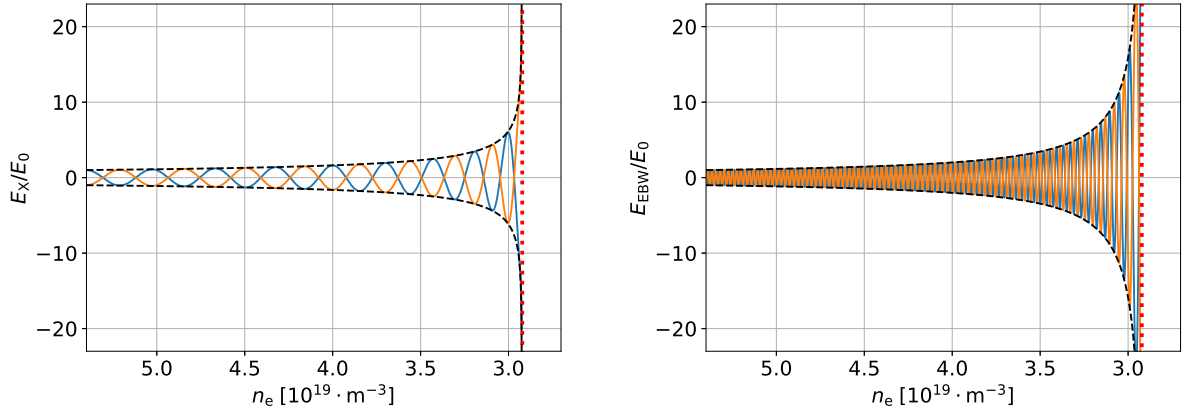
$$\gamma = \pm \sqrt{\nu_{12}\nu_{21}^*|E_0|^2 + \left(\frac{\Gamma_1 - \Gamma_2}{2}\right)^2} - \frac{\Gamma_1 + \Gamma_2}{2}, \quad (2.47)$$

where ν_{12}, ν_{21}^* are nonlinear coupling coefficients that reflect how well the pump and daughter waves couple, and Γ_1, Γ_2 are dampening rates for the daughter waves, we refer to [18] for expressions for these. Of the two possible signs in γ , one that gives $\text{Re}(\gamma) > 0$ may become unstable. If damping can be neglected, the homogeneous PDI growth rate is seen to be proportional to the pump electric field amplitude. This also means that the amplification of the electric field amplitude of the daughter waves is expected to go as the square of the pump wave amplitude.

Because it is the electric field amplitude and not the intensity that enters in the growth rate, amplification of slow X-mode at the UH layer leads to a reduced PDI power threshold since the same gyrotron power now gives a greater γ . The increasing amplitude of the electric field must still conserve power as the gyrotron beam comes closer to the UH layer, and the absolute square of the electric field can be related to the intensity of a beam, I , through[47]

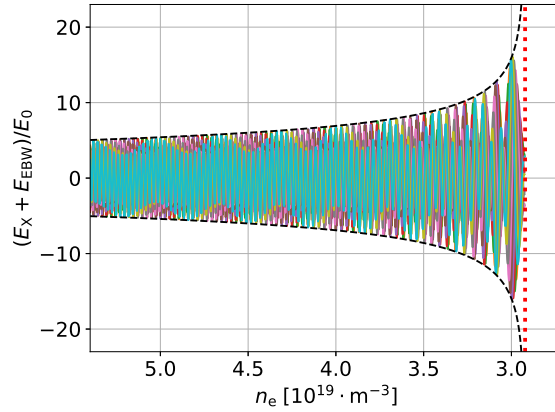
$$|E|^2 = \frac{4k^2 I}{\varepsilon_0 \omega |\nabla_{\mathbf{k}} \mathcal{D}|}, \quad (2.48)$$

where $\nabla_{\mathbf{k}} = (\partial_{k_x}, \partial_{k_y}, \partial_{k_z})$, and \mathcal{D} for X-mode and EBWs is given in equation (2.35). Figure 2.8 shows the amplification of the two waves in the vicinity of the UH layer. A WKB approximation is used such that a wave is described as $\phi_j \propto \exp\left(i \int_{x_0}^x k(x') dx'\right)$ and its electric field amplitude is position dependent and given by the equation above. For X-mode, the wavenumber is seen to increase with amplitude near the UH layer, whereas for EBWs, the wavenumber decreases near the UH layer but the amplitude also increases. Assuming a perfect linear conversion of an X-mode to an EBW, the returning wave gets a $\pi/2$ phase shift[63] and the resulting field is shown in figure 2.8c for a large number of phase shifts. The interference between the two waves means that a smaller degree of amplification may be observed near the UH layer as we will see



(a) Wave amplification of a slow X-mode near the UH layer using k_x^- from equation (2.37). Note that it was assumed that X-mode was entirely longitudinal everywhere in this plot. Although the x -axis shows density, it is related to a spatial axis, see the main figure text and, this gives rise to the phase along the axis.

(b) Wave amplification of a EBW near the UH layer using k_x^+ from equation (2.37). Although the x -axis shows density, it is related to a spatial axis, see the main figure text, and this gives rise to the phase along the axis.



(c) A superposition of the fields in (a) and (b) with an appropriate phase shift to show the resulting field from a linear conversion. The many different lines are at slightly different times to illustrate that interference patterns appear. Although the x -axis shows density, it is related to a spatial axis, see the main figure text, and this gives rise to the phase along the axis.

Figure 2.8: Figures showing wave amplification of a slow X-mode (a) and an EBW (b) propagating from high density to the UH layer using a WKB approximation. A blue and an orange line show the wave at π phase shifts, the dashed black lines mark the amplitude of the waves and the dotted red line marks the UH layer. Figure (c) show the resulting field from perfect linear conversion from an X-mode to an EBW with several phase shifts marked by lines in different colors to illustrate how the interference gives rise to lumps, especially near the UH layer. The parameters are $k_y = 0$, $0 \text{ mm} < x < 13.5 \text{ mm}$, $n_e(x) = n_i(x) = (5.4 + 200 \text{ m}^{-1} \cdot x) \times 10^{19} \text{ m}^{-3}$, $B = B_z = 3.35 \text{ T}$, $T_e = T_i = 300 \text{ eV}$ and $f = 105 \text{ GHz}$. These parameters correspond to the parameters of the inhomogeneous simulations in [61] which is included in chapter 4.

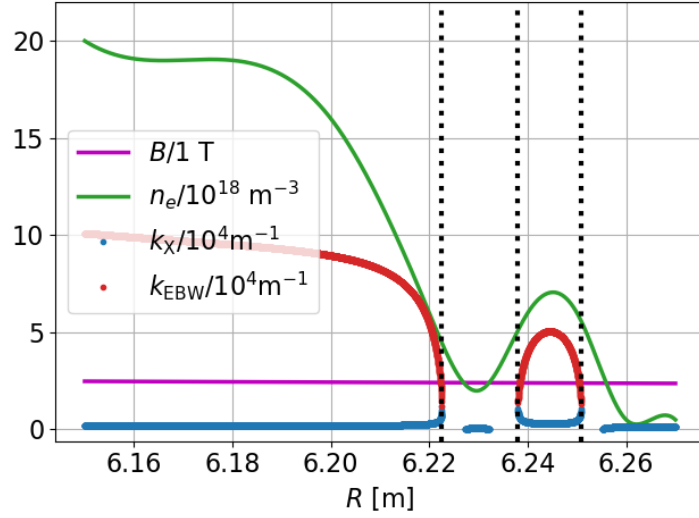


Figure 2.9: Example of a plasma profile where trapping of UH waves may occur. For 70 GHz waves, the blue lines show the X-mode wavenumber and the red line show EBW wavenumbers, both from equation (2.37). The non-monotonic density profile causes multiple UH layers to form, marked by the dotted black lines. Here the dispersion relations for X-mode and EBWs coincide and they will convert and backscatter. In the bump on the right, a closed loop means that the waves are trapped.

in chapter 4. We note, however, that the WKB criterion in equation (2.39) is violated at the UH layer as the change in wavenumber diverges. Still, as we will see in chapter 4, there is decent agreement with simulations.

This type of PDI was the first to be observed experimentally in magnetically confined fusion experiments[31, 64] as scattering shifted in frequency. The shifted EBW daughter wave may escape through inverse X-B and O-X-B processes to be picked up by diagnostics outside the plasma.

2.4.3 PDIs due to trapping between UH layers

Another possibility for a reduced power threshold, which is investigated in this work, is when the daughter waves are trapped and thereby not convected away from the decay region. We consider a situation where a non-monotonic plasma background density gives rise to multiple 2nd harmonic UH layers for a gyrotron pump wave which can cause trapping between fundamental UH layer for half frequency waves as seen in figure 2.9. Whilst the pump wave is not itself trapped, half frequency waves are and figure 2.10 shows how it is possible for the pump to excite two approximately half frequency waves through TPD in two places marked $x_{d,l}$ and $x_{d,r}$. In that situation, the trapped waves can make multiple passes through the decay regions and daughter waves may experience additional amplification with every pass. If the amplification of the trapped waves exceeds the losses in performing a round trip, the PDI can become an absolute instability that grows exponentially in time.

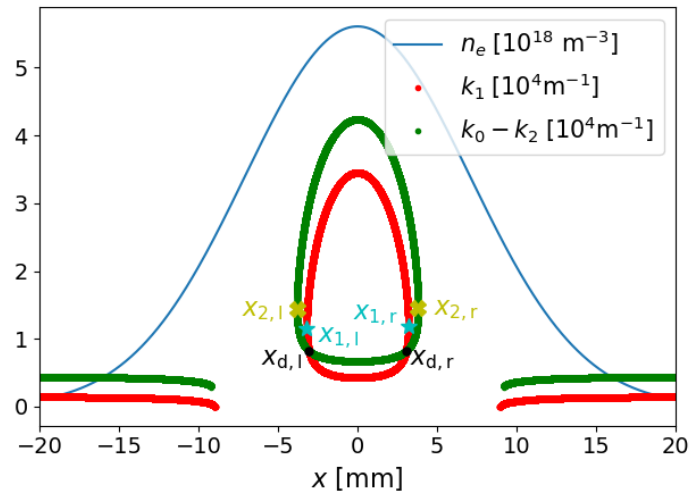


Figure 2.10: A non-monotonic density profile that allows for a pump wave, k_0 , to decay into two trapped daughter waves, k_1, k_2 . The pump is a fast X-mode wave with a frequency $f_0 = 140$ GHz and its dispersion relation is given by (2.19). The daughter waves are UH waves with a frequency separation of $f_1 - f_2 = 0.12$ GHz and a dispersion relation given by equation (2.37). Note that the sign of k_2 is flipped compared to the (2.37). The intersections of the eggs at $x_{d,l}$ and $x_{d,r}$ are marked with black dots. Here we get $f_0 = f_1 + f_2$ and $k_0 = k_1 + k_2$, and PDI is possible. Turning points for k_1 are marked by cyan stars, and are labeled $x_{1,l}$ and $x_{1,r}$; yellow x'es, and $x_{2,l}$ and $x_{2,r}$ mark the turning points for k_2 . The magnetic field is $B = B_y = 2.4$ T and the temperature is $T_e = 100$ eV.

As a trapped wave makes a round trip between two UH layers, the wave may interfere with itself. The models for reduced power threshold PDIs in [39, 40] assume that only waves at frequencies which get an integer times 2π phase shift during the round trip will build up since they experience constructive interference. In addition to the phase shift acquired as the waves propagate, they gain an additional $-\pi/2$ phase shift at the turning points, i.e. at $x_{j,l}$ and $x_{j,r}$ for wave j in figure 2.10, which add up to a shift of $-\pi$ for the whole round trip[63]. These waves can be thought of as eigenmodes of the background density profile which acts as a cavity. The eigenmodes satisfy Bohr-Sommerfeld quantization and assuming that the waves propagate only in the x -direction, this can be written as

$$\int_{x_{j,l}}^{x_{j,r}} |k_{x,j}^+| - |k_{x,j}^-| dx = (2m + 1)\pi, \quad (2.49)$$

where $m \in \mathbb{N}_0$ is the mode number and $k_{x,j}^\pm$ are the X-mode and EBW dispersion relations of the j th waves as found in equation (2.37). In principle, $m < 0$ is also possible if the absolute values are removed but these modes mirror $m > 0$ and simply correspond to wave propagating in the opposite directions and are essentially the same modes. The $m = 0$ mode corresponds to a wave whose phase acquired through a round trip is exactly cancelled by the phase shifts at the turning points.

Within the WKB approximation, the electrostatic potential created by an eigenmode in 1D, $\text{Re}(\Psi_j)$, has the form[39] $\Psi_j \propto \Psi_j^+ + \Psi_j^-$ with

$$\Psi_j^\pm = \frac{\exp\left(i \int^x k_{x,j}^\pm dx'\right)}{\sqrt{|v_{g,j}^\pm|}}, \quad (2.50)$$

where $v_{g,j}^\pm = (\partial_{\omega_j} k_{x,j}^\pm)^{-1}$ are the group velocities of equations (2.37) and example are shown in figure 2.11. The integral have an arbitrary lower integration bound which just has to be the same for both the X-mode and EBW component as it simply produces a phase offset. Figure 2.11a shows the lowest mode number, i.e. $m = 0$, for the "cavity" in figure 2.10. The eigenmode has an unintuitive shape, however, the phase contribution from Ψ_j^+ is approximately 4π while Ψ_j^- contributes with approximately -3π and the phase shifts finally gives another $-\pi$ phase shift totaling to zero phase shift as it should. This mode has the highest frequency of all the eigenmodes, i.e. closest to the UH frequency, because the EBW wavenumber, which is the main contributor to the phase, is smallest near the UH layer.

For the match shown in figure 2.10, the closest eigenmodes are $f_1 = 70.118$ GHz, which is mode number 19 and shown in figure 2.11b, and $f_2 = 69.88$ GHz which is mode number 39 and shown in figure 2.11c. For these higher modes, we see that the potential $\text{Re}(\Psi_j)$ displays short scale waves due to Ψ_j^+ which are modulated over longer scale lengths by Ψ_j^- . We also note that the amplitude and wave lengths of the waves increase near the turning points. This happens because the turning points are UH layers of the eigenfrequencies where UH waves are amplified and the wavenumber of EBWs decrease as was also seen in figures 2.8a-c. Because the UH frequency decreases with density, higher wavenumbers extend further out as hinted in figures 2.11a-c.

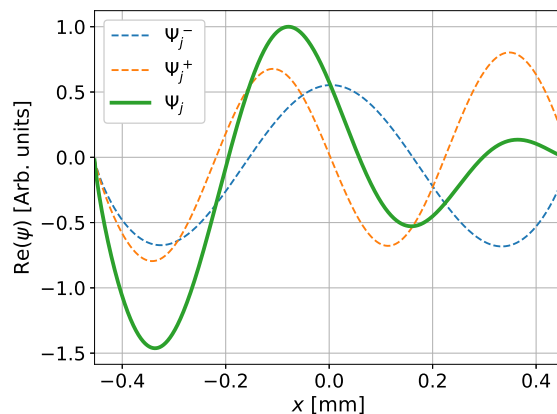
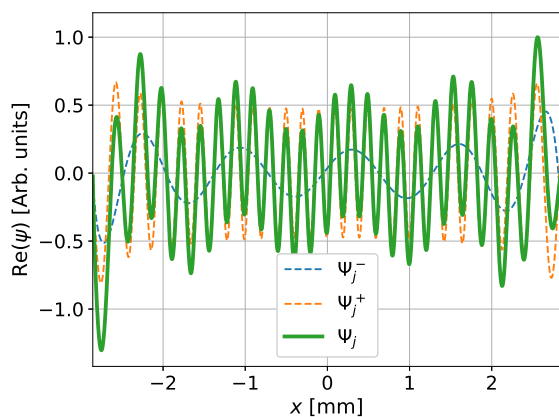
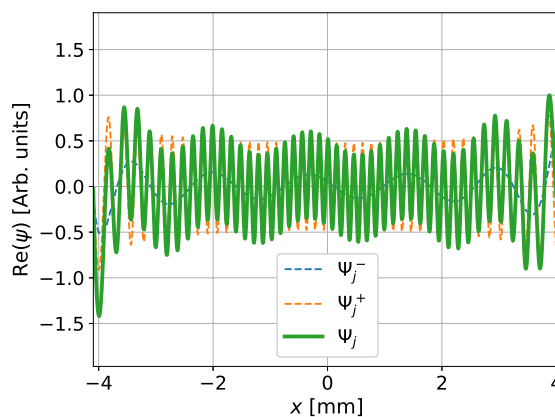
(a) $m = 0$ and $f_j = 70.356$ GHz(b) $m = 19$ and $f_1 = 70.118$ GHz(c) $m = 39$ and $f_2 = 69.88$ GHz

Figure 2.11: Normalized electrostatic potentials of selected eigenmodes plotted for the parameters outlined in figure 2.10. In all plots, the green line is the potential generated by the eigenmode, with the dashed blue line being the contribution from X-mode and the dashed orange line the contribution from the EBW. The mode number and corresponding frequency is indicated below each plot. Note that the extend of the x -axes differ for each plot.

With smaller losses for the trapped eigenmodes, the TPD instability can become absolute and eigenmodes will then grow exponentially in time until they exceed the amplitude threshold for secondary PDIs which may similarly become absolute if the secondary daughter waves are also trapped eigenmodes. The secondary PDIs would typically be of the kind described in section 2.4.2, where UH waves near the UH layer decay into a downshifted UH wave and an LH wave, IBW or ion acoustic wave. The secondary PDIs will saturate the primary PDIs by draining the primary daughter waves at the same rate that the primary PDI feeds energy into them. As the secondary daughter waves grow, they too can become unstable and cascade of subsequent PDIs can feed waves until PDIs are able to dissipate energy out of the cavity again at the same rate that it is absorbed by the primary PDIs. Typically this would be when the increasingly downshifted daughter waves have low enough frequencies to escape the non-monotonic density perturbation without being blocked by UH layers in all directions, or if they can recombine into escaping electromagnetic waves.

The excitation of primary trapped daughter waves is discussed further in chapter 5 and in chapter 6, we look into the eigenmodes of the cavities in greater detail.

Chapter 3

Particle-in-cell codes

In this chapter, we first discuss the PIC model in section 3.1 and derive an update scheme similar to that of EPOCH in section 3.2. Then we discuss PIC codes in comparison to other types of codes in section 3.3. Finally, we show that EPOCH is able to reproduce wave properties from chapter 2 in section 3.4.

3.1 Basic concept of particle-in-cell codes

When describing a plasma numerically, the simplest model would be to push every single particle around according to the forces that are working on them. However, at particle number densities of $10^{19} - 10^{21} \text{ m}^{-3}$ for fusion grade magnetically confined plasmas[43] and vacuum vessels that can fit people inside them, this approach is simply not feasible. Fortunately, the numerical workload can be lessened by reducing the problem analytically. Because the waves and wave interactions we are interested in are derived from kinetic theory, the model which we are to numerically integrate must not neglect kinetic effects. Typically, one is then left with the choice between a PIC code or a Vlasov solver.

PIC models are based on the principle of representing the physical particles by a smaller number of superparticle, also sometimes referred to as macroparticles or pseudoparticles. Each of the superparticles account for many of only a single species of particles but they are neither heavier nor charged differently from that particle species. Rather, they can be thought of as clouds of particles with a fixed physical extent which react to the Lorentz force as a single particle would. The update scheme is split in a field updater and a particle pusher. The electric and magnetic fields are updated according to Maxwell's equations using positions and velocities of all the real particles. With the updated fields, the superparticles can be updated in terms of positions and momenta according to the forces they experience which is weighted by a chosen shape function. When particles have been updated based on the fields, the fields can then be updated again based on the particles and so on.

In this work, we have made use of the PIC code EPOCH[65]. EPOCH was developed at the University of Warwick where it continues to be maintained. The aim with EPOCH was to develop a highly parallelizable relativistic PIC code based on slightly older models while bringing modern features to them and making the code easily extendable for developers and users. Unlike

some older PIC codes, EPOCH couples fields to particles through charge flux rather than through distribution functions and it includes collisions, higher order shape functions as well as more exotic high energy density modules for QED effects. EPOCH has previously been used to study PDIs in the context of X-B conversion[66]. EPOCH has also been applied in studies related to inertial confinement on how to avoid SRS and stimulated Brillouin scattering confinement[67] and on how to use the same PDIs as means of laser amplification[68].

3.2 Derivation of EPOCH's equations

The PIC code EPOCH is based on PSC by Hartmut Ruhl[69] which is a Birdsall and Langdon[70] type PIC code. In the following, we will derive and discuss an update scheme similar to that used by EPOCH. The update scheme is split between a field solver based on the finite difference time domain (FDTD) method discussed in section 3.2.2 and a particle pusher discussed in section 3.2.3. Before we go into that, we will mention some very basic concepts of discretization in numerical studies.

3.2.1 Discretization of continuous functions

Values for scalar and vector fields cannot be stored on a computer for all points of a continuous variable due to finite memory limitations. Instead, they must be mapped on to a representative grid of finite size and number of grid points. Choosing the grid size and resolution is imperative but is often a trade off between capturing the targeted physics and accomplishing it with manageable computational requirements. The typical approach is to make convergence tests to see if the results obtained from numerical simulations converge when the grid is changed. As a rule of thumb, the length and time scales to be captured must be much greater than the relevant numerical resolution.

The discretization of fields on to a grid obviously affects calculus involving the infinitesimal such as derivatives. A number of different discretizations of derivatives have been suggested with different accuracies and involving different numbers of grid points[71]. Here we shall only look at the ones relevant to this project. Suppose a function, $f(x)$, is known in the point x_j and is sampled with a grid spacing of Δx , a Taylor expansion of the function in $x_j + \Delta x$ then gives us

$$f(x_j + \Delta x) = \sum_{n=0}^{\infty} \frac{f^{(n)}(x_j)}{n!} \Delta x^n \quad (3.1)$$

$$\Rightarrow f'(x_j) = \frac{f(x_j + \Delta x) - f(x_j)}{\Delta x} - \sum_{n=2}^{\infty} \frac{f^{(n)}(x_j)}{n!} \Delta x^{n-1}, \quad (3.2)$$

where $f^{(n)}(x)$ is the n th derivative of $f(x)$. Because the grid spacing, Δx , is supposed to be chosen much smaller than any other length scale, larger powers of Δx only contribute as higher order corrections. This allows us to define the forward difference with an error on the order $\mathcal{O}(\Delta x)$ as

$$\partial_x^+ f(x_j) \equiv \frac{f(x_j + \Delta x) - f(x_j)}{\Delta x}. \quad (3.3)$$

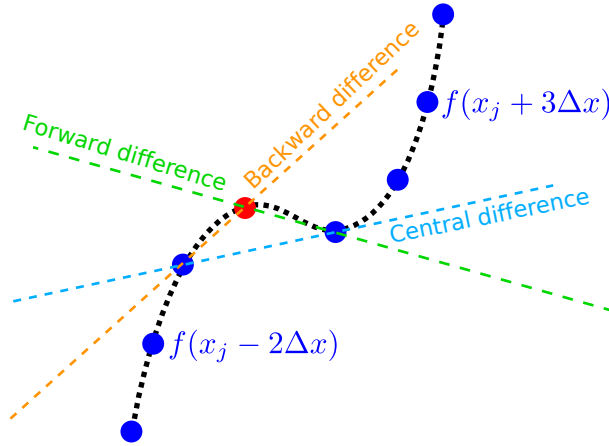


Figure 3.1: An illustration of how the forward- (green dashed line), backward- (orange dashed line) and central (light blue dashed line) difference schemes estimate the derivative of a function (black dotted line), which is sampled across a grid. The derivatives are estimated in the point x_j (red circle) based on neighboring sampled points (blue circles).

The backward difference uses the point before x_j instead and also has an error on the order $\mathcal{O}(\Delta x)$,

$$\partial_x^- f(x_j) \equiv \frac{f(x_j) - f(x_j - \Delta x)}{\Delta x}. \quad (3.4)$$

Finally, a finite difference scheme involving not the point x_j itself but only the neighboring points can be derived as

$$f(x_j + \Delta x) - f(x_j - \Delta x) = 0 \times \Delta x^0 + 2f'(x_j) \times \Delta x^1 + 0 \times \Delta x^2 + \mathcal{O}(\Delta x^3), \quad (3.5)$$

$$\partial_x^c f(x_j) \equiv \frac{f(x_j + \Delta x) - f(x_j - \Delta x)}{2\Delta x}, \quad (3.6)$$

which is known as the central difference with an error on the order $\mathcal{O}(\Delta x^2)$. The central difference scheme uses the same grid spacing and achieves higher precision. The three schemes are shown in figure 3.1 and although the grid spacing is unacceptably coarse for the sake of illustration, the central difference scheme is seen to give a more accurate estimate of the derivative in the red point.

3.2.2 The FDTD scheme and the Yee grid

The starting point of the field updating scheme is the two curl Maxwell equations, i.e. equations (2.3) and (2.4) on page 10. The current density, which appears in equation (2.4) is updated with a charge density continuity equation

$$\partial_t \rho(\mathbf{r}, t) = -\nabla \cdot \mathbf{J}(\mathbf{r}, t), \quad (3.7)$$

where $\rho(\mathbf{r}, t)$ is the charge density, which is handled by the particle pusher. Using a grid spacing of Δx , Δy and Δz along our axes, we write the position vector at some grid position as $\mathbf{r}_{jkl} =$

$(j\Delta x, k\Delta y, l\Delta z)$. Defining the time step of the full updating cycle as Δt , time can then be written as $t^n = n\Delta t$. To denote the fields on our grid, we use the short hand form $f_{jkl}^n \equiv f(j\Delta x, k\Delta y, l\Delta z, n\Delta t)$, however, EPOCH uses by standard a Yee grid[72] on which the grid of each component of the fields are shifted by half integer steps in physical space relative to each other. The electric field components are shifted half a step along their own axis and the magnetic field components are shifted along any axis but their own. The grid of the current density is the same as the one used for the electric field. To avoid having to carry these halves around we therefore define

$$\mathbf{E}_{jkl}^n \equiv \left((E_x)_{j+\frac{1}{2}kl}^n, (E_y)_{jk+\frac{1}{2}l}^n, (E_z)_{jkl+\frac{1}{2}}^n \right) \quad (3.8)$$

$$\mathbf{B}_{jkl}^n \equiv \left((B_x)_{jk+\frac{1}{2}l+\frac{1}{2}}^n, (B_y)_{j+\frac{1}{2}kl+\frac{1}{2}}^n, (B_z)_{j+\frac{1}{2}k+\frac{1}{2}l}^n \right) \quad (3.9)$$

$$\mathbf{J}_{jkl}^n \equiv \left((J_x)_{j+\frac{1}{2}kl}^n, (J_y)_{jk+\frac{1}{2}l}^n, (J_z)_{jkl+\frac{1}{2}}^n \right). \quad (3.10)$$

The Yee cell with electric and magnetic field component is shown in figure 3.2. The reason for using this staggered grid has to do with the curl operators in Maxwell's equations. The EPOCH field update scheme works by first updating the electric and magnetic fields by half a time step. Discretizing the time derivatives of our equations with a forward difference and rearranging, we get

$$\mathbf{E}_{jkl}^{n+\frac{1}{2}} = \mathbf{E}_{jkl}^n + c^2 \frac{\Delta t}{2} (\nabla \times \mathbf{B}_{jkl}^n - \mu_0 \mathbf{J}_{jkl}^n), \quad (3.11)$$

$$\mathbf{B}_{jkl}^{n+\frac{1}{2}} = \mathbf{B}_{jkl}^n - \frac{\Delta t}{2} \nabla \times \mathbf{E}_{jkl}^{n+\frac{1}{2}}. \quad (3.12)$$

When discretizing the curl operators, we notice how writing forward differences for the curl operator, i.e. $\nabla^+ \equiv (\partial_x^+, \partial_y^+, \partial_z^+)$, when it is working on the electric field allows us to effectively have central differences at all the positions of the magnetic field components in the Yee grid, i.e. $\partial_y^+(E_z)_{jkl}^n$ and $\partial_z^+(E_y)_{jkl}^n$ correspond to the central difference at the position of $(B_x)_{jkl}^n$ in figure 3.2. When working on the magnetic field, a backward difference, $\nabla^- \equiv (\partial_x^-, \partial_y^-, \partial_z^-)$, works as a central difference for the electric field in the Yee cell. The staggered Yee grid may seem confusing but its strength lies in the higher precision the central differences provide. Because \mathbf{E}_{jkl}^n and \mathbf{J}_{jkl}^n are defined on the same grid, no further modification to the current term is needed. The time step in EPOCH is by default 0.95 of the CFL condition[73, 70]. Having updated the electric and magnetic fields half a time step with the equations above and appropriate curl operators inserted, EPOCH's particle pusher then updates particle positions, momenta and the resulting current. This will be described in the next subsection. After the particle pusher has been called, the magnetic field is updated another half step followed by the electric field, and the field update

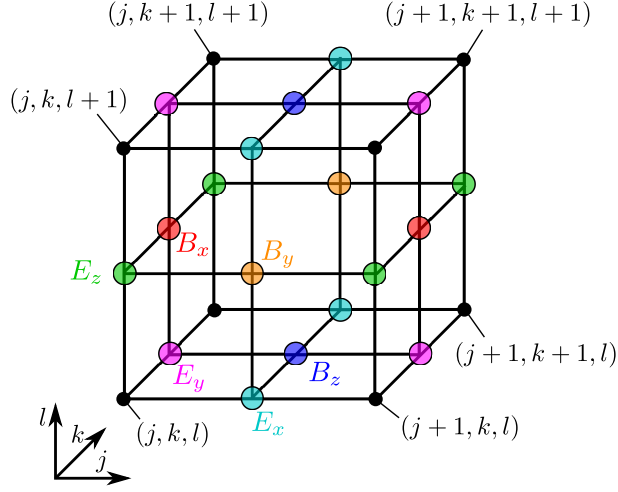


Figure 3.2: The Yee cell as with \mathbf{E}_{jkl} and \mathbf{B}_{jkl} components shifted as they are in EPOCH's update scheme. Black nodes correspond to grid points, however, fields are evaluated shifted by half indices for a more precise finite difference routine. The components of \mathbf{E}_{jkl} are shifted in the direction they are pointing whereas the components of \mathbf{B}_{jkl} are shifted along all directions except the direction they are pointing. The \mathbf{E}_{jkl} and \mathbf{B}_{jkl} components of the cell corresponding to (j, k, l) are labeled with a color matching the node at which they are evaluated and the colors extend to neighboring cells.

scheme then becomes

$$\mathbf{E}_{jkl}^{n+\frac{1}{2}} = \mathbf{E}_{jkl}^n + c^2 \frac{\Delta t}{2} (\nabla^- \times \mathbf{B}_{jkl}^n - \mu_0 \mathbf{J}_{jkl}^n), \quad (3.13)$$

$$\mathbf{B}_{jkl}^{n+\frac{1}{2}} = \mathbf{B}_{jkl}^n - \frac{\Delta t}{2} \nabla^+ \times \mathbf{E}_{jkl}^{n+\frac{1}{2}}. \quad (3.14)$$

$$\mathbf{J}_{jkl}^n \rightarrow \mathbf{J}_{jkl}^{n+1}, \quad (\text{Particle Pusher}) \quad (3.15)$$

$$\mathbf{B}_{jkl}^{n+1} = \mathbf{B}_{jkl}^{n+\frac{1}{2}} - \frac{\Delta t}{2} \nabla^+ \times \mathbf{E}_{jkl}^{n+\frac{1}{2}}, \quad (3.16)$$

$$\mathbf{E}_{jkl}^{n+1} = \mathbf{E}_{jkl}^{n+\frac{1}{2}} + c^2 \frac{\Delta t}{2} (\nabla^- \times \mathbf{B}_{jkl}^{n+1} - \mu_0 \mathbf{J}_{jkl}^{n+1}). \quad (3.17)$$

For the field boundary condition, this work uses EPOCH's `simple_laser`, `simple_outflow` and periodic boundary condition. The periodic boundary condition is a common boundary condition: two opposing periodic boundaries have the opposite boundary as their next outward neighboring point and the domain therefore effectively becomes infinite and periodic. The other boundary conditions need some more explanation. Both `simple_laser` and `simple_outflow` clamp the fields to zero at the specified boundaries but also updates the magnetic field at the boundary to allow for a wave to be excited and flow into or leave the domain. The update scheme follows [69] and is based around linear combinations of different components of Maxwell's curl equations. For an update scheme for waves propagating along the x -direction, the following

equations are obtained as linear combinations of Maxwell's curl equations in (2.3) and (2.4)

$$2\partial_t S(\mathbf{r}, t) \pm c\partial_x S(\mathbf{r}, t) = c^2\partial_z B_x(\mathbf{r}, t) \pm c\partial_y E_x(\mathbf{r}, t) - c^2\mu_0 J_y(\mathbf{r}, t), \quad (3.18)$$

$$2\partial_t P(\mathbf{r}, t) \pm c\partial_x P(\mathbf{r}, t) = -c^2\partial_y B_x(\mathbf{r}, t) \pm c\partial_z E_x(\mathbf{r}, t) - c^2\mu_0 J_z(\mathbf{r}, t). \quad (3.19)$$

Here, the polarization states S and P , also known as transverse-electric and transverse-magnetic respectively, have been introduced as

$$2S(\mathbf{r}, t) = E_y(\mathbf{r}, t) \pm cB_z(\mathbf{r}, t), \quad (3.20)$$

$$2P(\mathbf{r}, t) = E_z(\mathbf{r}, t) \mp cB_y(\mathbf{r}, t), \quad (3.21)$$

where $+$ refers to forward propagating and $-$ to backward propagating waves. On the Yee grid of the electric field component, they take the form

$$2S_{jk+\frac{1}{2}l}^n = (E_y)_{jk+\frac{1}{2}l}^n \pm c(B_z)_{jk+\frac{1}{2}l}^n \quad (3.22)$$

$$2P_{jkl+\frac{1}{2}}^n = (E_z)_{jkl+\frac{1}{2}}^n \mp c(B_y)_{jkl+\frac{1}{2}}^n. \quad (3.23)$$

The last term is not on the grid of the magnetic field components so a linear interpolation is applied. For the first term on the right hand side, the half step update scheme of the electric field component, i.e. the relevant component of equation (3.13), is inserted

$$\begin{aligned} 2S_{jk+\frac{1}{2}l}^n &= (E_y)_{jk+\frac{1}{2}l}^{n-\frac{1}{2}} + \frac{c^2\Delta t}{2\Delta z} \left((B_x)_{jk+\frac{1}{2}l+\frac{1}{2}}^n - (B_x)_{jk+\frac{1}{2}l-\frac{1}{2}}^n \right) \\ &\quad - \frac{c^2\Delta t}{2\Delta x} \left((B_z)_{j+\frac{1}{2}k+\frac{1}{2}l}^n - (B_z)_{j-\frac{1}{2}k+\frac{1}{2}l}^n \right) - \frac{\Delta t}{2\varepsilon_0} (J_y)_{jk+\frac{1}{2}l}^n \\ &\quad \pm \frac{c}{2} \left((B_z)_{j+\frac{1}{2}k+\frac{1}{2}l}^n + (B_z)_{j-\frac{1}{2}k+\frac{1}{2}l}^n \right), \end{aligned} \quad (3.24)$$

$$\begin{aligned} 2P_{jkl+\frac{1}{2}}^n &= (E_z)_{jkl+\frac{1}{2}}^{n-\frac{1}{2}} + \frac{c^2\Delta t}{2\Delta x} \left((B_y)_{j+\frac{1}{2}kl+\frac{1}{2}}^n - (B_y)_{j-\frac{1}{2}kl+\frac{1}{2}}^n \right) \\ &\quad - \frac{c^2\Delta t}{2\Delta y} \left((B_x)_{jk+\frac{1}{2}l+\frac{1}{2}}^n - (B_x)_{jk-\frac{1}{2}l+\frac{1}{2}}^n \right) - \frac{\Delta t}{2\varepsilon_0} (J_z)_{jkl+\frac{1}{2}}^n \\ &\quad \mp \frac{c}{2} \left((B_y)_{j+\frac{1}{2}kl+\frac{1}{2}}^n + (B_y)_{j-\frac{1}{2}kl+\frac{1}{2}}^n \right). \end{aligned} \quad (3.25)$$

In this work, beams are excited at the smallest x , i.e. left, boundary and propagate right so

terms with the $j - \frac{1}{2}$ index are collected and just the positive direction is kept

$$\begin{aligned} (B_z)_{j-\frac{1}{2}k+\frac{1}{2}l}^n &= \frac{1}{c + c^2\Delta t/\Delta x} \left[4S_{jk+\frac{1}{2}l}^n - 2(E_y)_{jk+\frac{1}{2}l}^{n-\frac{1}{2}} \right. \\ &\quad - \frac{c^2\Delta t}{\Delta z} \left((B_x)_{jk+\frac{1}{2}l+\frac{1}{2}}^n - (B_x)_{jk+\frac{1}{2}l-\frac{1}{2}}^n \right) \\ &\quad \left. + c \left(\frac{c\Delta t}{\Delta x} - 1 \right) (B_z)_{j+\frac{1}{2}k+\frac{1}{2}l}^n + \frac{\Delta t}{\varepsilon_0} (J_y)_{jk+\frac{1}{2}l}^n \right], \end{aligned} \quad (3.26)$$

$$\begin{aligned} (B_y)_{j-\frac{1}{2}kl+\frac{1}{2}}^n &= \frac{1}{c + c^2\Delta t/\Delta x} \left[-4P_{jkl+\frac{1}{2}}^n + 2(E_z)_{jkl+\frac{1}{2}}^{n-\frac{1}{2}} \right. \\ &\quad + \frac{c^2\Delta t}{\Delta y} \left((B_x)_{jk+\frac{1}{2}l+\frac{1}{2}}^n - (B_x)_{jk-\frac{1}{2}l+\frac{1}{2}}^n \right) \\ &\quad \left. + c \left(\frac{c\Delta t}{\Delta x} - 1 \right) (B_y)_{j+\frac{1}{2}kl+\frac{1}{2}}^n + \frac{\Delta t}{\varepsilon_0} (J_z)_{jkl+\frac{1}{2}}^n \right]. \end{aligned} \quad (3.27)$$

This can be used as a boundary condition to excite waves as a superposition of the user defined functions $S_{jk+\frac{1}{2}l}^n$ and $P_{jkl+\frac{1}{2}}^n$, representing two different linear polarizations. The `simple_outflow` boundary condition uses the same equations but with $S_{jk+\frac{1}{2}l}^n = 0$ and $P_{jkl+\frac{1}{2}}^n = 0$. To get an expression for this on the large x , i.e. right, boundary, the components $(B_z)_{j+\frac{1}{2}k+\frac{1}{2}l}^n$ and $(B_y)_{j+\frac{1}{2}k+\frac{1}{2}l}^n$ should be collected instead.

We note that the laser module in EPOCH only allows the user to specify linear combinations of transverse-electric and transverse-magnetic waves at the boundary. Currently, longitudinal waves cannot be specified at the boundaries. Furthermore, as was seen in [61], which is included in chapter 4, exciting waves that have both transverse and longitudinal electric field component may also unintentionally excite entirely longitudinal waves to compensate for the longitudinal component of the intended wave.

3.2.3 The particle pusher

The particle pusher in EPOCH gets the equations of motion for the superparticles from the Vlasov equation. Since EPOCH, unlike PSC, is relativistic, the Vlasov equation in terms of momentum \mathbf{p} takes the form

$$\partial_t f_\zeta(\mathbf{r}, \mathbf{p}, t) + \frac{\mathbf{p}}{\gamma_\zeta m_\zeta} \cdot \nabla_{\mathbf{r}} f_\zeta(\mathbf{r}, \mathbf{p}, t) + q_\zeta \left[\mathbf{E}(\mathbf{r}, t) + \frac{\mathbf{p}}{\gamma_\zeta m_\zeta} \times \mathbf{B}(\mathbf{r}, t) \right] \cdot \nabla_{\mathbf{p}} f_\zeta(\mathbf{r}, \mathbf{p}, t) = 0, \quad (3.28)$$

where $f_\zeta(\mathbf{r}, \mathbf{p}, t)$ is the distribution function for species ζ as a function of \mathbf{p} instead of \mathbf{v} , $\nabla_{\mathbf{p}}(\partial_{p_x}, \partial_{p_y}, \partial_{p_z})$ is the corresponding derivative in momentum space and $\gamma_\zeta = \sqrt{1 + p^2/(m_\zeta c)^2}$ is the Lorentz factor. Collision effects are not included at this point since no collision operator is included in the Vlasov equation. We will return to this point at the end of this section. The distribution function is approximated by a collection of contributions from superparticles. Each superparticle accounts for a group of real particles spread out in space but all with the same

momentum

$$f_\zeta(\mathbf{r}, \mathbf{p}, t) = \frac{n_\zeta}{N_c} \sum_{i=1}^{N_\zeta} \phi(\mathbf{r} - \mathbf{r}_{\zeta,i}(t)) \delta(\mathbf{p} - \mathbf{p}_{\zeta,i}(t)), \quad (3.29)$$

where n_ζ is the background density of species ζ , N_c is an arbitrary number that determines the required superparticle density, $\delta(\mathbf{p})$ is the three dimensional Dirac delta function in momentum space and $\phi(\mathbf{r})$ is the superparticle "cloud" shape which for EPOCH by standard is a B-spline of second order in the appropriate number of dimension. The superparticles each occupy only a single point in momentum space, presumably to retain its shape through time. In 3D, the shape function is

$$\phi(\mathbf{r}) = \prod_{\xi \in \{x,y,z\}} \begin{cases} 1 - \frac{|r_\xi|}{\Delta r_\xi} & , |r_\xi| \leq \Delta r_\xi \\ 0 & , |r_\xi| > \Delta r_\xi \end{cases}, \quad (3.30)$$

where $r_x = x$, $\Delta r_x = \Delta x$ etc. for the other spatial dimensions. We note that with this construction, each superparticle accounts for $\frac{n_\zeta}{N_c} \Delta x \Delta y \Delta z$ particles of the same species. Multiplying the Vlasov equation by momentum and integrating over all momentum space and the volume of a cell with the provided distribution function, the equations of motion are obtained

$$\frac{d\mathbf{r}_{\zeta,i}(t)}{dt} = \frac{\mathbf{p}_{\zeta,i}(t)}{\gamma_\zeta m_\zeta} \quad (3.31)$$

$$\frac{d\mathbf{p}_{\zeta,i}(t)}{dt} = \frac{1}{\Delta x \Delta y \Delta z} \int \phi(\mathbf{r} - \mathbf{r}_{\zeta,i}(t)) \mathbf{F}_\zeta(\mathbf{r}, t) d\mathbf{r} \quad (3.32)$$

$$\mathbf{F}_\zeta(\mathbf{r}, t) = q_\zeta \left[\mathbf{E}(\mathbf{r}, t) + \frac{\mathbf{p}_{\zeta,i}}{\gamma_\zeta m_\zeta} \times \mathbf{B}(\mathbf{r}, t) \right]. \quad (3.33)$$

The equations of motion show that the superparticles react to the forces like a single real particle would even though it accounts for several real particles. The positions of the superparticles are allowed to take any value inside the domain and is not restricted to grid points. The Lorentz force, however, is only defined on the grid so it is assumed that the force is constant inside a box centered around the grid points

$$\mathbf{F}_\zeta(\mathbf{r}, t)|_{t=n\Delta t} = \sum_{j,k,l} (F_\zeta)_{jkl}^n \prod_{\xi \in \{x,y,z\}} \text{rect} \left(\frac{(\mathbf{r}_{jkl} - \mathbf{r}_{\zeta,i}^n)_\xi}{\Delta r_\xi} \right), \quad (3.34)$$

$$\text{rect}(x) = \begin{cases} 1 & , |x| \leq \frac{1}{2} \\ 0 & , |x| > \frac{1}{2} \end{cases}, \quad (3.35)$$

where $(\mathbf{r}_{jkl} - \mathbf{r}_{\zeta,i}^n)_x$ is the x -component of the vector and similar for y and z . For the sake of making the arguments regarding calculating the integral in equation (3.32) easier to follow, we restrict ourselves to 1D in the following, keeping just the x -coordinate. Since the 1D superparticle shape function, $\phi(x - x_{\zeta,i}^n)$, extends Δx to either side of the particle position, $x_{\zeta,i}(t)$, it will overlap with 3 grid cells. Denoting the closest grid point by $x_j = j\Delta x$, the momentum equation gets

the following contributions

$$\begin{aligned} \left. \frac{dp_{\zeta,i}}{dt} \right|_{t=n\Delta t} &= \frac{1}{\Delta x} \left[(F_{\zeta})_{j-1}^n \int_{x_i-\Delta x}^{x_{j-1}+\Delta x/2} 1 - \frac{|x - x_{\zeta,i}^n|}{\Delta x} dx \right. \\ &\quad + (F_{\zeta})_j^n \int_{x_j-\Delta x/2}^{x_j+\Delta x/2} 1 - \frac{|x - x_{\zeta,i}^n|}{\Delta x} dx \\ &\quad \left. + (F_{\zeta})_{j+1}^n \int_{x_{j+1}-\Delta x/2}^{x_i+\Delta x} 1 - \frac{|x - x_{\zeta,i}^n|}{\Delta x} dx \right]. \end{aligned} \quad (3.36)$$

Solving the integrals analytically and discretizing the derivative, we get

$$\begin{aligned} p_{\zeta,i}^{n+1} &= p_{\zeta,i}^n + \frac{\Delta t}{2} \left[F_{j-1}^n \left(\frac{1}{2} + \frac{x_j - x_i}{\Delta x} \right)^2 + 2F_j^n \left(\frac{3}{4} - \frac{(x_j - x_i)^2}{\Delta x^2} \right) \right. \\ &\quad \left. + F_{j+1}^n \left(\frac{1}{2} - \frac{x_j - x_i}{\Delta x} \right)^2 \right]. \end{aligned} \quad (3.37)$$

Because the electric and magnetic fields are defined on the Yee grid, the Lorentz force felt by the superparticles in EPOCH must be pieced together from the staggered grid. Furthermore, the update is typically done using the Boris rotation algorithm[74] whereby the force contribution on the superparticle is split between acceleration from the electric field and rotation around the magnetic field lines. This step is both preceded and followed by half a time step of the discretized position equation

$$x_{\zeta,i}^{n+\frac{1}{2}} = x_{\zeta,i}^n + \frac{p_{\zeta,t}^n}{\gamma_{\zeta} m_{\zeta}}, \quad (3.38)$$

$$x_{\zeta,i}^{n+1} = x_{\zeta,i}^{n+\frac{1}{2}} + \frac{p_{\zeta,t}^{n+1}}{\gamma_{\zeta} m_{\zeta}}. \quad (3.39)$$

When a superparticle leaves the domain, the particle boundary condition used in the simulations of this work is to replace it with an incoming thermally distributed one of the same kind.

With the updated positions and momenta, the charge density can be found by mapping charge contributions of the superparticles onto the grid through their overlap with the grid cells. This procedure is similar to mapping the forces onto the superparticles, and each superparticle has an overlap with maximum three cells in 1D. The overlap, $\zeta_{i,j}$, of a particle at $x_{\zeta,i}^n$ with a cell at x_j is given by

$$\zeta_{i,j}^n = \frac{1}{\Delta x} \int_{x_j-\Delta x/2}^{x_j+\Delta x/2} \phi(x_j - x_{\zeta,i}^n) dx \quad (3.40)$$

$$= \begin{cases} \frac{3}{4} - \frac{|x_{\zeta,i}^n - x_j|^2}{\Delta x^2}, & |x_{\zeta,i}^n - x_j| \leq \frac{\Delta x}{2} \\ \frac{1}{2} \left(\frac{3}{2} - \frac{|x_{\zeta,i}^n - x_j|}{\Delta x} \right)^2, & \frac{\Delta x}{2} < |x_{\zeta,i}^n - x_j| \leq \frac{3\Delta x}{2} \\ 0, & |x_{\zeta,i}^n - x_j| > \frac{3\Delta x}{2} \end{cases}. \quad (3.41)$$

Finding the charge density, ρ_j^n , at the grid point x_j is then just a matter of summing the charge times the 3D overlap with the normalization from the distribution function for each superparticle. To get the mass density, one would use the mass of species ς instead of the charge. A similar procedure applies to other quantities one would want to map onto the grid.

EPOCH uses a Villasenor and Buneman[75] scheme to calculate the currents through the charge conservation equation in (3.7). The benefit of this is that it avoids having to solve Poisson's equation in (2.1) using spectral methods. The spectral methods are global whereas the Villasenor and Buneman scheme is local, which is better for parallelization. For the sake of getting 2nd order precision, charge densities are saved at $t = (n + \frac{1}{2}) \Delta t$ and are propagated to $t = (n + \frac{3}{2}) \Delta t$ after which the current density can be calculated to second order by discretizing equation (3.7) in 1D

$$(J_x)_{j+\frac{1}{2}}^{n+1} = J_{j-\frac{1}{2}}^{n+1} - \frac{\Delta x}{\Delta t} \left(\rho_j^{n+\frac{3}{2}} - \rho_j^{n+\frac{1}{2}} \right). \quad (3.42)$$

For a higher number of dimensions, this step is more complicated as the current must be separated into its components. This is shown [69] and the components of the current are calculated in three separate equations similar to the above. Regardless of the number of spatial dimension, EPOCH always has three components to all fields. For dimensions with no spatial extent assigned to them, the current is calculated as $J_\xi = n\rho v_\xi$.

For the equations of motions, the Vlasov equation was integrated which means that collisions have been neglected. Integrating instead the Boltzmann equation, [69] shows that an impractical particle pusher update scheme which requires on the order of N^2 operations, N being the total number of superparticles, is obtained. For this reason EPOCH instead uses a Monte Carlo model for relativistic binary collisions based on [76, 77, 78]. Instead of evaluating every single collision requiring on the order of N^2 operations, all superparticles are given a representative collision partner in the same cell with which their momenta are updated based on collision frequencies and certain parameters picked at random such as collision angles, see [65, 69]. This approach requires on the order of N operations.

3.3 Other types of codes

The benefit of using PIC codes for simulations is that they are fully kinetic and only make relatively small assumptions about how the plasma behaves. Our analytical models on the other hand, tend to rely on a large number of assumptions in order to make progress, in particular when it comes to modeling nonlinear effects. This means that we can generally trust the results obtained through PIC simulations provided that care is taken when we design our simulations and that we have the necessary resources available to run the simulations. PIC codes are expensive to run, and they have a number of weaknesses[79, 65] associated with that. In particular, since the real particles are represented by a smaller number of superparticles, particles which are found in the tails of the distribution in position and velocity space may require a large number of superparticles if dynamics, which are dependent on the tails, are of importance. Because of the smaller number of superparticles to real particles, the behavior of the plasma can be exaggerated if too few superparticles are used. Furthermore, PIC codes are known to be noisy due, in

part, to self-heating[80] which is an artificial stochastic heating of the domain. Self heating has reduced in newer PIC models such as EPOCH which employ higher order splines and current smoothing[81], but the numerical noise of PIC codes still only decreases as $N^{-1/2}$, where N is the number of superparticles. Put differently, it is necessary to increase the number of superparticles by two orders of magnitude in order to decrease the numerical noise by a single order of magnitude. Running PIC codes typically requires the use of high performance computing (HPC) clusters and timescales are generally limited with ion dynamics being harder to model.

In this section, we mention two other types of codes to use for simulations and discuss them in relation to PIC codes.

3.3.1 Vlasov solvers

When doing kinetic simulations, the choice of model is typically between PIC codes and Vlasov solvers. Like the name suggests, a Vlasov solver numerically integrates the distribution function in time by solving the Vlasov equation. Along with the Vlasov equation, Vlasov solvers also solve Maxwell's equations to update the electric and magnetic field. In particular if collisions and currents can be neglected, Vlasov solvers can be written as advection like equations which can be solved efficiently.

When comparing the resource requirements of PIC codes and Vlasov solvers, one can typically assume that the spatial grids and resolutions are similar as they both need to solve Maxwell's equations and similar update schemes for that can be implemented in in both of them. The way they deal with velocity space sets them apart, and the ratio in requirements can be estimated as[82]

$$\frac{N_{\text{Vlasov}}}{N_{\text{PIC}}} = \frac{N_v^{d_v}}{n_{\text{cell}}}, \quad (3.43)$$

where N_{Vlasov} and N_{PIC} represent the numerical effort for a Vlasov solver and a PIC code respectively, N_v is the number of grid points in one dimension, d_v is the number of dimensions in velocity space, and n_{cell} is the number of superparticles per cell. This is assuming that both methods need the same number of dimensions in position and velocity space and that the number of grid point in all dimensions of velocity space is the same. As a rule of thumb, the Vlasov solver is usually faster in 1D velocity space, the PIC code is faster in 3D velocity space, but in 2D velocity space the optimal choice of code is very dependent on the particular problem. We note, however, that the memory requirements for Vlasov solvers in full 3D can be substantial as one needs to store variables in 6 dimensions.

There are, of course, more to it than the simple relation above. In a PIC code, the superparticles are distributed according to the distribution function, typically initialized as a Maxwellian distribution. As a consequence, the majority of the CPU effort is spent on the peaks of the distribution function and little is spent on the tails. In the Vlasov solver, on the other hand, the distribution function is mapped onto a grid, typically with an even spacing, meaning that any part of the distribution function gets the same amount of CPU dedicated to it. The drawback to this, is that if a phenomenon that leads to very narrow filamentation in velocity space, it can require a correspondingly fine grid throughout to resolve the effect. Similarly, the occurrence of a narrow peak in the far tails of the distribution function could require a large number of CPUs

to manipulate vanishingly small values in the regions of the distribution function that bridge the main peak and the satellite.

Some Vlasov solvers have implemented higher order schemes to improve accuracy, which do not conserve monotonicity and may accentuate extrema. Some, again, compensate for this by using filtering or smoothing to get rid of fine scale artifacts. This can, however, lead to incorrect results if not done in a physical way[79]. Lastly, the distribution function cannot take a negative value which can prove challenging to enforce in a numerical code. Still, Vlasov solvers are widely used and are generally considered less noisy than PIC codes.

3.3.2 Beam tracers

Even with the simplifications of the kinetic dynamics in a plasma employed by PIC codes and Vlasov solvers, simulating an entire plasma is for the most part unrealistic with contemporary computational resources. Rather, kinetic codes can simulate a more academic plasma or a specific region of a plasma where the physics of interest may take plasma.

In an inhomogeneous plasma, beam propagation is not trivial and a closed expression for the propagation of a beam in a given plasma profile may not exist. Instead, a solution to the beam path is often sought within geometric optics based on WKB. The approximation is valid for an inhomogeneous plasma in which the characteristic length scale of inhomogeneity is much greater than the wavelength of the beam propagating through it. However, the WKB approximation neglects beam diffraction such as was discussed in section 2.3. This puts restrictions on the length of the beam path where geometrical optics can properly predict the amplitude and shape of the beam and therefore also the resulting local interaction with it. To allow for gyrotron beam planning in fusion devices, codes such as TORBEAM[83, 84] have been developed based on beam tracing[85] instead, to predict beam trajectory and absorption for frequencies in the electron cyclotron range in toroidal devices. The model behind beam tracing is valid in the short wavelength limit and is able to reduce the propagation of a beam to a set of ordinary differential equations whilst retaining effects due to diffraction.

Codes such as TORBEAM as well as codes based on WKB usually rely on background density profiles to calculate beam paths. Whilst this is usually a reasonable approach in most of a tokamak or stellarator plasma, turbulence in the edge region has been found to cause density fluctuations on the order of the background density level and with a size comparable to the wavelength of a gyrotron beam[86]. Because the dynamics of the turbulence are on timescales much slower than gyrotron frequencies, the gyrotron beams interact with them as if they were stationary structures. Studies using full-wave codes have shown that a broadening of the gyrotron beam can occur in the edge[87].

3.4 Proof of basic functionality in EPOCH

We device a number of simulations in EPOCH to show that it handles wave propagation in the electron cyclotron range as expected by comparing with results presented in the previous chapter.

3.4.1 Density and magnetic field gradients in EPOCH

EPOCH allows the user to define an initial density, temperature, and electric and magnetic field profile. To test the cold wave results presented in figures 2.1, density and magnetic field profiles can be chosen in a number of ways such that an O- and X-mode wave traverse the CMA-like diagrams in a desired way. In order to minimize the computational effort, however, it is preferable to do these tests in 1D when possible. Whilst an inhomogeneous background density profile can be chosen with little concern in any number of dimensions, the background magnetic field can only be homogeneous in 1D. For a constant background magnetic field, Maxwell's equations are quickly seen to be satisfied in any number of dimensions. In 1D, a field can only depend on, say, the x -coordinate, in which case the divergence equation for the magnetic field in (2.2) gives the condition

$$\nabla \cdot \mathbf{B}_0(x) = \partial_x B_{0,x}(x) = 0, \quad (3.44)$$

and the curl equation in (2.4) gives

$$(\nabla \times \mathbf{B}_0(x))_i = \partial_j B_{0,k}(x) - \partial_k B_{0,j}(x) = \mu_0 (\mathbf{J}(x, t) + \varepsilon_0 \partial_t \mathbf{E}(x, t))_i, \quad (3.45)$$

for any cyclic permutation of $(i, j, k) = (x, y, z)$. The divergence equation states that $B_{0,x}$ must be homogeneous. In the curl equation, the time derivative on the right side means that the predefined background magnetic field does not stay constant in EPOCH unless also $B_{0,y}$ and $B_{0,z}$ are homogeneous. In 1D, EPOCH therefore must have a homogeneous magnetic field.

In 2D, fields can depend on both the x - and y -coordinates so for a position dependent background magnetic field, the divergence equation for the magnetic field reads

$$\nabla \cdot \mathbf{B}_0(x, y) = \partial_x B_{0,x}(x, y) + \partial_y B_{0,y}(x, y) = 0. \quad (3.46)$$

This is satisfied if one lets none of the components depend on their own direction, however, the curl of the predefined background magnetic field can now be chosen such that it vanishes if $\partial_j B_{0,k}(x, y) = \partial_k B_{0,j}(x, y)$ for any cyclic permutation of $(i, j, k) = (x, y, z)$. It is not possible to have $B_{0,x}(x, y) = 0$ if $B_{0,y}(x, y) \neq 0$ but for mainly perpendicular propagation,

$$B_{0,x}(x, y) = \int^y \partial_x B_{0,y}(x, y') dy' \quad (3.47)$$

satisfies the equations. No lower bound on the integral has been given because any constant with respect to y will do.

Whilst it is possible to have a both inhomogeneous and stationary background magnetic field, we shall limit ourselves to only have an inhomogeneous density profile whenever it is possible. Furthermore, the simulations in this chapter are run on a laptop and plasma parameters are therefore chosen in order to lessen the computational effort.

3.4.2 O- and X-mode cutoffs

To test if waves are reflected at their cutoffs, an O- and an X-mode wave at a frequency $\omega < \omega_{ce}$ are propagated through a domain with increasing density, starting from vacuum. From section

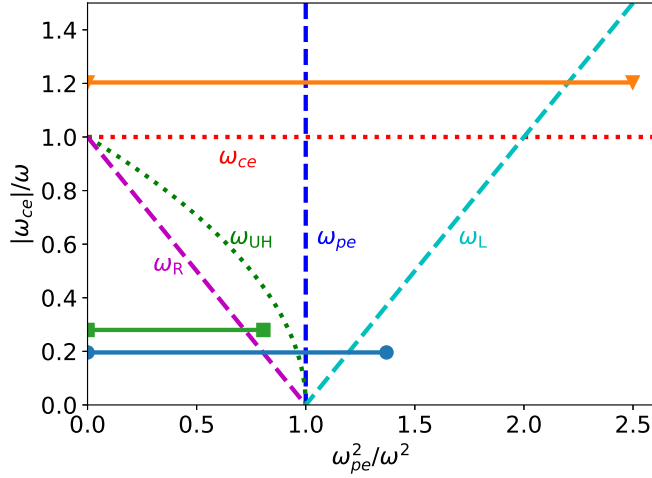


Figure 3.3: A CMA diagram with the x -axis being proportional to n_e and the y -axis to B_0 . Resonances are drawn with dotted lines and cutoffs with dashed lines. Both resonances and cutoffs are labeled with their relevant frequency. Solid lines with markers at the ends correspond to domain ranges for simulations in this chapter: blue circles are for figures 3.4a, 3.4b, 3.5a and 3.5b; orange triangles are for figures 3.4c and 3.5c; and green squares are for figure 3.6.

2.1, the O-mode wave is expected to be reflected at $\omega = \omega_{pe}$ whereas the X-mode wave is expected to be reflected already at the R cutoff. We run simulations for O- and X-mode waves using the parameters in table 3.1 which should lead both waves to a cutoff. To summarize the parameters listed in 3.1, we choose a 1D domain with $x_{\min} < x < x_{\max}$, a background magnetic field \mathbf{B}_0 that points in the z -direction, electron and deuteron background densities n_e and n_i , and temperatures T_e and T_i . We did not choose $T_e = T_i/10$ on purpose; it was a typo but ion dynamics do not play a significant role in these simulations so they were not rerun. Neither the ions nor the nonzero temperatures are really necessary in order to test the relations in section 2.1 but the relations are also not expected to be affected by them. A wave of frequency f_0 and intensity I_{pump} is excited at the x_{\min} boundary using the `simple_laser` field boundary condition as described in section 3.2. To avoid artifacts from large discontinuities in the field due to the wave excited at the boundary, the wave amplitude is ramped up using an arctan-function with a characteristic timescale of τ_{ramp} . For the x_{\max} boundary, a `simple_outflow` field boundary condition is used. The particle boundary conditions are `thermal` on both sides. These boundary conditions were also mentioned in section 3.2. The path of the wave through the plasma would correspond to the solid blue line with circles at the ends in figure 3.3. As can be seen in the figure, the O-mode wave will meet the cutoff at ω_{pe} whereas X-mode will meet a cutoff already at ω_R . The temporal evolution of the main component of the electric field for O-mode is shown in figure 3.4a and for X-mode in figure 3.4b.

Starting with O-mode in figure 3.4a, the propagation of the wavefront is seen to be agree with equation (2.22) as is indicated by the green solid line. The dotted line indicates the cutoff at the plasma density, however, the field is seen to continue past the dotted line. This is not as such in disagreement with theory since the wavelength of the wave diverges at the cutoff which

x_{\min}	x_{\max}	n_x	n_e, n_i	T_e	T_i	\mathbf{B}_0	I_{pump}	τ_{ramp}	f_0
0 m	0.68 m	1000	$\frac{1.7x}{x_{\max}} \times 10^{18} \text{ m}^{-3}$	10 eV	100 eV	0.07 T $\hat{\mathbf{z}}$	$1 \frac{\text{kW}}{\text{mm}^2}$	0.1 ns	10 GHz

Table 3.1: A table showing simulation parameters for the simulations shown in figures 3.4a, 3.4b, 3.5a and 3.5b. Parameters correspond to the blue line with circles in figure 3.3.

x_{\min}	x_{\max}	n_x	n_e, n_i	T_e	T_i	\mathbf{B}_0	I_{pump}	τ_{ramp}	f_0
0 m	0.68 m	1000	$\frac{3.1x}{x_{\max}} \times 10^{18} \text{ m}^{-3}$	10 eV	100 eV	0.43 T $\hat{\mathbf{z}}$	$1 \frac{\text{kW}}{\text{mm}^2}$	0.1 ns	10 GHz

Table 3.2: A table showing simulation parameters for the simulations shown in figures 3.4c and 3.5c. Parameters correspond to the orange line with triangles in figure 3.3.

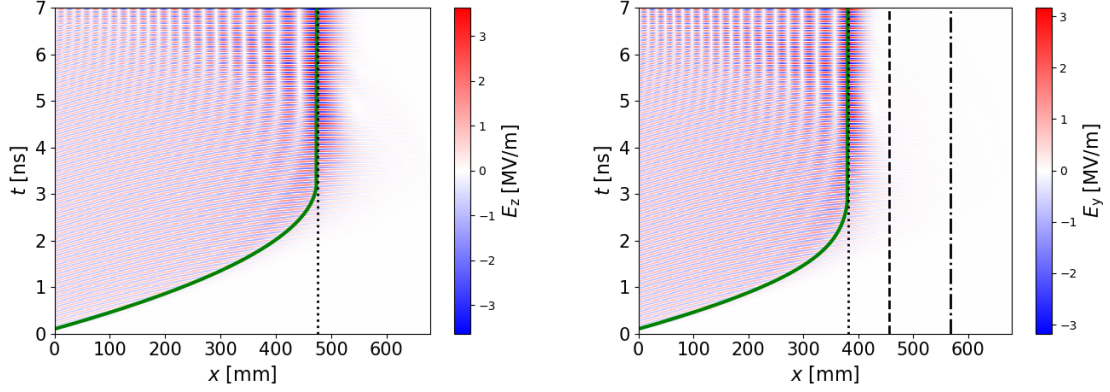
means that the WKB approach used for the green line breaks down according to equation (2.39). Past the cutoff, the field becomes evanescent and dies off as is observed. The superposition of incoming and reflected waves from the cutoff are seen to give rise to standing waves. For X-mode in figure 3.4b, the picture is very similar except the wave front is reflected already at the R cutoff also marked by a dotted line. Had the UH layer been placed closer to the R cutoff, a noticeable part of the waves might have tunneled through and propagated on to the L cutoff.

To test the L cutoff, the R cutoff must be bypassed. This can be done by increasing the magnetic field so that the injected frequency is below the cyclotron frequency. To bring the L cutoff inside the domain, the density has to also be increased. The new parameters are shown in table 3.2 and correspond to the orange line with triangles in figure 3.3. Figure 3.4c shows that also the slow X-mode wavefront propagates in agreement with the group velocity in equation (2.23) and stops at the L cutoff marked by the dash-dotted line. After reaching the L cutoff, the wavefront is reflected. Common for all of these plots is also that some amplification appears to take place near the cutoffs.

3.4.3 O- and X-mode wavenumbers

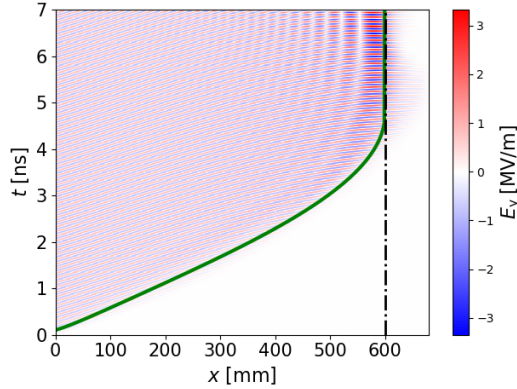
Using the same three simulations, we investigate if our simulations agree with the cold dispersion relations in equations (2.18) and (2.19). For this, a continuous wavelet transform (CWT) using a complex Morlet wavelet is applied to the appropriate electric field component once the injected waves have reached their cutoff. Starting with O-mode in figure 3.5a, the wavenumber decreases monotonically towards the cutoff and agrees well with the found dispersion relation. At the cutoff, the wavenumber goes to zero and while the CWT seems to agree with this, the beam becomes less localized when it gets to a wavelength close to the size of the domain.

For fast X-mode, figure 3.5b shows a similar plot to that of O-mode and the simulation appears to be in agreement with cold wave theory. For slow X-mode in figure 3.5c, the wavenumber does not monotonically decrease. Instead there is an initial increase followed by a steady decrease until it, again, goes to zero at the cutoff. Again, simulations agree with cold wave theory.



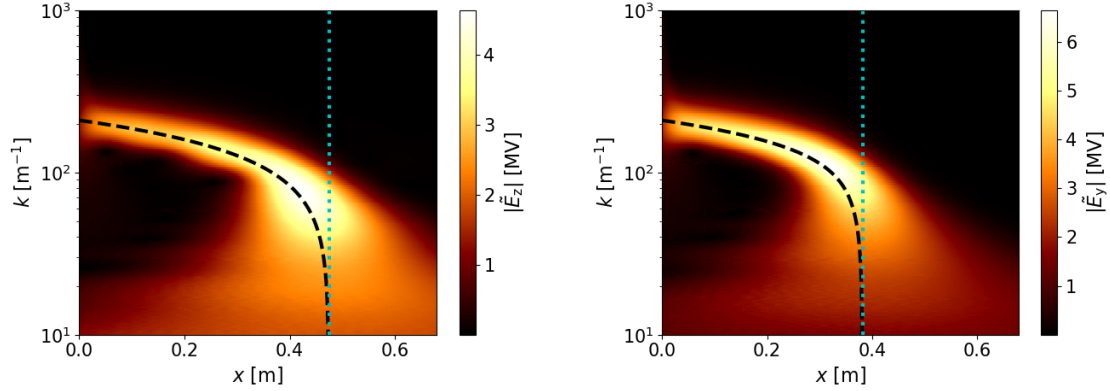
(a) O-mode propagation, showing the transverse electric field component parallel to the magnetic field. The green solid line is $\int^x v_{g,O}^{-1} dx + \tau_{\text{ramp}}$, dotted line is the cutoff at $\omega = \omega_{pe}$. O-mode is polarized in the z -direction.

(b) Fast X-mode propagation, showing the transverse electric field component perpendicular to the magnetic field. The green solid line is $\int^x v_{g,X}^{-1} dx + \tau_{\text{ramp}}$, dotted line is the R cutoff, the dashed line is the UH resonance and the dash-dotted line is the L cutoff. X-mode is mainly polarized in the y -direction.



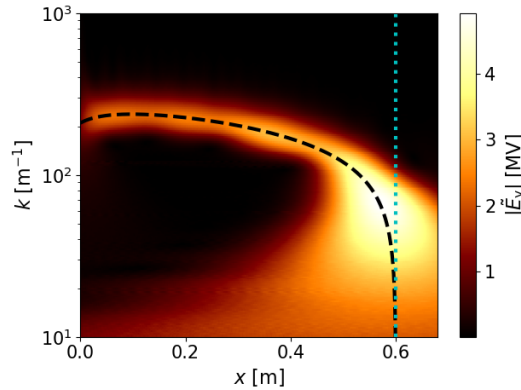
(c) Slow X-mode propagation, showing the transverse electric field component perpendicular to the magnetic field. The green solid line is $\int^x v_{g,X}^{-1} dx + \tau_{\text{ramp}}$, and the dash-dotted line is the L cutoff. X-mode is mainly polarized in the y -direction.

Figure 3.4: Simulations showing wavefront propagation of O- and X-mode from vacuum to higher densities. The indicated wavefront are found by integrating the group velocities in equations (2.22) and (2.23).



(a) Wavenumber of O-mode, showing a CWT of the transverse electric field component parallel to the magnetic field. The snapshot is at $t = 4$ ns, the black dashed line is equation (2.18) and the dotted cyan line is the cutoff at $\omega = \omega_{pe}$. O-mode is polarized in the z -direction.

(b) Wavenumber of fast X-mode, showing a CWT of the transverse electric field component perpendicular to the magnetic field. The snapshot is at $t = 3$ ns, the black dashed line is equation (2.19) and the dotted cyan line is the R cutoff. X-mode is mainly polarized in the y -direction.



(c) Wavenumber of slow X-mode, showing a CWT of the transverse electric field component perpendicular to the magnetic field. The snapshot is at $t = 6$ ns, the black dashed line is equation (2.19) and the dotted cyan line is the L cutoff. X-mode is mainly polarized in the y -direction.

Figure 3.5: Simulations showing the wavenumber of propagating O- and X-mode from vacuum to cutoffs at higher densities. The plots show CWTs of appropriate electric field components with wavenumbers from equations (2.18) and (2.19) indicated by black dashed lines. Parameters are the same as for the plots in figure 3.4.

x_{\min}	x_{\max}	n_x	n_e, n_i	T_e, T_i	\mathbf{B}_0	I_{pump}	τ_{ramp}	f_0
0 m	1 m	1000	$\exp\left(\frac{x - x_{\max}}{0.1 \text{ m}}\right) \times 10^{18} \text{ m}^{-3}$	$\{10^{-4}, 10\} \text{ eV}$	0.1 T $\hat{\mathbf{z}}$	$0.1 \frac{\text{kW}}{\text{mm}^2}$	0.1 ns	10 GHz

Table 3.3: A table showing simulation parameters for the simulation shown in figure 3.6. Parameters correspond to the green line with squares in figure 3.3.

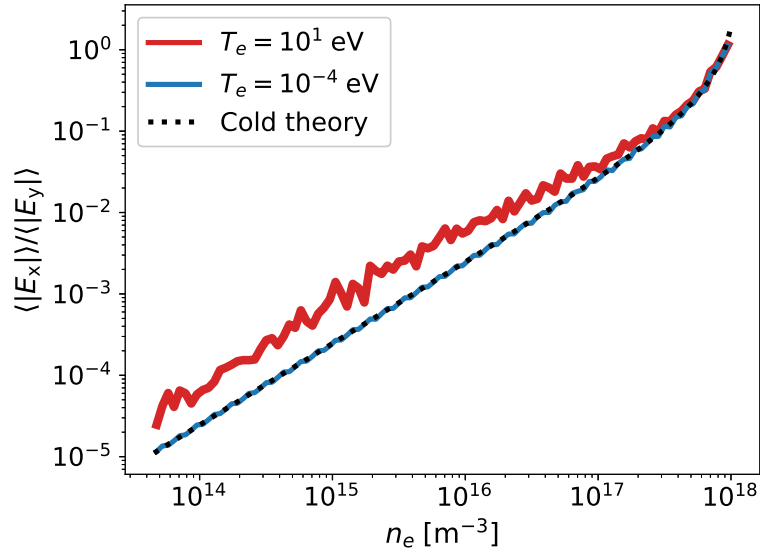


Figure 3.6: Fast X-mode polarization as indicated by the y -axis for different plasma temperatures. The dotted black line is ratio provided by cold wave theory in equation (2.25). Fields are averaged over 20 ns and 10 mm.

3.4.4 X-mode polarization

Now, we set up a simulation to test the polarization of fast X-mode, i.e. equation (2.25), over different orders of magnitude of electron density. The domain size is changed for convenience and the density is now increasing exponentially with position so as to get the polarization over several orders of magnitude. Two simulations are run at different temperatures and other parameters are also changed a bit. The parameters are shown in table 3.3 which corresponds to the green line with squares in figure 3.3.

Averaging the transverse and longitudinal components and taking the ratio of the components, the polarization obtained in EPOCH is compared to cold theory in figure 3.6. As can be seen in the figure, there is excellent agreement between theory and simulation over several orders of magnitude when the temperature is very low. For a higher temperature, the trend and order of magnitude still agrees with theory but the longitudinal component is generally greater than the cold model predicts. This could be due to noise or thermally excited waves which interfere with the ratio, affecting the smaller longitudinal component more.

x_{\min}	x_{\max}	y_{\min}	y_{\max}	n_x	n_y	n_e, n_i	T_e, T_i	\mathbf{B}_0	f_0
-0.5 m	0.5 m	-0.25 m	0.25 m	500	250	10^{16} m^{-3}	1 eV	0.1 T \hat{y}	10 GHz

Table 3.4: A table showing simulation parameters for the 2D simulation shown in figure 3.7.

3.4.5 Gaussian wave propagation in 2D

As a final point to this chapter, a 2D simulation is run to investigate Gaussian wave propagation. For the second dimension, y , we use half the number of gridpoints and generally cut down on numbers to allow us to run it on a laptop in decent time. As such, the density and temperature are lowered to reduce noise. The x boundary conditions are unchanged while the y boundaries are `simple_outflow` for the fields and `thermal` for the particles. The amplitude envelope function and phase at the boundary are chosen to be that of a Gaussian beam, i.e. equation (2.42), with waist $w_0 = 0.05$ m located at $x = 0$ m. The frequency is still 10 GHz and the wavenumber is determined from equation (2.18). Parameters are shown in table 3.4.

The simulation is run and the resulting time averaged main absolute electric field component is shown in figure 3.7. Contour lines and theoretical contour lines are plotted on top with good agreement near the waist at $x = 0$ and less so near the edges. It is unexpected that the disagreement is largest at the boundaries as the field is excited at the left boundary with the profile and phase that also generates the theoretical contours. Perhaps it is the averaging procedure that gives rise to the discrepancy since the placement and size of the beam waist fits well with predictions. In spite of being averaged over 10 periods in 100 steps, the field clearly retains some oscillatory behavior.

It is clear from this simulation that the notion of beam power requires a bit of careful thinking. PDI thresholds are typically measured in terms of power because the power that a microwave source injects into a plasma is the known quantity in experiments. Above some level of injected power, waves excited by PDIs can be measured and this is then typically the power threshold. In 1D simulations, the beam does not focus as it is essentially an infinite plane wave. This can be seen as an advantage; we can reduce physics in 1D and estimate the power at any point with greater ease. However as the wave has an infinite and non-vanishing extent in two dimensions, the power carried by the wave is infinite. As is the power in 2D. The way we measure power levels in 1D simulations in this work is to use intensity instead and relate it to the mean intensity inside the full width at half maximum (FWHM) of a beam. For a Gaussian, FWHM corresponds to 2.4 standard deviations from the maximum and the tails outside therefore contribute with little power. As an example of how to choose an intensity level, a gyrotron beam of FWHM $d_{\text{FWHM}} = 3$ cm and power of $P_{\text{pump}} = 0.7$ MW will correspond to an intensity of $I_{\text{pump}} = \frac{4P_{\text{pump}}}{\pi d_{\text{FWHM}}^2} = 0.1$ MW/cm². In order to convert the intensity of our 1D simulations into power in an experiment, a beam size is then necessary.

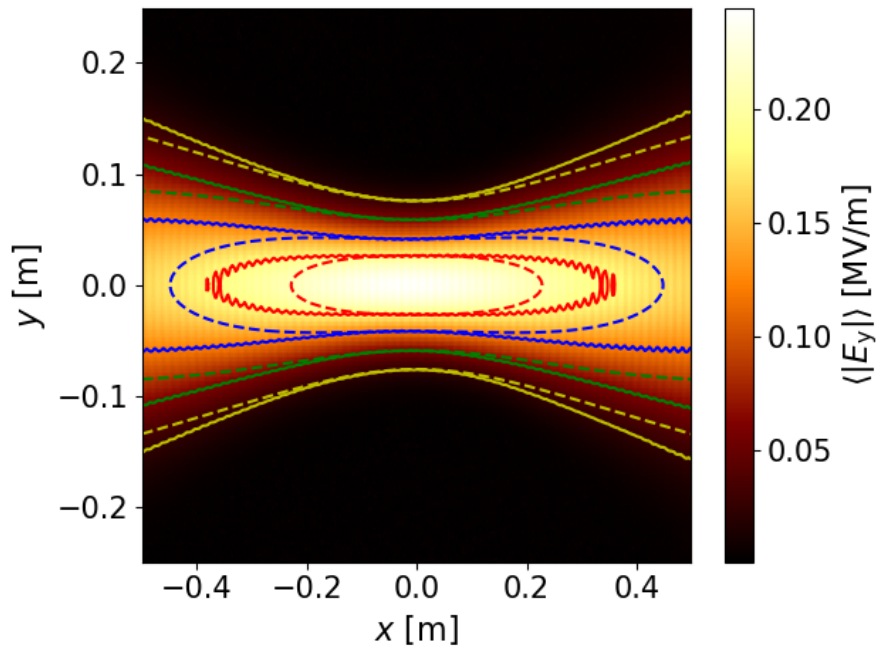


Figure 3.7: Main absolute electric field component of a Gaussian beam averaged over 1 ns in 100 steps. The solid lines are contour lines for 0.1 (yellow), 0.25 (green), 0.5 (blue) and 0.75 (red) of the maximum value of the averaged field. Dashed lines are the theoretical placements of the corresponding lines according to equation (2.42).

Chapter 4

PDI at the UH layer

In this chapter we review results from the simulations presented in [61].

4.1 Summary of the article

4.1.1 Physical setting

In section 3.4, we showed PIC simulations of O- and X-mode waves entering from vacuum and propagating towards cutoffs. The focus of the article presented in this chapter is exclusively on slow X-mode and EBWs near the UH layer. As was discussed in section 2.3, slow X-mode can be excited either by converting O-mode at the plasma frequency or by tunneling initially fast X-mode through the evanescent region between the R cutoff and the UH layer. In this work, we do not investigate these conversion schemes but assume that slow X-mode has already been excited and base parameters on CTS experiments where the slow X-mode was excited by conversion of O-mode gyrotron radiation. Since the purpose of the experiments was CTS, the conversion was not at the optimal angle and only a small fraction was converted into X-mode. As the slow X-mode wave propagates to the UH layer, its wavenumber changes significantly and it is likely that the conservation equations for PDIs into an EBW and an LH wave are satisfied locally near the UH layer, as was illustrated in figure 2.7. At the same time, wave amplification means that the interaction rates for PDIs increase and signatures of PDIs can be expected even if only a small fraction of the original O-mode wave makes it to the UH layer. Because of conservation of frequency, the EBW daughter wave will have a frequency equal to the difference between the pump and the LH wave. After this PDI has excited a larger population of LH waves, they may interact with the pump wave in another PDI to generate an upshifted or further downshifted EBW. Once the EBW PDI daughter waves have been excited, they will need to undergo a number of conversion processes, e.g. an inverse O-X-B conversion, in order to be detected outside the plasma. This also hints that a lot of power goes into PDI daughter waves when even the fraction that makes it back out to a detector can be picked up by it. The fraction of the pump wave that is converted in PDIs depends nonlinearly on the pump wave. The fraction that is not converted in PDIs can be expected to propagate on to the UH layer where it is linearly converted into an EBW at the same frequency. Because the analytical theory surrounding the same experiment already has been presented in [33, 34] and later corroborated

experimentally in [35], the setting provides an excellent test case to see how EPOCH handles both linear and nonlinear mode coupling. Furthermore, the analytical theory relies on an ion wave being excited as one of the daughter waves of the PDI but this waves was not verified experimentally.

4.1.2 Simulation design choices

For the simulations, we chose a density profile with two homogeneous regions and one inhomogeneous region bridging the two homogeneous ones, see figure 4 in the article[61] which is included at the end of this chapter. A slow X-mode wave is excited at one boundary and its UH layer is located in the inhomogeneous region. The two homogeneous regions allowed us to characterize waves on either side of the UH layer. The density of the first homogeneous region was a trade-off between simulation length and noise. As X-mode slow down significantly near the UH layer, the density in the homogeneous region should not be too close to the UH layer density as this would result in a lot of CPU hours spent on simply propagating an X-mode wave towards the UH layer. On the other hand, amplification of X-mode near the UH layer also meant that the amplitude of the X-mode wave would see greater amplification from the point of excitation to the UH layer if the difference in densities was greater. An objective was to investigate a pump intensity threshold for the PDIs by scanning pump intensity over two orders of magnitude. With greater amplification, the low intensity simulations would have to be excited closer to the noise floor and superparticles would have to be added to reduce the noise. The spatial resolution was chosen such that the downshifted EBW, which has the highest wavenumber, was decently resolved with 20 gridpoints per wavelength. Halving the number of grid points for the sake of testing the robustness did produce similar results. The output file frequency was 10.3 times the pump frequency so that the pump frequency was below the Nyquist frequency and at the same time not an integer times the output frequency, which may artificially boost its apparent magnitude in frequency space.

4.1.3 Analysis of data and results

The majority of the article was devoted to characterizing the excited modes in terms of frequency, wavenumber and group velocity to make sure that EPOCH was displaying accepted wave properties. For the most part, the longitudinal electric field components were used as both slow X-mode, EBWs and LH waves are mainly longitudinal near the UH layer, however, it was also shown that the electron waves give rise to waves in the electron density and momentum as expected.

We were able to clearly demonstrate linear conversion from slow X-mode into a returning EBW at the UH layer as well as excitation of several EBWs and an LH wave by Fourier transforming the longitudinal electric field into frequency and wavenumber space. The LH wave and one of the EBWs satisfied the PDI conservation equations at the UH layer, however, so did the the linearly converted EBW in the homogeneous region. The homogeneous PDI would have a significantly lowered intensity threshold as daughter waves would then not be convected out of the decay region. A number of entirely inhomogeneous simulations were therefore necessary to investigate the intensity threshold for the inhomogeneous PDI of the X-mode pump which had

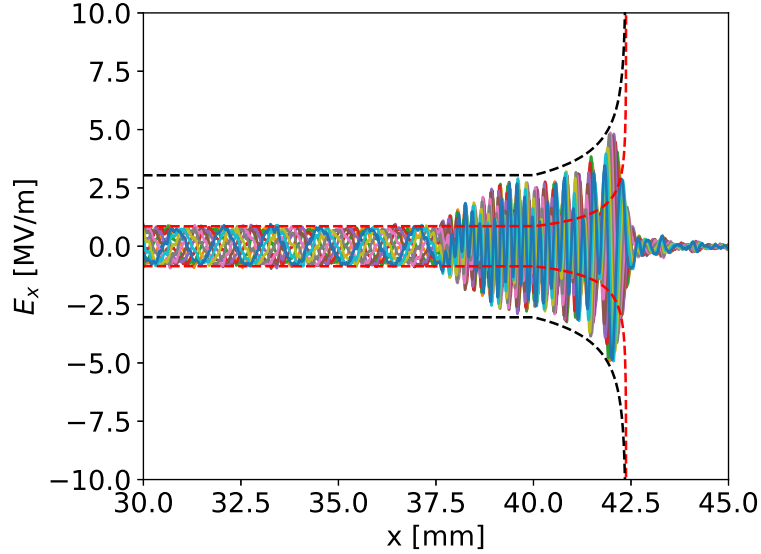


Figure 4.1: Wave amplification near the UH layer in simulations presented in [61]. The many colored lines in the figure are the longitudinal electric field at several time instances separated by the outputted timestep over the interval $15.20 \text{ ns} < t < 15.21 \text{ ns}$ to better show the interference pattern. The dashed red lines are a fitted amplitude of the incoming X-mode pump and the dashed black lines are an amplitude of the total field assuming perfect linear X-mode to EBW conversion, compare with figure 2.8c. The pump intensity is $I_{\text{pump}} = 21.2 \pm 0.9 \text{ MW m}^{-2}$ and signatures of PDIs were observed in this simulation.

good agreement with the analytical result in [34] in spite of a debatable dipole approximation employed in the analytical model. To our knowledge, this article provides the first numerical evidence based on fully kinetic simulations that a gyrotron beam may become unstable to PDIs for a relatively large contemporary tokamak like ASDEX Upgrade.

Whilst EPOCH's `simple_laser` boundary condition outlined in section 3.2.2 works well when exciting O- and fast X-mode at the boundaries, slow X-mode turned out to be a challenge. EPOCH's laser module excites the transverse component but slow X-mode has a significant longitudinal component near the UH layer. As a result, both a slow X-mode and an EBW at the same frequency were excited simultaneously at the boundary. Fortunate differences in properties such as magnitude and sign of the group velocity meant that the dynamics from the pump wave and the unintended boundary wave could be separated out. The unintended boundary EBW was identical to the linearly converted EBW except for a difference in the sign of the wavenumber, and it could therefore be used for an intensity sweep for the homogeneous PDI of the EBWs.

We were surprised to find that the longitudinal fields of the pump waves in our simulations did not display the expected large scale amplification that X-mode experiences at the UH layer in theory, see for instance figure 5 in the article. As was discussed in section 2.4.2, the superposition of the incoming X-mode and the returning linearly converted EBW creates an interference

pattern which may hide the extend of the amplification that both waves experience. Figure 4.1 shows the amplification and interference between the pump and EBWs. The perceived amplification of the pump is clearly not as apparent as one might expect from the dashed red lines. However, comparing to figure 2.8c on page 30, the field produces the same interference patterns and the lack of amplification can be expected as a result of the superposition of the pump and the linearly converted returning wave. Note that the dashed black lines in figure 4.1 assume perfect linear conversion of the pump but the particular simulation is with $I_{\text{pump}} = 21.2 \pm 0.9 \text{ MW m}^{-2}$. At this pump intensity, signatures of PDIs were observed so the linear conversion cannot be perfect. We repeat the observation that the WKB approximation breaks down in the immediate vicinity of the UH layer and note that the simulation was in 1D whereas the experiments in [35] were, of course, in 3D. Still, there is good agreement and the majority of the intensity of the pump wave is linearly converted into the EBW.

Particle-in-cell simulations of parametric decay instabilities at the upper hybrid layer of fusion plasmas to determine their primary threshold

M G Senstius^{1,4} , S K Nielsen¹ , R G Vann²  and S K Hansen^{1,3} 

¹ Department of Physics, Technical University of Denmark, Fysikvej, DK-2800 Kgs. Lyngby, Denmark

² York Plasma Institute, Department of Physics, University of York, York YO10 5DD, United Kingdom

³ Max-Planck-Institut für Plasmaphysik, Boltzmannstraße, D-85748 Garching bei München, Germany

E-mail: mgse@fysik.dtu.dk

Received 14 June 2019, revised 24 September 2019

Accepted for publication 1 October 2019

Published 29 November 2019



CrossMark

Abstract

Parametric decay instabilities (PDIs) are nonlinear processes by which energy from a strong pump wave may be directed into other waves at other frequencies, in particular natural modes of the medium, provided that energy and momentum are conserved. The particle-in-cell code EPOCH is used to simulate PDIs in a magnetically confined fusion plasma converting a 105 GHz microwave X-mode pump wave into electrostatic daughter waves at the upper hybrid layer. Modes associated with the PDIs as well as a linearly converted electron Bernstein wave are identified in f - and k -space. The PDI daughter modes are found to agree with experimental observations from ASDEX Upgrade as well as with analytical predictions, showing a nonlinear increase in power above a predicted threshold.

Keywords: parametric decay instabilities, particle in cell, upper hybrid layer, electron Bernstein waves

(Some figures may appear in colour only in the online journal)

1. Introduction

Parametric decay instabilities [1–6] (PDIs) are a group of fundamental nonlinear processes involving interactions and a transfer of energy between different waves. Any type of wave may take part provided that certain selection rules are satisfied and that an amplitude threshold is exceeded. Both mechanical oscillations and electromagnetic waves may undergo PDI [7, 8]. In plasmas, large amplitude waves have been known to undergo PDI in the ionosphere [9], in inertial confinement fusion experiments [10] as well as in magnetic confinement plasmas [11–21].

High power microwaves are important in the study of magnetically confined fusion plasmas due, in part, to the electron cyclotron (EC) frequency typically being in the

microwave range. PDI driven by high power microwaves has been observed in a number of experiments related to electron cyclotron resonance heating (ECRH) and EC current drive [12, 22]. Furthermore, PDI has been observed during electron Bernstein wave (EBW) heating [16] and scattering experiments such as collective Thomson scattering [20]. The waves produced by PDI can potentially alter plasma behavior and damage first wall and diagnostic components. Additionally, PDI may divert energy into unintended waves, causing heating and current drive to take place in the wrong location of the plasma.

PDI involving externally launched microwave gyrotron radiation was experimentally first indicated at Versator II [12] and has recently been demonstrated consistently at ASDEX Upgrade [20, 21]. This special case where an X-mode wave decays into two electrostatic daughter waves near the upper hybrid (UH) layer has received renewed attention by a

⁴ Author to whom any correspondence should be addressed.

number of authors [23, 24]. Based on observations in ASDEX Upgrade, Hansen *et al* [23] derived dispersion relations for the implicated waves in the PDI as well as a power threshold which is lowered due to wave amplification near the UH layer. The decay of trapped waves near UH layer is also a key element in determining the power threshold for the two plasmon decay instability in ECRH experiments [25, 26]. Although these analytical models yield fitting results, they are often based on a dipole approximation, i.e. the wavenumber of the pump is much smaller than that of the daughter waves. Under most conditions, the wavenumber of an X-mode pump wave is much smaller than the daughter waves, thus justifying the dipole approximation. However at the UH layer, the wavenumber of the X-mode wave is increased significantly, making it comparable to that of the electrostatic daughter waves. Furthermore, the analytical models require prior knowledge of the interacting waves.

Numerical codes allows for studies of PDI without the need for the assumptions applied in analytical models and can therefore be used to test the validity of the models. Particle-in-cell (PIC) code simulations of X–B conversion have shown indications of concurrent nonlinear conversion through a PDI [27]. In this article, PIC code simulations are set up to systematically investigate PDI near the UH layer of a magnetized plasma. The simulations allow for identification of implicated modes in terms of both frequency and wavenumber. With this information, the validity of the dipole approximation, often employed in analytical work, is assessed and PDI selection rules are checked to determine which waves interact. The dipole approximation is assessed dubious near the UH layer. Nevertheless, the analytically derived threshold for the PDI of an X-mode pump wave near the UH layer is still found to agree with numerical observations. Additionally, EBWs generated at the UH layer through linear conversion are found to also undergo PDI and a power threshold for this PDI is estimated.

2. PDI theory

The parametric decay processes of focus in the present article are three-wave interactions where an X-mode pump wave, denoted by its wave vector \mathbf{k}_0 and frequency f_0 , near the UH frequency decays into a downshifted EBW, \mathbf{k}_2 and f_2 , and a warm lower hybrid (LH) wave, \mathbf{k}_1 and f_1 , at a much lower frequency. The warm LH daughter may then recombine with the pump wave to produce an upshifted EBW daughter, \mathbf{k}_3 and f_3 . This is illustrated in figure 1. The rate at which these processes occur depends nonlinearly on the amplitudes of all the implicated waves. Above some threshold pump wave amplitude, the decay processes become unstable and only then will the daughter waves of the PDI grow above the thermal noise level. Conservation of energy and momentum leads to the following matching conditions for the two processes

$$\omega_0 = \omega_1 + \omega_2, \quad \mathbf{k}_0 = \mathbf{k}_1 + \mathbf{k}_2, \quad (1a)$$

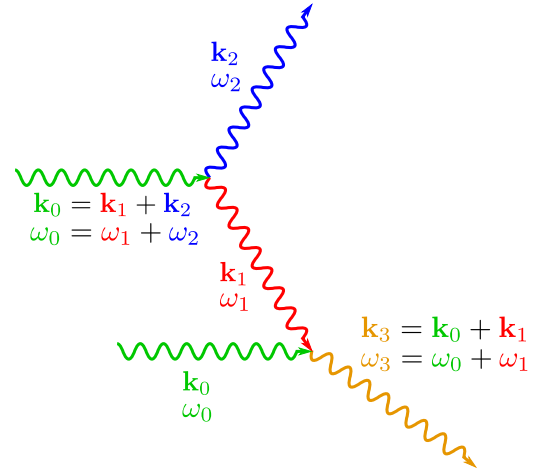


Figure 1. An idealized representation of parametric decay as described in equations (1a), (1b). A pump wave, \mathbf{k}_0 , ω_0 , may decay into two daughter waves, \mathbf{k}_1 , ω_1 and \mathbf{k}_2 , ω_2 , provided that the sum of wave vectors and of angular frequencies are conserved. One of the daughters may then recombine with the pump to produce another wave, \mathbf{k}_3 , ω_3 .

$$\omega_3 = \omega_0 + \omega_1, \quad \mathbf{k}_3 = \mathbf{k}_0 + \mathbf{k}_1, \quad (1b)$$

where the angular frequencies, of course, relate to the frequencies by $\omega = 2\pi f$. In a homogeneous plasma, the matching conditions may be satisfied over a large physical extent, lowering the pump power threshold of a PDI [4–6]. In an inhomogeneous plasma, the matching conditions may only be satisfied in a very limited range of positions, thus increasing the threshold. Amplification of the pump wave at the UH layer, however, means that the power threshold of an X-mode beam propagating to the UH layer is lowered and growth rates can be greater. The \mathbf{k} - and f -matching just have to be satisfied locally in an inhomogeneous plasma for the decay to take place.

The daughter waves investigated in this article are electrostatic waves with $\omega_1 \approx \omega_{\text{LH}}$ and $\omega_2 \approx \omega_{\text{UH}}$, which means that $\omega_1 \ll \omega_2$. An analytical expression for the frequency shifts is derived in [23] by employing a dipole approximation, i.e. $\mathbf{k}_0 \approx 0$. Assuming that the propagation is perpendicular to the magnetic field, the frequency shift can be further reduced to

$$\omega_1 \approx \omega_{\text{LH}} \left(1 + \frac{A_1 \omega_{\text{UH}}^2 - \omega_0^2 + 2\omega_0 \omega_{\text{LH}}}{2 A_2 \omega_{\text{pe}}^2 - A_1 \omega_0 \omega_{\text{LH}}} \right), \quad (2)$$

with the dimensionless parameters A_1, A_2 defined as

$$A_1 = 3 \left[\frac{\omega_{\text{pe}}^2}{4\omega_{\text{UH}}^2} + \frac{T_i}{Z_i T_e} \frac{\omega_{\text{UH}}^2}{\omega_{\text{pe}}^2} \right], \quad (3)$$

$$A_2 = \left(1 - \frac{\omega_{\text{pe}}^2}{3\omega_{\text{ce}}^2} \right)^{-1}. \quad (4)$$

Here $\omega_{c\sigma} = q_\sigma B / m_\sigma$ and $\omega_{p\sigma} = \sqrt{n_\sigma q_\sigma^2 / (\epsilon_0 m_\sigma)}$ are the cyclotron and plasma angular frequency for particle $\sigma \in \{e, i\}$, where e is for electron and i is for ion. The thermal velocity and Larmor radius of particle species σ are

$v_{l\sigma} = \sqrt{2T_\sigma/m_\sigma}$ and $r_{L\sigma} = v_{l\sigma}/(\sqrt{2}|\omega_{c\sigma}|)$ respectively. The quantities m_σ , n_σ and T_σ are particle mass, density and temperature, and the angular frequencies $\omega_{UH} = \sqrt{\omega_{ce}^2 + \omega_{pe}^2}$ and $\omega_{LH} = |\omega_{ce}\omega_{pi}/\omega_{UH}|$ are the UH and LH angular frequency. The warm LH and downshifted EBW daughter waves are described by the dispersion relations

$$k_1^2 \approx \left(\frac{\omega_1^2}{\omega_{LH}^2} - 1 \right) / (A_1 r_{Le}^2), \quad (5)$$

$$k_2^2 \approx \frac{\omega_{UH}^2 - \omega_2^2}{A_2 r_{Le}^2 \omega_{pe}^2}, \quad (6)$$

where $\omega_2 = \omega_0 - \omega_1$ following equation (1a).

The pump is here described by the warm X-mode dispersion relation [28], which for propagation perpendicular to the magnetic field becomes

$$0 = \left(1 - \sum_\sigma S_{1\sigma} \right) \left(1 - \frac{k_0^2 c^2}{\omega_0^2} - \sum_\sigma S_{2\sigma} \right) - \left(\sum_\sigma S_{3\sigma} \right)^2, \quad (7)$$

where

$$S_{1\sigma} = \frac{\omega_{p\sigma}^2 e^{-\lambda_\sigma}}{\omega_0 \lambda_\sigma} \sum_{n=-\infty}^{\infty} \frac{n^2 I_n(\lambda_\sigma)}{\omega_0 - n\omega_{c\sigma}} \quad (8)$$

$$S_{2\sigma} = \frac{\omega_{p\sigma}^2 e^{-\lambda_\sigma}}{\omega_0 \lambda_\sigma} \sum_{n=-\infty}^{\infty} \frac{n^2 I_n(\lambda_\sigma) + 2\lambda_\sigma^2 I_n(\lambda_\sigma) - 2\lambda_\sigma^2 I_n'(\lambda_\sigma)}{\omega_0 - n\omega_{c\sigma}} \quad (9)$$

$$S_{3\sigma} = \frac{\omega_{p\sigma}^2 e^{-\lambda_\sigma}}{\omega_0} \sum_{n=-\infty}^{\infty} \frac{n [I_n'(\lambda_\sigma) - I_n(\lambda_\sigma)]}{\omega_0 - n\omega_{c\sigma}}, \quad (10)$$

for $\lambda_\sigma = k_0^2 r_{L\sigma}^2$ and $\sigma \in \{e, i\}$. $I_n(\lambda_\sigma)$ is the n th modified Bessel function and $I_n'(\lambda_\sigma)$ is its derivative. As the pump gets closer to the UH layer, it becomes increasingly electrostatic and eventually coincides with the first EBW branch. The pump wave can therefore be linearly converted into an EBW at the UH layer [16]. This EBW, unlike the frequency shifted EBW PDI daughter waves, is exactly at the pump frequency. The dispersion relation for EBWs is given by [28]

$$0 = 1 - \frac{\omega_{pe}^2 e^{-\lambda_{eL}}}{\omega_L \lambda_{eL}} \sum_{n=-\infty}^{\infty} \frac{n^2 I_n(\lambda_{eL})}{\omega_L - n\omega_{ce}}, \quad (11)$$

where $\lambda_{eL} = k_L^2 r_{Le}^2$, and ω_L , k_L are the angular frequency and wave number of the linearly converted EBW. The notable differences between this linearly converted EBW and the pump are that the EBW propagates much slower, i.e. $|v_0/v_L| \ll 1$, and has a greater absolute wave number, i.e. $|k_0/k_L| \ll 1$, when the waves are not at the UH layer. The pump and the linearly converted EBW propagate in different directions; in 1D, they propagate in opposite directions.

3. Numerical setup

3.1. Accessibility to the UH layer

The simulations of this article are designed so that the parameters at the UH layer resemble that of the ASDEX Upgrade discharge described in [23]. Strong scattering was observed

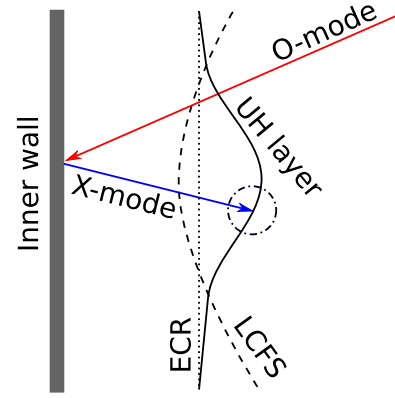


Figure 2. A sketch showing the typical placement of resonances and beam paths that lead to strong scattering in ASDEX Upgrade. The red arrow represents an incoming O-mode gyrotron beam that is converted to X-mode at the inner wall. The X-mode, represented by a blue arrow, propagates back into the plasma, passing the last closed flux surface (LCFS), the electron cyclotron resonance (ECR) and reaches the upper hybrid (UH) layer. The interaction region where the scattering is believed to emanate from is marked by the dashed-dotted line.

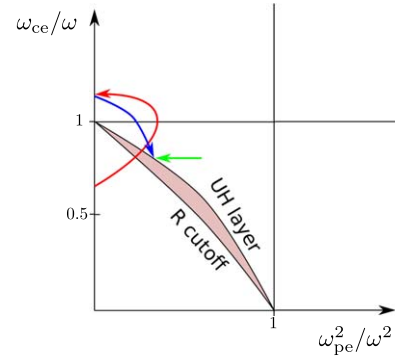


Figure 3. A simplified CMA diagram featuring the approximate beam path to reach the UH layer (red and blue arrows) in ASDEX Upgrade shot 28286 and the beam path to be used in simulations (green arrow). The red arrow represents the path of an O-mode launched from the low field side. The blue arrow is the X-mode that is generated from the O-mode at the high field side and reflected back into the plasma. The green arrow represents the path of an X-mode beam generated in simulations.

when an X-mode beam reached the UH layer. Getting an X-mode beam to the UH layer, however, is not straightforward as it is reflected at the R-cutoff when launched from the low field side. An O-mode beam launched from the low field side, which passes through the plasma, is reflected and partly converted to X-mode on the high field side inner wall. Before reaching the UH layer, the reflected X-mode passes the electron cyclotron resonance where it is partly absorbed. A fraction of the X-mode nevertheless makes it to the UH layer and scattering is then observed at approximately $f_0 \pm f_{LH}$. This trajectory is illustrated in figure 2 while figure 3 shows the path in a CMA diagram. Having reached the UH layer, the X-mode is unable to propagate further and is then converted either through PDI or by a linear conversion into an EBW [26], which changes its direction of propagation. In this work, only an X-mode already near the UH layer is considered,

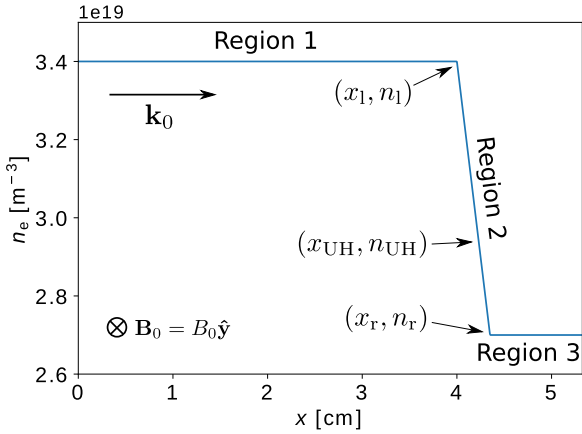


Figure 4. The geometry of the computational domain. All initial parameters except for the density are constant throughout the domain. The density profile is divided into three regions, two being constant (regions 1 and 3) and one bridging the other two (region 2). Positions and densities mentioned in the text are shown in brackets. The pump, \mathbf{k}_0 , is generated at the $x = 0$ boundary and propagates right in the figure. The background magnetic field is constant and points perpendicularly to the direction of propagation.

i.e. the green arrow is followed to lower the computational costs. The reflection and conversion of O-mode will not be discussed in further detail.

3.2. Simulations

The code used for the simulations is the second order relativistic PIC code EPOCH [27, 29]. Like any PIC code, physical particles are modeled as a smaller number of pseudoparticles that represent clouds of physical particles, adding up to the same properties as that of the desired plasma. The routine is a split step process between updating particle dynamics due to the electromagnetic fields and updating the electromagnetic fields due to the currents induced by the moving charged particles using a finite difference approach.

While EPOCH is capable of doing both 2D and 3D simulations, the simulations in this article were in 1D as all the important dynamics are expected to rely on changes in the direction of propagation, provided that this is perpendicular to the magnetic field. Although the simulations are 1D, EPOCH retains 3 dimensions on all vector quantities such as the electric field, the magnetic field and the velocity of the pseudoparticles. In only one inhomogeneous spatial dimension, a position dependent background magnetic field that is both stationary and divergence free is not possible. For this reason, the beam path of the experiment described earlier is not possible. Instead, the magnetic field is kept constant, an X-mode pump, \mathbf{k}_0 , is generated inside a plasma and is propagated to the UH layer by varying only the density with position. The two different approaches are illustrated in figure 3.

The computational domain is illustrated in figure 4 and can be split into 3 regions, denoted as shown in the figure. The plasma is a deuterium plasma with the initial electron density equal to the initial ion density, $n_e = n_i = n(x)$. The

density varies with position and is described by

$$n(x) = \begin{cases} n_1 & x < x_1 \\ n_1 + (n_r - n_1) \frac{x - x_1}{x_r - x_1} & x_1 \leq x < x_r, \\ n_r & x_r \leq x \end{cases} \quad (12)$$

where $n_1 = 3.4 \times 10^{19} \text{ m}^{-3}$, $n_r = 2.7 \times 10^{19} \text{ m}^{-3}$, $x_1 = 4.00 \text{ cm}$, $x_r = 4.35 \text{ cm}$. The extent of the entire domain is $0.00 \text{ cm} \leq x \leq 5.35 \text{ cm}$ and there are a total of $n_x = 6600$ grid points and $n_{\text{part}} = 60000n_x$ pseudoparticles of which half are electrons and the other half are deuterons. Regions 1 and 3 are constant for easier mode identification while region 2 bridges them. The initial background magnetic field and temperature are homogeneous and given by $B_0 = B_{0y} = 3.35 \text{ T}$ and $T_e = T_i = 0.3 \text{ keV}$. The time step is chosen so that it is 0.95 multiplied the longest allowed time step by the Courant–Friedrichs–Lewy stability condition [30]. The output time step is $\delta t = (10.3f_0)^{-1} = 9.25 \times 10^{-13} \text{ s}$ and the length of the simulations is around 50 ns.

A pump wave at $f_0 = 105 \text{ GHz}$, denoted \mathbf{k}_0 in figure 4, is generated at the $x = 0.00 \text{ cm}$ boundary which propagates through regions 1 and 2 until it reaches the UH layer at $x_{\text{UH}} = 4.25 \text{ cm}$ and $n_e = n_i = 2.91 \times 10^{19} \text{ m}^{-3}$. The pump intensity is ramped up using an arctan-function with a characteristic time scale of $\tau_{\text{ramp}} = 0.20 \text{ ns}$ and the amplitude is varied over a number of simulations. The pump wave is generated in EPOCH by an oscillating pseudo-current at the boundary which, like an antenna, is able to excite an electromagnetic wave that can propagate into the domain. The wave has an initial amplitude at the $x = 0 \text{ cm}$ boundary but is free to interact with the plasma throughout the domain. The pump wave is an X-mode wave which gets increasingly longitudinal near the UH layer. EPOCH can currently only excite transverse electromagnetic components which turns out to also excite an EBW wave at the same frequency. This unintended wave will be referred to either as the boundary wave or by k_B, f_B . The field boundary conditions are found by rewriting Maxwell's equations, using a current to excite waves at the $x = 0.00 \text{ cm}$ boundary and blocking incoming waves at the $x = 5.35 \text{ cm}$ boundary. The particles are initially thermally distributed and the particle boundary conditions at both boundaries replace any leaving particle with a new thermally distributed one. The thermally distributed particles give rise to thermally excited natural modes throughout the plasma.

Figure 5 shows the longitudinal component of the resulting electric field at two different points in time. The first shows the pump, k_0 , ramping up and propagating through region 1. The boundary wave, k_B , can be seen near the $x = 0.00 \text{ cm}$ boundary. At the later time, the boundary wave has propagated further into region 1, the pump has made it into region 2 and amplification is observed at the UH layer. Emerging from the UH layer, what appears to be the linearly converted wave, k_L , is seen propagating back through region 1. A greater wavenumber and slower group velocity are contributing to a greater wave amplitude in order to conserve energy. While the pump only leads to relatively small density perturbations, the boundary and linearly converted wave,

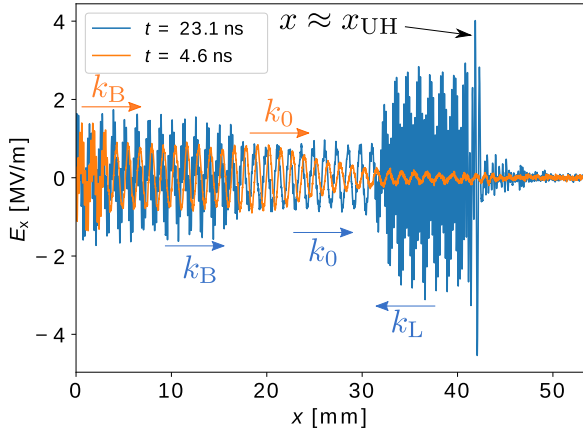


Figure 5. The longitudinal component of the electric field, E_x , at two points in time as indicated in the legend. Colored labels refer to the waves present, and x_{UH} is the position of the UH layer. The pump intensity is $I_{\text{pump}} = 17.4 \pm 0.5 \text{ MW m}^{-2}$.

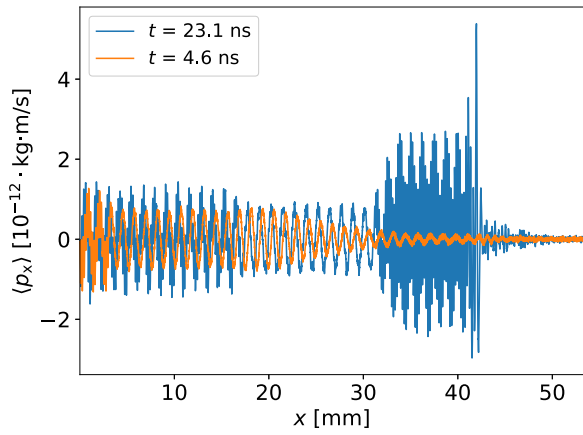


Figure 6. Averaged longitudinal electron momentum throughout the computational domain at the same points in time as shown in figure 5. The pump intensity is $I_{\text{pump}} = 17.4 \pm 0.5 \text{ MW m}^{-2}$.

being EBWs, are carried by electron density perturbations [16] and reach relative amplitudes of $\max(n_e(t)/n_e(0)) \approx 1.2$ for $I_{\text{pump}} = 17.4 \pm 0.5 \text{ MW m}^{-2}$ and $\max(n_e(t)/n_e(0)) \approx 1.3$ for $I_{\text{pump}} = 35 \pm 1 \text{ MW m}^{-2}$. In figure 6, the average longitudinal electron momentum is shown for the same time instances as in figure 5. Except for some minor differences, perhaps a small phase shift noticeable near the UH layer, the main features are the same as those observed in figure 5. The longitudinal waves in the electric field lead to acceleration of the electrons and thereby also to corresponding wave features in electron momentum. Lastly, figure 7 shows the electron density in time and space along with sketched out wavefronts of the waves excited at the boundary and the waves returning from the UH layer. The EBWs, which propagate as electron density perturbations, are clearly seen whereas the X-mode pump makes less of an impression on the background density. However, interference patterns are seen in the presence of multiple waves, e.g. above the k_B -line where both the X-mode pump and the boundary wave propagate. Again, the same features are observed in this figure as the EBWs propagate as density perturbations which lead to longitudinal electric field

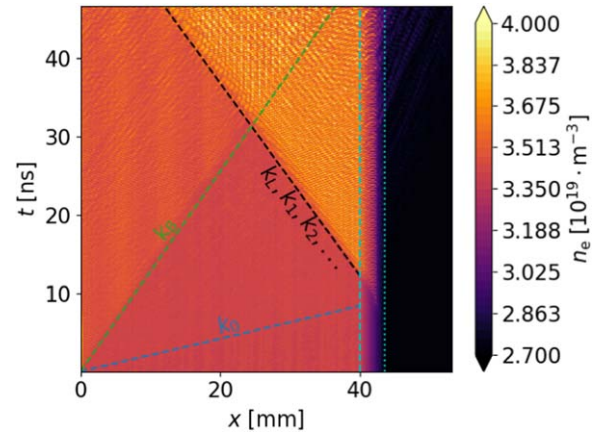


Figure 7. Electron density plotted in space and time. The dashed blue, green and black lines are the approximate wave fronts of the waves indicated. The vertical dashed and dotted lines mark x_l and x_r as illustrated in figure 4. The pump intensity is $I_{\text{pump}} = 17.4 \pm 0.5 \text{ MW m}^{-2}$.

which then cause longitudinal electron momentum to change. A plot similar to figure 7 but for the longitudinal electric field can be seen in figure 16.

An entirely inhomogeneous setup is also considered due to the possibility of lower threshold homogeneous PDIs in the homogeneous region 1 leading up to the UH layer. While observed frequency lines in this setup will not be due to homogeneous PDI, k -analysis cannot be performed on the waves. The inhomogeneous setup has all the same physical parameters except the extend of the domain is $0.00 \text{ cm} < x < 1.35 \text{ cm}$ with the density profile given again by equation (12) but for $n_1 = 5.4 \times 10^{19} \text{ m}^{-3}$, $n_r = 2.7 \times 10^{19} \text{ m}^{-3}$, $x_l = 0.00 \text{ cm}$, $x_r = 1.35 \text{ cm}$. This means that all parameters are exactly the same at the UH layer and the parameters at $x = 1.00 \text{ cm}$ correspond to the homogeneous region 1 for the setup illustrated in figure 4.

4. Results

4.1. Group velocity found by tracking the returning wave front

To show that the wavefront labeled as k_L in figure 5 is indeed an EBW, the group velocity is estimated by tracking the position of the wavefront in time. The tracking is done by averaging $|E_x|$ in space over 3 EBW wavelengths and fitting the function $y(x) = A_0 \arctan((x - x_0)/l) + y_0$ to it at particular points in time. The parameter x_0 is then taken to be the position of the wave front, see figure 8. The group velocity should be constant throughout region 1 so doing this for a number of different times as the wave front propagates through region 1 should provide at linear relation between $x_0(t)$ and t , the slope of which is the group velocity, see figure 9. Using this approach gives the group velocity $v_{g,L} = -(7.45 \pm 0.07) \times 10^5 \text{ m s}^{-1}$ for the simulation shown in figure 5. The group velocity can also be found from the dispersion relations as $v_g = \partial\omega/\partial k$. Solving the warm X-mode dispersion relation and the EBW dispersion relation numerically and calculating the group velocities at the pump

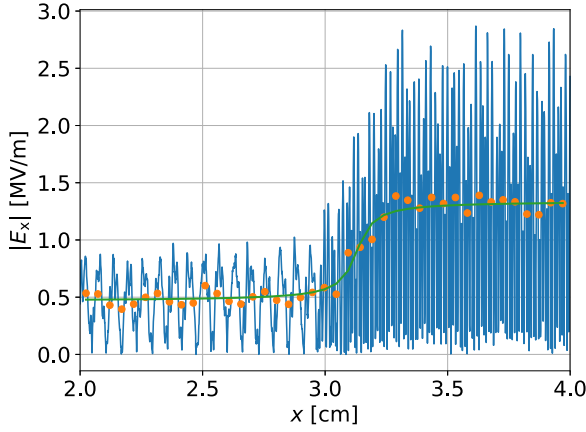


Figure 8. The process of tracking the wave front of the returning EBWs. The blue line shows the absolute value of the longitudinal component of the electric field, E_x . The orange dots are the average of the blue line over 3 EBW wavelengths according to theory. The green line is an arctan fit to the orange dots, the center of the fit is taken to be the position of the wave front. The pump intensity is $I_{\text{pump}} = 21.2 \pm 0.9 \text{ MW m}^{-2}$ and the time is $t = 25.0 \text{ ns}$.

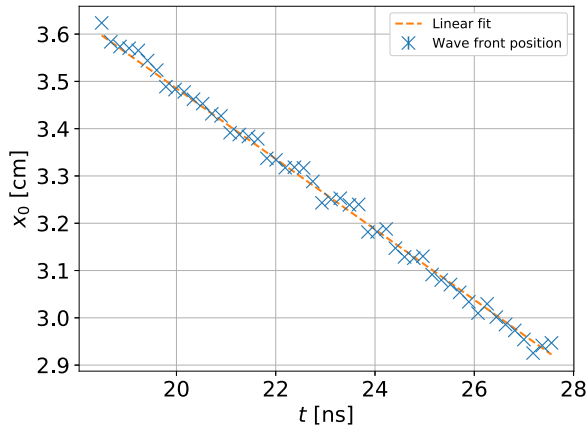


Figure 9. The tracked wave front position as a function of time (blue crosses) with a linear fit to give an estimate of the group velocity of the returning EBWs. The pump intensity is $I_{\text{pump}} = 21.2 \pm 0.9 \text{ MW m}^{-2}$.

frequency using the input parameters of the homogeneous region 1 as stated in section 3.2 yields $|v_{g,0,\text{theo}}| = 6.92 \times 10^6 \text{ m s}^{-1}$ and $|v_{g,L,\text{theo}}| = 7.43 \times 10^5 \text{ m s}^{-1}$ respectively. From this, it is seen that the returning wave is much too slow to be an X-mode wave. On the other hand, $v_{g,L,\text{theo}}$ is within the error of $v_{g,L}$ supporting the hypothesis that the returning waves are EBWs with a frequency around the pump frequency.

4.2. Spatial spectrum contains several peaks

The origins of the returning EBWs is investigated by means of a continuous wavelet transform (CWT) in space using the Morlet wavelet as base function to look at the spatial spectrum as a function of position. Figure 10 shows the resulting spectrum when transforming the longitudinal component of the electric field after the pump has reached the UH layer. As the pump wave gets closer to the UH layer, k_0 increases by half an order of magnitude in good agreement with the warm

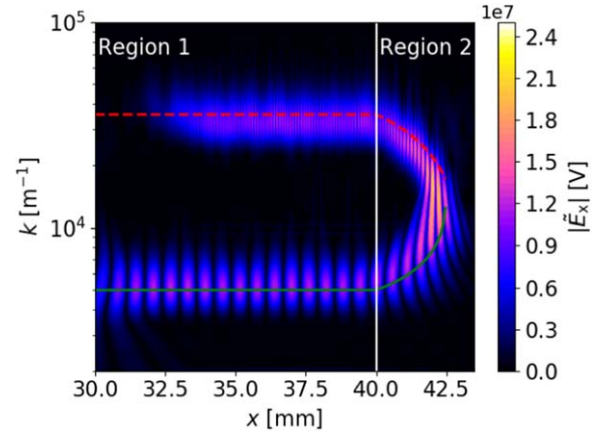


Figure 10. The absolute value of a CWT of the longitudinal component of the electric field, E_x , near the UH layer at $t = 22.5 \text{ ns}$. The vertical solid white line marks the end of the first homogeneous region. The dashed red line and solid green line are numerical solutions to equation (11) for the linearly converted EBW and (7) for warm X-mode respectively. The Morlet wavelet is used as base function and the pump intensity is $I_{\text{pump}} = 21.2 \pm 0.9 \text{ MW m}^{-2}$.

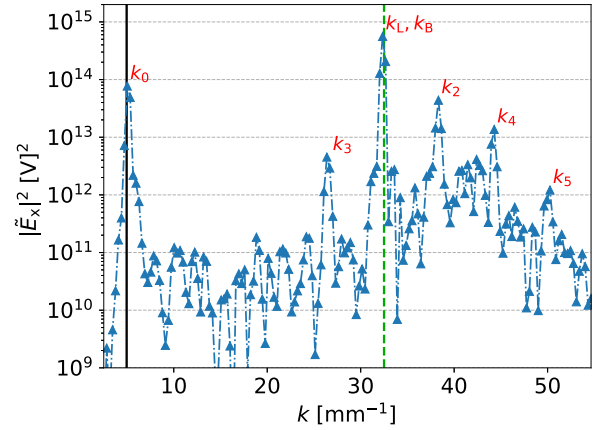


Figure 11. The square of the FFT of the longitudinal component of the electric field, E_x , into k -space in the range of X-mode and EBW at the pump frequency (blue triangles connected by a dashed-dotted line). The solid black line marks the numerical solution to warm X-mode at the pump frequency. The dashed green line marks the numerical solution to an EBW at the pump frequency. Red labels mark peaks that are discussed in the text. The pump intensity is $I_{\text{pump}} = 21.2 \pm 0.9 \text{ MW m}^{-2}$ and the transform is over $2 \text{ cm} < x < 4 \text{ cm}$ at $t = 46.5 \text{ ns}$.

X-mode dispersion relation. At the UH layer, the wave experiences amplification and comes to a halt. It is then seen that a wave starts propagating backwards, increasing the wavenumber in good agreement with the dispersion relation of a linearly converted EBW, confirming that X-B conversion has taken place.

To get a better resolution of the spectrum, the returning waves are transformed using a fast Fourier transform (FFT) in space as they propagate in region 1. Any FFT in this article will be using the orthonormal definition provided by the Python library Numpy. The absolute square of the resulting spectrum is shown in figure 11 along with a number of labels.

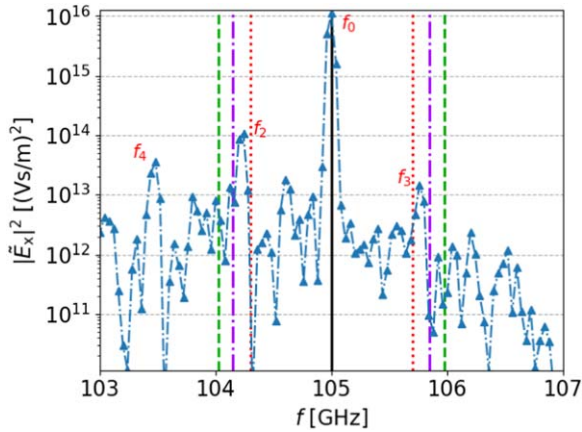


Figure 12. The spectral density of the longitudinal component of the electric field, E_x , near the pump frequency (blue triangles connected by a dashed–dotted line). The solid black line marks the pump frequency. The red dotted lines, the purple dashed–dotted lines and the green dashed lines are shifts corresponding to the LH frequency, experimental observations [23] and equation (2) respectively. The pump intensity is $I_{\text{pump}} = 21.2 \pm 0.9 \text{ MW m}^{-2}$ and the transform is over $20 \text{ ns} < t < 45 \text{ ns}$ at $x = 3.5 \text{ cm}$.

The peak denoted by k_0 coincides with the pump and the one denoted by k_L , k_B is the combined peak associated with the linearly converted wave and the boundary wave. The four remaining labeled peaks, k_2 through k_5 , are all shifted by an integer times $5.9 \pm 0.2 \text{ mm}^{-1}$ relative to the k_L , k_B -peak. These peaks are likely due to PDIs as described in equations (1a)–(1b), k_2 and k_3 being the downshifted and upshifted EBW respectively, as the downshifted EBW is typically the larger peak. While it is now seen that the returning waves consist of several EBWs, it does, however, appear that the pump is mainly converted into k_L . All the above mentioned peaks are also observed when transforming the longitudinal electron momentum phase space.

4.3. Spectral density shows scattering at shifted frequencies

The spectral density of the returning waves is found using an FFT of time into frequency space and is compared to the experimentally observed peaks. Figure 12 shows the spectral density of E_x near the UH frequency in region 1 after the returning waves have reached it. The main peak, labeled f_0 , coincides with the pump frequency and has contributions from the pump wave, the linearly converted wave and the boundary wave. Found symmetrically around the main peak are the two smaller shifted peaks labeled f_2 and f_3 . The shift in frequency of the peaks agrees well with the experimentally observed shifts. It is noted that approximating the shift by the LH frequency underestimates it while equation (2) overestimates it. This is in agreement with [23]. An additional peak, labeled f_4 , is found at twice the shift of f_2 . This peak could be a further PDI daughter and is likely to be the wave that leads to k_4 in figure 11.

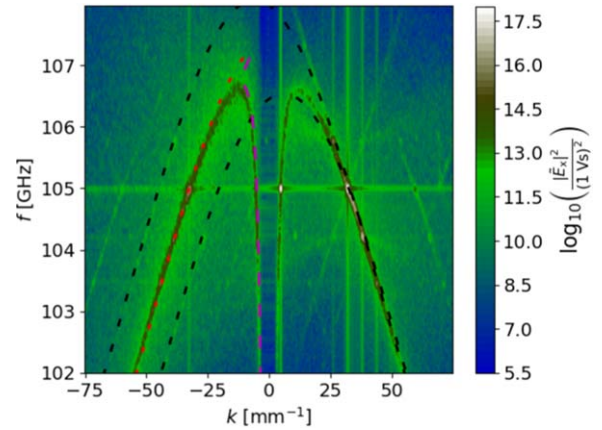


Figure 13. f - and k -space of the longitudinal component of the electric field, E_x , near the pump frequency. The dashed purple line is the expected X-mode dispersion line and the dotted blue line is the EBW branch. The black dotted lines are EBW dispersion lines shifted by the observed LH daughter mode in figure 15. The pump intensity is $I_{\text{pump}} = 21.2 \pm 0.9 \text{ MW m}^{-2}$ and the transform is over $2 \text{ cm} < x < 4 \text{ cm}$, $20 \text{ ns} < t < 46.5 \text{ ns}$.

4.4. Dispersion curves and relevant peaks along them

To connect the peaks observed in the spectra shown in figures 11 and 12, the longitudinal component of the electric field is transformed in both x and t to give a spectrum in k and f using a 2D FFT. The absolute square of the resulting spectrum near the pump frequency is shown in figures 13 and 14. A number of lines and peaks are visible in this part of the spectrum. The warm X-mode and EBW dispersion relations from section 2 have been plotted in figure 13 for negative k as a dashed purple line and red dotted line respectively. Both lines fit well with dispersion lines present in the spectrum except where the observed lines meet. According to the dispersion relations, the lines do not meet, however, the EBW dispersion relation relies on a large k approximation [28] which becomes doubtful in this point. The two lines are in fact expected to meet, as this is where linear conversion between X-mode and EBW can take place. The same lines are observed at the corresponding positive k -values. Additional lines are present and some will be addressed after the major peaks have been analyzed.

Figure 14 shows the same spectrum as figure 13 but the dispersion lines have been replaced by labels at the major peaks, and circles mark the analytical predictions presented in section 2. Keeping in mind that $v_g = \partial\omega/\partial k$ and following the dispersion lines, a peak found along a line with a steep slope is a mode that propagates faster than one with a less steep slope. Furthermore, a mode at a positive slope propagates in the positive x -direction while a negative slope indicates that the waves propagate in the negative x -direction. With this, the peak labeled A is seen to be a right propagating X-mode at the pump frequency, i.e. the pump wave. B and C are both EBWs at the pump frequency. Based on the direction of propagation and peak value, B is the linearly converted EBW while C is the boundary EBW. Lastly, D is a

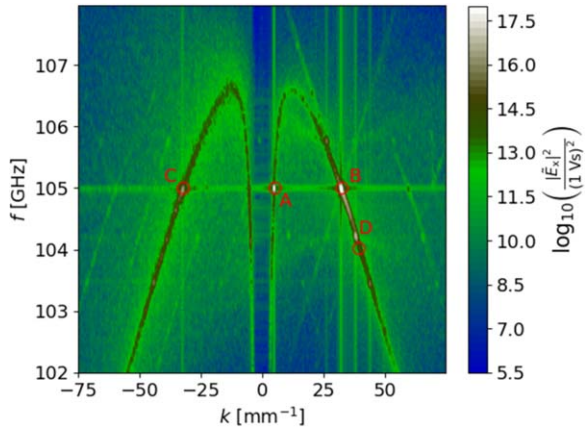


Figure 14. Same spectrum as shown in figure 13 without the dispersion lines but with major peaks labeled. Labels A through D mark selected peaks, A being the pump, B the linearly converted wave, C the boundary wave and D the downshifted EBW. The red circles denote theoretical predictions based on equations (1a), (2), (6), (7) and (11).

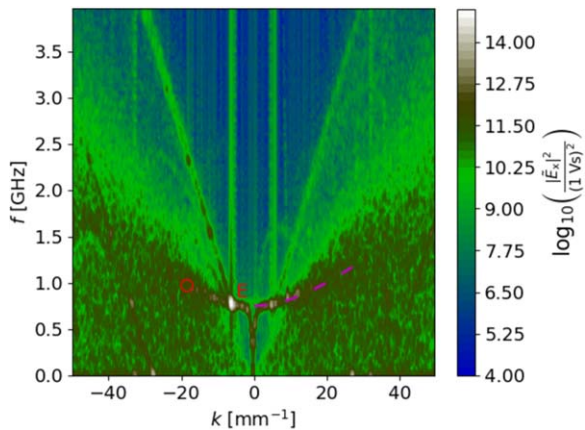


Figure 15. f - and k -space of the longitudinal component of the electric field, E_x , near the LH frequency. The label E marks the warm LH daughter while the red circle is the theoretical location found using equations (2) and (5). The magenta dashed line is the dispersion line of equation (5) for positive k . The pump intensity is $I_{\text{pump}} = 21.2 \pm 0.9 \text{ MW m}^{-2}$ and the transform is over $2 \text{ cm} < x < 4 \text{ cm}$, $20 \text{ ns} < t < 46.5 \text{ ns}$.

downshifted EBW, which is seen to propagate left like the linearly converted EBW. The circles mark the predictions based on the relevant dispersion relations. In agreement with figure 12, the prediction for the downshifted EBW (D) overestimates the frequency shift but is found along the EBW dispersion line as expected. In addition to the marked peaks, a number of additional peaks are present, most notably some smaller peaks around the EBW dispersion line that B and D lie on, in particular $(k_4, f_4) \approx (45 \text{ mm}^{-1}, 103.5 \text{ GHz})$ as it is labeled in figures 11 and 12. It should be noted that all the above mentioned features are also present when transforming the electron density instead the longitudinal electric field component.

A PDI producing the downshifted EBW labeled D in figure 14 must also produce a low frequency daughter. The f

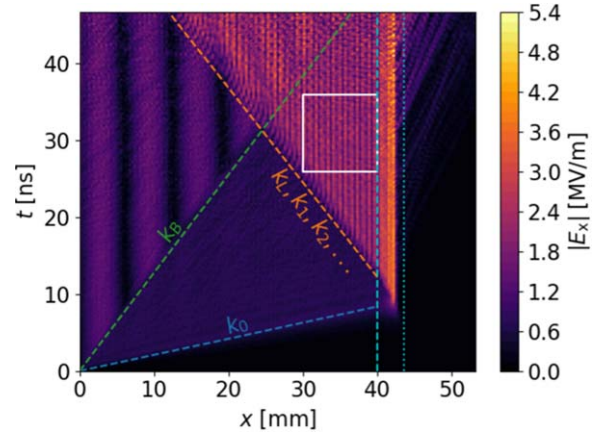


Figure 16. The absolute value of the longitudinal component of the electric field, E_x , plotted in space and time. The dashed blue, green and orange lines are the approximate wavefronts of the waves indicated. The vertical dashed and dotted lines mark x_1 and x_2 as illustrated in figure 4. The white box enclosing $26 \text{ ns} < t < 36 \text{ ns}$ and $30 \text{ mm} < x < 40 \text{ mm}$ marks the domain used for the Fourier analysis on which the power plot in figure 17 is based. The pump intensity is $I_{\text{pump}} = 21.2 \pm 0.9 \text{ MW m}^{-2}$.

and k spectrum near the LH frequency is shown in figure 15 and the expected position of the warm LH daughter wave, found in [23], is marked by a red circle. As noted about the downshifted EBW, the overestimated prediction of the frequency shift means that the frequency of the warm LH daughter is also overestimated. The actual peak associated with the warm LH daughter is labeled E. Plotting the dispersion relation for the warm LH daughter, equation (5), gives the dashed magenta line which fits the observed dispersion line and the prediction is then seen to lie on the correct dispersion line. It is noted that the warm LH daughter must be back propagating like the downshifted EBW, judging from the slope of the dispersion line. A number of other smaller peaks can be seen, in particular at $(2k_1, 2f_1)$ and at $(3k_1, 3f_1)$. It is noted that the relative position of these three peaks resembles that of (k_L, f_L) , (k_2, f_2) and (k_4, f_4) in figure 14. Shifting the EBW dispersion lines in figure 13 by adding and subtracting the observed warm LH daughter results in the two dotted black lines. The two shifted lines are seen to overlap for positive k , perhaps explaining why this EBW branch looks more smeared out between the peaks denoted B and D as is seen more clearly in figure 14.

The absolute longitudinal component of the electric field is shown in figure 16 as a function of both position and time. The approximate wavefronts in region 1 of the relevant waves are indicated with lines and appropriate labels. Interference is observed when waves of comparable amplitude are found in the same space. The indicated white window in the figure is now used for FFTs. In these FFTs, the position in (k, f) -space of the pump wave, linearly converted EBW, downshifted EBW and warm LH daughter are determined as the local maximum near the expected location. To check if (k, f) is conserved in the PDI and to see if the linearly converted EBW could act as an additional pump, two quantities are

Table 1. Observed peaks in figures 14 and 15 found by locating the local maximum as well as the calculated quantities $\Delta_{\text{PDI},0}$ and $\Delta_{\text{PDI},L}$ introduced in the text. k -values are given in units of mm^{-1} and f in GHz. The values at the UH layer are calculated using initial values at x_{UH} as stated in section 3.2. Bold numbers for $\Delta_{\text{PDI},0}$ and $\Delta_{\text{PDI},L}$ indicate conservation of both k and f within the error.

(k, f) (mm^{-1} , GHz)	Observed in region 1	Calculated at the UH layer
Pump wave	$(4.4 \pm 0.3, 105.00 \pm 0.05)$	$(13 \pm 2, 105.00 \pm 0.05)$
Linearly converted EBW	$(31.7 \pm 0.3, 105.00 \pm 0.05)$	$(17.4 \pm 0.9, 105.00 \pm 0.05)$
Downshifted EBW	$(37.7 \pm 0.3, 104.20 \pm 0.05)$	$(26.8 \pm 0.5, 104.20 \pm 0.05)$
Warm LH daughter	$(-6.3 \pm 0.3, 0.80 \pm 0.05)$	$(-11 \pm 4, 0.80 \pm 0.05)$
$\Delta_{\text{PDI},0}$	$(27.0 \pm 0.9, 0.0 \pm 0.2)$	$(3 \pm 7, 0.0 \pm 0.2)$
$\Delta_{\text{PDI},L}$	$(-0.3 \pm 0.9, 0.0 \pm 0.2)$	$(-2 \pm 5, 0.0 \pm 0.2)$

introduced as $\Delta_{\text{PDI},0} \equiv (k_1 + k_2 - k_0, f_1 + f_2 - f_0)$ and $\Delta_{\text{PDI},L} \equiv (k_1 + k_2 - k_L, f_1 + f_2 - f_L)$. A PDI can only take place if there is conservation of both k and f , which means that a PDI converting the X-mode pump wave into the observed downshifted EBW and warm LH wave is only possible when $\Delta_{\text{PDI},0} = 0$. Likewise, it is possible for the linearly converted EBW to act as the pump, producing the same daughter waves, when $\Delta_{\text{PDI},L} = 0$. Recall that the wavenumbers depend on a number of parameters, including the density which varies throughout the numerical domain. While the frequency of a wave identified in the homogeneous region 1 is the same when the wave is at the UH layer, its wavenumber may have changed. It is expected that $\Delta_{\text{PDI},0}$ is zero only at the UH layer so wavenumbers at the UH layer are calculated using the observed frequencies, the initial parameters at the UH layer and the relevant dispersion relations. The results are summarized in table 1 and the pump and the suspected PDI products show both frequency and wavenumber match at the UH layer, i.e. the error of $\Delta_{\text{PDI},0}$ is greater than its value. In the homogeneous region 1, on the other hand, $\Delta_{\text{PDI},0} \neq 0$ and this PDI is therefore only possible somewhere in region 2 near the UH layer where the selection rules of equation (1a) are exactly satisfied. Surprisingly, $\Delta_{\text{PDI},L} = 0$ within the error both at the UH layer and in the homogeneous region 1. Theoretical thresholds and growth rates of this PDI are likely different from those of the PDI involving an X-mode pump wave. The implications of this are discussed in section 5.

4.5. Power of the daughter modes depends nonlinearly on pump intensity

To investigate the relation between the intensity of the pump and of the PDI daughter wave, the pump intensity is varied over a number of simulations, keeping the simulation geometry constant. For each simulation, the window indicated in figure 16 is used for FFTs into (k, f) -space and the spectral density is then found as the absolute square of the transformed fields. This window is chosen so that the wave composition and average parameters do not change significantly throughout. The window is placed close to the UH layer to minimize interactions occurring in the homogeneous region 1. Integrating the relevant peaks of the spectral density yields a quantity proportional to the power contained in the peak via Parseval's theorem. Some peaks are found to shift slightly as the pump intensity is increased so the peaks are

integrated by first locating the local maximum of the spectral density inside a box of dimensions 5.7 mm^{-1} by 0.70 GHz near the expected position of the peak. Having located the maximum, another box of same dimensions is centered around it and the spectral density is numerically integrated inside this box. The error is estimated by calculating a mean level based on the spectrum around the edge of the box, including the first layer of points on either side of it. For a discussion of this shift, see section 5. The pump intensity is determined using the relations in chapter 5.4 of [31] with a cold approximation. The absolute squared fields are found by averaging the field components over an interval $2.3 \text{ ns} < t < 3.7 \text{ ns}$ at positions from $x = 2 \text{ mm}$ to $x = 7 \text{ mm}$ in 1 mm steps where the X-mode pump intensity should be far exceeding any other mode. A normalized power, P_{norm} , is introduced as the integrated peak values of the spectral density normalized to that of a low pump intensity setting above the PDI threshold, i.e. the normalization depends on what mode is being looked at and it provides a measure of how the power in that particular mode changes with the pump intensity. Based on [23], the inhomogeneous threshold is calculated to be $I_{\text{inhom}} = 14.2 \text{ MW m}^{-2}$. The $I_{\text{pump}} = 17.4 \pm 0.5 \text{ MW m}^{-2}$ simulation just above the inhomogeneous threshold is chosen as the normalization point since this is approximately the level that reaches the UH layer in [23].

Figure 17 shows the resulting plot of the normalized power of selected modes against the pump wave intensity scan. Above I_{inhom} the power level of the PDI daughters, (k_1, f_1) for the warm LH daughter and (k_2, f_2) for the downshifted EBW, increase at a rate that looks to be more aggressive than linear dependence as suggested by the line proportional to I_{pump}^4 . The curves of the daughter waves above I_{inhom} follow each other closely, suggesting that the same nonlinear process is the main contributor to both waves. The daughter waves appear to increase nonlinearly with pump intensity until the last point where they start decreasing. The relative increase of power in the pump wave, (k_0, f_0) , and the linearly converted EBW, (k_L, f_L) , are seen to follow a linear dependence on pump intensity fairly well at lower pump intensities. At higher pump intensities, the pump and consequently the linearly converted EBW drop off slightly from the line indicating linear dependence. It is likely because new wave interactions start draining the pump as it is propagating to the UH layer which would cause the PDI daughter waves to drop off in the

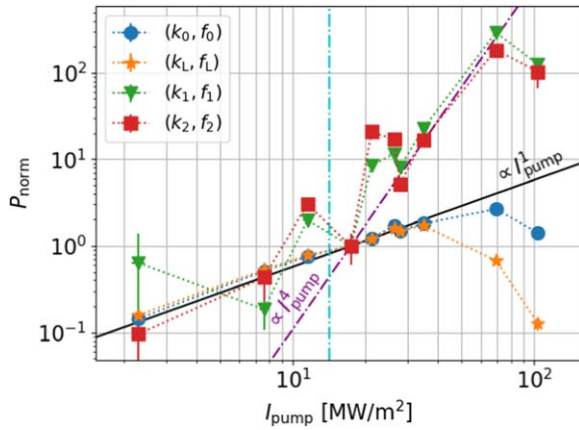


Figure 17. The normalized power contained in selected modes as the pump intensity is increased. The power is found by integrating peaks in the absolute squared 2D FFT of the electric field, E_x , into f - and k -space. The FFTs are over $26 \text{ ns} < t < 36 \text{ ns}$ and $20 \text{ mm} < x < 30 \text{ mm}$. The power is normalized so that $P_{\text{norm}}(I_{\text{pump}} = 17.4 \pm 0.5 \text{ MW m}^{-2}) = 1$ for all modes and the plot therefore does not show the relative power between modes. The black solid line is proportional to I_{pump} and the purple dashed-dotted line to I_{pump}^4 . The theoretical inhomogeneous threshold is indicated by the vertical cyan dashed line.

end. This is discussed in further in section 5. Around I_{inhom} , the daughter waves display a correlated fluctuating behavior but no obvious trend is seen. Below I_{inhom} , the power level of the warm LH daughter fluctuates but stays at roughly the same level, showing that this is below the threshold and is dominated by a background level. This is supported by a noise test without a pump wave where only thermally excited waves and numerical noise contribute. The downshifted EBW follows an approximate linear dependence on the pump intensity. A similar analysis on the homogeneous region 1 before the returning waves return from the UH layer suggests a linear dependence on pump intensity throughout the X-mode and EBW branches. It appears that the pump wave also feeds energy into the branches through other means than the PDI of interest.

In the entirely inhomogeneous simulations, where the homogeneous region 1 has been replaced by a continuation of the linear density profile in region 2, there is no possibility of interfering homogeneous PDI daughter waves. The price is that modes cannot be separated in k . A measure of normalized power is found through an FFT of E_x from time into f -space at the position $x = 1.00 \text{ cm}$ where the initial parameters are the same as is the homogeneous region 1 used in the preceding analysis. The FFT is over the interval $5 \text{ ns} < t < 15 \text{ ns}$ and the absolute squared spectrum is numerically integrated over an interval of 0.70 GHz centered around the frequencies corresponding to the experimentally observed shifts. If one or more local minima are found inside the interval, the integral is cut short, stopping at the minima. As with the homogeneous case, an error is estimated based on a mean level of the surrounding spectrum. Again, the first pump intensity level above the threshold is chosen as the normalization point, the resulting plot is shown in figure 18. The LH, f_1 , and the downshifted EBW, f_2 , daughter waves follow a similar

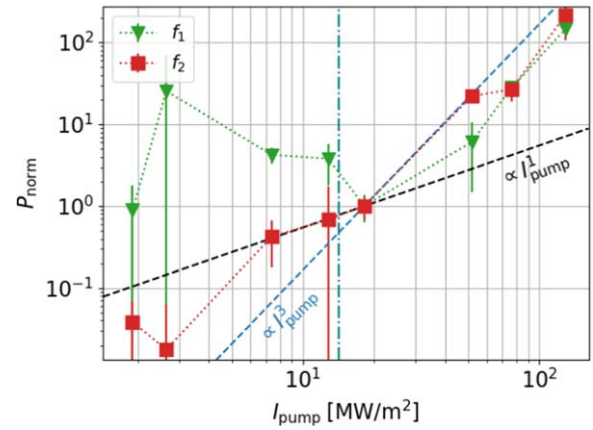


Figure 18. The normalized power at the PDI daughter frequencies, f_1 for the warm LH wave and f_2 for the downshifted EBW, in an entirely inhomogeneous density profile as the pump intensity is increased. The power is found by integrating the spectral density of the longitudinal component of the electric field, E_x , around the PDI daughter frequencies. The FFTs are over $5 \text{ ns} < t < 15 \text{ ns}$. The power of each PDI daughter is normalized to the power of the first point above the theoretically predicted PDI threshold. The plot therefore does not show the relative power between modes. The black solid line is proportional to I_{pump} and the blue dashed-dotted line to I_{pump}^3 . The theoretical inhomogeneous threshold is indicated by the vertical cyan dashed line.

nonlinear trend above the predicted threshold. Below the threshold, the LH daughter wave fluctuates with some large uncertainties on some points while the downshifted EBW daughter wave displays a trend closer to linear dependence on the pump intensity. The figure is further discussed in the following section.

5. Discussion

As shown in section 4, the PIC code EPOCH was able to model nonlinear mode conversion through PDI under conditions similar to those of a magnetically confined fusion plasma. In particular, figure 12 displays a frequency spectrum with side peaks around the pump frequency, resembling that shown in [23]. Because of the homogeneous region 1, the waves could be identified in both f - and k -space, and it was confirmed that all the waves necessary for the PDIs described in section 2 were present. It was assumed that the decay takes place exactly at the UH layer as this is where the pump wave experiences the greatest amplification and the decay is therefore most likely to occur there. Figures 5 and 16 both show that E_x is greatest at the UH layer, and table 1 confirms that the PDI conserves both wavenumber and frequency, i.e. $\Delta_{\text{PDI},0} = (0, 0)$, at the UH layer. However, some of the dispersion relations are very sensitive around the UH layer and the error of the calculated wavenumbers therefore increases a lot. This means that $\Delta_{\text{PDI},0} = (0, 0)$ is found within the error at a range of positions around the UH layer. It was noted that the position of various peaks in k - and f -space shift slightly with pump intensity. The decay may take place whenever the selection rules are satisfied so this shift can be explained by

the pump reaching the PDI threshold further and further away from the UH layer as the intensity is increased. As the wavenumbers depend on position, the selection rules may then require a different frequency shift if the decay takes place at a different position due to the increase in pump intensity. This also explains why the linearly converted EBW appears to fall off quicker than the pump wave at higher pump intensities as less of the pump wave would then make it to the UH layer where the linear conversion takes place. It is also possible that the large amplitude density and temperature fluctuation carried by the EBWs in particular causes the position of the UH layer to shift around. Likewise, a portion of the injected energy may be deposited throughout the domain, causing the temperature to increase and the UH layer to shift. The electron temperature averaged over the entire domain at the end of the FFT window, i.e. at $t = 36$ ns, is increased up to 6% within the error for a relatively high pump intensity simulation with $I_{\text{pump}} = 69 \pm 2 \text{ MW m}^{-2}$. The ion temperature increase is even smaller, 0.5% for the same parameters and they therefore represent fairly small changes to the parameters.

The theoretical predictions are based on a dipole approximation saying that $k_0 = k_1 + k_2 \approx 0$, although [23] notes that this approximation is perhaps not particularly accurate and may be the reason why the predicted frequency shift overshoots as is seen in figures 12, 14 and 15. While table 1 shows that $\Delta_{\text{PDI}} = (0, 0)$ at the UH layer, it also shows that the dipole approximation does not appear to be valid according to the dispersion relations. This is confirmed by the CWT plotted in figure 10 where a dipole approximation would have been appropriate only in the homogeneous region 1 but the significant increase in wavenumber leading up to the UH layer means that k_0 becomes comparable to that of the EBWs. Interestingly, table 1 also shows that another PDI would be possible, namely decay of the linearly converted EBW into the same downshifted EBW and warm LH wave as the other process. This process appears to satisfy both $k_L = k_1 + k_2$ and $f_L = f_1 + f_2$ within the error at the UH layer but also in the homogeneous region 1. Moving the FFT window shown in figure 16 along the propagating returning waves suggests that more of the PDI daughter waves are generated as they propagate through the homogeneous region 1. This indicates that both the X-mode and the linearly converted EBW act as a pump for PDIs in the homogeneous simulations.

As seen in figure 17, the pump wave power near the UH layer is not exactly linear with the injected pump intensity. In particular the pump power is seen to drop off for the two highest pump intensity simulations which suggests that additional wave dynamics take place in the homogeneous region. As the pump intensity is increased, the spectra corresponding to figures 14 and 15 go from showing mainly just the expected dispersion lines and the peaks of interest in this article, to showing several additional peaks and lines. Some of these lines can easily be shown to conserve wave number and frequency in PDI processes involving natural modes and large peaks that are already present in the spectra. This includes mixing of the pump wave, linearly converted EBW and boundary EBW with the first several EBW bands

and harmonics. The first harmonic EBW branches eventually get so smeared out that the notion of individual peaks are lost and even the pump and linearly converted wave drop off significantly. At this point, a stationary state is not reached at the end of the simulation and the description in section 2 is insufficient. The power of the all the waves of interest drop off, perhaps because a secondary PDI threshold has been reached.

The threshold of a homogeneous PDI is generally much lower than that of an inhomogeneous threshold, however, the growth rate of in the homogeneous region is expected to be lower than that of the amplified pump wave in the inhomogeneous region. Placing the FFT window close to the UH layer therefore limits the effects of a homogeneous PDI of the linearly converted EBW. An analysis of the boundary wave in the part of the homogeneous region 1 that is never reached by the returning waves from the UH layer suggests that an EBW may indeed decay into the observed daughter wave. The homogeneous threshold of this process appears to be around the $34.7 \pm 0.1 \text{ MW m}^{-2}$ simulation. By assuming that pump wave and boundary wave are the main contributions to the electric field for $3 \text{ mm} < x < 16 \text{ mm}$ and $25 \text{ ns} < t < 27 \text{ ns}$, i.e. in the leftmost region in figure 16, the threshold of this homogeneous PDI with an EBW as pump is found to be $3.6 \pm 0.5 \text{ MW m}^{-2}$ in terms of the power of the EBW using results from [26, 31]. As the boundary wave is the same as the linearly converted wave, differing only by the sign of k , the homogeneous threshold for the linearly converted EBW is the same. Furthermore, the threshold is the same in terms of the X-mode pump wave, i.e. the horizontal axis in figure 17, since the majority of the pump is converted linearly into EBW at the UH layer for this power level. For this reason, the observed modes have a contribution from both the inhomogeneous PDI of the pump wave at the UH layer and the homogeneous PDI of EBWs. This setup is good for mode identification within the homogeneous region, but the resulting power plot in figure 17 is therefore also affected by contributions from several processes. Because of that, a number of simulations with no homogeneous region at different pump intensities were run and peaks associated with PDI in f -space were still observed and these inhomogeneous simulations resulted in the power plot in figure 18. Modes at the pump frequency are omitted in the inhomogeneous power plot as they cannot be separated, but comparing figures 17 and 18, the latter is easier to read. In both plots, both PDI daughter modes increase nonlinearly with pump intensity although the homogeneous region appears to cause a more aggressive trend. In both plots, the warm LH mode fluctuates and displays no obvious trend below the theoretical threshold whereas the downshifted EBW appears to increase with pump intensity albeit slower than above the threshold. It is noted that the inhomogeneous simulations produced relatively high power levels for the warm LH daughter below the threshold. As seen in figure 15 the general level of the spectrum near the LH frequency is close to the dispersion line of the LH waves, producing a less peaked spectrum which the sometimes large error bars testament. It should be added that frequency is not conserved in PDI for some of the simulations below the

threshold if the frequency of the local maximum in the integration intervals is used. This suggests that some of the relatively large values in the power plot below the threshold are not from PDI. All in all, the entirely inhomogeneous simulations support that the observed inhomogeneous threshold agrees with the theoretical prediction of 14 MW m^{-2} within a margin of 5 MW m^{-2} .

In the simulations, the X-mode pump has a significant longitudinal component on the incoming side of the UH layer but EPOCH can only excite the transverse components which is likely why both an X-mode and an EBW at the pump frequency are excited at the boundary. The amplitude of the EBW is comparable to the X-mode but propagates much slower. If the unintended EBW reaches the UH layer, it may introduce new dynamics and this sets a limit on the length of the simulation and, as a consequence, also a limit on the FFT frequency resolution. A better resolution would require a larger domain but the simulations are already quite expensive. Improving the resolution could potentially allow for identification of smaller peaks in the ion gyro frequency range associated with secondary PDI processes which are expected to be important for higher pump intensities. The 1D approximation may also be problematic considering that the k -selection rule in equation (1a) could have a preferred direction for the PDI daughter waves that might not be possible in 1D. All of this could be the reason for the discrepancy between the observed frequency shifts in experiments and in the simulations of the present article, however, it may also just be due to experimental uncertainty in measured plasma parameters.

To extend the work presented in this article, different density gradient length scales could be compared and the effects of an inhomogeneous magnetic field and temperature profile should be taken into account as well. The location of the UH layer also depends on these parameters and a nonzero gradient length scale for any of the parameters therefore changes the width of the PDI interaction region and thus also affects the threshold. However, as mentioned earlier, an inhomogeneous magnetic field requires a 2D simulation which is outside the scope of this article.

Lastly, some waves appear to actually propagate past the UH layer. In figure 16, a weak wavefront beyond the UH layer in region 3 is seen to appear in the last 10 ns of the simulation. An FFT suggests that the wave propagating is a twice downshifted EBW with $(k, f) = (-k_4, f_4)$ where k_4 and f_4 are as seen in figures 11 and 12. The wave can propagate because it is shifted below the UH frequency at any point of the domain. This is, however, highly dependent on the density profile and does not translate to the experiments in question.

6. Conclusion

For the first time, it was confirmed through mode identification that PIC codes are capable of modeling parametric decay of waves in the EC range of an underdense magnetically confined fusion plasma by reproducing experimental spectra for ASDEX Upgrade relevant plasma parameters. Propagating an X-mode pump to its UH layer produced a spectrum in

f - and k -space with several modes which satisfied the selection rules necessary for PDI. It was confirmed that an X-mode pump can indeed be converted into a downshifted EBW and a warm LH wave near the UH layer. The frequency shift of the downshifted EBW was found to be similar to the observed shift, located between the theoretically predicted shift based on a dipole approximation and a simple LH frequency shift, which provided an upper and lower bound respectively as has previously been noted about experimental data. An upshifted peak corresponding to recombination of the warm LH daughter and the pump was also observed. Additionally, linear X-B conversion was observed and another PDI with the linearly converted EBW as pump was found to occur as well. The EBW pump was able to decay through PDI with a much lower threshold in the homogeneous region where the selection rules of the X-mode pump were not satisfied. The remaining modes displayed shifts in f and k that suggest that they were the products of either similar PDIs or further decay of the products of the PDI of interest. The power of the linearly converted EBW was seen to depend approximately linearly on the pump intensity, I_{pump} , whereas the power of the PDI daughter waves was seen to increase faster than linearly above a theoretically predicted threshold, approximately as I_{pump}^4 for simulations with a homogeneous region and as I_{pump}^3 for entirely inhomogeneous simulations. Below this threshold, the daughter waves depend differently on the pump intensity. This confirms that the suspected linearly converted EBW is created through a linear process whereas the suspected daughter waves are created in a nonlinear process and the threshold of this nonlinear process agrees with the theoretical prediction.

Following the results of this article, PIC codes can be used to study PDI in microwave experiments in magnetically confined plasmas. For future experiments, it is favorable to plan shots to avoid PDI, which simulations like the ones presented here can assist in. One such microwave experiment is 2nd harmonic ECRH. According to [26], a pump wave in a nonmonotonic density profile may decay through a PDI, producing a pair of daughter waves trapped between two UH layers. With each passing at an UH layer, the daughter waves experience a situation similar to the pump wave described here. Another subject of interest is to investigate PDIs from an EBW pump wave. This is of interest in X-B and O-X-B heating schemes as EBWs may be used to heat overdense plasmas but could potentially distribute energy in a much less localized manner. Instabilities like the ones described in this article are expected to be important in future machines such as ITER.

Acknowledgments

This work has been supported by research grant 15483 from VILLUM FONDEN, it has been carried out within the framework of the EUROfusion Consortium and has received funding from the Euratom research and training programme 2014-2018 and 2019-2020 under grant agreement No 633053.

The views and opinions expressed herein do not necessarily reflect those of the European Commission. This work was performed using resources provided by the ARCHER HPC through grant EP/R029148/1, the Marconi HPC, as well as by the Cambridge Service for Data Driven Discovery (CSD3) operated by the University of Cambridge Research Computing Service (<http://csd3.cam.ac.uk/>), provided by Dell EMC and Intel using Tier-2 funding from the Engineering and Physical Sciences Research Council (capital grant EP/P020259/1), and DiRAC funding from the Science and Technology Facilities Council (www.dirac.ac.uk). The datasets used for the figures in this paper can be found at <https://doi.org/10.11583/DTU.9963614>.

ORCID iDs

M G Senstius  <https://orcid.org/0000-0001-9596-7457>

S K Nielsen  <https://orcid.org/0000-0003-4175-3829>

R G Vann  <https://orcid.org/0000-0002-3105-2546>

S K Hansen  <https://orcid.org/0000-0002-5146-1056>

References

- [1] Silin V P 1965 *Sov. Phys.—JETP* **21** 1127 (http://jetp.ac.ru/cgi-bin/dn/e_021_06_1127.pdf)
- [2] Aliev Y M *et al* 1966 *Sov. Phys.—JETP* **23** 626 (http://jetp.ac.ru/cgi-bin/dn/e_023_04_0626.pdf)
- [3] Amano T *et al* 1969 *J. Phys. Soc. Japan* **26** 529
- [4] Piliya A D 1971 *Proc. 10th Int. Conf. Phenomena in Ionized Gases (Oxford)* ed R N Franklin (Oxford: Donald Parsons & Co. Ltd) p 320
- [5] Rosenbluth M N 1972 *Phys. Rev. Lett.* **29** 565
- [6] Piliya A D 1973 *ZhETF. Pis. Red.* **17** 374
- [7] Landau L D and Lifshitz E M 1969 *Course of Theoretical Physics vol 1: Mechanics* 2nd edn (Oxford: Pergamon)
- [8] Falk J *et al* 1978 *Appl. Phys. Lett.* **32** 2
- [9] Gusev G A *et al* 1975 *Radiophys. Quantum Electron.* **18** 7
- [10] Seka W *et al* 2009 *Phys. Plasmas* **16** 052701
- [11] Hendel H W *et al* 1973 *Phys. Rev. Lett.* **31** 4
- [12] McDermott F S *et al* 1982 *Phys. Fluids* **25** 1488
- [13] Porkolab M and Cohen B I 1988 *Nucl. Fusion* **28** 239
- [14] Li J *et al* 2001 *Plasma Phys. Control. Fusion* **43** 1227
- [15] Surkov A *et al* 2005 *32nd EPS Conf. on Plasma Physics* vol 29C (ECA)P-5.103
- [16] Laqua H P 2007 *Plasma Phys. Control. Fusion* **49** R1
- [17] Bongers W A *et al* 2012 *EPJ Web Conf.* **32** 03006
- [18] Nielsen S K *et al* 2013 Experimental characterization of anomalous strong scattering of mm-waves in TEXTOR plasmas with rotating islands *Plasmas Phys. Control. Fusion* **55** 115003
- [19] Kubo S *et al* 2016 *JINST* **11** C06005
- [20] Nielsen S K *et al* 2017 Recent development of collective Thomson scattering for magnetically confined fusion plasmas *Phys. Scr.* **92** 024001
- [21] Hansen S K *et al* 2019 *Phys. Plasmas* **26** 062102
- [22] Gusakov E Z *et al* 2006 *Plasma Phys. Control. Fusion* **48** B443
- [23] Hansen S K *et al* 2017 Parametric decay instability near the upper hybrid resonance in magnetically confined fusion plasmas *Plasma Phys. Control. Fusion* **59** 105006
- [24] Dodin I Y *et al* 2017 *Phys. Plasmas* **24** 032119
- [25] Gusakov E Z and Popov A Y 2010 Low-threshold parametric decay instabilities in the experiments on the electron cyclotron resonance heating in tokamaks and stellarators *JETP Lett.* **91** 655
- Gusakov E Z and Popov A Y 2010 *Pisma Zh. Eksp. Teor. Fiz.* **91** 724
- [26] Gusakov E Z *et al* 2016 *Phys. Plasmas* **23** 082503
- [27] Arefiev A V *et al* 2017 Kinetic simulations of X-B and O-X-B mode conversion and its deterioration at high input power *Nucl. Fusion* **57** 116024
- [28] Fitzpatrick R 2015 *Plasma Physics: An Introduction* (Boca Raton, FL, London: CRC Press, Taylor and Francis)
- [29] Arber T D *et al* 2015 Contemporary particle-in-cell approach to laser-plasma modelling *Plasma Phys. Control. Fusion* **57** 113001
- [30] Lavrinenko A V, Læsgaards J, Gregersen N, Schmidt F and Søndergaard T 2015 *Numerical Methods in Photonics* (Boca Raton, FL: CRC Press)
- [31] Swanson D G 2003 *Plasma Waves* 2nd edn (Boca Raton, FL: CRC Press)

Chapter 5

PDI in non-monotonic density profiles

The results in this chapter have been submitted to the journal *Physics of Plasmas* and has been conditionally accepted for publishing at the time of writing. The submitted version is included at the end of this chapter.

5.1 Summary of the article

5.1.1 The simplified model

In this chapter, we will focus on PDIs that excite slow X-mode and EBWs with reduced power threshold due to trapping in non-monotonous density profiles as was introduced in section 2.4.3. The analytical models outlined in that section rely on several wave interactions which must take place before the experimentally observed signatures of PDIs can be observed. Put differently, the models have many hypothetical steps that connect an injected gyrotron beam to the observed PDI signatures. While the UH layer still plays an important role, it is not the UH layer of the pump wave but instead the UH layer of half frequency waves that lowers the PDI power threshold in this chapter, see figure 2.9 on page 31. This is relevant in particular to second harmonic X-mode ECRH where the gyrotron beam must pass the 2nd harmonic UH layer first.

Using a toy model, we attempt to distill the physics by limiting the number of decays that can take place and favoring particular decays. To this end, we send a wave through a density bump and investigate which trapped waves can be excited in it through PDIs similar to figure 2.10 on page 32. The main objective of the article is to study the initial excitation of trapped waves through PDIs. While the primary decay into trapped waves is different from the PDIs in the previous chapter, the trapped X-mode and EBW daughter waves traveling to and from the UH layers are in a situation akin to the waves in the previous chapter.

5.1.2 Simulation design choices

As was seen in the previous chapter, EPOCH's `simple_laser` boundary condition can lead to the excitation of unintended waves if the intended wave to be injected has a significant longitudinal

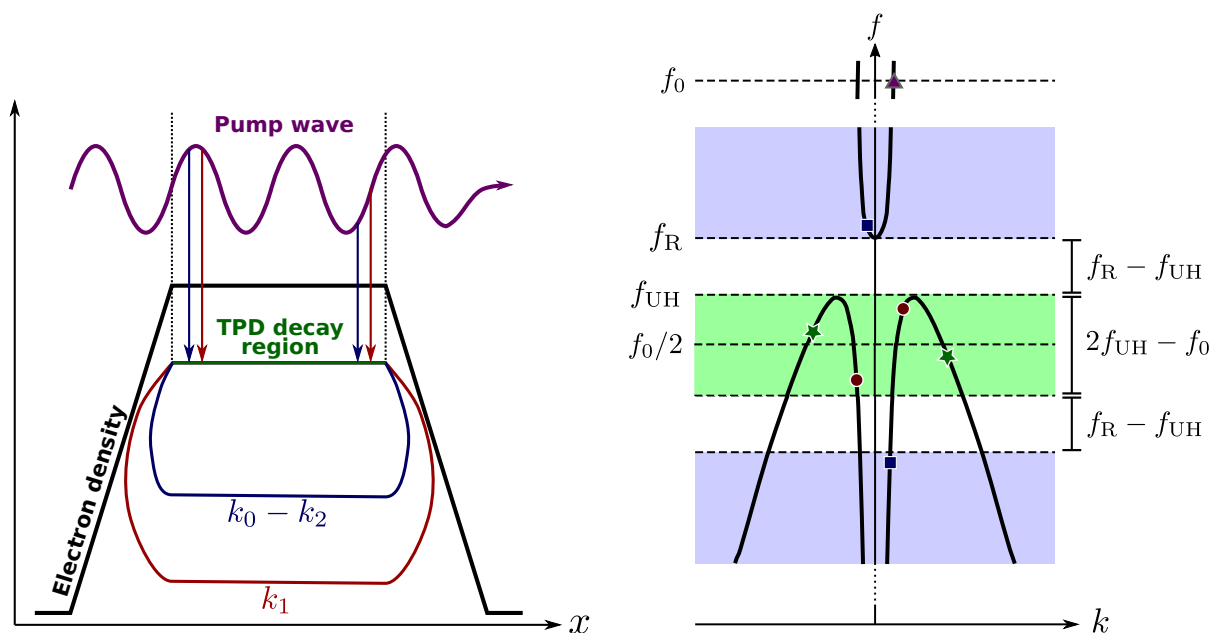
component. Similarly, longitudinal waves leaving the domain cause unwanted reflections with the `simple_outflow` boundary condition. For this reason, the density profiles in this chapter were chosen to be symmetric functions surrounded by vacuum rather than a non-monotonic density perturbation to a typical plasma density profile. For the majority of the simulations a homogeneous region was used at the center of the domain. Whereas a homogeneous region lead to extra PDI's in the previous chapter, they were used here to strongly favor certain PDI's and thereby simplify the analysis, see figure 5.1a.

In this setup, there are two classes of PDI's which can excite trapped waves: a TPD instability as well as an SRS instability. In TPD, the pump wave decays into two UH waves, where the daughter waves can be any combination of slow X-mode and EBWs. For the TPD instability, the peak density of the bump has to be above the 2nd harmonic UH layer of the pump wave such that conservation of frequency allows both daughter waves to be below the UH frequency. For TPD, both daughter waves are trapped in this setup and their growth rates are therefore expected to be significantly increased. In SRS, only one wave is an UH wave whereas the other is a fast X-mode wave. For SRS, the peak density can be lower but the frequency difference between the daughter waves must exceed the frequency gap that separates the UH layer and the R cutoff, see again figure 5.1a. Since the fast X-mode wave can escape, the growth rate of the daughter waves in an SRS instability is not expected to be as greatly increased as in a TPD instability. By choosing a peak density very close to the 2nd harmonic UH layer, the frequency range of daughter waves that can be excited by TPD is limited, see figure 5.1b. In the simulations in this chapter, the green region is much narrower. These considerations are made into figure 4 in the submitted article at the end of this chapter, which gives an overview of what frequencies can be excited at what density. Furthermore, subsequent parametric processes involving the daughter waves are suppressed in the sense that upshifted daughter waves cannot propagate if the resulting frequency is found between f_{UH} and f_R . The majority of the simulations have a peak density just above that of the 2nd harmonic UH layer. Additionally, one simulation is run at twice the density where TPD is also possible, and one at half the density so that only SRS is possible.

For the simulation parameters, the spatial resolution is chosen such that EBWs at half the pump frequency have just over 20 grid points per wavelength. Again, waves with only around 10 gridpoints per wavelength produces similar results. The number of superparticles is chosen such that the pump wave intensity can be reduced several orders of magnitude to study comparably very slow excitation of daughter waves. We ensure ourselves of this by convergence checks with fewer superparticles.

5.1.3 Analysis of data and results

With our simulations, we were able to show excitation of trapped waves both through TPD and SRS, with the former dominating when the selection rules for it are satisfied. A scan of pump intensities showed that the growth rate of the primary decay had a square root dependence on it. Above a threshold daughter wave amplitude, the waves became unstable to other wave interactions. The shape of the density bump was varied from a "hard" profile with a homogeneous region into various smooth but similar profiles and the primary decay showed little dependence thereof in terms of growth rate and further wave interactions. Escaping waves at three halves



(a) Illustration of how TPD into particular modes can be favored by introducing a homogeneous region. Inside the homogeneous region, selection rules may be satisfied for TPD of the pump into two EBWs, k_1 and k_2 . Note that k_2 would have to be the negative solution. The long decay region means that interaction between the daughter waves is much stronger than a process that can decay in the inhomogeneous regions. Compare with figure 2.10.

(b) Illustration of how TPD and SRS can excite waves in bands of frequencies, shown on top of the relevant dispersion curves, see figure 2.3. The pump wave is the purple triangle. The green stars are daughters waves of TPD into two EBWs and the red circles of TPD into two slow X-mode waves. The blue squares are daughter waves of SRS. TPD can occur within the green region and SRS in the blue region. Important frequencies are marked on the left; note that the UH layer is not exactly at f_{UH} . Frequency intervals are marked on the right. The dotted sections of the f -axis represent large jumps in frequency.

Figure 5.1: Illustrations of measures to promote desired PDI into desired trapped waves. Figure (a) shows how a particular PDI may be promoted by introducing a homogeneous region. Figure (b) shows how the range of possible decays can be limited by choosing parameters so that $f_0/2$ is close to f_{UH} .

the pump frequency were observed due to recombination of a primary daughter wave with the pump wave.

In the article, focus was not on the individual eigenmodes of the density bump. With the used parameters, the individual eigenmodes are placed very closely in frequency and even more so near the UH frequency at the density peak as the wavenumber of the UH waves are more sensitive to frequency there. Perhaps for that reason, the growth rates are not significantly affected by the shape of the bump. In chapter 6, simulation parameters are chosen to study eigenmodes in greater detail. Although it was not included in the submitted article, as the article was focused on the primary decay, it should be mentioned that only the high density simulation showed indications of localized peaks possibly due to subsequent PDIs involving ion waves. This shall also be investigated in greater detail in chapter 6.

Numerical investigations of parametric decay into trapped waves in magnetized plasmas with a non-monotonic density background

M. G. Senstius,^{1, a)} S. K. Nielsen,¹ and R. G. L. Vann²

¹⁾*Department of Physics, Technical University of Denmark, Fysikvej, DK-2800 Kgs. Lyngby, Denmark*

²⁾*York Plasma Institute, Department of Physics, University of York, York YO10 5DD, United Kingdom*

(Dated: 15 February 2020)

Parametric decay instabilities (PDIs) exciting daughter waves trapped inside a magnetized plasma with a non-monotonic density profile are investigated numerically. The investigation is motivated in particular by observations of low threshold PDI signatures during 2nd harmonic electron cyclotron resonance heating (ECRH) experiments in magnetically confined fusion experiments. We use the particle-in-cell (PIC) code EPOCH to study conversion of a fast X-mode pump wave into a combination of half frequency X-mode and electron Bernstein waves (EBWs), and identify two regimes where PDIs can excite trapped electrostatic waves. Above the 2nd harmonic upper hybrid (UH) density, a PDI known also as a two plasmon decay (TPD) instability excites a pair of UH waves which we locate in frequency and wavenumber space. At lower densities, a PDI known as stimulated Raman scattering may produce one trapped and one returning X-mode daughter wave with a much slower growth rate than the TPD instability. In both cases, we show that the frequency separation of the daughter waves depends on the density in a predictable manner. With little loss from the decay region, the trapped daughter waves become unstable with respect to secondary parametric instabilities (PIs), leading to distinctly different phases of the UH spectrum. Unlike the primary instability, the secondary PIs are shown to depend on ion dynamics. Furthermore, we observe escaping waves near the $3/2$ pump frequency resulting from tertiary PIs in agreement with recently proposed backscattering during magnetically confined fusion experiments.

I. INTRODUCTION

Parametric instabilities (PIs) are nonlinear wave interaction instabilities of which three-wave interactions form a notable subgroup. These wave interactions occur typically when a strong pump wave is sent through a nonlinear medium such as a plasma, a fluid^{1,2} or a nonlinear optical crystal³. The pump wave may then decay into or combine with natural modes of the medium to produce other waves. A decay instability is typically referred to as a parametric decay instability (PDI). PDIs obey conservation of frequency and wave vector, leading to selection rules which in an inhomogeneous medium may only be satisfied locally. Early work on PDIs⁴⁻⁹ in plasmas showed that the pump wave amplitude threshold in an inhomogeneous plasma could be significantly higher than in a homogeneous plasma due to convection of the daughter waves out of the decay region.

Signatures of PDIs are typically observed in plasmas as emission patterns stimulated by externally launched electromagnetic waves. Such stimulated emission spectra have been observed directly in studies of the ionosphere since the early 1980s¹⁰ where high power radio waves were launched from the ground into the ionosphere and the obtained scattering spectra contained peaks shifted from the injected frequency by natural frequencies of the plasma. Since the waves involved in PDIs depend on the plasma parameters in the decay region, the scattering spectra produced by PDIs can be used to diagnose the ionosphere¹¹. However, the waves launched from the ground might not directly act as pumps for PDIs in the iono-

sphere. Instead, a number of wave conversion processes typically transform the incoming electromagnetic waves into slow X-mode waves which, due to wave amplification at the upper hybrid (UH) layer, can overcome PDI amplitude thresholds at reduced power levels¹². The UH layer also plays an important role in exciting electron Bernstein waves (EBWs) from externally launched waves in O-X-B¹³ and X-B¹⁴ conversion schemes. Amplification in the conversion region can lead to PDIs, which have been observed in low temperature laboratory plasmas¹⁵, and the escaping signatures of the PDIs can be taken as an indication that a strong X-mode wave has made it to the UH layer and that linear conversion into EBWs therefore also has occurred. In magnetically confined fusion plasmas, signatures of PDIs near the UH layer were first observed in the Versator II tokamak during electron cyclotron resonance heating (ECRH)¹⁶. Later, observations have been made at a number of devices including during EBW heating at the Wendelstein 7-AS¹⁷ stellarator and during collective Thomson scattering (CTS)¹⁸⁻²⁰ at the ASDEX Upgrade tokamak.

Although wave amplification of X-mode waves at the UH layer can facilitate PDIs at a reduced power threshold, the amplification is not a necessary condition for the nonlinear wave interactions to become unstable and there are other effects which may lower the PDI power threshold. Numerical simulation of striations in the ionosphere have shown that it is possible to excite UH waves which are trapped in the striations^{21,22}. Because there is little convection out of the trapping region, the trapped waves may become unstable to cascades of PDIs, and the build up of large amplitude electrostatic waves has been proposed as a means of plasma heating. In inertial confinement fusion, the high power lasers used to compress fuel pellets may become unstable to a PDI known as a two plasmon decay (TPD) instability^{23,24} near the quarter critical sur-

^{a)}Electronic mail: mgse@fysik.dtu.dk.

face where half the laser pump frequency corresponds to the plasma frequency. Because the quarter critical surface is close to the 2nd harmonic UH layer, the injected wave experiences no significant amplification and is not trapped but the process still becomes unstable due to the high intensity of the lasers. This PDI was also observed experimentally in the 1980s²⁵ and leads to strong electron heating which in turn deteriorates pellet detonation significantly. Signatures of PDIs have also been observed in tokamaks during 2nd harmonic ECRH where the fundamental UH layer typically is not found inside the confined plasma and the gyrotron beam therefore is not significantly amplified anywhere. Although modern tokamaks and stellarators have installed multiple gyrotrons for heating, current drive and diagnostics, each producing 1 MW beams, traditional estimates for PDI power thresholds during 2nd harmonic ECRH suggest a PDI power threshold on the order of 1 GW and thus far exceed what the gyrotrons are capable of delivering^{26–29}. Still, strong scattering was observed during 2nd harmonic ECRH on the TEXTOR tokamak^{30–32} at a much lower ~ 100 kW gyrotron power. The scattering was observed in the presence of a magnetic island and showed modulation at a frequency matching the island rotation. Similar observations have been made on ASDEX Upgrade^{33,34} in the presence of islands and edge localized modes. This has led to the idea that there is a mechanism that lowers the PDI power threshold in a non-monotonic density profile caused by such structures.

The PDI signatures observed at TEXTOR were peaks shifted in frequency from the gyrotron line by approximately an integer times the lower hybrid (LH) frequency. It was first proposed that the non-monotonic plasma density perturbation caused by the rotating island would allow for ion Bernstein waves (IBWs) near the LH frequency to be trapped inside the island. Theoretical estimates showed that a PDI of the gyrotron into an IBW and a downshifted backscattered wave would have a significantly reduced power threshold^{29,35} whenever the gyrotron passed through the island. However, the model showed slightly different frequency shifts than what was observed experimentally. Later, more elaborate models were proposed^{36–38} involving an initial TPD instability into two trapped half frequency UH waves which further decay through cascades of secondary PDIs into an IBW and an increasingly downshifted UH wave. Secondary daughter waves could then build up and combine into escaping waves in tertiary PDIs, bringing better agreement with the experimental observations to the theoretical models. The models suggest a number of complications to gyrotron operation in non-monotonic plasma density profiles such as a large unintentional power deposition into the islands and excitation of potentially damaging escaping waves at different harmonics of the gyrotron frequency. The non-monotonic density profile can be caused by a number of mechanisms which means that such cascades of PDIs might be common during gyrotron operation across many machines without being noticed simply because no diagnostic is looking for it.

In this article, we use the particle-in-cell (PIC) code EPOCH^{40,41} to study PDIs into one or two trapped UH waves due to a non-monotonic plasma density profile. Using X-mode and EBW dispersion relations, we investigate two pro-

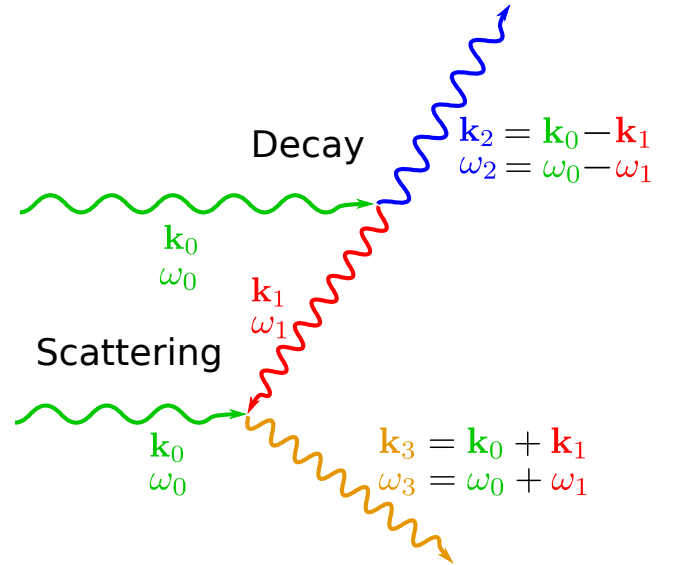


FIG. 1: An illustration of two types of PDIs involving three waves: a decay into two waves, and scattering or combination of two waves. Both satisfy equations (1). As indicated, a long wavelength wave may decay into two short wavelength waves provided that their k -vectors point in different directions; such would be the typical situation for TPD.

cesses, TPD and stimulated Raman scattering, which may produce the trapped waves from an X-mode pump wave. This is the necessary first step of the models explaining the PDI signatures during 2nd harmonic ECRH at tokamaks such as TEXTOR and ASDEX Upgrade. We show that trapped daughter waves of such PDIs can be excited numerically and locate them in frequency and wavenumber space. Examining spectra for different density profiles, we investigate how the frequency of the primary daughter waves depend on them and discuss growth rates for different instabilities. We compare simulations with mobile and immobile ions to confirm that the primary PDIs are independent of ion waves but that the secondary PDIs are not. We look into and confirm numerically that a backscattered $3/2f_0$ wave is generated due to the plasma profile and the trapped waves within it. Lastly, we compare 1D and 2D simulations in terms of their growth rate and show that wave structures, which cannot be excited in 1D, appear in 2D.

II. THEORY OF TPD AND PIC CODES

PDIs can occur whenever a strong pump wave propagates through a medium that has a second order nonlinearity. Conservation of energy and momentum of the waves can be expressed as conservation of frequency, f , and wave vector, \mathbf{k} , leading to the selection rules for the daughter waves

$$f_0 = f_1 + f_2, \quad \mathbf{k}_0 = \mathbf{k}_1 + \mathbf{k}_2, \quad (1)$$

where f_j and \mathbf{k}_j are the frequency and wave vector of the j th wave, see figure 1. Index 0 refers to the pump wave while 1

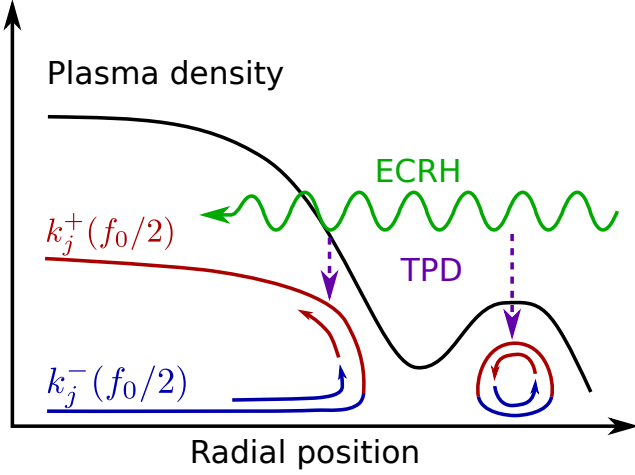


FIG. 2: A sketch showing how a non-monotonic density profile caused by a magnetic island can allow for UH waves to become trapped locally. An ECRH gyrotron beam, aiming for the plasma core, may decay through TPD near the 2nd harmonic UH layer and excite two trapped half frequency waves inside the island. Linear conversion between X-mode and EBWs at the UH layer is the trapping mechanism. In the plasma core, waves can be convected away from the decay region.

and 2 refer to the daughter waves which for the TPD instability will be referred to as the primary daughter waves. The interaction rate depends on the amplitude of all the implicated waves and parametric decay becomes unstable if the decay rate exceeds the losses and convection of the daughter waves inside the decay region where the selection rules are satisfied. This means that decay into waves other than natural modes, which are heavily dampened, is unlikely to occur. Decay into waves that are somehow not lost from the decay region, on the other hand, have a lowered pump amplitude threshold.

In a plasma, electromagnetic and electrostatic waves cause mobile charges, i.e. electrons and ions, to be accelerated by the Lorentz force, generating a current. For large wave amplitudes, the induced current is not linear in the wave amplitude and kinetic effects can then facilitate nonlinear wave interactions such as PDIs. A large amplitude ECRH beam will pass the 2nd harmonic UH layer before it reaches the 2nd harmonic electron cyclotron resonance. Here, thermally excited half frequency UH waves, more specifically slow X-mode and EBWs, may interact with the gyrotron beam if the selection rules in (1) are satisfied. In a monotonic density region, the primary daughter waves are converted and reflected at the UH layer but are free to propagate towards the plasma core. In a non-monotonic density profile caused by an island, multiple UH layers may trap the primary daughter waves in the poloidal direction as displayed in figure 2. Which combination of X-mode and EBWs that will satisfy the conservation rules will depend on local parameters, but in general, \mathbf{k}_1 and \mathbf{k}_2 will be of opposite sign in order to add up to that of the fast X-mode pump wave, which has a comparably low wave number. The primary daughter waves need not be exactly at

half the frequency; a small mismatch in the frequencies is expected but they must add up to that of the pump. As EBWs do not propagate below the electron cyclotron frequency, this is the lower bound for daughter wave frequencies. As the amplitudes of trapped waves build up, the waves can become unstable to secondary PDIs involving LH waves, IBWs and ion acoustic waves which drain the primary daughter waves and thereby saturate the primary instability. Without ion dynamics, the secondary PDIs cannot saturate the primary TPD instability. Lastly, the secondary daughter waves recombine in tertiary PIs to produce the escaping waves shifted in frequency which were observed during experiments; see figure 3 for an overview of the cascade of PIs. In theory, it is also possible for the primary daughter waves to recombine directly with the pump wave to produce escaping fast X-mode waves near $3f_0/2$.

For the pump wave, a cold X-mode description will suffice far from the fundamental resonances. The dispersion relation is given by³⁸

$$k_0 = \frac{2\pi f_0}{c} \sqrt{1 - \frac{f_{pe}^2}{f_0^2} \frac{f_0^2 - f_{pe}^2}{f_0^2 - f_{UH}^2}}, \quad (2)$$

where k_0 and f_0 are the pump wavenumber and frequency respectively, $f_{UH}^2 = f_{pe}^2 + f_{ce}^2$ is the UH frequency, $f_{p\sigma}^2 = q_\sigma^2 n_\sigma / (4\pi^2 \epsilon_0 m_\sigma)$ and $f_{c\sigma} = q_\sigma B_0 / (2\pi m_\sigma)$ are the plasma and cyclotron frequencies for species σ , above species e refers to electrons, q_σ , n_σ and m_σ are the charge, density and mass of species σ respectively, c is the speed of light, ϵ_0 is the vacuum permittivity, and B_0 is the background magnetic field. The primary daughter waves are either fast X-mode or EBWs, both satisfying the dispersion relation^{38,39}

$$k_j^\pm = \frac{1}{\ell_T} \sqrt{-\frac{S}{2} \mp \frac{S}{2} \sqrt{1 + \frac{16\pi^2 f_j^2 (S^2 - D^2)}{c^2} \ell_T^2}}, \quad (3)$$

where $\ell_T^2 = 3v_{Te}^2 f_{pe}^2 / (8\pi^2 [4f_{ce}^2 - f_j^2][f_j^2 - f_{ce}^2])$ with the electron thermal velocity defined as $v_{Te}^2 = 2T_e/m_e$ from the electron temperature T_e , and $S = 1 - f_{pe}^2/(f_j^2 - f_{ce}^2)$ and $D = f_{ce} f_{pe}^2 / [f_j(f_j^2 - f_{ce}^2)]$ being the sum and difference cold dielectric tensor elements as they are called in Stix notation. In the above equation, + refers to an EBW while - refers to X-mode, and the expression is valid near the UH layer, where the two modes coincide. Typically, k_j^\pm is real on one side of the UH layer and complex on the other, and as X-mode waves are forward propagating waves and EBWs are backward propagating waves, one wave incident on the UH layer will convert into the other and reflect.

The PIC code we use in this article is EPOCH⁴⁰. It uses a second order split step routine, updating the electric and magnetic field using discretized Maxwell's equations over a specified grid, and propagating the particle positions and momenta with a relativistic particle pusher. To cut down on the computational demands of pushing every single particle around, particles are represented by a smaller number of clouds of real particles, also known as pseudo- or superparticles. The clouds are modeled using triangular distribution functions.

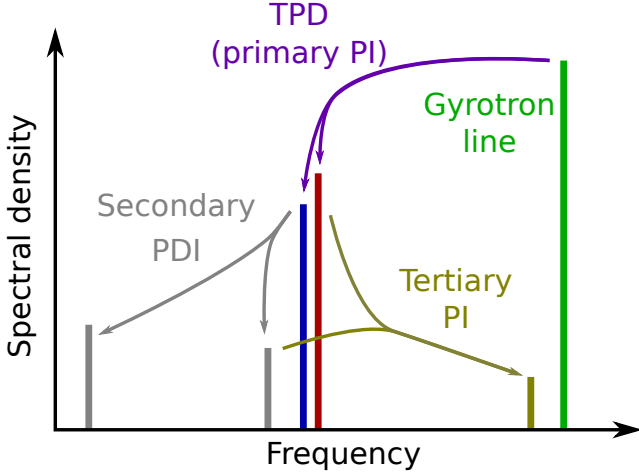


FIG. 3: A sketch of a parametric decay cascade which is initiated by TPD of a gyrotron pump wave. First, two trapped half frequency UH waves are excited through PDI; these are the primary daughter waves. The primary daughter waves may decay further through secondary PDIs involving both UH and LH waves. Lastly, tertiary PDIs may combine excited trapped UH waves into escaping waves, shifted from the gyrotron in frequency.

EPOCH is capable of simulations featuring 1 to 3 spatial dimensions. Regardless of the number of spatial dimensions, all fields have 3 components. The remaining spatial dimensions are assumed homogeneous. PDI has previously been observed in EPOCH simulations of EBW conversion schemes⁴² and of CTS experiments⁴¹.

III. EXCITATION OF TRAPPED DAUGHTER WAVES

Using EPOCH, 1D simulations are devised to investigate the excitation of trapped primary daughter waves of a TPD instability in a deuterium plasma with non-monotonic density profile. The plasma consists of two species, e for electrons and i for deuterons, both assumed to be at a temperature of $T_e = T_i = 100$ eV. The magnetic field is assumed to be constant over the entire domain and pointing perpendicular to the direction of inhomogeneity, $B = B_y = 2.4$ T. A fast X-mode wave is sent from vacuum through a symmetric density bump and out into vacuum again along the x -axis. Inside the density bump, parameters are chosen such that the pump passes the 2nd harmonic UH layer twice and half frequency UH waves excited through TPD are trapped. We choose the frequency of the injected fast X-mode pump wave to be the common gyrotron frequency $f_0 = 140$ GHz used in machines such as TEXTOR, ASDEX Upgrade and Wendelstein 7-X. The primary daughter waves might not both be exactly $f_0/2 = 70$ GHz, so combining equations (1-3), i.e. the selection rules and dispersion relations, and allowing for a daughter frequency mismatch, the possible decays are shown in figure 4. This figure shows that a continuum of X-mode and EBWs around 70 GHz may be excited by TPD. The aim of this article is to validate that decay

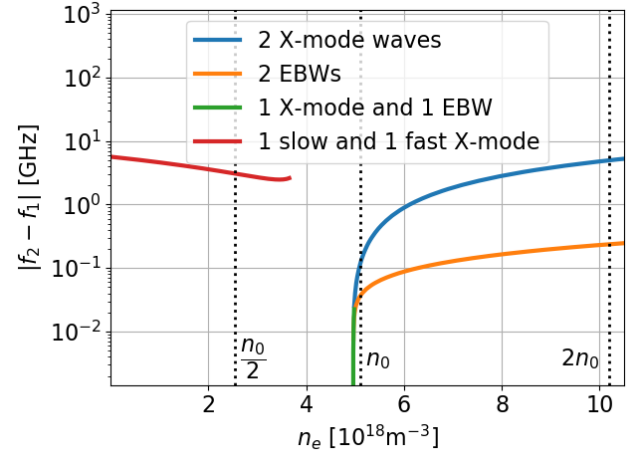


FIG. 4: Frequency mismatch of the primary daughter waves that satisfy the selection rules in equation (1) against density for $B = 2.4$ T and $T_e = 100$ eV. Colored solid lines refer to different types of primary decay daughter waves. Dotted lines mark peak densities in simulations that are run in this article.

into trapped waves occur in agreement with the theory that is distilled into figure 4.

The density profile for the first simulation is chosen to be

$$n(x) = \begin{cases} n_0, & |x| \leq \delta \\ n_0 \left(1 - \frac{|x| - \delta}{\ell}\right), & \delta \leq |x| \leq \delta + \ell \\ 0, & \delta + \ell \leq |x| \leq w \end{cases} \quad (4)$$

where $n_e(x) = n_i(x) = n(x)$, $n_0 = 5.1 \times 10^{18} \text{ m}^{-3}$ is the maximum density inside a homogeneous region of width $2\delta = 10$ mm at the center, $\ell = 4$ mm is the gradient length on either side of the domain over which the density drops linearly from n_0 to vacuum, and $2w = 20$ mm is the total width of the numerical domain. A 1 MW gyrotron beam of width 20 mm corresponds to an intensity of $I_{\text{pump}} \sim 1 \text{ kW/mm}^2$, which is a more convenient quantity to work with in 1D simulations. The pump is excited as an X-mode wave at the left $x = -10$ mm boundary and is allowed to flow out of the right $x = 10$ mm boundary. The pump wave amplitude is ramped up using the amplitude envelope function $\frac{2}{\pi} \arctan\left(\frac{t}{\tau_r}\right)$, where $\tau_r = 0.2$ ns. Particles leaving through the boundary are replaced by identical thermal particles entering the same boundary. This setup is run with $n_x = 1600$ grid points and a total of $n_{\text{part}} = 3 \times 10^4 n_x$ particles.

Figure 5 shows the density profile along with the wave number for UH waves at half the pump frequency. As is required for wave trapping, the X-mode and EBW lines form a closed loop, meeting at the UH layers, which means that a forward propagating X-mode wave reaching one end of the loop will be converted linearly into a backward propagating EBW and vice versa, preventing either from escaping. Due to the homogeneous center region, waves that satisfy the selection rules for $n_e = 5.1 \times 10^{18} \text{ m}^{-3}$ are expected to have the highest growth rate as they are found in their decay region for longer.

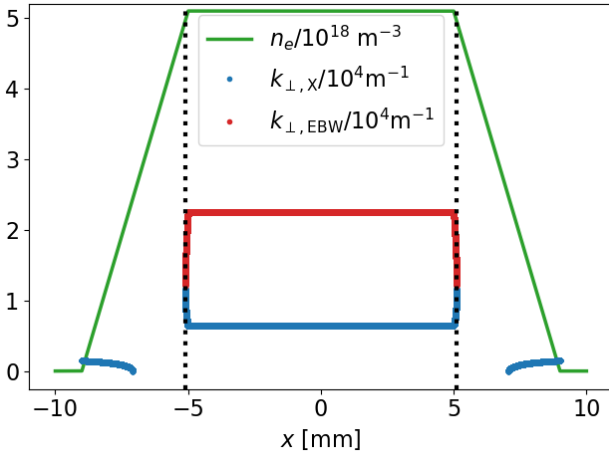
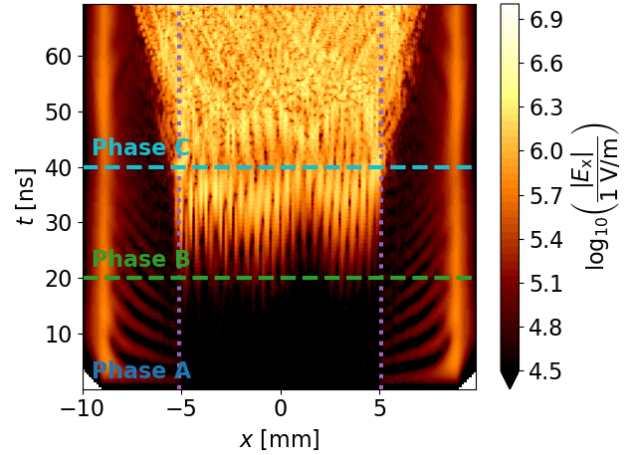


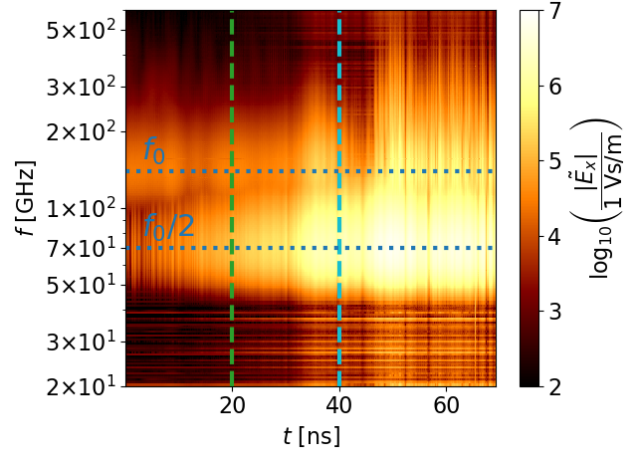
FIG. 5: Density profile for simulations of TPD near the 2nd harmonic UH layer. Red and blue lines are the + and - respectively of equation (3) for $f_j = f_0/2 = 70$ GHz. The electron temperature is $T = 100$ eV, the magnetic field is $B = B_y = 2.4$ T and the black dotted lines mark positions of the UH layer of the trapped $f_0/2$ waves. The pair of daughter waves excited in the homogeneous center have a small frequency mismatch and produce two such loops of different sizes.

This means that a pair of EBWs, 0.04 GHz apart, and a pair of X-mode waves, 0.11 GHz apart, will be dominating the k - and f - power spectrum near 70 GHz.

With the simulation parameters described above and a pump intensity of $I_{\text{pump}} = 1$ kW/mm², EPOCH is run. Whilst EBWs are almost entirely longitudinal, the trapped slow X-mode waves also have a transverse component but near the UH layer, they are mostly longitudinal, making the longitudinal component the component of immediate interest. The simulation produces the time evolution of the longitudinal electric field shown in figure 6a. The temporal evolution of the longitudinal electric field in the homogeneous region, i.e. $|x| \leq 5$ mm, can be separated into three distinct phases. Phase A is the starting phase where plasma noise dominates. Phase B starts roughly at $t \approx 20$ ns where simple wave patterns appear and grow to a level greater than thermally excited longitudinal waves. Finally, phase C starts at about $t \approx 40$ ns when the excited waves turn into more complicated patterns. The phases are indicated by the blue, green and teal labels and lines in figure 6a. It is noted that the excited waves in phase B seem to stay roughly inside the indicated trapping region of 70 GHz waves but in phase C, waves start propagating further out. The waves in phase B are expected to be the trapped primary daughter waves whereas the escaping waves in phase C could be daughter waves of secondary decay processes and will be referred to as secondary daughter waves. The waves will be discussed in greater detail in the next paragraphs. Other noticeable features of the longitudinal field are the slow waves and fields near the boundaries. The frequency is found to be 250 ± 30 MHz $\approx f_{\text{pi}}$ for $x = 7$ mm and



(a) Longitudinal electric field component in time and space. Colored dashed horizontal lines mark the beginning of the phase as labeled above it, used for reference in the text. Dotted vertical purple lines mark the UH layer for 70 GHz UH waves. The slow oscillations outside the homogeneous region are ion waves, see the text.

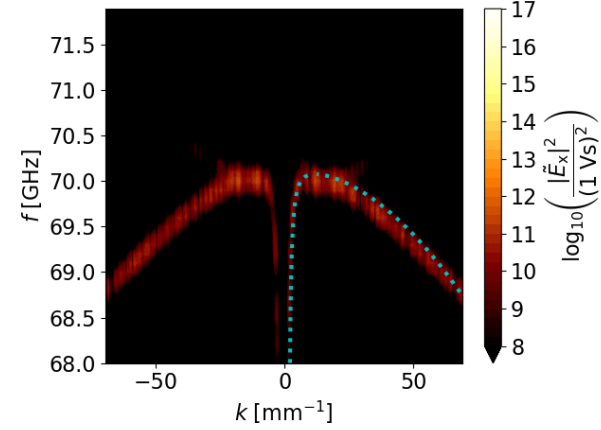


(b) A CWT of figure 6a at the $x = 0$ mm center line. Dotted horizontal blue lines mark frequencies as labeled above them. Dashed vertical lines indicate phases as shown by corresponding colors in figure 6a.

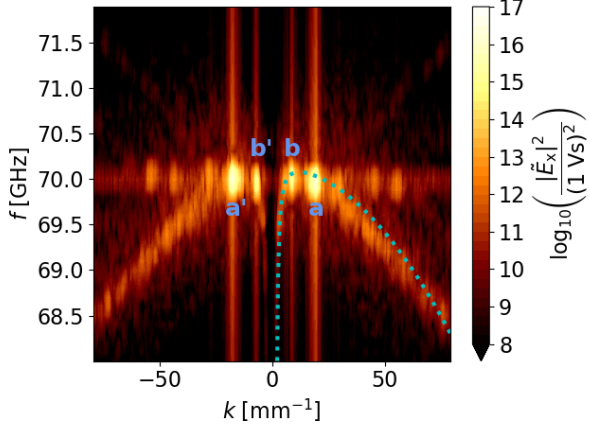
FIG. 6: The longitudinal electric field component resulting from a simulation of the profile shown in figure 5 and a pump intensity of $I_{\text{pump}} = 1$ kW/mm².

$2 \text{ ns} < t < 22 \text{ ns}$ and the oscillations are therefore likely to be ion plasma waves from the ions that are able to travel further out than the electrons. These slow waves, however, are independent of the pump wave intensity and are therefore not the focus of this investigation. Inspecting instead the transverse component, little is seen other than the pump wave and this figure is therefore omitted.

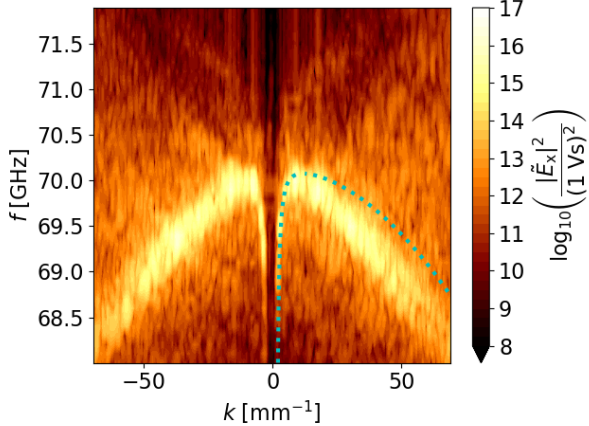
Along the $x = 0$ mm center line, a continuous wavelet transform (CWT) into frequency is applied to the longitudinal electric field and is shown in figure 6b. At the pump frequency, the level is found to be fairly stable until $t \approx 30$ ns. At half the



(a) FFT for $-5 \text{ mm} < x < 5 \text{ mm}$ and the time interval $0 \text{ ns} < t < 10 \text{ ns}$, corresponding to phase A in figure 6a.



(b) FFT for $-5 \text{ mm} < x < 5 \text{ mm}$ and the time interval $25 \text{ ns} < t < 35 \text{ ns}$, corresponding to phase B in figure 6a.



(c) FFT for $-5 \text{ mm} < x < 5 \text{ mm}$ and the time interval $50 \text{ ns} < t < 60 \text{ ns}$, corresponding to phase C in figure 6a.

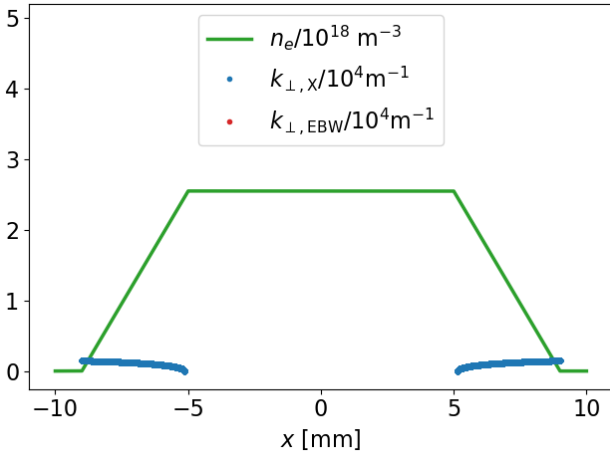
FIG. 7: FFTs into k - and f -space of the longitudinal electric field in the homogeneous region shown in figure 6a during different phases as indicated in the subcaptions. Cyan dotted lines show positive solutions to equation (3). Bold blue letters are labels for nearby peaks mentioned in the text.

frequency, the level is seen to build up several orders of magnitude until the same $t \approx 30 \text{ ns}$ after which a correlated slow oscillatory behavior starts at both pump and half pump frequency. This supports the expectation that the waves in phase B of figure 6a are the primary daughter waves, excited by the pump.

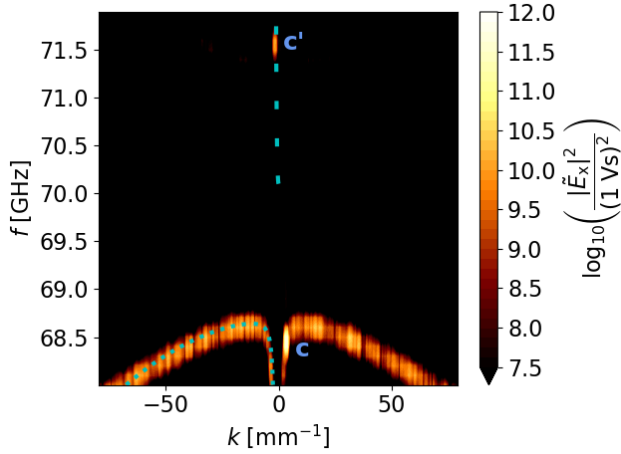
Applying fast Fourier transforms (FFTs) to the longitudinal electric field from x, t into k, f , waves near the UH frequency throughout the homogeneous region are investigated in the phases A, B and C. In phase A, figure 7a, the thermally excited X and EBW dispersion lines are observed. The dispersion relation in equation (3) are also shown in figure 7a. These thermally excited lines are independent of pump intensity.

In phase B, figure 7b, four strong peaks have appeared along the dispersion lines, all with peaks values at $70.00 \pm 0.05 \text{ GHz}$. The peaks are labeled **a**, **a'**, **b** and **b'**. Referring to figures 4 and 5, TPD in the homogeneous should produce a pair of EBWs at 69.98 GHz and 70.02 GHz which is inside the error of the observed EBW peaks labeled **a** and **a'**. TPD could also produce a pair of X-mode waves at 69.94 GHz and 70.06 GHz which is just outside the error margin for the peaks labeled **b** and **b'** and therefore not in agreement with theory. The X-mode peaks may simply be the EBW daughter waves which have been linearly converted at the UH layers. However, visually inspecting the spectra, the X-mode peaks seem slightly shifted in frequency compared to the EBWs which they should not be if they were simply linearly converted. Perhaps the growth rate of the EBWs is greater and this shifts the observed maxima of the X-mode peaks towards 70 GHz . A better resolution might have revealed separate peaks but the rapid evolution of the electric field set a limit on the resolution that can be attained in these spectra.

In phase C, figure 7c, the general level along the X and EBW branches has increased such that it is at the same level as the primary daughter waves in phase C which do not appear to have further increased in intensity. This, along with the figures 6, suggests that the TPD daughter waves have exceeded the threshold of secondary wave interactions, saturating the level of the primary daughter waves. The secondary daughter waves at lower frequencies are able to travel further out of the density bump before it meets the UH layers and this agrees well with observations in figure 6a. The secondary wave interactions might be PDIs involving ion modes which ideally produce distinct peaks all along the UH branches. However, due to the low frequency resolution attainable with such rapid evolution of the spectrum, individual peaks are not observed but rather a general lift of the level throughout the dispersion lines can be seen in this figure. We note that the EBW branches no longer follow the dispersion relation based on initial parameters, possibly because the excited waves modify the electron distribution function. Averaging the electron temperature in the homogeneous region as provided by EPOCH does indicate an increase which produces a better fitting dispersion line. Electron heating due to high amplitude UH waves has previously been reported in simulations²¹. Comparing FFTs of the transverse electric field in the outer homogeneous side regions, i.e. for $|x| \geq 9 \text{ mm}$ in figure 5, the transmitted pump intensity drops by about 10% during the primary instability,



(a) A density profile where half frequency UH waves cannot propagate in side and TPD is therefore not possible. Waves at lower frequencies may still be trapped inside the density bump.



(b) k - and f -space for $55 \text{ ns} < t < 65 \text{ ns}$ with the profile shown in figure 8a and an intensity of $I_{\text{pump}} = 10 \text{ kW/mm}^2$; one trapped, **c**, and one escaping wave, **c'**, are excited. The dotted cyan line in the lower half shows dispersion lines for trapped wave in negative k , equation (3), while the more spaced out dotted line in the top half indicates escaping X-mode waves in negative k , equation (2). This spectrum is not directly comparable to figure 7c due to a change in both density and pump intensity.

FIG. 8: Density profile and FFT spectrum of the longitudinal electric field for a simulation where TPD is not possible, compare with figure 5.

suggesting that a significant amount of energy might be absorbed in such a non-monotonic density profile.

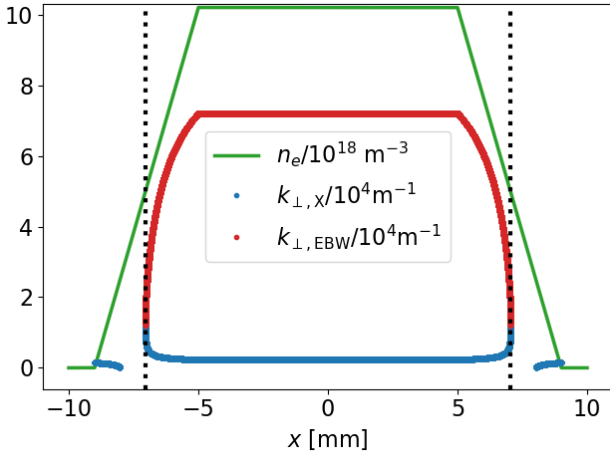
To support the idea that the waves discussed above are excited through a TPD instability, a simulation at half density is run. The density profile is shown in figure 8a and since the UH frequency for this profile is 68.6 GHz in the homogeneous region, $f_0/2 = 70 \text{ GHz}$ X-mode and EBWs do not propagate there and it is therefore not possible for the pump to decay through TPD into two trapped UH waves. Looking

at figure 4, decay into one trapped UH wave and one escaping electromagnetic wave is possible. This type of parametric decay is also known as stimulated Raman scattering²⁸ and is expected to have a lower growth rate since one of the daughter waves is convected away from the decay region, similar to Ref. 39. At the pump intensity used for the previous simulations, there were indications of a trapped daughter wave but its growth rate was rather small and would require a very long simulation to be run. Therefore the simulation was run again with the pump intensity increased by a factor of ten to $I_{\text{pump}} = 10 \text{ kW/mm}^2$ and an FFT spectrum at a relatively late $55 \text{ ns} < t < 65 \text{ ns}$ is shown in figure 8b. As the density has been decreased, the UH layer is now found at a lower frequency and the dispersion lines are found lower in the plot compared to the previous simulation. The spectrum shows a peak on the positive slow X-mode branch at $68.45 \pm 0.05 \text{ GHz}$, labeled **c**, and one fast X-mode peak at $71.55 \pm 0.05 \text{ GHz}$, labeled **c'**. From figure 4, decay in the homogeneous center region produces the same types of waves at frequencies 68.47 GHz and 71.53 GHz , which agrees well with observations. We note that the scale in figure 8b is different from figure 7c in spite of a greater pump intensity, confirming that this decay has a much lower growth rate. However, 70 ns is a very short window of time assuming that the non-monotonic density profile is caused by MHD modes.

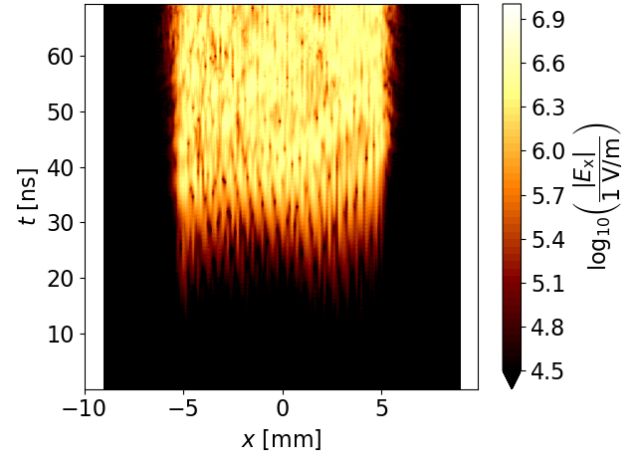
Raising the density, on the other hand, should still allow for TPD to take place as indicated by figure 9a where the density has been doubled. The resulting spectrum in figure 9b now shows a situation where the UH layer is at higher frequency. Once again, there are two X-mode and two EBW peaks near 70 GHz . This time equations (1-3) predict a pair of EBWs at 69.88 GHz and 70.12 GHz and that the low frequency wave has positive k , which agrees with the observed $69.90 \pm 0.05 \text{ GHz}$, **d**, and $70.10 \pm 0.05 \text{ GHz}$, **d'**, with the lower frequency wave corresponding to positive k . However, the pump may also decay into two X-mode waves at 67.44 GHz and 72.56 GHz , the high frequency one having positive k , which are not observed, possibly due to a lower growth rate. The X-mode peaks that are observed, **e** and **e'**, lie at the same frequencies as the observed EBW peaks, suggesting that these are simply linearly converted from the EBWs.

IV. EFFECT OF IONS ON FURTHER DECAY PROCESSES

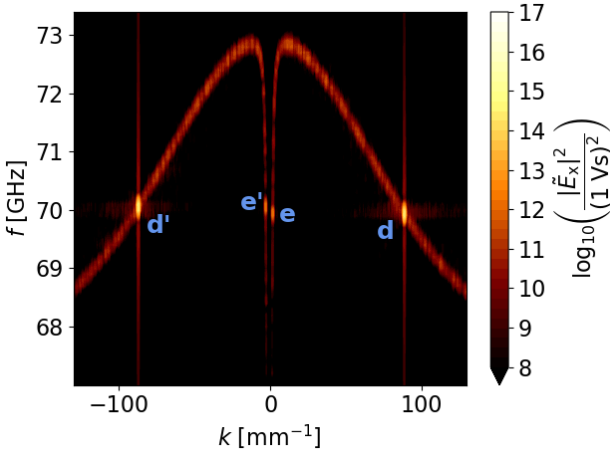
The TPD instability involves only electron waves and therefore should not depend on ion motion. The secondary PDIs, which were seen to populate the lower frequency parts of the UH spectrum shown in figure 7c, are expected to be an interaction between UH waves and ion waves, such as LH, Ion acoustic or IBWs, which gradually downshift the trapped waves. Without ion dynamics, the secondary PDIs therefore should not take place. To confirm this, the simulation presented in figures 5 - 7 is rerun but with the ions taken out of the particle pusher algorithm, making them immobile. As a result, ion waves will not be able to propagate and parametric instabilities involving wave dynamics will not be observed. Looking at the temporal and spatial evolution of the longitudinal elec-



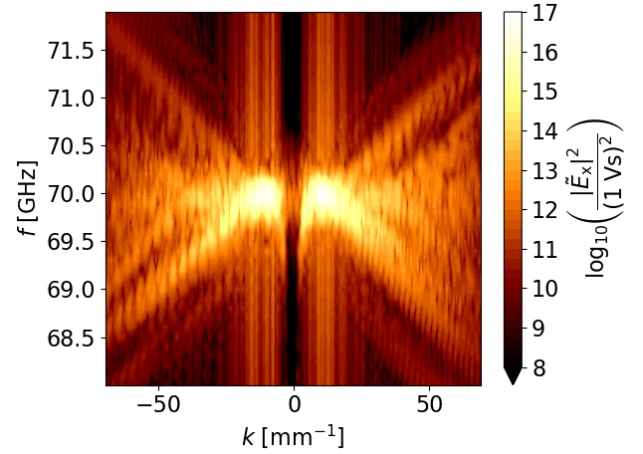
(a) Density profile with the red and blue lines being the + and - respectively of equation (3) for $f_j = f_0/2 = 70$ GHz. The UH layers are indicated by the vertical dotted lines.



(a) Evolution of the longitudinal electric field for immobile ions in time and space, compare with figure 6a where plasma parameters are the same but ions are mobile.



(b) k - and f -space for $I_{\text{pump}} = 1 \text{ kW/mm}^2$ and $25 \text{ ns} < t < 35 \text{ ns}$ like in figure 7b. Bold blue letters are labels for nearby peaks mentioned in the text.



(b) k - and f -space for $50 \text{ ns} < t < 60 \text{ ns}$, compare with figure 7c where plasma parameters are the same but ions are mobile.

FIG. 9: Density profile and FFT spectrum of the longitudinal electric field for a simulation with a higher density setup further from the 2nd harmonic UH layer, compare with figure 5.

FIG. 10: Resulting longitudinal electric field from a simulation with immobile ions. Parameters are otherwise identical to those in figure 5.

tric field in figure 10a, the slow oscillations near the boundaries that were seen in figure 6a have now disappeared, confirming that they were ion waves. The TPD daughter waves are still excited as they should since they are three wave interactions between electron waves. The third phase, where other wave interactions come into play and the waves start spreading out, is not seen in this simulation, confirming that it is PDIs involving both electron and ion waves that cause the cascading of energy to lower frequency. Comparing figures 7c with 10b, it is seen that without the ion dynamics, the waves excited from TPD still clearly stand out and their peaks have continued to grow as the saturation mechanism provided by

interactions with ion waves is no longer possible.

V. DENSITY PROFILE HAS LITTLE EFFECT ON GROWTH

Up until this point, it has been assumed that TPD was taking place in the homogeneous region because this is where the pump intensity threshold is lowest. In the following, we compare the hard density profile from before to a number of inhomogeneous profiles seen in figure 11 to investigate the effect of the density profile on the decay rate. Furthermore, the size of the trapping region is varied by changing the profile to see if that has any influence on the temporal evolution of

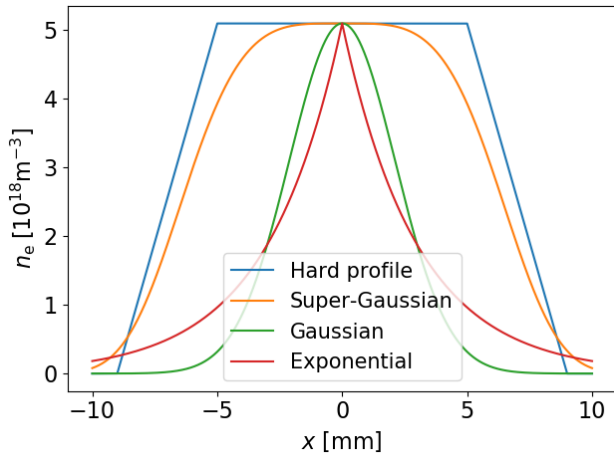


FIG. 11: Different density profiles to be compared. The hard profile refers to the simulation based on figure 5. The remaining profiles are of the form $n(x) = \exp(-|x/\ell_n|^\gamma)$ with the relevant parameters shown in table I. Resulting longitudinal fields using an intensity of $I_{\text{pump}} = 1 \text{ kW/mm}^2$ are shown in figure 12.

Profile	γ	ℓ_n [mm]
Super-Gaussian	4	7
Gaussian	2	3
Exponential	1	3

TABLE I: Parameters for the density profiles in figure 11 which are on the form $n(x) = \exp(-|x/\ell_n|^\gamma)$. Resulting longitudinal fields using an intensity of $I_{\text{pump}} = 1 \text{ kW/mm}^2$ are shown in figure 12.

the trapped waves. All the inhomogeneous profiles are on the form $n(x) = \exp(-|x/\ell_n|^\gamma)$ where ℓ_n and γ are listed in the table I.

The super-Gaussian profile is very similar to the hard profile, being essentially homogeneous in the center. Comparing figures 12a, which is a cropped duplicate of 6a, and 12b, the dynamics are also very similar albeit the TPD waves are confined to a narrower region as the UH layers of $\sim 70 \text{ GHz}$ waves are closer than in the hard profile. For the Gaussian profile in figure 12c, the center can no longer be considered homogeneous over a 70 GHz X-mode wave but the TPD daughter waves still build up to the same level, on the same time scale and with the same three phases placed roughly at the same times. As the bounce time of the TPD daughter waves is greatly reduced by going from the hard profile to the Gaussian, this suggests that the growth rate of TPD daughter waves inside the density bump is largely independent on the homogeneous region and on the size of the density bump. The TPD theory that is believed to explain the strong scattering during 2nd harmonic ERCH^{29,38} is based on excitation of eigenmodes of the profile which satisfy conditions on the wave vector similar to Bohr-Sommerfeld quantization. By choosing a profile such as figure 5, we have made decay into the homogeneous region more favorable, i.e. primary daughter waves

which might not be eigenmodes. However, the time evolution of the longitudinal field in the Gaussian profile, where one would expect decay into eigenmodes to dominate, does not show any sign of a reduced growth rate. Finally, for the exponential profile in figure 12d, the peak density does exceed that of the UH layer for 70 GHz waves but it would appear that the UH layers are so close that the daughter waves are not supported inside density bump and no build up of waves is observed.

VI. PUMP INTENSITY COMPARISON

By scanning the pump intensity of the density profile shown in figure 5, the growth rate of the first TPD daughter waves is investigated. Averaging the square longitudinal electric field over the homogeneous region, the time evolution of the resulting signal is assumed to first be dominated by a background level due to plasma fluctuations followed by a phase where an absolute instability gives rise to an exponential growth. Eventually, other processes become important but only the growth rate of the initial TPD instability is sought so a function of the form $\phi(t) = \langle E_0^2 \rangle + a \exp(2\gamma_{\text{TPD}} t)$ is fitted to the mean squared longitudinal electric field up until it reaches a level of 10^{10} (V/m)^2 . Figure 13a shows a number of signals for different pump intensities with ϕ fits. As a general feature, the squared mean fields start at a constant level which is seen to vary with pump intensity. An exponential growth takes over next, growing several orders of magnitude. Lastly, the field overshoots a threshold level and saturates at a lower level, arguably because threshold levels of secondary PDIs saturate the growth inside the homogeneous region. The overshoot also depends on pump intensity but they appear to relax, following the same asymptotic curve. Plotting the fitted growth rates against pump intensities in figure 13b, they are found to go as $2\gamma_{\text{TPD}} \propto I_{\text{pump}}^{0.5}$. This agrees with Ref. 38 if the pump is assumed to be of infinite width but finite intensity. A similar approach applied to the low density simulation presented in figure 8, where Raman scattering was observed instead of TPD, gives a growth rate of $\gamma_{\text{TPD}} = 5.0 \times 10^{-2} \text{ ns}^{-1} = 5.7 \times 10^{-5} (2\pi f_0)$ at an increased pump intensity of $I_{\text{pump}} = 10 \text{ kW/mm}^2$.

VII. ESCAPING WAVES

Once the primary daughter waves have been excited, they can interact with other waves in the plasma. One of the simplest wave interactions to observe is recombination with the pump wave. The resulting wave would be an escaping X-mode wave at approximately $3/2 f_0 = 210 \text{ GHz}$. The possibility of observing the $3f_0/2$ signal due to trapping of TPD daughter waves in a magnetically confined plasma has also been proposed analytically⁴³. On one hand, the escaping $3f_0/2$ waves provide a diagnostic opportunity as indications of trapped waves may be observed without having to look near the pump frequency where stray radiation from the gyrotron can damage sensors. While backscattered waves in the pump

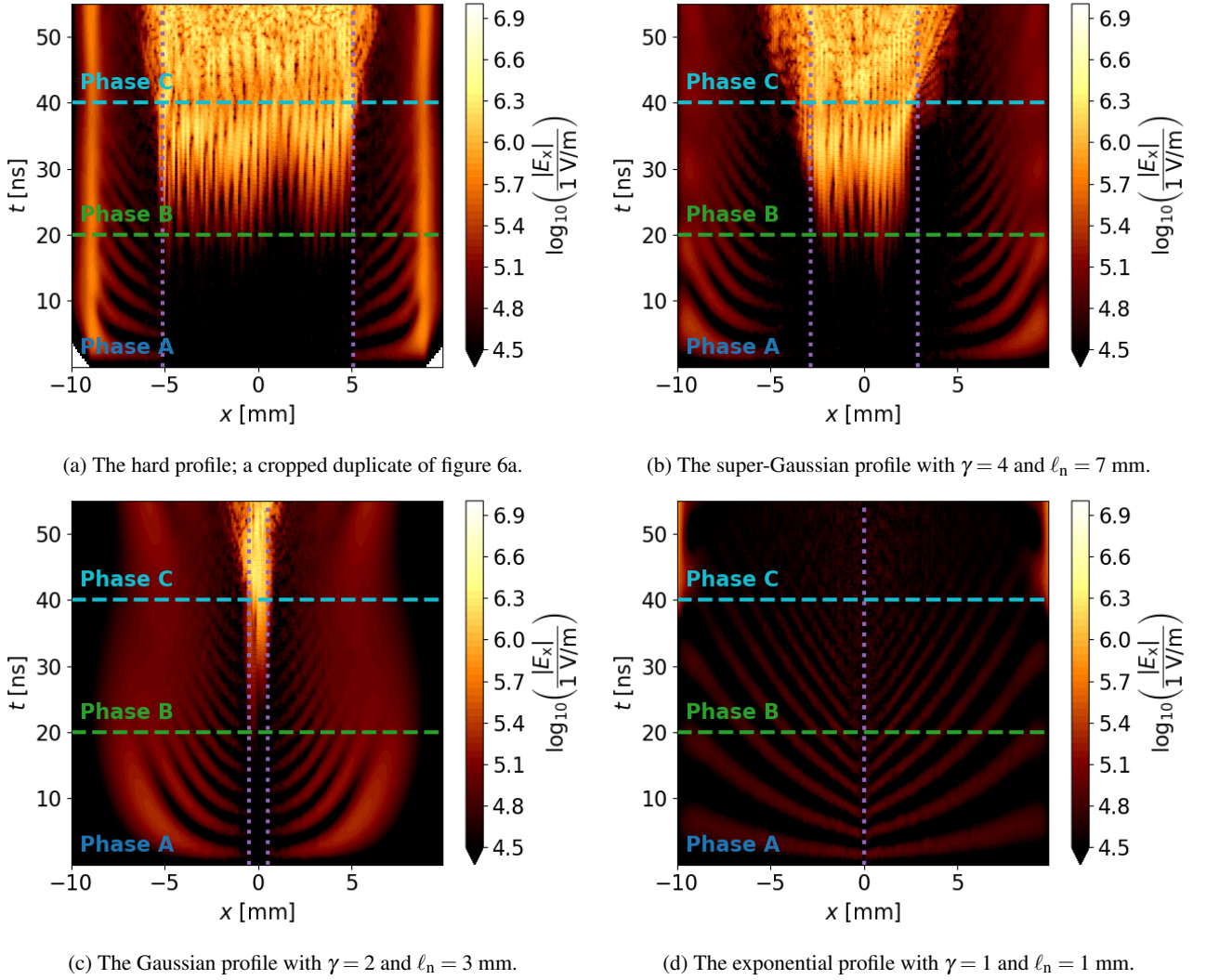


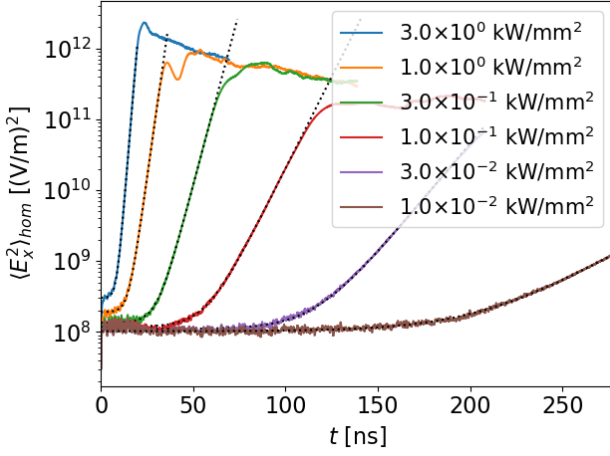
FIG. 12: Evolution of the longitudinal electric field in time and space for four density profiles shown in figure 11. The marked phases refer to the phases observed in figure 6a whilst the purple lines conform to the individual plots, showing the confines of the trapping region for 70 GHz waves.

frequency range is the result of tertiary PIs, the $3f_0/2$ waves are the result of just 2 PIs, both involving the strong pump wave, and may therefore provide a more direct indication of trapped UH waves. On the other hand, the escaping waves pose a risk for detectors that happen to be sensitive to the particular frequency range, but might not be taking radiation due to PIs into account.

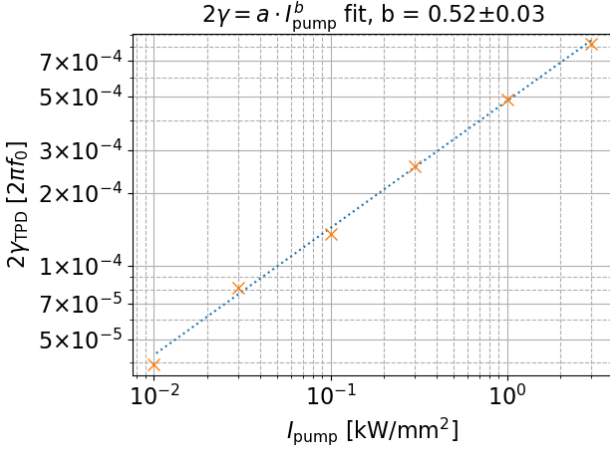
The difference in k for such a process, $\Delta k = k_0 + k_1 - k_{210}$, can be seen in figure 14a for left and right propagating escaping waves as a function of TPD daughter frequency. A match, i.e. $\Delta k = 0$, is only possible for a left propagating wave, escaping back where the pump came from. Figure 14b shows a comparison of the f -spectrum near 210 GHz at the boundaries of the domain. Both spectra display similar trends except in the immediate vicinity of 210 GHz where a large peak is present in the spectrum at the left boundary, agreeing with the k -match analysis.

VIII. 2D SIMULATIONS

The presented simulations have until now been 1D. Besides the concern that homogeneous regions would lead to excitation of primary daughter waves which were not eigenmodes, PDIs were restricted to the k -match condition $|k_0| = |k_1 \pm k_2|$. Through simple geometric arguments, it can be shown that if the inequalities $|\mathbf{k}_0| \leq |\mathbf{k}_1| + |\mathbf{k}_2|$ and $|\mathbf{k}_0| \geq ||\mathbf{k}_1| - |\mathbf{k}_2||$ both are satisfied, it will be possible to find a set of angles in 2D such that k -match is possible. This means that TPD can lead to wave propagating at a continuum of angles, perhaps allowing for other decay into eigenmodes to take place in the presence of a homogeneous region. A 2D simulation is devised to investigate if new wave dynamics arise with an additional dimension to propagate in. For this simulation, an initially entirely homogeneous y -direction has been added. The domain



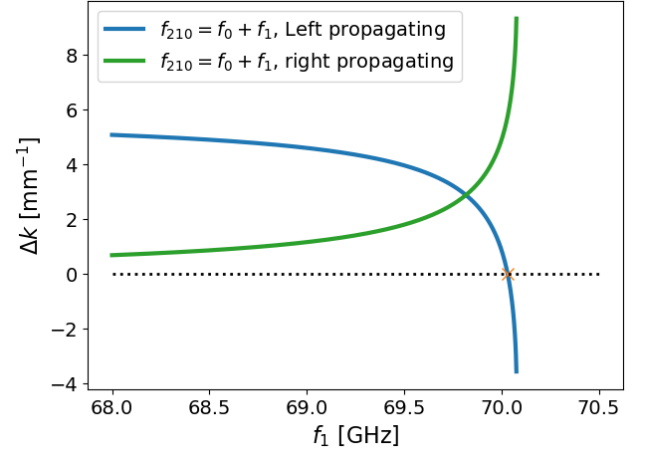
(a) Mean squared longitudinal electric field averaged over the homogeneous center of the domain for a number of pump intensities. The plotted curves are averaged over 50 time steps. The dotted black lines are fits of the form $\phi(t) = \langle E_0^2 \rangle + a \exp(2\gamma_{\text{TPD}} t)$.



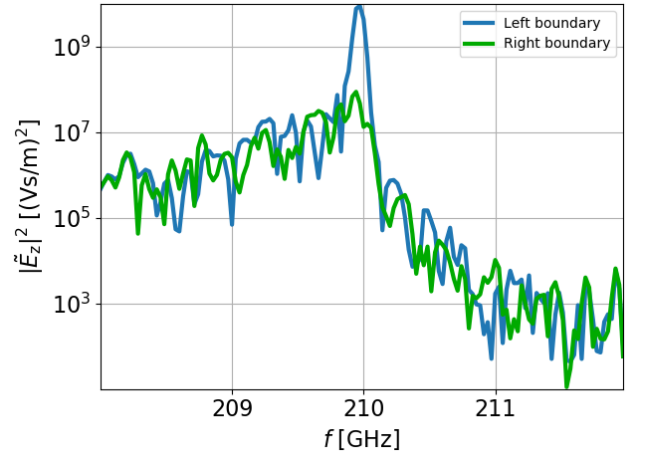
(b) A plot of the fitted growth rates in figure 13a against pump intensity shown with orange crosses. The dotted blue line is the fit indicated above the plot.

FIG. 13: A scan of pump intensity for the profile shown in figure 5. The for each simulation, the growth rate of the primary decay instability is determined and a power law is fitted to the found growth rate plotted against the pump intensity.

width along the y -direction is $w_y = 1.0375$ mm with $n_y = 83$ grid points and periodic boundary conditions. This way, the longest expected TPD daughter wave can fit inside and the grid size remains unchanged. The direction of the magnetic field is changed to point in the z -direction, i.e. $B = B_z$, so that both the x - and y -directions are perpendicular to the magnetic field. The pump wave has to be transverse so its electric field is now polarized in the y -direction. Parameters along the x -direction are kept mostly unchanged with the exception of the number grid points now given by $n_{\text{part}} = 3 \times 10^3 n_x n_y$. For an



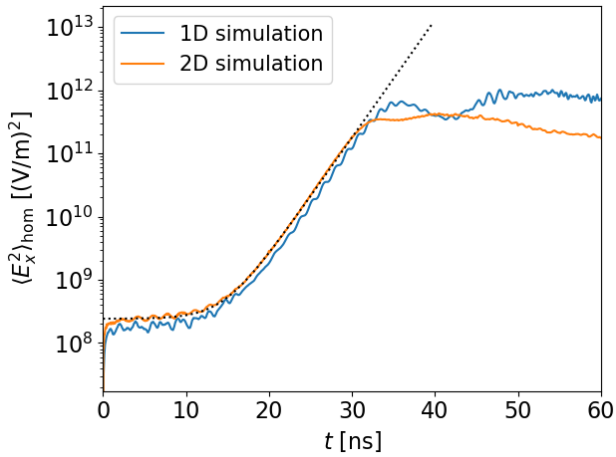
(a) A plot of the necessary k -match condition for left and right propagating ~ 210 GHz waves in the homogeneous region of the profile shown in figure 5. The y -axis shows $\Delta k = k_0 + k_1 - k_{210}$ and $\Delta k = 0$ means that the selection rules are satisfied, this is marked by the horizontal dotted black line and an orange cross shows the intersection with the left propagating blue line.



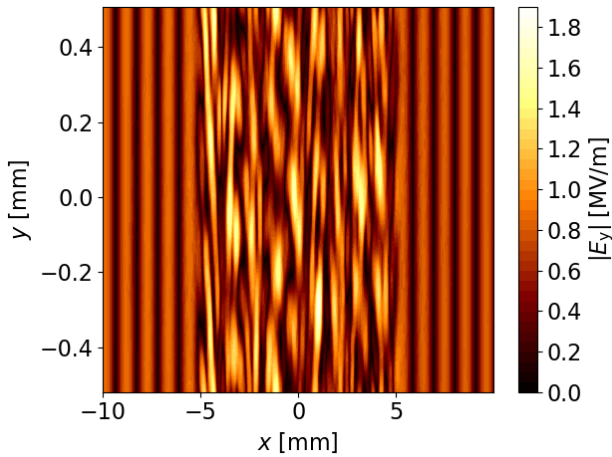
(b) The f -spectrum at the boundaries of figure 5 for $25 \text{ ns} < t < 60 \text{ ns}$ near the $3/2 f_0$ frequency. A much higher peak is present on the left boundary, corresponding to back scattering.

FIG. 14: Justification for and observation of $3/2 f_0$ frequency backscattering for the profile shown in figure 5 and the simulation shown in figure 6a.

intensity of $I_{\text{pump}} = 1 \text{ kW/mm}^2$, the growth rate is estimated in the same manner as was discussed in section VI, averaging now not only over $-5 \text{ mm} < x < 5 \text{ mm}$ but also along the entire y -axis. Unlike 1D, which used all available data point, the 2D fit is applied to a signal sampled with a time step of 0.05 ns due to the increase in data size but this time step should be sufficient for the targeted time scale. As is seen in figure 15a, allowing waves to propagate at an angle to the pump does not change the growth rate significantly. Figure 15b, however, shows that waves with wave vector components in the y -direction are also excited. These waves might



(a) Mean squared x -component of the electric field averaged over the homogeneous center of the 2D domain for a simulation with a pump intensity of $I_{\text{pump}} = 1 \text{ kW/mm}^2$. The mean squared field is compared to a 1D simulation of similar parameters and the growth of the 2D simulations is fitted with an exponential function. The growth rate is found to be $2\gamma_{\text{TPD}} = 4.3 \times 10^{-1} \text{ ns}^{-1} = 4.9 \times 10^{-4} (2\pi f_0)$ for the 2D simulation.



(b) A snapshot of the y -component of the electric field at $t = 30 \text{ ns}$, after the primary daughter waves have visibly formed. Note that the scales on the x - and y -axes are not the same. Unlike the pump wave, the trapped waves not only propagate in the x -direction. Compare to the 1D figure in figure 6a.

FIG. 15: 2D simulations using parameters similar to figure 5 but with a narrow periodic y -direction and the magnetic field pointing in the z -direction.

not contribute much to the estimated growth rate if they are longitudinal. It is, nevertheless, more challenging to include them in the growth rate as the presence of the pump wave elevates the background level significantly, making the growth of an instability less apparent. As suggested by figure 15a, a more stochastic saturated phase similar to phase C in figure 6a and 7c follows at greater t , suggesting that 1D simulations

capture the primary and secondary PIs of this 2D simulation to a fair degree. Future 2D simulations should explore the effect of a dimension parallel to the magnetic field. This should not affect the primary instability much as the implicated waves are transverse and longitudinal, however, secondary daughter waves may benefit from being able to propagate at an oblique angle to the magnetic field. Similarly, pump waves incident at an angle and finite bump size in both dimensions should be explored.

IX. CONCLUSION

Using the PIC code EPOCH, we have demonstrated that an X-mode pump wave can excite half frequency trapped daughter waves through TPD, provided the UH frequency exceeds the daughter wave frequencies. Even when the UH frequency is just below half the pump frequency, stimulated Raman scattering may excite trapped daughter waves, albeit at a much lower growth rate. Trapping implies that the daughter waves can build up and become unstable at low pump intensities as they are not convected out of the decay region. In particular 2nd harmonic X-mode ECRH is at risk of exciting trapped TPD daughter waves if the gyrotron beam passes a non-monotonic region, which may be due to islands, filaments or other mechanisms.

For the first time, we have numerically validated the recent hypothesis that non-monotonic fusion plasmas may facilitate PDIs at a reduced gyrotron power thresholds using fully kinetic simulations. A comparison of shapes and sizes of density profiles showed unexpectedly that absorption of gyrotron power into trapped waves can occur even in structures smaller than 1 cm and that the addition of a homogeneous region had little effect on the growth rate of the primary instability. We found that the transmission of the pump intensity dropped by about 10% during the primary instability. For a 1 MW gyrotron, this could potentially account for a significant waste of energy which is deposited in the wrong parts of the plasma. We characterized the growth rate of the primary instability versus pump intensity in 1D and found an approximate square-root dependence. There was no sign of a low pump intensity threshold.

Extending to 2D with another dimension perpendicular to the magnetic field did not affect the growth rate significantly. For gyrotron power levels, the simulations show a fast initial TPD growth time scale on the order of 10 ns. The primary instability saturates on the order of 100 ns due to secondary PDI. The secondary PDI depend on ion dynamics, coupling to IBWs to populate UH waves at various frequencies.

We show that the primary daughter waves are able to recombine with the pump into waves at $\sim 3/2f_0$ which are not trapped but instead travel back where the pump wave came from. This may pose a problem for microwave sensitive equipment not shielded against such waves but could also provide a means of diagnosing the trapped waves without having to measure in the frequency range of the pump, where stray radiation from a gyrotron could easily cause trouble.

In conclusion, we have demonstrated that TPD of ECRH

beams can occur in small scale density perturbation of magnetically confined fusion plasmas at power levels typically applied in present day experiments. This can potentially modify power depositions profiles and hamper microwave diagnostics. In the light of the present article, it is now possible to assess such concerns in fusion experiments.

X. ACKNOWLEDGMENTS

This work has been supported by research grant 15483 from VILLUM FONDEN and the Enabling Research grant ENR-MFE19.DTU-03 from the EUROfusion Consortium. The work has been carried out within the framework of the EUROfusion Consortium and has received funding from the Euratom research and training programme 2014-2018 and 2019-2020 under grant agreement No 633053. The views and opinions expressed herein do not necessarily reflect those of the European Commission. This work was performed using resources provided by the ARCHER HPC through grant EP/R029148/1, the Marconi HPC, as well as by the Cambridge Service for Data Driven Discovery (CSD3) operated by the University of Cambridge Research Computing Service (<http://www.csd3.cam.ac.uk/>), provided by Dell EMC and Intel using Tier-2 funding from the Engineering and Physical Sciences Research Council (capital grant EP/P020259/1), and DiRAC funding from the Science and Technology Facilities Council (www.dirac.ac.uk).

XI. DATA AVAILABILITY

The data that support the findings of this study are openly available in DTU Data at <http://doi.org/10.11583/DTU.11847174>, reference number 44.

REFERENCES

- ¹M Faraday Philos. Trans. R. Soc. London **121**, 319 (1831)
- ²C M Topaz, J Porter, and M Silber 2004 Physical Review E **70**, 066206
- ³A A Sukhorukov, Yu S Kivshar, O Bang, and C M Soukoulis 2000 Physical Review E **63**, 016615
- ⁴V P Silin 1965 Sov. Phys. JETP **21** 1127
- ⁵Yu M Aliev, V P Silin, and C Watson 1966 Sov. Phys. JETP **23** 626
- ⁶T Amano and M Okamoto 1969 J. Phys. Soc. Japan **26** 529
- ⁷A D Piliya 1971 Proc. 10th Int. Conf. Phenomena in Ionized Gases (Oxford) ed R N Franklin (Oxford: Donald Parsons & Co. Ltd) p 320
- ⁸M N Rosenbluth 1972 Phys. Rev. Lett. **29** 565
- ⁹A D Piliya 1973 ZhETF. Pis. Red. **17** 374
- ¹⁰B Thidé, H Kopka, and P Stubbe 1982 Phys. Rev. Lett., **49**, 1561-1564
- ¹¹A Samimi, W A Scales, H Fu, P A Bernhardt, S J Briczinski, and M J McCarrick 2012 JGR: Space Physics, vol. 118, 502-514
- ¹²R B White and F F Chen 1974 Plasma Physics **16** 565-587
- ¹³J Preinhaelter and V Kopecký 1973 J. Plasma Phys. **10**, 1
- ¹⁴A K Ram and S D Schultz 2000 Phys. Plasmas **7**, 4084
- ¹⁵G Castro, D Mascali, S Gammino, G Torrì, F P Romano, L Celona, C Altana, C Caliri, N Gambino, D Lanaia, *et al* 2017 Plasma Sources Sci. Technol. **26** 055019
- ¹⁶F S McDermott, G Bekefi, K E Hackett, J S Levine, and M Porkolab 1982 Phys. Fluids **25** 1488
- ¹⁷H P Laqua 2007 Plasma Phys. Control. Fusion, **49** R1
- ¹⁸S K Nielsen, P K Michelsen, S K Hansen, S B Korsholm, F Leipold, J Rasmussen, M Salewski, M Schubert, M Stejner, J Stober, *et al* Phys. Scr. **92** (2017) 024001
- ¹⁹S K Hansen, S K Nielsen, M Salewski, M Stejner, J Stober and the ASDEX Upgrade team Plasma Phys. Control. Fusion **59** (2017) 105006
- ²⁰S K Hansen, S K Nielsen, J Stober, J Rasmussen, M Salewski, M Stejner and ASDEX Upgrade Team Phys. Plasmas **26**, 062102 (2019)
- ²¹A Najmi, B Eliasson, X Shao, G M Milikh, and K Papadopoulos (2016) Radio Science, 51, 704–717
- ²²D C Speirs, B Eliasson, and L K S Daldorff (2017) Journal Geophysics Research Space Physics, 122, 10,638–10,650
- ²³N E Andreev, V V Pustovalov, V P Silin, and V T Tikhonchuk 1973 ZhEFT. Pis. Red. **18** 10
- ²⁴W Seka, D H Edgell, J F Myatt, A V Maximov, R W Short, V N Goncharov, and H A Baldis Physics of Plasmas **16**, 052701 (2009)
- ²⁵H A Baldis and C J Walsh Phys. Rev. Lett. **47**, 1658 (1981)
- ²⁶A G Litvak, A M Sergeev, E V Suvorov, M D Tokman, and I V Khazanov 1993 Phys. Fluids B **5** 4347
- ²⁷B I Cohen, R H Cohen, W M Nevins, and T D Rognlien 1991 Rev. Mod. Phys. **63** 949
- ²⁸M Porkolab and B I Cohen 1988 Nucl. Fusion **28** 006
- ²⁹E Z Gusakov and A Yu Popov 2011 Nucl. Fusion **51** 073028
- ³⁰E Westerhof, S K Nielsen, J W Oosterbeek, M Salewski, M R De Baar, W A Bongers, A Bürger, B A Hennen, S B Korsholm, F Leipold, *et al* 2009 Phys. Rev. Lett. **103** 125001
- ³¹S K Nielsen, M Salewski, E Westerhof, W Bongers, S B Korsholm, F Leipold, J W Oosterbeek, D Moseev, M Stejner, and the TEXTOR Team 2013 Plasma Phys. Control. Fusion **55** 115003
- ³²S K Nielsen, A Jacobsen, S K Hansen, S B Korsholm, F Leipold, J Rasmussen, M Salewski, M Stejner, S Denker, J Stober, *et al* 2016 IEEE 07758400
- ³³S K Hansen PhD thesis *Parametric Decay Instabilities in the Electron Cyclotron Resonance Heating Beams at ASDEX Upgrade*, 31 August 2019
- ³⁴S K Hansen *et al* 2020, in writing.
- ³⁵E Z Gusakov and A Yu Popov 2009 AIP Conference Proceedings **1187**, 645
- ³⁶A Yu Popov and E Z Gusakov 2015 Journal of Experimental and Theoretical Physics, vol. 121, No. 2, pp. 362-374
- ³⁷A Yu Popov and E Z Gusakov Plasma Phys. Control. Fusion **57**, 025022 (2015)
- ³⁸E Z Gusakov and A Yu Popov Physics of Plasmas **23**, 082503 (2016)
- ³⁹E Z Gusakov, A Yu Popov, and A N Saveliev Physics of Plasmas **25** (2018) 062106
- ⁴⁰T D Arber, K Bennett, C S Brady, A Lawrence-Douglas, M G Ramsay, N J Sircombe, P Gillies, R G Evans, H Schmitz, A R Bell and C P Ridgers Contemporary particle-in-cell approach to laser-plasma modelling Plasma Phys. Control. Fusion **57** (2015) 113001
- ⁴¹M G Senstius, S K Nielsen, R G Vann, and S K Hansen Plasma Phys. Control. Fusion **62** (2020) 025010
- ⁴²A V Arefiev, I Y Dodin, A Köhn, E J Du Toit, E Holzhauser, V F Shevchenko, and R G L Vann 2017 Nucl. Fusion **57** 116024
- ⁴³E Z Gusakov, A Yu Popov, and P V Tretinnikov Nucl. Fusion **59** (2019) 106040
- ⁴⁴M G Senstius, S K Nielsen, and R G L Vann (2020). *Data for "Numerical investigations of parametric decay into trapped waves in magnetized plasmas with a non-monotonic density background"*, DTU Data. <http://doi.org/10.11583/DTU.11847174>

Chapter 6

PDI of eigenmodes of a non-monotonic density profile

In this chapter, we continue to study trapped waves in non-monotonic density profiles. Whereas the previous chapter was focused on the excitation of the trapped primary PDI daughter waves, this chapter focuses on showing that excited modes are eigenmodes, as they were discussed in section 2.4.3, and investigates how the eigenmodes interact in further decay processes.

6.1 Manifestation of eigenmodes

In this section we aim to find evidence that only a discrete spectrum of frequencies of trapped waves will be excited through TPD in a given density profile. These frequencies correspond to the eigenmodes of the density bump in the sense that waves at those frequencies will satisfy Bohr-Sommerfeld quantization when they perform an X-mode to EBW to X-mode conversion roundtrip as it was introduced in equation (2.49).

6.1.1 Stationary structures

When a gyrotron beam is feeding energy into eigenmodes of a density bump through PDIs, we expect one or two eigenfrequencies to dominate the spectrum near the UH frequency inside the density bump. As the eigenmodes are able to build up in amplitude with minor losses, they may eventually reach an amplitude where they start modifying even the background density of the cavity itself and a standing wave-like density perturbation can occur. To investigate this, we continue to use most of the parameters from the typical simulation in the previous chapter, but

x_{\min}	x_{\max}	n_x	n_e, n_i	T_e, T_i	\mathbf{B}_0	I_{pump}	f_0
-25 mm	25 mm	4000	$0.51e^{-(x/10 \text{ mm})^2} \times 10^{18} \text{ m}^{-3}$	100 eV	2.4 T $\hat{\mathbf{y}}$	$0.3 \frac{\text{kW}}{\text{mm}^2}$	140 GHz

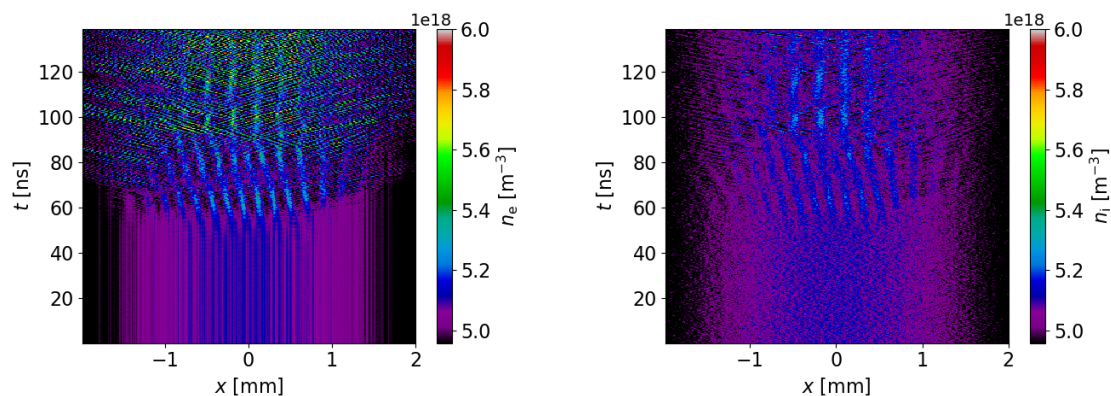
Table 6.1: A table showing the most relevant simulation parameters for the simulation in section 6.1.1. Remaining parameters are the same as those presented in chapter 5.

we pick a smooth and relatively wide density bump and decrease the pump intensity slightly. The most important parameters are shown in table 6.1. The time evolution of the electron density near the peak of the density is shown in figure 6.1a. The shown density is averaged over 10 periods of 70 GHz waves such that it corresponds to the background felt by waves near 70 GHz. The colorscale is chosen such that black regions approximately correspond to the UH layer for 70 GHz waves. After 60 ns, new structures clearly start to appear and at 100 ns they become more stationary. Around the same time as the structures appear, shorter scale waves start emanating outward from the center region. Similar observations are made even in the ion density in figure 6.1b with the exception that the propagating waves are of smaller amplitude. In the electron density, some sort of smaller amplitude stationary structure seems to be present for $t < 60$ ns whereas the ion density lacks this and appears to be more fuzzy. The associated longitudinal field is shown in 6.1c. While the stationary structures are also seen here, they appear to oscillate in time which is not seen in the densities. This might look different from the fields that were shown in chapter 5 but that is simply because we are only looking at the region around the peak density in these plots. We also note that the line integrated density, $\bar{n}_e(t) = \int_{x_0}^{x_1} n_e(x, t) dx$, changes only by $\bar{n}_e(t)/\bar{n}_e(0) \sim 10^{-7}$ over the entire domain and $\bar{n}_e(t)/\bar{n}_e(0) \sim 10^{-3}$ in the shown center region bounded by $x_1 = -x_0 = 2$ mm.

6.1.2 Smallest density structure

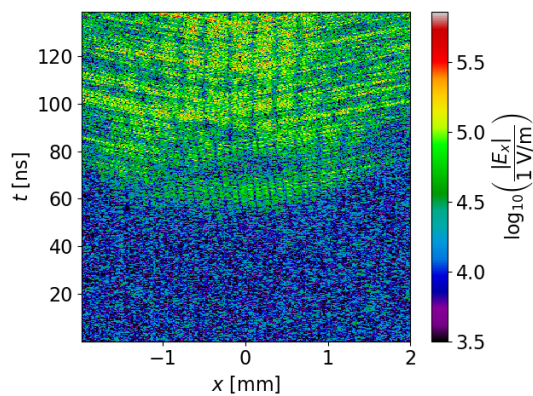
If the excited waves are indeed eigenmodes, they should be strongly dependent on the width and magnitude of the density bump. Near the UH layer, X-mode and EBWs have almost the same wavenumber so the fundamental $m = 0$ eigenfrequency will be close enough to the upper hybrid layer that the integrated phase difference during a roundtrip exactly cancels the phase shifts due to the linear mode conversions. For higher modenumbers, the difference in the wavenumber of X-mode and EBWs should be greater so the frequency drops as then the wavenumber of X-mode decreases whereas it increases for EBWs. However, mode frequencies will be placed closely near the UH layer since wavenumber are more sensitive to frequency there. At some point, the frequency will have decreased so much that the frequency of mode m , denoted f_m , becomes similar to the EC frequency. At the EC frequency, UH waves are absorbed but more importantly for us, the wavenumbers of X-mode and EBWs diverge. Because the wavenumber of EBWs goes to infinity in a less localized manner, high modenumbers are also placed closely near the EC frequency. Between the UH layer and the EC resonance, we expect more spread out and evenly spaced eigenmodes.

In the figures in figure 6.2, we scan the width and maximum density of a density bump of the form $n_e(x) = n_{\max} e^{-(x/\ell_n)^4}$ and find its eigenfrequencies by solving the Bohr-Sommerfeld quantization equation in (2.49) for integer m . Both the width and density scans in figures 6.2a and 6.2c show that the fundamental, i.e. $m = 0$, eigenfrequency is always close to the UH layer and that the higher modenumbers decrease in frequency but do not go below the EC frequency as argued above. The eigenfrequencies take on a sigmoid shape in the plots with a flattening at both low and high modenumbers, and with a steep section that bridges the ends. Figures 6.2b and 6.2d show the decrease in frequency when going up one modenumber for the same parameter scans. As was argued earlier, the modes are placed more closely in frequency near the UH layer and near the EC frequency. Between these frequencies, the modes become better



(a) The electron density near the density peak in time. The lower limit on the density scale is chosen so that it corresponds to the UH layer for 70 GHz waves. At least one of the main TPD daughter waves cannot propagate in the black regions.

(b) The ion density near the density peak in time. Density limits are chosen similar to figure 6.1a.



(c) The longitudinal electric field associated with eigenmodes which perturb the background density.

Figure 6.1: Eigenmodes manifest themselves by displacing electrons and ions which gives rise to stationary structures. The plots above show densities and electrostatic field averaged over 10 periods of a 70 GHz wave near the peak of the density profile.

separated. A narrower cavity will have better frequency separation because a shorter mode roundtrip will result in a smaller integrated phase difference throughout the trapping region. Increasing the density means that the UH layer and EC frequency get increasingly separated and the wavenumber of EBWs therefore become less sensitive to frequency as the EC resonance is further away. This means that eigenfrequencies also become more separated with greater density provided that the magnetic field and electron temperature are unchanged.

In the context of exciting these eigenmodes from a TPD instability of a 140 GHz gyrotron beam, we see in figure 6.2a that making the density bump narrower results in fewer eigenfrequencies in our permissible TPD decay range around $f_0/2$, as was illustrated in figure 5.1b on page 75. For the most narrow series using $\ell_n = 0.5$ mm, there are only two modes in this range at 70.04 GHz for $m = 0$ and 69.93 GHz for $m = 1$ which do not add up to $f_0 = 140$ GHz. In general, we cannot expect any two modes to add up to the pump exactly to the pump but TPD will still be possible into frequencies that are sufficiently close to the eigenfrequencies. This motivates us to investigate if there is a smallest density bump that will allow for excitation of eigenmodes through TPD.

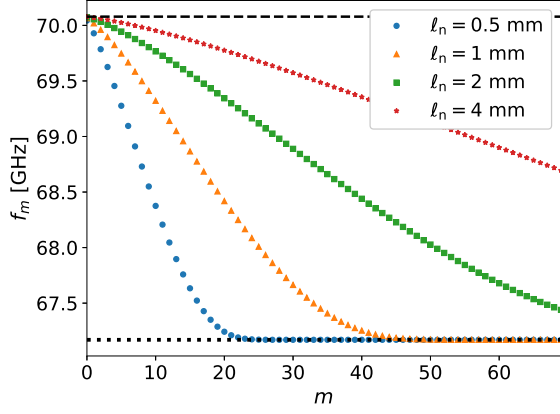
We run a number of simulations with the same super-Gaussian density profile as it allows for a more compact domain setup and thereby for cheaper simulations. The pump intensity is set to $I_{\text{pump}} = 1$ kW/mm² and the characteristic lengthscale of the density profile, ℓ_n , is varied. A selection of simulations is shown in figure 6.3. The mode number of an $f_0/2 = 70$ GHz wave, m_{70} , is introduced through the Bohr-Sommerfeld quantization in equation (2.49) as a measurement of the size of the cavity versus the wavenumber of the waves that are being excited

$$m_{70} = \frac{\int_{x_{j,1}}^{x_{j,r}} |k_{x,j}^+| - |k_{x,j}^-| dx \Big|_{f_j=70 \text{ GHz}} - \pi}{2\pi}. \quad (6.1)$$

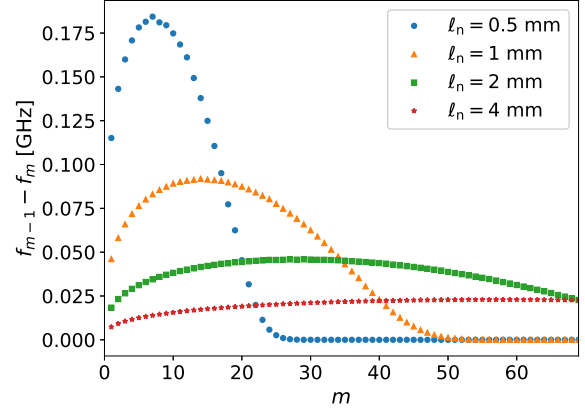
Waves at exactly 70 GHz will generally not be an eigenmode and m_{70} will therefore generally not be an integer. Note that it is possible for m_{70} to be negative from its definition if the phase difference between the X-mode trip and the EBW trip is less than the phase shift when converting at the turning points.

As can be seen in the figures in 6.3a-f, trapped waves are consistently excited with a comparable growth rate at various cavity sizes except when $m_{70} \lesssim 0$ in figure 6.3a. This suggests that as long as the cavity can support eigenmodes for frequencies greater than $f_0/2$, some pair of TPD daughter waves can be excited. However, when $m_{70} < 0$, only SRS can excite eigenmodes and at a lower growth rate. We also note that although eigenmodes are visibly excited in the second smallest simulation in figure 6.3b, they do not appear to become unstable to secondary wave interactions like in the larger cavities.

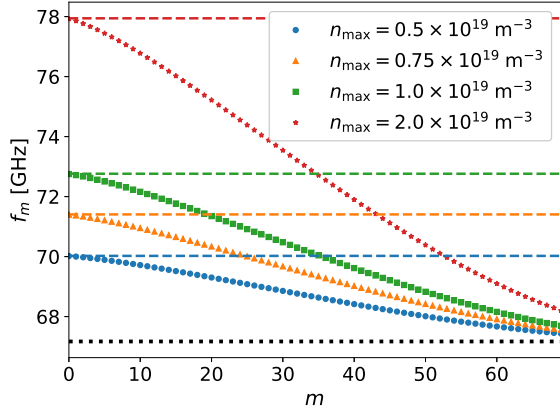
The growth rate of the excited eigenmodes is estimated as was done in the previous chapter; an exponential with a background level is fitted to the mean square longitudinal electric field inside the density bump, here for $|x| < 0.4\ell_n$. The characteristic growth rate of the fit is taken as an estimate of the growth rate of the primary PDI daughter waves. No estimate is made for the simulation in 6.3a. The estimated growth rates are shown against density bump size in figure 6.4. There is no clear dependence on the size from the estimates. Integer values of m_{70} close to simulations are plotted on top of the growth rates. Although it seems that the growth rate



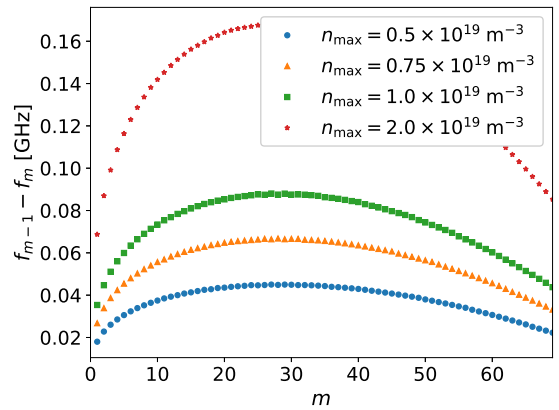
(a) Eigenfrequencies at different cavity widths as indicated in the legend. The dashed black line marks the UH layer and the black dotted line marks the EC frequency. The peak density is $n_{\max} = 0.51 \times 10^{19} \text{ m}^{-3}$.



(b) Difference in the eigenfrequencies shown in 6.2a as a function of modenum.



(c) Eigenfrequencies at different bump peak densities as indicated in the legend. The dashed colored lines mark the UH layer for the series of matching color in the legend. The black dotted line marks the EC frequency. The cavity width is $\ell_n = 2 \text{ mm}$.



(d) Difference in the eigenfrequencies shown in 6.2c as a function of modenum.

Figure 6.2: Eigenfrequencies of density bumps of the form $n_e(x) = n_{\max} e^{-(x/\ell_n)^4}$ with a temperature of $T_e = 100 \text{ eV}$ and a background magnetic field of $B = B_y = 2.4 \text{ T}$. Figures 6.2a and 6.2b show mode frequencies and change in frequency with modenum whilst scanning the width of the density bump. Figures 6.2c and 6.2d similarly show mode frequencies and change in frequency with modenum whilst keeping the width constant but changing the maximum density.

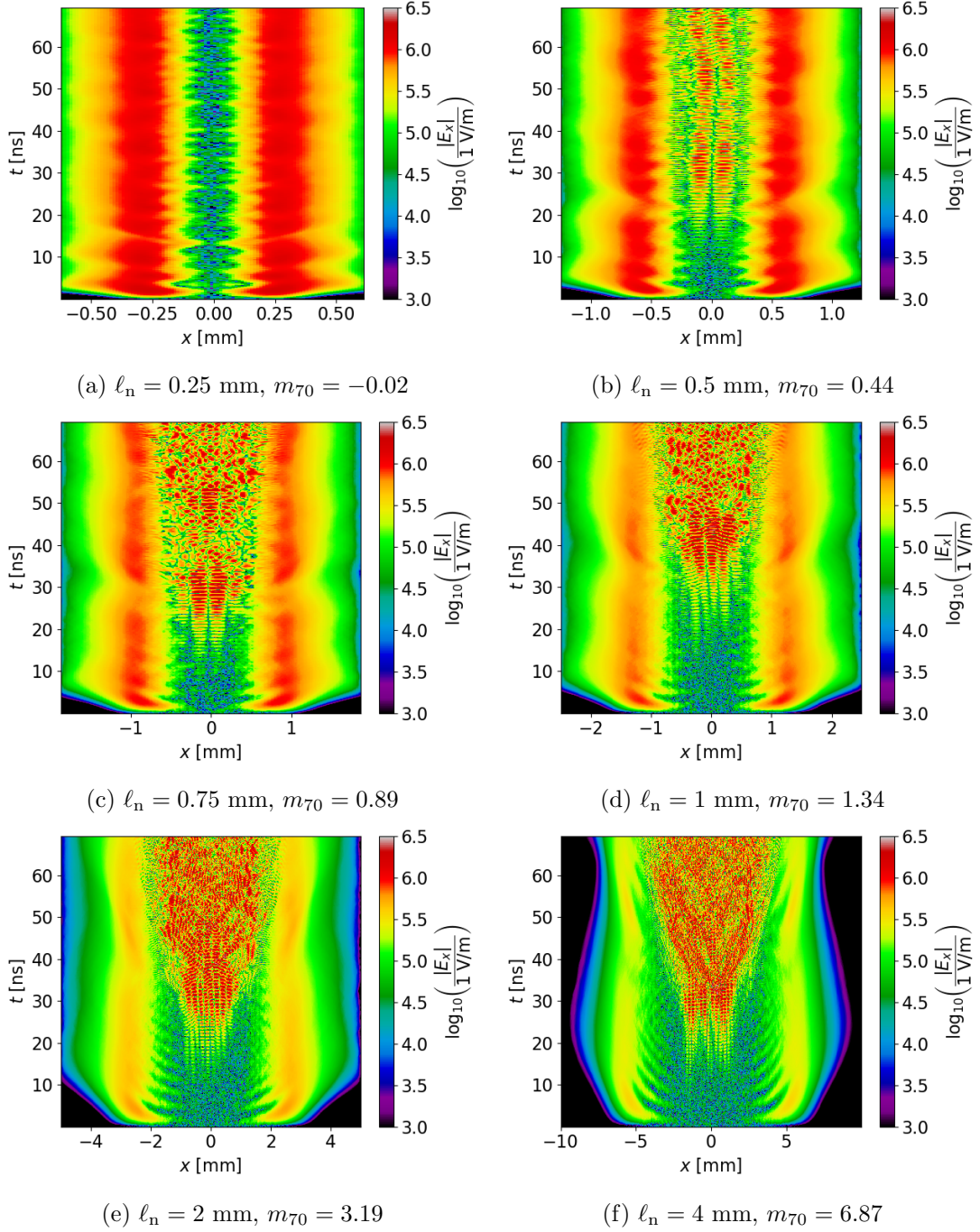


Figure 6.3: Time evolution of the longitudinal electric field when varying the size of the density bump. All simulations use $T_e = T_i = 100$ eV, $B = 2.4$ T, $f_0 = 140$ GHz and $I_{\text{pump}} = 1$ kW/mm². The density profiles are given by $n_e(x) = n_i(x) = 5.1 \times 10^{18} \text{ m}^{-3} \cdot \exp(-|x/\ell_n|^4)$, where ℓ_n is given below the plots along with the mode number for a 70 GHz wave, m_{70} , calculated from equation (2.49).

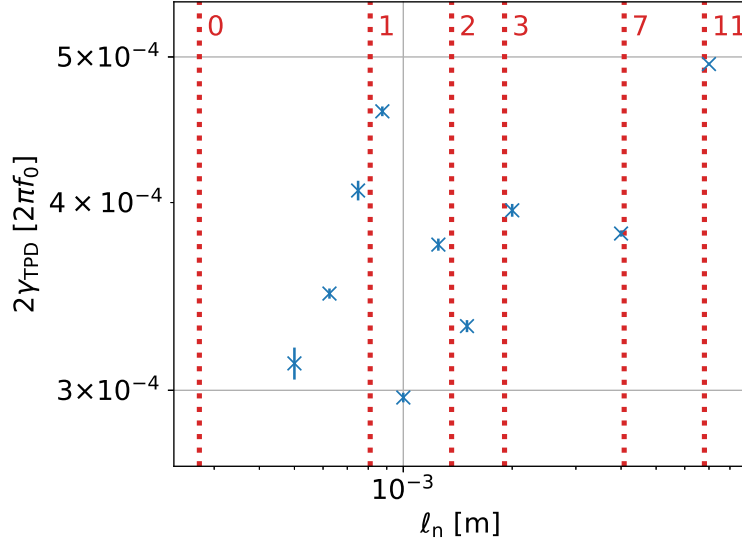


Figure 6.4: Growth rates for primary daughter waves versus the characteristic density lengthscale ℓ_n . The growth rate is found by fitting an exponential to the mean square longitudinal electric field for $|x| < 0.4\ell_n$. The longitudinal electric field of some simulations are shown in figure 6.3. The thick red dotted vertical lines are values of ℓ_n that correspond to integer of m_{70} as indicated at the top of the plot. Only integers of m_{70} that are close to a point are included.

is higher near the integers, it is not guaranteed that it is the eigenmode at $f_0/2$ that is excited but it is possible as was shown in figure 4 of the article in chapter 5. With a finer sweep, one might find an oscillatory behavior with a faster growth rate when an eigenmodes can be excited exactly and slower growth rate when the selection rules are only approximately satisfied for a particular eigenmode.

6.1.3 Absorption

As the primary PDIs feed energy into their daughter waves, the pump wave is correspondingly drained. Because the interaction rate increases with the amplitudes of the daughter waves, the absorption of the pump due to PDIs can expect to peak around when secondary wave interactions become unstable. Because the secondary PDIs drain the primary daughter waves, the absorption must temporarily decrease. This dynamic absorption should be measurable in simulations.

For this, we go back to the simulations in chapter 5 with different peak densities and vacuum at the boundaries where we can compare the intensity of the pump wave at either side of the density bump. This would be the density profiles in figures 5, 8a and 9a of the included article. In order to estimate the absorption we want to compare the incoming pump intensity at the left boundary with the pump intensity leaving the domain at the right boundary. We do this by first transforming the electric field in the homogeneous vacuum regions at both boundaries into

frequency and wavenumber space. Next, we integrate the peak in the squared field spectrum at the pump frequency and for positive k to avoid including backscattered waves in our estimate of the injected and transmitted pump intensity. By taking the fraction of the two, a measure of the transmitted field is obtained and subtracting it from unity, we obtain an absorption due to PDIs which we define as $\alpha_{\text{PDI}} \equiv (E_{\text{pump},\text{in}}^2 - E_{\text{pump},\text{out}}^2) / E_{\text{pump},\text{in}}^2$. We transform the electric field in the outermost 1 mm regions during a 10 ns window of time which we shift in order to get a time evolution of the absorption. The absorption is shown in figure 6.5 and a short simulation at virtually vacuum is included in addition to the simulations of the article in chapter 5. All simulations have a magnetic field of $B = 2.4$ T, a particle temperature of $T_e = T_i = 100$ eV and a pump intensity of $I_{\text{pump}} = 1$ kW/mm².

Starting with the simulation of vacuum marked by the red line in figure 6.5, we see that there is a short time in the beginning where there appears to be some degree of absorption but this is just due to a lag in the pump wave amplitude when comparing the level at the boundaries as the injected wave amplitude ramps up. Like in chapter 3, the pump wave ramps up using an arctan-function to avoid large discontinuities in the electric and magnetic fields. After the ramp up of the pump wave, the absorption in the vacuum simulation vanishes as it should. At higher density, the green line is at approximately half the density of the second harmonic UH layer of the pump wave so TPD is not possible. Whilst SRS is still possible the growth rates of the daughter waves are much smaller and no significant absorption is observed in the first 60 ns. The standard simulation density in chapter 5, i.e. $n_0 = 0.51 \times 10^{19}$ m⁻³ marked by the orange line, allows for TPD and here a large peak on the order of 10% is found after approximately 30 ns. The absorption drops off as secondary PDIs drain the primary PDI daughter waves. As the secondary PDIs saturate, the primary PDI picks up again and an oscillatory behavior is observed, albeit the subsequent peaks during the first 60 ns are approximately half the amplitude of the initial peak in absorption. For even higher density, i.e. the blue line, where TPD is still possible, the absorption takes longer to develop and do not reach exactly the same absorption as the simulation marked by the orange line but the order is comparable. Perhaps the interaction between the primary daughter waves happens to be weaker in this particular simulation. This could happen if the daughter waves are further away from the eigenfrequencies. For the orange and blue lines representing simulations where TPD is possible, we do not reach a steady state of absorption within the duration of our simulations.

Although 1-10% absorption does not mean that the gyrotron beam is anywhere near fully absorbed, it is still a significant effect when a 1 MW gyrotron beam might lose 100 kW power because it passes through a 1 cm density perturbation. Whilst the density bumps in the simulations are surrounded by vacuum, it is only a potentially small increase in density relative to the background, which allows for trapping, that really matters. As mentioned above, we do not see a stationary state situation where the absorption saturates at some level within our simulations. In the literature [39, 40, 41, 42], simulations using a reduced model with a limited number of predetermined PDIs following the initial TPD instability show that the PDIs drain each other's waves in an oscillatory manner which eventually saturates. The levels of all the PDI pump and daughter waves saturate such that total losses balance the absorption of the pump wave in the primary PDI. The power absorption in [41] for a simple PDI cascade involving only one secondary PDI is estimated to be 10% for TEXTOR parameters. The magnitude of the absorption in our simulations is then not out of proportion with literature. In our 1D simulations, losses of the

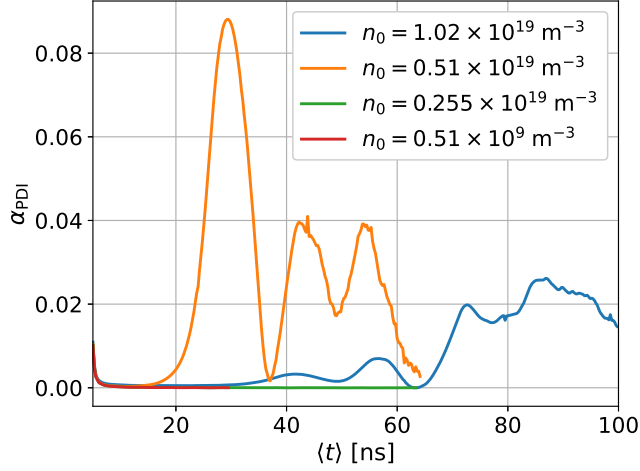


Figure 6.5: The absorption of a pump wave traversing a density bump due to PDIs. The time axis is an average of the 10 ns Fourier windows that generated the graph. The simulations correspond to figures 5, 8a and 9a of the included article in chapter 5. Note that simulations are of different length and that the red lines has a much lower density, representing virtually vacuum.

PDI daughter waves are fairly small. The cited literature identifies diffraction of the eigenmodes along the magnetic field lines as a significant loss mechanism. Extending our simulations to 2D with a direction parallel to the magnetic field might give more realistic absorption dynamics. However, the article [41] considers absorption to reach a stationary level of 10% on a timescale on the order of 100 ns. Although this timescale is similar to the length of our simulations, other articles such as [39, 42] consider characteristic timescales for the subsequent decay interactions to be on the order of μs - ms which is a lot longer than our simulations. This suggests that the dynamics might change after much more time has passes, however, it is challenging to simulate such timescales using a PIC code within available HPC resources. In general, we have to tailor our PIC simulations to investigate certain effects within a μs as the simulations might otherwise be too expensive.

6.2 Subsequent decay

In this section, we redesign our simulations to better investigate escaping waves that are generated due to PDIs involving the eigenmodes of a density bump. In section 6.2.1, we show a simulation where several evenly spaced peaks can be seen in frequency and wavenumber space near the half pump frequency. It is argued that each of these peaks are eigenmodes. In section 6.2.2, we show escaping waves in different parts of the frequency spectrum of the same simulation. We then proceed to look at interactions between the eigenmodes that can explain the observed frequencies.

x_{\min}	x_{\max}	n_x	δ	ℓ	w	n_0	T_e, T_i	\mathbf{B}_0	I_{pump}
-5 mm	5 mm	1600	2.5 mm	2 mm	5 mm	$2 \times 10^{19} \text{ m}^{-3}$	100 eV	2.2 T $\hat{\mathbf{y}}$	$0.03 \frac{\text{kW}}{\text{mm}^2}$

Table 6.2: A table showing the most relevant simulation parameters for the simulation in section 6.2. Remaining parameters are the same as those presented in chapter 5.

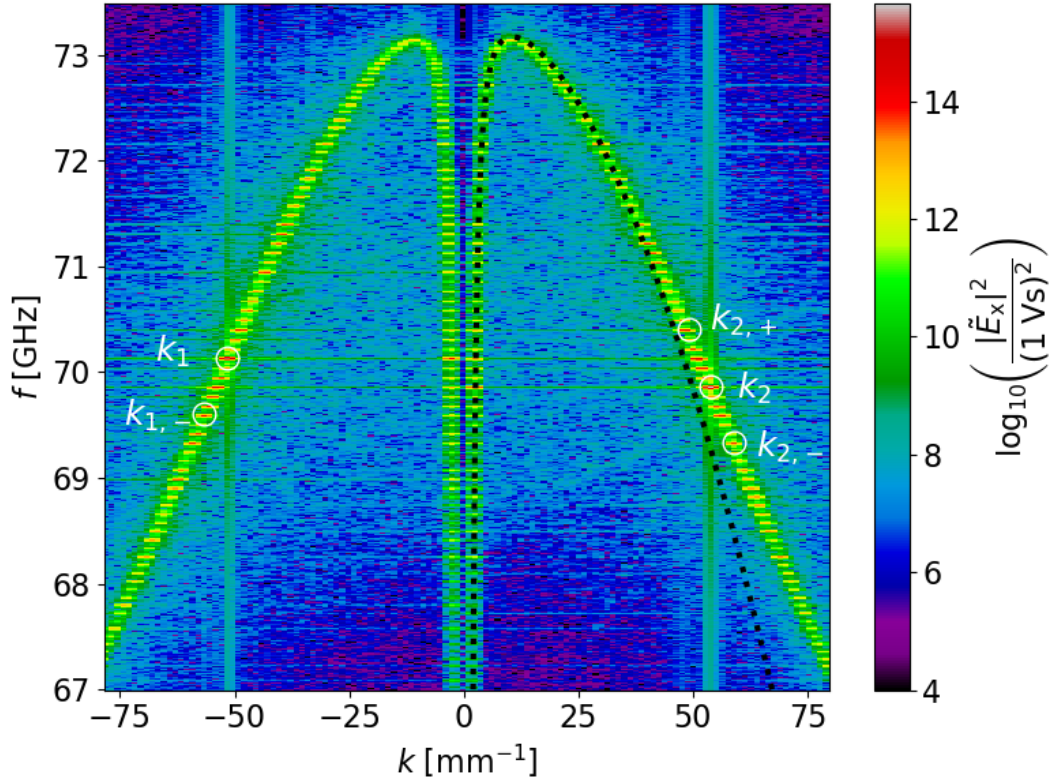
6.2.1 Eigenmodes in the Fourier spectrum

We now change the plasma parameters of our simulations a bit in order to place the $f_0/2$ frequency further away from the UH layer such that more modes might be excited both in primary PDIs, see figure 5.1b on page 75, but also in subsequent PDIs since ion modes may then combine with the primary daughter waves to produce upshifted daughter waves. At the same time, the ECR frequency is reduced to provide a faster group velocity for EBWs and thereby also a greater slope of its dispersion curve in wavenumber and frequency space. This is favorable because secondary PDIs involving ion waves will produce EBWs with an only slightly different wavenumber which puts lower demands on the spatial grid, and the greater slope also means that eigenmodes become more separated as was shown in figure 6.2 albeit by changing the density. To facilitate this, the density is once again chosen to be on the form

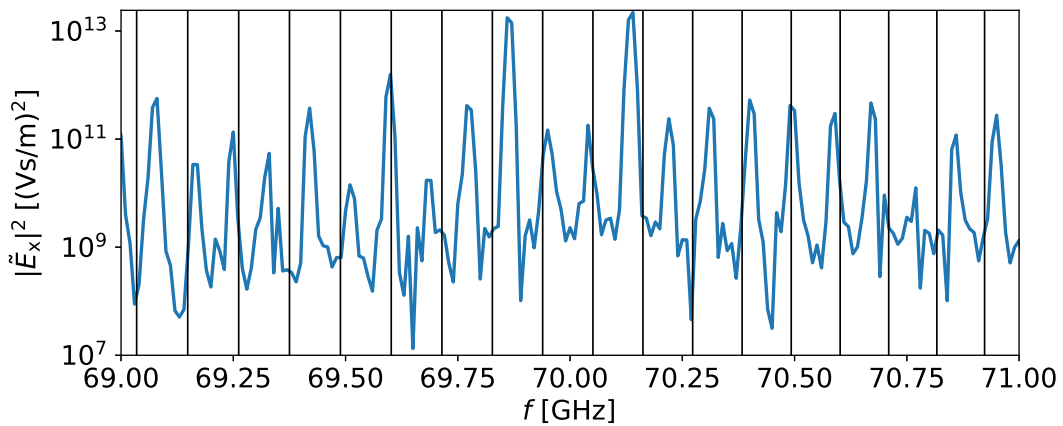
$$n_e(x) = n_i(x) = \begin{cases} n_0, & |x| \leq \delta \\ n_0 \left(1 - \frac{|x| - \delta}{\ell}\right), & \delta \leq |x| \leq \delta + \ell \\ 0, & \delta + \ell \leq |x| \leq w \end{cases}, \quad (6.2)$$

where the parameters are summarized in table 6.2. The pump intensity is reduced to also reduce the growth rate of the primary PDI daughter waves according to figure 13 in the article included in chapter 5. By reducing the growth rates of eigenmodes, we get longer windows of time to do FFTs over and this allows for a better frequency resolution to be obtained.

The resulting fast fourier transform (FFT) spectra over the homogeneous center region for $316 \text{ ns} < t < 416 \text{ ns}$ is shown in figure 6.6a. At this point, eigenmodes have been excited but the stochastic behavior observed in chapter 5 has not yet set in even though 416 ns is much longer than our previous simulations. The particular window of time is chosen so that the frequency resolution is sufficient to separate individual eigenfrequencies but still coarse enough that we can see the peaks in our spectrum without having to zoom in too much. Looking at figure 6.6a, the X-mode and EBW dispersion lines appear once again but with the UH layer found at a higher frequency. The dispersion relations in equation (2.37) are plotted on top for positive wavenumber and the agreement is best near the UH layer. Towards the ECR at 61.5 GHz, the dispersion relation begins to noticeably underestimate the wavenumber of EBWs. As opposed to the spectra in the previous chapters, this spectrum contains several separated peaks along the X-mode and EBW lines. We also note that the peaks are found at the same frequency along all four dispersion lines. Transforming only into frequency space, figure 6.6b confirms that peaks are found at seemingly regular frequency intervals away from the resonances. Combining the dispersion relations in equations (2.37) with the quantization condition in equation (2.49) and using the plasma parameters, the eigenmode frequencies are marked in figure 6.6b as black vertical lines. It is clear that the peaks do not fit perfectly in general, however, the overall



(a) The frequency and wavenumber spectrum near $f_0/2$. The dotted black line plotted on top is the cold and warm solutions to equation (2.37). Note that the agreement with the numerically found dispersion lines is better near the UH layer. The many peaks of different magnitude along the X-mode and EBW branches are the eigenmodes of the density bump. The white circles with white labels are particular eigenmodes of interest.



(b) Frequency spectrum at the center of the homogeneous region shown with the blue line. The vertical black lines are the frequencies of the eigenmodes as predicted by equations (2.37) and 2.49.

Figure 6.6: FFT spectra of the longitudinal electric field showing several peaks associated with eigenmodes of the cavity. The spectra are over a time window of $316 \text{ ns} < t < 416 \text{ ns}$. For figure 6.6a, the entire homogeneous region is transformed, whereas figure 6.6b only uses the $x = 0 \text{ mm}$ center line.

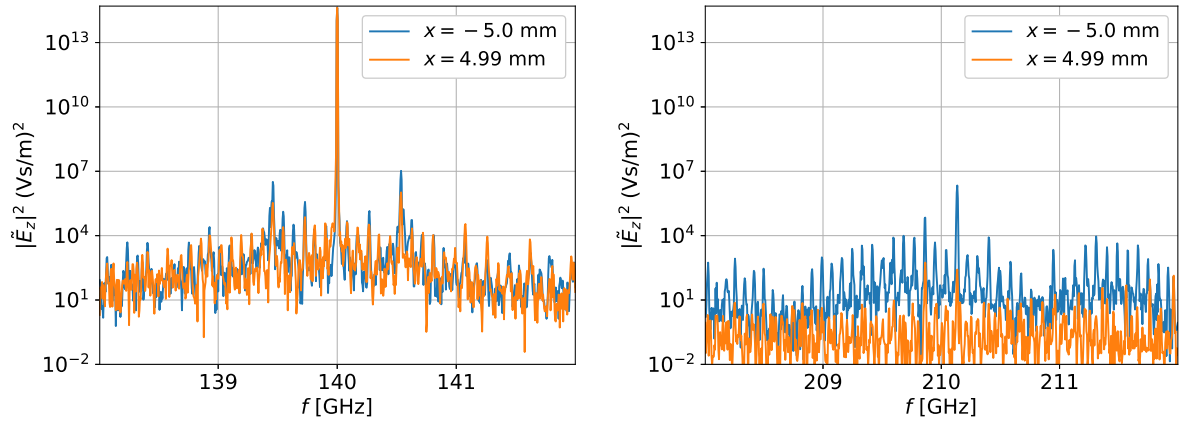
placement and separation appears to be appropriate. Looking at the two peaks closest to 70 GHz, the eigenfrequencies are rather close but the frequency shift is overestimated and this discrepancy increases with every following peak. Calculating the eigenmodes is very sensitive to the geometry and wavenumbers, and underestimating the wavenumber of EBWs means that the frequency shift between eigenmodes is overestimated. In principle, the many peaks might not be eigenmodes but could instead be excited from PDIs involving higher branches of IBWs as the frequency shift between peaks is approximately $90 \text{ MHz} \approx 5.4f_{ci}$. The result of this would be a noticeable population in the IBW spectrum with similar separation but as we will see in figure 6.9b in the next section, no such peaks are visible. We conclude that the many peaks actually are eigenmodes which have been excited to different amplitudes. The peaks labeled k_1 and k_2 satisfy the selection rules for the primary PDI in the homogeneous region, i.e. $k_0 = k_1 + k_2$ and $f_0 = f_1 + f_2$ where k_0, f_0 is a 140 GHz X-mode pump wave.

6.2.2 Escaping waves

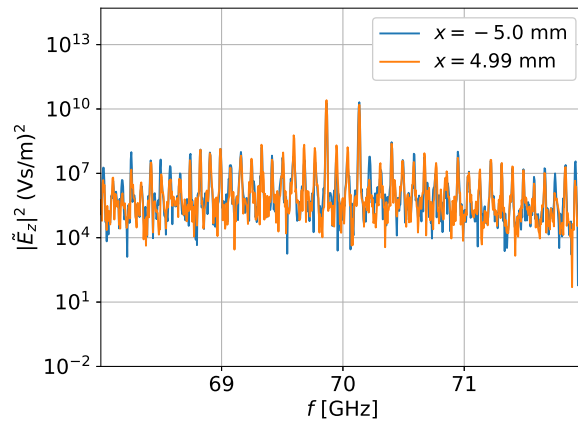
In magnetically confined fusion experiments, indications of PDIs involving a gyrotron beam are observed as stimulated emissions in different parts of the microwave spectrum. In the tokamaks TEXTOR and ASDEX, stimulated emission in the form of side bands to the 140 GHz gyrotron lines has been reported previously[36, 37, 18]. The side bands are typically shifted approximately by an integer times the LH frequency which is believed to be the result of a cascade of PIs involving both trapped UH and LH waves. The term PI is here used instead of PDI because some of these wave interactions are not necessarily decay of a wave but could be scattering or recombination processes. Stimulated emissions at approximate half gyrotron frequency, i.e. near 70 GHz, has also been reported at ASDEX Upgrade[18] and it has been proposed that emissions at higher half harmonics of the gyrotron frequency might also be observable[42]. In this section, we look for escaping waves near $f_0/2, f_0$ and $3f_0/2$, and look for evidence that they may be produced by PDIs.

By Fourier transforming the transverse electric field perpendicular to the magnetic field into frequency space at the left and right boundaries of the simulation in figure 6.6, we obtain a spectrum similar to a backscattered spectrum on the left, $x = -5 \text{ mm}$, boundary. The spectrum on the right, $x = 4.99 \text{ mm}$, boundary shows the waves that would continue past the density bump. The figures 6.7 show the frequency spectra at different frequency ranges of interest.

Starting with the pump frequency range, figure 6.7a shows that the majority of the pump wave is transmitted through the domain. However, several peaks with similar separation as the eigenmodes are also present, for the most part 1-2 orders of magnitude above what appears to be the noise level. These peaks are likely different combinations of eigenmodes. Aside from the pump wave, there are two peaks that are significantly greater than the rest of the spectra. These peaks are found symmetrically shifted around the pump frequency by $0.55 \pm 0.01 \text{ GHz}$. This is strong evidence that PDIs involving LH waves have been involved since $f_{LH} = 0.55 \text{ GHz}$ using the initial plasma parameters. By studying the eigenmodes in figure 6.6a and comparing with the corresponding spectra in the pump range in figure 6.9a and in the LH range in figure 6.9b, a cascade of PIs which can produce the desired two lines is illustrated in figure 6.8 and conservation of frequency and momentum is shown in table 6.3. In the figure and table, the term PI is used rather than PDI when it may not be a decay process. Furthermore, we employ the



(a) The frequency spectrum in the pump frequency range. (b) The frequency spectrum in the three halves pump frequency range.



(c) The frequency spectrum in the half pump frequency range, i.e. eigenfrequency range.

Figure 6.7: The frequency spectrum of escaping X-mode waves near half integers of the pump frequency on the boundaries. The blue lines represent waves that would be backscattered whereas the orange lines would continue on the other side of the density bump.

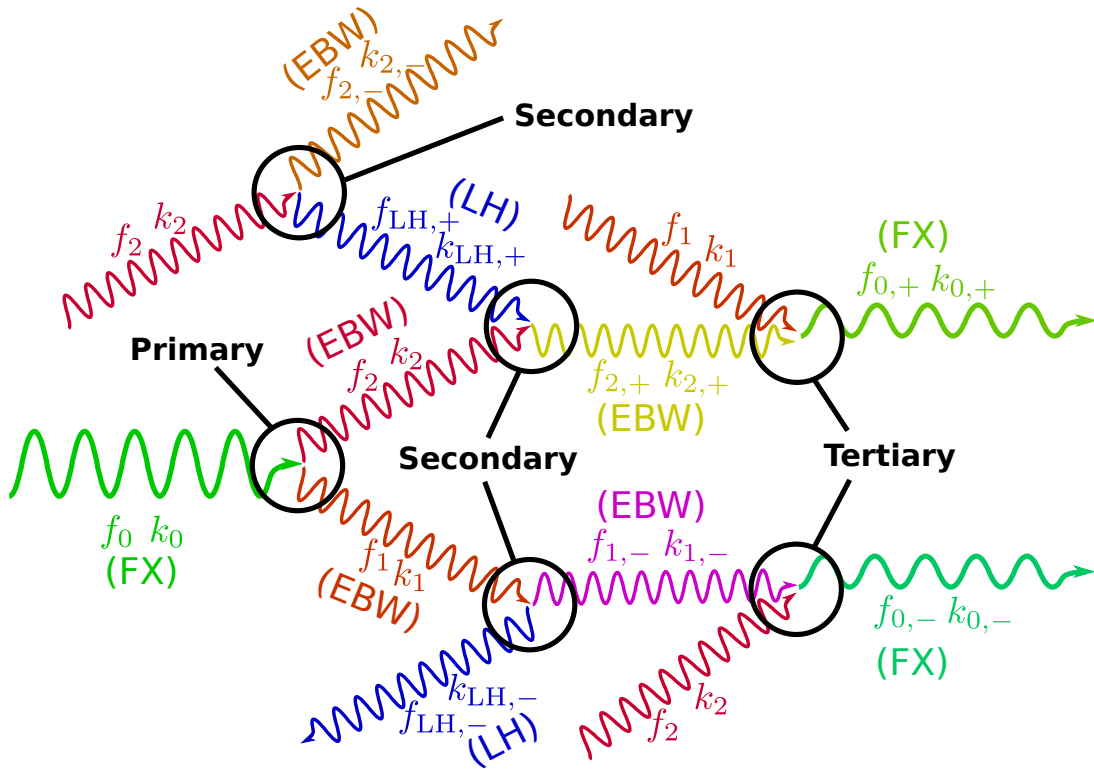


Figure 6.8: Illustration of a cascade of PIs that produces the up- and downshifted main sidebands in figure 6.7a. Each wave is labeled by its frequency and wavenumber as well as the type of wave in brackets. The short hand notation FX for fast X-mode and LH for LH wave has been used. The cascade consists of one primary TPD instability to produce two half frequency waves, three secondary PIs to produce up- and downshifted half frequency waves and finally two tertiary PIs to produce the sidebands.

Primary PDI

k_0	=	k_1	+	k_2	Δk	
2.5 ± 0.6		-51.5 ± 0.6		54.0 ± 0.6	0 ± 2	[mm ⁻¹]
f_0	=	f_1	+	f_2	Δf	
140.000 ± 0.005		70.140 ± 0.005		69.860 ± 0.005	0.00 ± 0.02	[GHz]

Secondary PIs

k_1	=	$k_{LH,-}$	+	$k_{1,-}$	Δk	
-51.5 ± 0.6		5.0 ± 0.6		-56.6 ± 0.6	0 ± 2	[mm ⁻¹]
f_1	=	$f_{LH,-}$	+	$f_{1,-}$	Δf	
70.140 ± 0.005		0.560 ± 0.005		69.600 ± 0.005	-0.02 ± 0.02	[GHz]

k_2	=	$k_{LH,+}$	+	$k_{2,-}$	Δk	
54.0 ± 0.6		-5.0 ± 0.6		59.1 ± 0.6	0 ± 2	[mm ⁻¹]
f_2	=	$f_{LH,+}$	+	$f_{2,-}$	Δf	
69.860 ± 0.005		0.560 ± 0.005		69.330 ± 0.005	-0.03 ± 0.02	[GHz]

k_2	+	$k_{LH,+}$	=	$k_{2,+}$	Δk	
54.0 ± 0.6		-5.0 ± 0.6		49.0 ± 0.6	0 ± 2	[mm ⁻¹]
f_2	+	$f_{LH,+}$	=	$f_{2,+}$	Δf	
69.860 ± 0.005		0.560 ± 0.005		70.400 ± 0.005	-0.02 ± 0.02	[GHz]

Tertiary PIs

k_1	+	$k_{2,+}$	=	$k_{0,+}$	Δk	
-51.5 ± 0.6		49.0 ± 0.6		-2.5 ± 0.6	0 ± 2	[mm ⁻¹]
f_1	+	$f_{2,+}$	=	$f_{0,+}$	Δf	
70.140 ± 0.005		70.400 ± 0.005		140.540 ± 0.005	0.00 ± 0.02	[GHz]

$k_{1,-}$	+	k_2	=	$k_{0,-}$	Δk	
-56.6 ± 0.6		54.0 ± 0.6		-2.6 ± 0.6	0 ± 2	[mm ⁻¹]
$f_{1,-}$	+	f_2	=	$f_{0,-}$	Δf	
69.600 ± 0.005		69.860 ± 0.005		139.460 ± 0.005	0.00 ± 0.02	[GHz]

Table 6.3: A table showing that the proposed PIs satisfy the energy and momentum conservation equations with the exception of one process. Δk and Δf are the right hand side subtracted from the left hand side of the shown equations. Only $\Delta k = 0$ and $\Delta f = 0$ means that both energy and momentum are satisfied and the PI can occur. This is the case for all the above PIs within the indicated errors except for the secondary PI that produces $k_{LH,+}$, $f_{LH,+}$ where a small frequency mismatch is marked with a bold font.

terms primary, secondary and tertiary PIs a bit loosely. We use primary for PDIs of the injected X-mode wave into UH waves. Secondary is used for all of the PIs that involve both UH and LH waves. Tertiary is used for the PIs where UH waves combine into escaping fast X-mode waves.

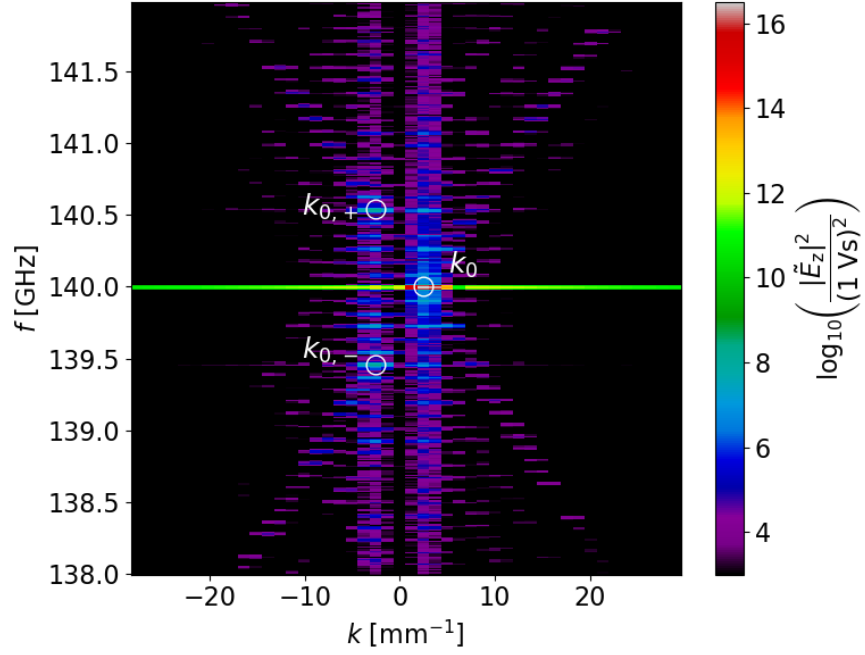
The first step of the proposed cascade is that the pump decays into two EBWs labeled k_1, f_1 and k_2, f_2 , where $f_1 - f_2 = f_{\text{LH}}/2$ and $k_1 \approx -k_2$. Next, each of the primary daughter waves decay into a downshifted EBW, $k_{1,-}, f_{1,-}$ and $k_{2,-}, f_{2,-}$ respectively, as well as an LH wave, $k_{\text{LH},-}, f_{\text{LH},-}$ and $k_{\text{LH},+}, f_{\text{LH},+}$. The LH waves have the same frequency but the wavenumbers are of opposite sign. The daughter wave $k_{2,-}, f_{2,-}$ does not further contribute to this cascade but the LH wave $k_{\text{LH},+}, f_{\text{LH},+}$ does. By recombining with the primary daughter wave k_2, f_2 , an upshifted EBW, $k_{2,+}, f_{2,+}$, is produced. Lastly, as the secondary daughter waves, $k_{1,-}, f_{1,-}$ and $k_{2,+}, f_{2,+}$, combine with the primary daughter waves, k_1, f_1 and k_2, f_2 , two left propagating fast X-mode waves are produced: one downshifted by f_{LH} and the other upshifted by the same amount.

Of all the mentioned processes, only one does not conserve both frequency and momentum and that is the process that produces the LH wave $k_{\text{LH},+}, f_{\text{LH},+}$. In principle, there are many other eigenmodes in figure 6.9a with a large amplitude and perhaps some other PIs that we have not looked into may be producing the LH waves. It is also possible that a small frequency mismatch is permissible. In 1D on a discrete grid, it is unlikely that any PI involving eigenmodes will satisfy the conservation equations perfectly but energy might still make it into the eigenmodes if the match is close enough. Because of the prominent homogeneous region, all the PDIs take place there and this means that other cascades of PDIs can produce the same results. The simplest possibility is direct scattering on the LH waves, i.e. $f_0 = f_{\text{LH}} + f_{0,-}$ and $f_0 + f_{\text{LH}} = f_{0,+}$ and similar for the wavenumbers. Another possibility is that the two secondary PDIs is replaced by four-wave interactions, i.e. $f_1 + f_2 = f_{1,-} + f_{2,+}$, however, this is a higher order process and would not produce LH waves at all. Figure 6.9a shows that the same eigenfrequencies are excited for both positive and negative wavenumbers. The eigenmodes that excite the left propagating escaping waves also exist with opposite sign of the wavenumber and may therefore excite right propagating escaping waves at the same frequencies. However, these modes may require a more extensive cascade of wave interactions to be excited from the pump wave. With this, the left propagating peaks should be greater than the right propagating ones, which they are.

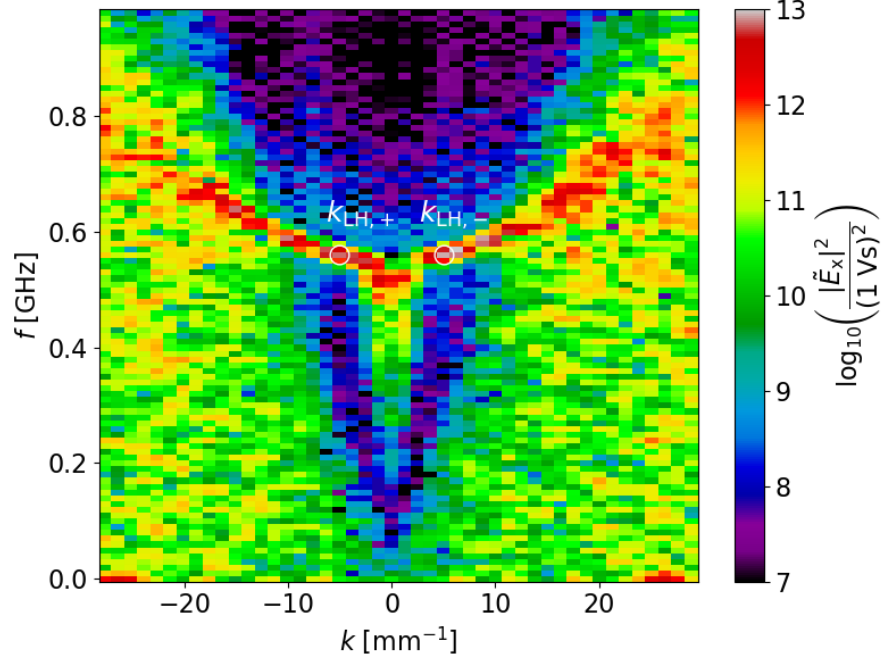
Looking at figure 6.7b, the spectrum at the three halves pump frequency is at a much lower level. This part of the spectrum also shows a number of peaks resembling the eigenmode structure but waves in this range primarily propagate left. To rationalize this, we argue that these waves must be combinations of the pump wave with an eigenmode. Due to the steep slope of fast X-mode in wavenumber and frequency space, $v_G \approx c$, only eigenmodes with negative wavenumbers are likely to satisfy the selection rules in combination with the pump, and this would produce another fast X-mode wave with negative wavenumber, i.e. one that propagates opposite of the pump. The two largest peaks correspond to $f_0 + f_1$ and $f_0 + f_2$.

Lastly, the half frequency spectrum is shown in figure 6.7c. The waves in this range are excited through PDIs and are supposed to be trapped by the UH layers, however, slow X-mode may tunnel through to the R cutoff and escape. Because there is vacuum at the boundaries, the intensities at different frequencies are directly comparable through their squared electric fields. With this in mind, it appears that the main radiative losses out of the cavity is actually in the trapped frequency range in this simulation. This might not be as significant with less steep

density profiles as waves will then have to tunnel further.



(a) Spectrum of the transverse electric field component near the pump frequency.



(b) Spectrum of the longitudinal electric field component near the LH frequency.

Figure 6.9: Spectra in wavenumber and frequency space near the pump frequency and near the LH frequency. White circles mark peaks of interest and the nearest white label is how they are references in the text.

Chapter 7

Conclusions and outlook

In this thesis, we have investigated PDIs of strong microwaves in magnetically confined fusion plasmas numerically using a fully kinetic PIC code. We have used a PIC code to study this because analytical theory of PDIs typically revolves around making assumptions that simplifies the plasma dynamics and allows for desired quantities to be isolated. Making the assumptions is a trade off between keeping the necessary physics for the problem at hand while simplifying the mathematics such that analytical progress can be made. In contrast to this, kinetic simulations using PIC codes model the plasma with only minor assumptions about how it behaves. The sought effects should then show themselves provided that the simulations have been designed with care and that no unexpected effects interfere. Interpreting the data can be challenging and certain simulations design choices can turn out to promote unexpected dynamics. The downside to kinetic simulations is that they generally take a lot of computational effort to complete and so they must often be run on an HPC cluster. Provided that the HPC resources are available, PIC code simulations offer a tool to validate that our analytical models include the relevant physical mechanisms, especially for intermediate steps which may not have been observed experimentally.

We started the thesis with introducing the basic terms and motivated the investigation in chapter 1. Fusion energy fits a growing demand that other present day sources of energy cannot satisfy. To get good performance in a magnetically confined fusion reactor, we must be able to heat and diagnose it, and high power microwave beams can be used for both. Although linear theory has described microwave operation well in the past, observations of nonlinear effects have been reported in recent years. The nonlinear effects are three-wave interactions known as PDIs and are believed to occur due to either wave amplification near the UH layer or due to trapping between multiple UH layers.

In chapter 2, we went on to discuss analytical theory on microwaves in plasmas. We derived wave characteristics for cold X-mode propagating perpendicularly to the magnetic field. This was relevant when describing the microwave pump beam in our simulations. We also discussed hot corrections to X-mode near the UH layer as well as the electrostatic EBWs and IBWs which are typical daughter waves of PDIs. We ended the chapter by introducing the theory necessary to understand why the UH layer may facilitate PDIs at a reduced pump intensity threshold, i.e. through wave amplification and trapping of waves between multiple UH layers.

Having introduced the analytical theory on microwave propagation in a plasma, chapter 3

discussed the numerical simulations of plasmas. In particular, we focused on PIC codes as we used the PIC code EPOCH in the following chapters. We derived an update scheme similar to the one used by EPOCH and demonstrated that simulations in EPOCH agree with wave properties of the analytical theory outlined in chapter 2. The chapters up until this point can be considered as an introduction to the subject without introducing many novel points.

In chapter 4, we specifically looked at PDIs of X-mode and EBWs near the UH layer due to amplification of the pump wave and its wavenumber changing by half an order of magnitude. The simulations showed nonlinear conversion of the X-mode pump into EBWs and an LH wave as well as linear conversion of the pump into an EBW at the UH layer. A series of simulations with a homogeneous region for wave identification in terms of wavenumber showed that also a PDI of the linearly converted EBW was possible in the homogeneous region. For this reason, an additional set of entirely inhomogeneous simulations were run, scanning the pump intensity. A PDI pump intensity threshold in both sets of simulations was found to be in agreement with analytical theory. This chapter served to verify that EPOCH displayed the expected wave behavior near the UH layer as well as to numerically validate that it is indeed PDIs that produce the stimulated emissions originating from the UH layer. Kinetic simulations of PDI at the UH layer have not previously been performed for parameters corresponding to a medium sized tokamak like ASDEX Upgrade to our knowledge.

Next, excitation of trapped X-mode and EBWs was the topic of chapter 5. Here, simulations of a beam passing through a density bump showed PDI of the pump wave into X-mode and EBWs that were trapped between two UH layers. The excitation was consistent over a range of plasma parameters and bump shapes. Two classes of PDIs were identified as being responsible for exciting the trapped waves, the fastest being TPD in which the pump decays into two trapped waves, and SRS being a slower process by which one trapped wave and one escaping wave are excited. If the density and magnetic field do not reach the 2nd harmonic UH layer for the pump wave, the fast TPD instability is not possible and only SRS is then possible. Whilst the simulations were of density bumps surrounded by vacuum for simulation purposes, the trapping regions were seen to amount to a small range in densities around the 2nd harmonic UH layer of the pump. In practice, this means that the density perturbation relative to the background need not be greater than what allows the PDI daughter waves to be trapped.

Lastly, chapter 6 focused on identifying the trapped waves excited through PDIs as being eigenmodes of the density bump. It was shown that the eigenmodes can grow to a magnitude where they even modify the stationary background density. A scan of density bump widths showed that there did seem to be a lower limit for PDIs to show themselves on the simulation timescale. However, excitation of trapped waves through PDIs was possible even when the width was comparable to the wavelength of EBWs at half the pump frequency, and their growth rates depended only weakly on the exact size. It was shown that there is a nonlinear absorption due the PDIs with an absorption rate which oscillates and may reach $\approx 10\%$. It was also shown how cascades of PDIs involving particular eigenmodes and ion waves can lead to escaping waves both in the pump frequency range as well as at three halves the pump frequency. However, for the particular simulation, escaping radiation due to tunneling of eigenmodes out of the density bump was greater than in the other frequency ranges.

Throughout this thesis, we have established PIC codes as a tool to study PDIs at ECRH relevant parameters. Because PDIs can lead to emissions at levels much higher than ECE in the

microwave spectrum and the level depends nonlinearly on pump intensity, it is imperative that we know when and how much we need to shield our microwave sensitive diagnostics. Gyrotrons are installed at many medium and large tokamaks and stellarators, and ECRH at the 2nd and 3rd harmonic are becoming more common. With our kinetic simulations, we have shown that density perturbations in the wrong part of the plasma may lead to strong scattering or a significant widening of the power deposition because of the absorption of the gyrotron into trapped modes near the 2nd harmonic UH layer. Finally, we note that the novelty also carries with it exciting new possibilities. Our simulations demonstrate that it is possible to excite waves in different frequency ranges including ion waves by injecting microwaves. This may turn out to be a means of generating fast ions or to run current locally in non-monotonic parts of the confined fusion plasma and it is especially promising if modes can be triggered inside the plasma core and targeted. The escaping radiation due to PDIs may also find diagnostic uses.

Bibliography

- [1] D. Eckhartt. Nuclear fuels for low-beta fusion reactors: Lithium resources revisited. *Journal of Fusion Energy*, 14(4), 1995.
- [2] Jeffrey P. Freidberg. *Plasma Physics and Fusion Energy*. Cambridge University Press, 2007.
- [3] J. Ongena and G. Van Oost. Energy for future centuries: Prospects for fusionpower as a future energy source. *Fusion Science and Technology*, 61:2T:3–16, 2012.
- [4] V. Shevchenko, G. Cunningham, A. Gurchenko, E. Gusakov, B. Lloyd, M. O’Brien, A. Saveliev, A. Surkov, F. Volpe, and M. Walsh. Development of electron Bernstein wave research in mast. *Fusion Science and Technology*, 52:2(202-215), 2007.
- [5] H. Maaßberg, M. Romé, V. Erckmann, J. Geiger, H. P. Laqua, N. B. Marushchenko, and the W7-AS Team. Electron cyclotron current drive in the wendelstein 7-as stellarator. *Plasma Physics and Controlled Fusion*, 47:1137–1163, 2005.
- [6] M. A. Van Zeeland, W. W. Heidbrink, S. E. Sharapov, D. Spong, A. Cappa, Xi Chen, C. Collins, M. García-Muñoz, N. N. Gorelenkov, G. J. Kramer, et al. Electron cyclotron heating can drastically alter reversed shear alfvén eigenmode activity in diii-d through finite pressure effects. *Nuclear Fusion*, 56(112007), 2016.
- [7] K. K. Kirov, F. Leuterer, G. V. Pereverzev, F. Ryter, W. Suttrop, and the ASDEX Upgrade team. Ecrh power deposition studies in asdex upgrade. *Plasma Physics Controlled Fusion*, 44:2583–2602, 2002.
- [8] J. Stober, M. Reisner, C. Angioni, A. Bañón Navarro, V. Bobkov, A. Bock, G. Denisov, E. Fable, R. Fischer, G. Gantenbein, et al. Exploring fusion-reactor physics with high-power electron cyclotron resonance heating on asdex upgrade. *Plasma Physics Controlled Fusion*, 62(024012), 2020.
- [9] S. Marsen, Y. Corre, H. P. Laqua, V. Moncada, D. Moseev, H. Niemann, M. Preynas, T. Stange, and The W7-X Team. First results from protective ecrh diagnostics for wendelstein 7-x. *Nuclear Fusion*, 57(086014), 2017.
- [10] V. F. Andreev, Yu. N. Dnestrovskij, M. V. Ossipenko, K. A. Razumova, and A. V. Sushkov. The ballistic jump of the total heat flux after ecrh switching on in the t-10 tokamak. *Plasma Physics and Controlled Fusion*, 46:319–335, 2005.

- [11] D. Rapisarda, B. Zurro, V. Tribaldos, A. Baciero, and TJ-II team. The role of a fast ion component on the heating of the plasma bulk. *Plasma Physics and Controlled Fusion*, 49:309–324, 2007.
- [12] Hans jürgen Hartfuß and Thomas Geist. *Fusion Plasma Diagnostics with mm-Waves*. Wiley-VCH, 2013.
- [13] M. Kikuchi and Y. Okumura. *Fusion Physics*. Fusion R&D Directorate, 2012.
- [14] J. Hovingh and R. W. Moir. Efficiency of injection of neutral beams into thermonuclear reactions. *Nuclear Fusion*, 34:629, 1974.
- [15] V. F. Shevchenko, R. G. L. Vann, S. J. Freethy, and B. K. Huang. Synthetic aperture microwave imaging with active probing for fusion plasma diagnostics. *Journal of Instrumentation*, 7:P10016, 2012.
- [16] P. Woskoboinikow, R. Erickson, and W. J. Mulligan. Submillimeter-wave dumps for fusion plasma diagnostics. *International Journal of Infrared and Millimeter Waves*, 4:1045–1059, 1983.
- [17] S. K. Nielsen, P. K. Michelsen, S. K. Hansen, S. B. Korsholm, F. Leipold, J. Rasmussen, M. Salewski, M. Schubert, M. Stejner, J. Stober, D. Wagner, and The ASDEX Upgrade Team. Recent development of collective thomson scattering for magnetically confined fusion plasmas. *Physica Scripta*, 92(024001), 2017.
- [18] S. K. Hansen. *Parametric Decay Instabilities in the Electron Cyclotron Resonance Heating Beams at ASDEX Upgrade*. PhD thesis, Technical University of Denmark, 2019.
- [19] M. Faraday. On a peculiar class of acoustical figures; and on certain forms assumed by groups of particles upon vibrating elastic surfaces. *Philosophical Transactions of the Royal Society of London*, 121:229–340, 1831.
- [20] A. A. Sukhorukov, Yu. S. Kivshar, O. Bang, and C. M. Soukoulis. Parametric localized modes in quadratic nonlinear photonic structures. *Physical Review E*, 63(016615), 2000.
- [21] F. Brau, H. Vandeparre, A. Sabbah, C. Poulard, A. Boudaoud, and P. Damman. Multiple-length-scale elastic instability mimics parametric resonance of nonlinear oscillators. *Nature Physics*, 7:56–60, 2011.
- [22] B. Thidé, H. Kopka, and P. Stubbe. Observations of stimulated scattering of a strong high-frequency radio wave in the ionosphere. *Physical Review Letters*, 49:1561–1564, 1982.
- [23] A. Samimi, W. A. Scales, H. Fu, P. A. Bernhardt, S. J. Briczinski, and M. J. McCarrick. Ion gyroharmonic structures in stimulated radiation during second electron gyroharmonic heating. *Journal of Geophysical Research: Space Physics*, 118:502–514, 2013.
- [24] A. Najmi, B. Eliasson, X. Shao, G. M. Milikh, and K. Papadopoulos. Simulations of ionospheric turbulence produced by hf heating near the upper hybrid layer. *Radio Science*, 51:704–717, 2016.

- [25] W. Seka, D. H. Edgell, J. F. Myatt, A. V. Maximov, R. W. Short, V. N. Goncharov, and H. A. Baldis. Two-plasmon-decay instability in direct-drive inertial confinement fusion experiments. *Physics of Plasmas*, 16(052701), 2009.
- [26] P. Michel, L. Divol, E. L. Dewald, J. L. Milovich, M. Hohenberger, O. S. Jones, L. Berzak Hopkins, R. L. Berger, W. L. Kruer, and J. D. Moody. Multibeam stimulated raman scattering in inertial confinement fusion conditions. *Physical Review Letters*, 115(055003), 2015.
- [27] A. V. Maximov, J. Myatt, W. Seka, R. W. Short, and R. S. Craxton. Modeling of stimulated brillouin scattering near the critical-density surface in the plasmas of direct-drive inertial confinement fusion targets. *Physical of Plasmas*, 11(2994), 2004.
- [28] A. D. Piliya. Decay instability in weakly inhomogeneous plasma. *10th International Conference on Phenomena in Ionized Gases 1971*, (320), 1971.
- [29] M. N. Rosenbluth. Parametric instabilities in inhomogeneous media. *Physical Review Letters*, 29(9), 1972.
- [30] A. D. Piliya. Threshold of decay instability in an inhomogeneous plasma. *ZhETF. Pis. Red.*, 17(7, 374), 1973.
- [31] F. S. McDermott, G. Bekefi, K. E. Hackett, J. S. Levine, and M. Porkolab. Observation of the parametric decay instability during electron cyclotron resonance heating on the versator tokamak. *The Physics of Fluids*, 25(1488), 1982.
- [32] H. P. Laqua, V. Erckmann, H. J. Hartfuß, H. Laqua, et al. Resonant and nonresonant electron cyclotron heating at densities above the plasma cutoff by o-x-b mode conversion at the w7-as stellarator. *Physical Review Letters*, 78(18), 1997.
- [33] S. K. Hansen. Parametric decay and anomalous scattering from tokamak plasmas. Master's thesis, Technical University of Denmark, 2016.
- [34] S. K. Hansen, S. K. Nielsen, M. Salewski, M. Stejner, J. Stober, et al. Parametric decay instability near the upper hybrid resonance in magnetically confined fusion plasmas. *Plasma Physics and Controlled Fusion*, 59(105006), 2017.
- [35] S. K. Hansen, S. K. Nielsen, J. Stober, J. Rasmussen, M. Salewski, M. Stejner, and AS-DEX Upgrade Team. Power threshold and saturation of parametric decay instabilities near the upper hybrid resonance in plasmas. *Physics of Plasmas*, 26(062102), 2019.
- [36] E. Westerhof, S. K. Nielsen, J. W. Oosterbeek, M. Salewski, M. R. De Baar, W. A. Bongers, A. Bürger, B. A. Hennen, S. B. Korsholm, F. Leipold, et al. Strong scattering of high power millimeter waves in tokamak plasmas with tearing modes. *Physical Review Letters*, 103(125001), 2009.
- [37] S. K. Nielsen, M. Salewski, E. Westerhof, W. Bongers, S. B. Korsholm and F. Leipold, J. W. Oosterbeek, D. Moseev, M. Stejner, et al. Experimental characterization of anomalous

- strong scattering of mm-waves in textor plasmas with rotating islands. *Plasma Physics and Controlled Fusion*, 55(115003), 2013.
- [38] E. Z. Gusakov and A. Yu. Popov. Low threshold parametric decay backscattering instability in tokamak electron cyclotron resonance heating experiments. *Physical Review Letters*, 105(115003), 2010.
- [39] A. Yu. Popov and E. Z. Gusakov. Low-threshold absolute two-plasmon decay instability in the second harmonic electron cyclotron resonance heating experiments in toroidal devices. *Plasma Physics and Controlled Fusion*, 57(025022), 2015.
- [40] E. Z. Gusakov and A. Yu. Popov. On a saturation mechanism of two-upper-hybrid-plasmon parametric decay instability in the second harmonic ecrh experiment. *Plasma Physics and Controlled Fusion*, 59(025005), 2017.
- [41] E. Z. Gusakov and A. Yu. Popov. Influence of the pump depletion on the anomalous absorption of the extraordinary wave in the second harmonic ecrh experiments. *Plasma Physics and Controlled Fusion*, 60(025001), 2018.
- [42] E.Z. Gusakov, A. Yu Popov, and P. V. Tretinnikov. The possibility of anomalous gyrotron frequency sub-harmonics emission in the ecrh experiments at toroidal devices. *Nuclear Fusion*, 59(106040), 2019.
- [43] Paul M. Bellan. *Fundamentals of Plasma Physics*. Cambridge University Press, 2006.
- [44] Thomas H. Stix. *Waves in Plasmas*. American Institute of Physics, 1992.
- [45] Ernesto Mazzucato. *Electromagnetic Waves for Thermonuclear Fusion Research*. World Scientific Publishing, 2014.
- [46] George B. Arfken and Hans J. Weber. *Mathematical Methods for Physicists*. Elsevier Academic Press, 2005.
- [47] D. G. Swanson. *Plasma Kinetic Theory*. CRC Press, 2008.
- [48] R. B. White and F. F. Chen. Amplification and absorption of electromagnetic in overdense plasmas. *Plasma Physics*, 16(565), 1974.
- [49] W. P. Allis, S. J. Bauchsbaum, and A. Bers. *Waves in anisotropic plasmas*. MIT Press, 1963.
- [50] Richard Fitzpatrick. *Plasma Physics: An Introduction*. CRC Press, Taylor and Francis Group, 2014.
- [51] M. Bornatici. Electron cyclotron emission and absorption in fusion plasmas. *Nuclear Fusion*, 23(1153), 1983.
- [52] Ira B. Bernstein. Waves in a plasma in a magnetic field. *Physical Review*, 109(1), 1958.

- [53] F. W. Crawford, G. S. Kino, and H. H. Weiss. Excitation of cyclotron harmonic resonances in a mercury-vapor discharge. *Physical Review Letters*, 13(7), 1964.
- [54] M. Thumm. Advanced electron cyclotron heating systems for next-step fusion experiments. *Fusion Engineering and Design*, 30(139-170), 1995.
- [55] J. Preinhaelter and V. Kopecký. Penetration of high-frequency waves into a weakly inhomogeneous magnetized plasma at oblique incidence and their transformation to Bernstein modes. *Journal of Plasma Physics*, 10(1, 1-12), 1973.
- [56] A. K. Ram and S. D. Schultz. Excitation, propagation, and damping of electron Bernstein waves in tokamaks. *Physics of Plasmas*, 7(10), 2000.
- [57] K. G. Budden. *Radio waves in the ionosphere*. Cambridge University Press, 1961.
- [58] N. A. Lopez and A. K. Ram. Mode-conversion of the extraordinary wave at the upper hybrid resonance in the presence of small-amplitude density fluctuations. *Plasma Physics and Controlled Fusion*, 60(125012), 2018.
- [59] M. Porkolab. Parametric processes in magnetically confined ctr plasmas. *Nuclear Fusion*, 18(367), 1978.
- [60] M. Porkolab and B. I. Cohen. Parametric instabilities associated with intense electron cyclotron heating in the mtx tokamak. *Nuclear Fusion*, 28(239), 1988.
- [61] M. G. Senstius, S. K. Nielsen, R. G. Vann, and S. K. Hansen. Particle-in-cell simulations of parametric decay instabilities at the upper hybrid layer of fusion plasmas to determine their primary threshold. *Plasma Physics and Controlled Fusion*, 62(025010), 2020.
- [62] M. Porkolab. Parametric decay instabilities in ecr heated plasmas. *Proceedings of 2nd Workshop Hot Electron Ring Physics*, 1:237–246, 1982.
- [63] H. L. Berk and D. L. Book. Plasma wave regeneration in inhomogeneous media. *The Physics of Fluids*, 12(3), 1969.
- [64] R. Wilhelm, V. Erckmann, G. Janzen, W. Kasperek, G. Müller, E. Räuchle, P. G. Schüller, K. Schwörer, and M. Thumm. Electron cyclotron resonance heating and confinement in the w VII-A stellarator. *Plasma Physics and Controlled Fusion*, 26(12A):1433–1444, 1984.
- [65] T. D. Arber, K. Bennett, C. S. Brady, A. Lawrence-Douglas, M. G. Ramsay, N. J. Sircombe, P. Gillies, R. G. Evans, H. Schmitz, A. R. Bell, and C. P. Ridgers. Contemporary particle-in-cell approach to laser-plasma modelling. *Plasma Physics and Controlled Fusion*, 57(113001), 2015.
- [66] A. V. Arefiev, I. Y. Dodin, A. Köhn, E. J. Du Toit, E. Holzauer, V. F. Shevchenko, and R. G. L. Vann. Kinetic simulations of x-b and o-x-b mode conversion and its deterioration at high input power. *Nuclear Fusion*, 57(116024), 2017.

- [67] I. Barth and N. J. Fisch. Reducing parametric backscattering by polarization rotation. *Physics of Plasmas*, 23(102106), 2016.
- [68] M. R. Edwards, Q. Jia, J. M. Mikhailova, and N. J. Fisch. Short-pulse amplification by strongly coupled stimulated brillouin scattering. *Physics of Plasmas*, 23(083122), 2016.
- [69] H. Ruhl. *Classical Particle Simulations with the PSC code*.
- [70] C. K. Birdsall and A. B. Langdon. *Plasma Physics via Computer Simulations*. CRC Press, 2004.
- [71] B. Fornberg. Generation of finite difference formulason arbitrarily spaced grids. *Mathematics of Computation*, 51(184):699–705, 1988.
- [72] K. S. Yee. Numerical solution of initial boundary value problems involving maxwell’s equations in isotropic media. *IEEE Transactions on Antennas and Propagation*, AP-14(3), 1966.
- [73] R. Courant, K. Friedrichs, and H. Lewy. Über die partiellen differenzengleichungen der mathematischen physik. *Mathematische Annalen*, 100:32–74, 1928.
- [74] J. Boris. Relativistic plasma simulation - optimization of a hybrid code. *Proceedings of the Fourth Conference on Numerical Simulation of Plasmas (Naval Research Laboratory, Washington DC)*, pages 3–67, 1970.
- [75] J. Villasenor and O. Buneman. Rigorous charge conservation for local electromagnetic field solvers. *Computer Physics Communications*, 69:306–316, 1992.
- [76] Y. Sentoku and A. J. Kemp. Numerical methods for particle simulations at extreme densities and temperatures: Weighted particles, relativistic collisions and reduced currents. *Journal of Computational Physics*, 227:6846–6861, 2008.
- [77] F. Pérez, L. Gremillet, A. Decoster, M. Drouin, and E. Lefebvre. Improved modeling of relativistic collisions and collisional ionization in particle-in-cell codes. *Physics of Plasmas*, 19(083104), 2012.
- [78] K. Nanbu and S. Yonemura. Weighted particles in coulomb collision simulations based on the theory of a cumulative scattering angle. *Journal of Computational Physics*, 145:639–654, 1998.
- [79] T. D. Arber and R. G. L. Vann. A critical comparison of eulerian-grid-based vlasov solvers. *Journal of Computational Physics*, 180:339–357, 2002.
- [80] A. B. Langdon. Effects of the spatial grid in simulation plasmas. *Journal of Computational Physics*, 6(2):247–267, 1970.
- [81] F. Fiuza, M. Marti, R. A. Fonseca, L. O. Silva, J. Tonge, J. May, and W. B. Mori. Effects of the spatial grid in simulation plasmas. *Plasma Physics and Controlled Fusion*, 53(074004), 2011.

- [82] N. Besse, G. Latu, A. Ghizzo, E. Sonnendrücker, and P. Bertrand. A wavelet-mra-based adaptive semi-lagrangian method for the relativistic vlasov–maxwell system. *Journal of Computational Physics*, 227:7889–7916, 2008.
- [83] E. Poli, A. G. Peeters, and G. V. Pereverzev. Torbeam, a beam tracing code for electron-cyclotron waves in tokamak plasmas. *Computer Physics Communications*, 136(90-104), 2001.
- [84] E. Poli, A. Bock, M. Lochbrunner, et al. Torbeam 2.0, a paraxial beam tracing code for electron-cyclotron beams in fusion plasmas for extended physics applications. *Computer Physics Communications*, 225(36-46), 2018.
- [85] C.V. Pereverzev. Beam tracing in inhomogeneous anisotropic plasmas. *Physics of Plasmas*, 5(3529), 1998.
- [86] S. J. Zweben, J. A. Boedo, O. Grulke, C. Hidalgo, B. LaBombard, R. J. Maqueda, P. Scarin, and J. L. Terry. Edge turbulence measurements in toroidal fusion devices. *Plasma Physics and Controlled Fusion*, 49:S1–S23, 2007.
- [87] A. Köhn, M. E. Austin, M. W. Brookman, K. W. Gentle, L. Guidi, E. Holzhauser, R. J. La Haye, J. B. Leddy, O. Maj, and C. C. Petty. The deteriorating effect of plasma density fluctuations on microwave beam quality. *EPJ Web of Conferences*, 203(1005), 2019.